Universitat Autònoma de Barcelona

Hybrid approach to obtain high-quality $BaMO_3$ perovskite nanocrystals for YBa_2Cu_3 O7–δsuperconducting nanocomposite

Natalia Chamorro Garcia

Universitat Autònoma de Barcelona

ICMAB INSTITUT DE CIÈNCIA DE MATERIALS DE BARCELONA

EXCELENCIA SEVERO OCHOA

CSIC Consejo Superior de Investigaciones Científicas

PhD Thesis

Hybrid approach to obtain high-quality $BaMO_3$ perovskite nanocrystals for $YBa_2Cu_3O_{7-\delta}$ superconducting nanocomposite

Natalia Chamorro Garcia

Supervised by:

Dr. Ramón Yáñez

Dr. Susagna Ricart

Tutor : Prof. Josep Ros

PhD program in Material Science

Chemistry department-Science faculty

2020

Report submitted for the achievement of Doctor degree in Material Science by:

Natalia Chamorro Garcia

Checked and accepted:

Dr. Ramón Yáñez

Universitat Autònoma de Barcelona

Dr. Susagna Ricart

ICMAB Institut de Ciència de Materials de Barcelona

Excelencia Severo Ochoa

CSIC

Prof. Josep Ros

Universitat Autònoma de Barcelona

Bellaterra, November 2020

Contents

Acknowledgments····· i

Abbreviations····· iii

Abstract····· vii

1. Introduction

1.1 Problem definition····· 1

1.2 Nanoscale system····· 2

1.2.1 Ceramic nanocomposite and oxide nanocrystals····· 2

1.2.2. BMO_3 perovskite family ····· 3

1.2.3 Synthesis strategies of BMO_3 NCs····· 6

1.2.3.1 Sol-gel····· 7

1.2.3.2 Hydro/solvothermal synthesis····· 8

1.2.3.3 Microwave synthesis····· 10

1.3 Superconducting nanocomposite····· 11

1.3.1 From nanocrystals synthesis to application····· 11

1.3.2 Basic principles in superconductivity ····· 13

1.3.3 Types of superconductors····· 14

1.3.4 $YBa_2Cu_3O_{7-\delta}$ superconductor material ····· 15

1.3.5 Vortex pinning ····· 16

1.3.6 Artificial pinning centers····· 17

1.4 Objectives and Outline····· 17

1.5 References····· 19

2 Experimental Methodologies

2.1 Nanocrystals synthesis procedures…… 26
2.2 Nanocomposites procedures…… 28
2.2.1 YBCO solution precursors…… 28
2.2.2 Preparation of YBCO colloidal precursor solution …… 29
2.2.3 Deposition technique via CSD…… 30
2.2.3.1 Spin-coating…… 30
2.2.3.2 Ink-jet printing…… 30
2.2.3.3 Substrate treatment…… 31
2.2.4 Nanocomposite thermal process…… 31
2.3 Characterization techniques …… 33
2.3.1 Dynamic light scattering…… 35
2.3.2 Spectroscopy…… 37
2.3.2.1 Raman spectroscopy…… 37
2.3.2.2 Energy Dispersive X-Ray Analysis …… 37
2.3.2.3 X-ray Photoelectron Spectroscopy…… 38
2.3.2.4 Infrared Spectroscopy …… 38
2.3.3 Thermal Gravimetric Analysis…… 39
2.3.4 Microscopy techniques…… 39
2.3.4.1 Optical Microscopy…… 39
2.3.4.2 Transmission Electron Microscopy …… 40
2.3.4.3 Scanning Electron Microscopy…… 41
2.3.5 X-ray Diffraction…… 42
2.3.6 Solid-state Nuclear Magnetic Resonance…… 43
2.3.7 Selected Area Diffraction Pattern…… 43
2.3.8 Physical characterization of superconducting properties…… 45
2.4 References…… 46

3 Novel hybrid approach to obtain high-quality $BaZrO_3$ perovskite nanocrystals

3.1 Introduction····· 50

3.2 Barium Zirconate synthesis····· 51

3.2.1 Previous Experiments····· 51

3.2.2 The optimization of $BaZrO_3$ NCs synthesis····· 53

3.2.3 Homogeneity and stability of the $BaZrO_3$ NCs colloidal solution··· 54

3.2.4 IR and 13C solid NMR spectra $BaZrO_3$ NCs····· 57

3.2.5 Importance of the stoichiometry ratio on $BaZrO_3$ NCs synthesis··· 58

3.3 Tuning the synthesis parameters····· 60

3.3.1 Effect of the temperature ····· 60

3.3.2 Effect of the reaction time····· 61

3.3.3 Concentration and polyol type effect····· 63

3.3.4 Concentration effect on NCs sizes and shape····· 65

3.4 Microwave methodology ····· 66

3.5 Hybrid solvothermal method····· 68

3.5.1 Which is the role of ammonia? ····· 68

3.5.2 Importance of water····· 70

3.5.3 Monodispersity and crystallinity····· 71

3.5.4 Unraveling the mechanism insight····· 73

3.6 Conclusions····· 74

3.7 References····· 75

4 General hybrid approach to synthesise BMO_3 perovskite nanocrystals

4.1 Introduction····· 82

4.2 Changing the tetravalent cation····· 82

4.2.1 $BaMO_3$ (M= Ti^{4+}, Zr^{4+} and Hf^{4+}) synthesis····· 83
4.2.2 Tuning synthetic parameters ····· 86
4.2.2.1 Temperature and time····· 86
4.2.2.2 Water effect····· 90
4.2.3 The different behaviour of $BaTiO_3$ NCs····· 93
4.2.3.1 Control of the sizes and shape of $BaTiO_3$ NCs····· 93
4.2.3.2 $BaTiO_3$ structure····· 96
4.2.4 Microwave route····· 97
4.3 Changing the divalent cation····· 98
4.3.1 $SrTiO_3$ NCs····· 99
4.3.2 $SrZrO_3$ and $SrHfO_3$ NCs····· 100
4.4 Doped Barium Zirconate····· 101
4.5 Conclusions····· 104
4.6 References····· 105

5 Nanocomposites of of $YBa_2Cu_3O_{7-\delta}$ layers

5.1 Introduction····· 112
5.2 Stability of the NCs onto YBCO matrix····· 114
5.2.1 TFA-YBCO precursor solution····· 115
5.2.2 LF-YBCO and FF-YBCO precursors solution····· 119
5.3 YBCO nanocomposite····· 121
5.3.1 TFA-YBCO nanocomposites····· 124
5.3.1.1 The pyrolysis process····· 124
5.3.1.2 Growing process via convectional thermal annealing····· 126
5.3.1.3 Growth process via flash heating ····· 131
5.3.1.4 Multideposition process····· 133
5.3.2 LF-YBCO nanocomposites····· 134
5.3.3 FF-YBCO nanocomposite····· 136

Contents

5.4 Conclusions····· 138
5.5 References····· 139

6 General conclusions····· 144

Scientific output····· 149

Acknowledgements

In this section, I would like to thank all the people who have supported me during this Thesis. I want to express my acknowledgments to all the people who in one way or another have accompanied me during this period, which has been a very important stage in my life. To thanks all of them I prefer to write this section in my mother tongue.

En primer lugar, agradecer a mis directores de tesis: Dr. Susagna Ricart y Dr. Ramón Yáñez y a mi tutor: Prof. Josep Ros, quienes me dieron la oportunidad de iniciar mi doctorado, confiaron en mí y me dieron su apoyo para completarlo. A Susagna por estar siempre disponible a debatir, ayudar y guiarme por este camino. A Ramon por darme alas para poder volar en diferentes direcciones y apoyarme en todo momento. También mencionar a la Prof. Teresa Puig y Prof. Xavier Obradors los cuales aun no siendo mis directores han seguido mi trabajo de cerca y se han involucrado en él. El hecho de haber podido realizar mi doctorado en UAB en colaboración con el grupo de SUMAN del ICMAB me ha permitido vislumbrar y trabajar en un nuevo campo científico para mí, lo cual me ha aportado nuevos conocimientos científicos.

Esta tesis no hubiera sido posible sin la ayuda del personal administrativo y técnico de UAB y ICMAB. Por ello quiero agradecer el personal del departamento de química por toda la ayuda que me han dado al realizar el papeleo de estos años. Así como la administración del ICMAB. También agradecer a los servicios técnicos tanto de UAB como ICMAB los cuales sin ellos no estaría aquí: (Servei de microscòpia (UAB), TEM (ICMAB), TGA, XPS, Sala blanca (ICMAB), Rayos-X, ect...)

Ahora que empiezo a ver el final de este camino, puedo decir que hay una gran diferencia desde que empecé el doctorado hasta ahora. Durante estos años siento

que he crecido tanto profesional como personalmente, todo esto gracias al apoyo que he recibido por todas aquellas personas que han estado a mi lado y que sin ellas no habría llegado a donde estoy hoy en día. Poco a poco esta gente que te rodeada diariamente empieza a formar parte de tu propia familia.

Empezando por mi compañero de laboratorio durante casi todo mi doctorado Jordi Martínez (grumpy). El cual me ha enseñado lo que significa perseverancia, lidiar con dificultades científicas, valorarse y mucho más. Ha sido mi compañero de batallas durante muchos años y un gran amigo. Además, por el laboratorio han pasado mucha gente, alumnos, TFG, veranitos los cuales siempre dejan una pequeña huella. En especial Diana que empezó como TFG y se ha quedado en la familia hasta acabar el doctorado (mucha suerte peque) y Abel que también decidió quedarse con la family.

Alguien que se ha hecho muy importante dentro y fuera del ámbito laboral, Coco, me has enseñado muchísimo tanto científicamente como de la propia vida. Contigo he podido ver cuál será mi futuro :). Gracias.

No solo a mi grupo de investigación sino a todos aquellos grupos de la planta de química inorgánica. Han pasado muchísima gente por ellos la cual no necesitáis que me ponga a nombrar uno a uno ya sabéis perfectamente quienes sois. Habéis estado ahí siempre en los momentos bajos, en las alegrías, en las fiestas, en las resacas, en la salud y en la enfermad. Y lo bonito de esto es que aun acabando esta etapa de mi vida sé que con la mayoría de vosotros voy a seguir en contacto. Aún me quedan muchas chapas que aguantar lo sé.

Additionally, I would like to thanks to Prof. Nicola Pinna for give me the opportunity to stay in his research group (functional materials) at the Humboldt-Universität zu Berlin. In particular thanks to Alex, my German brother who taught me and advise me in all moment and remind me that German people could be funny too ;). Giulia my crazy Italian lab mate, it wouldn't be the same without her happiness there.

Finalmente, agradecer a mi gente fuera del ámbito científico que durante este camino siempre han estado ahí para animarme. Lidia que ha sabido plasmar lo que quería para hacer en la portada, Gracias. Y como no, a mi familia por estar siempre ahí y haberme ayudado y apoyado en todo.

Gracias.

Abbreviations

NP	Nanoparticle
NC	Nanocrystal
REBCO	$REBa_2Cu_3O_7$ (RE = rare earths)
YBCO	$YBa_2Cu_3O_7$
TREG	Tryethilene glycol
DEG	Diethylene glycol
TEG	Tetraethylene glycol
LTS	Low temperature superconductors
HTS	High temperature superconductors
HRTEM	High-resolution transmission electron microscopy

STEM	Scanning Transmission Electron Microscope
MW	Microwave
SAED	Selected-Area Electron Diffraction
TGA	Thermodynamic Analysis Gravimetric
TEA	Triethylamine
EDX	Energy Dispersive X-ray Spectroscopy
XRD	X-ray Diffraction
XPS	X-ray Photoemission Spectroscopy
CSD	Chemical solution deposition
YBCO	$YBa_2Cu_3O_{7-\delta}$
H_c	Critical Magnetic field
J_c	Critical Current
T_c	Critical Temperature
LAO	$LaAlO_3$
STO	$SrTiO_3$
CSD	Chemical solution deposition
YBCO-TFA	YBCO-trifluoroacetate
YBCO-LF	YBCO -low fluorine

YBCO-FF	YBCO-Fluor free
SC	Spin-coating
IJP	Ink-jet printing
SQUID	Superconductor Quantum Interference Device
CCs	Coated conductors
CTA	Conventional Thermal Annealing
FH	Flash Heating
CTA	Conventional thermal annealing
APC	Artificial pinning centers

Abstract

This thesis describes the synthesis and characterization of novel perovskite BMO_3 nanocrystals and its application improving properties of superconducting material. The developed synthesis protocols allowed to tune nanocrystals' size and achieve long-time stability in solutions with high salt media content. These new properties in the nanocrystals were exploited to embed them into a superconducting material, $YBa_2Cu_3O_{7-\delta}$, enhancing the superconducting properties of the material.

The general trends of BMO_3 have been unravel using a hybrid solvothermal methodology based on the specific combination of aqueous sol-gel and solvothermal treatments. Using this methodology we reported a general, easy, fast and reproducible synthesis route of BMO_3 nanocrystals. Moreover, we present detailed studies of different synthetic conditions as well as insights in the mechanism of the nanocrystal's formation. Considering previous approximations to this perovskite family, our methodology provides highly crystalline shape-defined nanocrystals with a drastic reduction on reaction time. Through the study of $BaZrO_3$ nanocrystals we postulated the governing mechanism tunning the sizes of the nanocrystals. This proposed mechanism proved to be not only specific to this case but also applicable to other perovskites. Our hybrid methodology demonstrated the successful synthesis of $BaMO_3$ M= (Ti^{4+}, Zr^{4+} and Hf^{4+}) nanocrystals, besides of, obtaining $SrTiO_3$ when changing the divalent cation for Sr^{2+}.

We have studied the applications of the synthesized nanocrystals improving the superconducting properties of nanocomposites films prepared by chemical solution deposition using precursor solution of Yttrium, Barium and Copper salts. Additionally, the nanocrystals showed long term high stability in different $YBa_2Cu_3O_{7-\delta}$ precursor solutions even at high nanocrystals concentration.

Herein, we demonstrate for the first time, that non-reactive BMO_3 (M= Zr^{4+} and Hf^{4+}) nanocrystals are suitable for growing high quality thin and thick films using chemical solution deposition. Furthermore, we also demonstrated that the composition and sizes of the nanocrystals are a crucial factor for tailoring vortex pinning performances in applied magnetic fields.

In conclusion, we not only present the achievement of easily tunable-size and high-stable BMO_3 perovskite nanocrystals but demonstrated their effectiveness to enhance the superconducting properties when the nanocrystals are mixed into $YBa_2Cu_3O_7$ matrix. Given the novelty and potential relevance of our hybrid method in a deep range of nanoscale systems.

1

Introduction

1.1 Problem definition

In the era of electricity, the use of sustainable energy sources worldwide has become a real need. This requires investment in a methodology that improves our living standards. Almost 20% of the generated electricity is lost in the form of heat or light, due to the resistance of the material and the device. For that reason, one of the main goals nowadays is to reduce the resistance of the materials to improve the electrical efficiency. Among the different strategies, one of the most promising alternatives that have emerged in the last decades is the use of superconducting materials.

One of the most feasible superconductors that could lead to a real breakthrough in the energy department is $YBa_2Cu_3O_{7-\delta}$. The aim of this thesis is to improve the superconducting properties of $YBa_2Cu_3O_{7-\delta}$ films by adding nanocrystals in the superconducting matrix. The addition of nanocrystals in the matrix has been proved to be quite effective in terms of improving the performances of these layers. The nanocrystals can act as artificial pinning centres if some requirements are meet. These requirements are related to the nanocrystals size, morphology, and the manner in which they are distributed through the superconductive matrix. In order to control all these parameters a deep knowledge about the insights of these nanoscale systems is required.

In this thesis we attempt to acquire this knowledge and transfer it to the nanocomposite application. For this we studied a specific nanocrystal family (BMO_3) compound. Firstly, the attention was focused on the importance of the nanoscale systems, optimizing the synthesis of the BMO_3 NCs and tune the parameters of these NCs to comply with the requirements needed for our application. Secondly, we tested the applicability and effectiveness of these NCs in a superconductor matrix $YBa_2Cu_3O_{7-\delta}$ (nanocomposite).

1.2. Nanoscale system

In the last 30-35 years nanoscale systems began to attract the attention of the scientist in different fields of science like physics, chemistry, biology, etc. The transition from macro size to nanoscale (1–100 nm) lead to important changes in physicochemical properties of individual compounds and systems.[1]

When a material decreases in size, the ratio between their surface area and unit volume increases.[2] This brings a higher percentage of atoms/molecules on the surface, making them more reactive. This particularity makes nanostructures interesting to surface processes, because the surface area by unit of mass is larger and their electronic configuration is different. Therefore, the ability to tailor the nanostructures size (*i.e.,* nanoparticles, nanotubes, fibres, etc.) can open an important pathway for a whole range of applications. This effort has led to interesting applications such optical switches,[3] catalytic reactions,[4] superconducting layers[5] and other sensing devices.[6]

Unfortunately, nanoparticles tend to aggregate in order to minimize the surface free energy. Therefore, one of the major aspects necessary to consider is the ability to synthesise nanoparticles of the required size with a controlled size distribution and agglomeration tendency.

1.2.1 Ceramic nanocomposite and oxide nanocrystals

Nanocomposites[7–9] are defined as a broad range of materials consisting of two or more components, with at least, one of the components having a dimension of less than 100 nanometres (nm). This system is divided in two phases called nano size phase and matrix phase. The concept of ceramic nanocomposites was first proposed by Niihara et al. in 1991.[10,11] This work presents a silicon nitride-based ceramics proving a good mechanical properties such as high thermal and chemical stability and high strength. Nonetheless, ceramic nanocomposites are brittle. This brings several limitations to be used in industry. Ceramic-matrix nanocomposites[7,9,12,13] have been receiving attention lately because of the incorporation of components such fibres, nanotubes, nanoplatelets or nanoparticles to overcome this limitation. The addition of nanostructured features on the matrix allows a fine-tuning of the thermal and mechanical properties of the composite. Therefore, a key point in this system is the ability to tailor the nanostructure properties (*i.e.,* sizes, morphology, etc.).

However, recently it has been explored the possibility to improve other properties using the same concept, a matrix of ceramic material surrounding by nanoparticles. In particular, due to the performance required in power applications, superconductor nanocomposites are one of the most promising materials. The system is composed by a superconducting matrix, being $REBa_2Cu_3O_{7-\delta}$ (RE= rare earths) and a nano-size structure being a inorganic non-superconducting nanocrystal (NCs) one of the most used nowadays.

In the specific case of superconducting nanocomposite the applicability of oxide NCs is not a new thing. The compatibility of numerous oxide NCs has been studied. (*i.e.,* CeO_2, ZrO_2, $CoFe2O_4$, $BaHfO_3$, $BaZrO_3$)[14–21]. In some cases, an improvement in the performances of the nanocomposites has been found. However, one of the main issues when using these NCs has been the chemical reactivity of these NCs with the superconducting matrix. This has led to different composition of the NCs after the growth process,[22,23] which translates in an unreproducible growth process of the superconductor nanocomposites. Therefore, the synthesis of stable NCs that are non-reactive to REBCO matrix is one of the main challenges nowadays. It is known that several compositions of binary or ternary oxide perovskites are chemical compatible with REBCO. Particularly, perovskite NCs are one of the most promising and suitable ones, the lattice parameters have a good mismatch with REBCO structure. Binary perovskite compounds BMO_3 like $BaZrO_3$ and $BaHfO_3$ or tertary perovskite like Ba_2YTaO_6 and Ba_2YNbO_6 seems to be suitable candidates for this purpose.[15,16,19] The main challenge is to synthesise these NCs in such a way to comply with the requirements mentioned above and also, ensure their stability in alcoholic media.

1.2.2 BMO_3 perovskite family

The name “perovskite” comes from the eminent Russian mineralogist Count Lev Alexevivh von Perovski. In 1839, he discovered the mineral $CaTiO_3$, with crystalline structure that will become specific for the entire perovskite materials.

The perovskites represents any materials with a general formula of BMO_3,[24,25] where B and M sites are the divalent and tetravalent cations respectively and O is the anion. Generally, standard perovskites (BMO_3) are considered as a three-dimension (3D) perovskite.[26] The ideal structure for perovskite is cubic with a Pm-3m space group. The B site correspond to the largest cation and M to the smaller. In the crystalline structure B sites have a six-fold coordination, while M site (body center occupied) have a twelvefold coordination with the anions [24,25,27] (Figure 1.1).

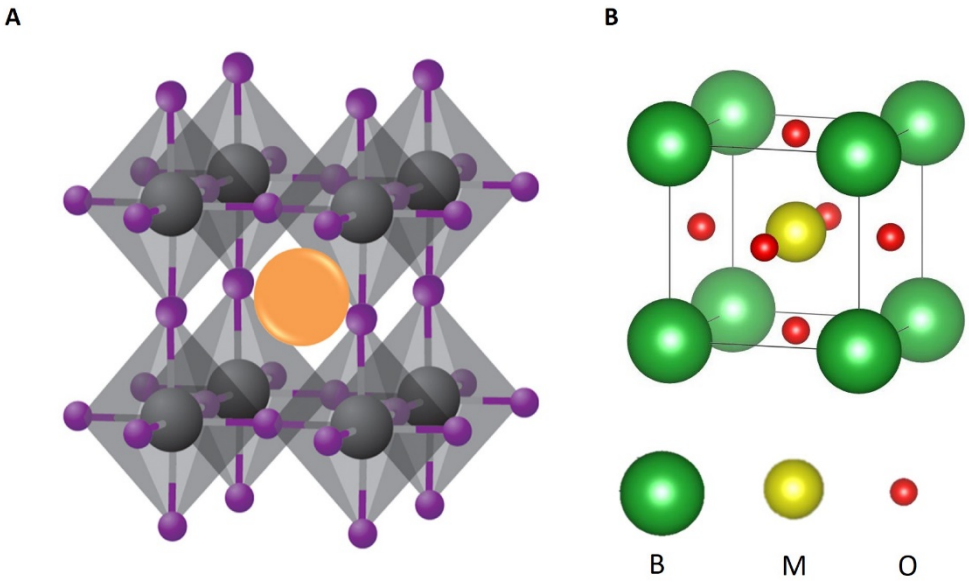

Figure 1.1. BMO_3 ideal perovskite structure (A) shows the body center cation M and the B cation showing a six-coordination to oxygens. (B) VESTA representation of a unit cell of BMO_3.

A powerful tool to predict the crystal stability based only on the BMO_3 perovskite compounds is Goldschmidt tolerance factor (t) equation $t=(r_B + r_O)/\sqrt{2}(r_M + r_O)$.[28,29] This equation has a direct dependence on the ionic radii of each element (BMO_3). Where r_B is the ionic radius of B, r_M the ionic radius of and r_O the ionic radius of oxygen.

To corroborate the stability of a cubic perovskite by tolerance factor the range of values should be between 0.8 and 1.06. A tolerance factor of $t = 1$ is considered as the ideal cubic structure, where the ions are in a perfect cubic lattice. In the case of $t \neq 1$ the crystal structure may present some distortions, not being the perfect cubic lattice the one who govern the crystal structure.

B and M sites on a BMO_3 crystalline structure can accommodate nearly every element of the periodic table, resulting in a wide range of perovskites with different properties (*i.e.,* high absorption coefficient, high dielectric constant, ferroelectricity, etc.).[26,30–33] Figure 1.2 lists some of the properties of perovskites by the different values of tolerance factor. This range maximizes the accuracy of tolerance factor (t) on the classification of more than 570 compounds. Each component shows different behaviour depending on the chemical composition and the modification of the perovskite-type crystal structure.

Von Hippel et al.,[34] in 1946 evidenced for the first time the ferroelectric behaviour in $BaTiO_3$ perovskite. Depending on the substitutions of B or M sites a crystal distortion from the cubic phase to tetragonal phase can appear.[35,36] This crystal modification is governed by an off-centre of M-sites in the perosvkites structure bestowing a ferroelectric behaviour.

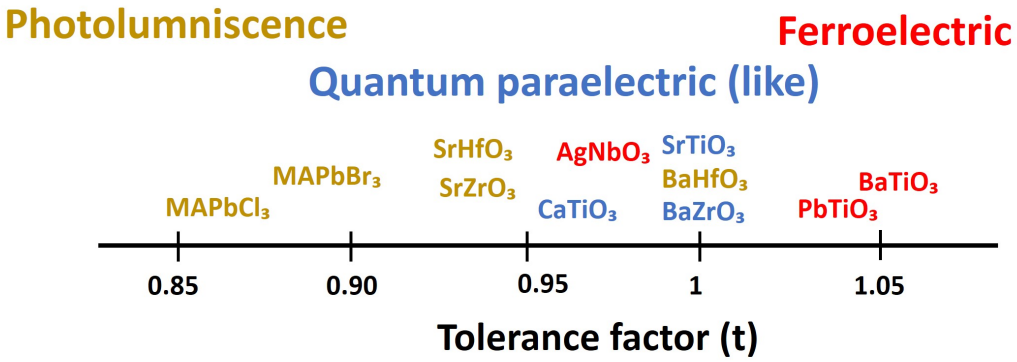

Figure 1.2. Schematic of the tolerance factor (t) of different perovskite compounds of BMO_3 family and their final physical NCs properties.

Moreover, changing the B-cations can also tune the band gap of the perovskites NCs. Modifying the average crystalline dimension by increasing the ionic radius of B-cations leads to an expansion of the cell and the absorption spectrum is red-shifted. In contrast at decreasing the ionic radius the cell shrinks, thus the absorption spectrum is blue-shifted. This modification leads to a photoluminescence behaviour.[26,37,38]

Some of the most relevant properties have been summarized in Table 1.1. Perosvkites can exhibit properties as , ferroelectricity,[35,39] photoluminescensce,[26,40] magnetoelectricity,[41,42] etc. Due to these properties, perovskites have gained a huge interest in the last decades for applications such as: electronics,[43] medicine,[44,45] catalysis,[46,47] energy storage [48,49] and sensing.[50]

Table 1.1. Sum up of the proprieties of some perovskite

Property	Compound
Ferromagnetic property	BaTiO3, PdTiO3
Piezoelectricity	Pb(Zr, Ti)O3, (Bi, Na)TiO3
Electrical conductivity	SrFeO3, LaCoO3, LaNiO3, LaCrO3
Superconductivity	La0.9Sr0.1CuO3, YBa2Cu3O7, HgBa2Ca2Cu2O8
Catalytic property	LaCoO3, LaMnO3, BaCuO3
Magnetic property	LaMnO3, LaFeO3, La2NiMnO6

1.2.3 Synthesis strategies of BMO_3 NCs

The search for methods to synthesises nanomaterials with controlled shape, crystallinity, size and composition still remains a challenge nowadays.

There are two main synthesis strategies to fabricate nano-sized structures: top-down and bottom-up approach[51] (Figure 1.3). Top-down approach consist of a successive cutting of a bulk material by etching processes, mostly using physical methods (*i.e.,* laser ablation, chemical etching, explosion process, etc.).

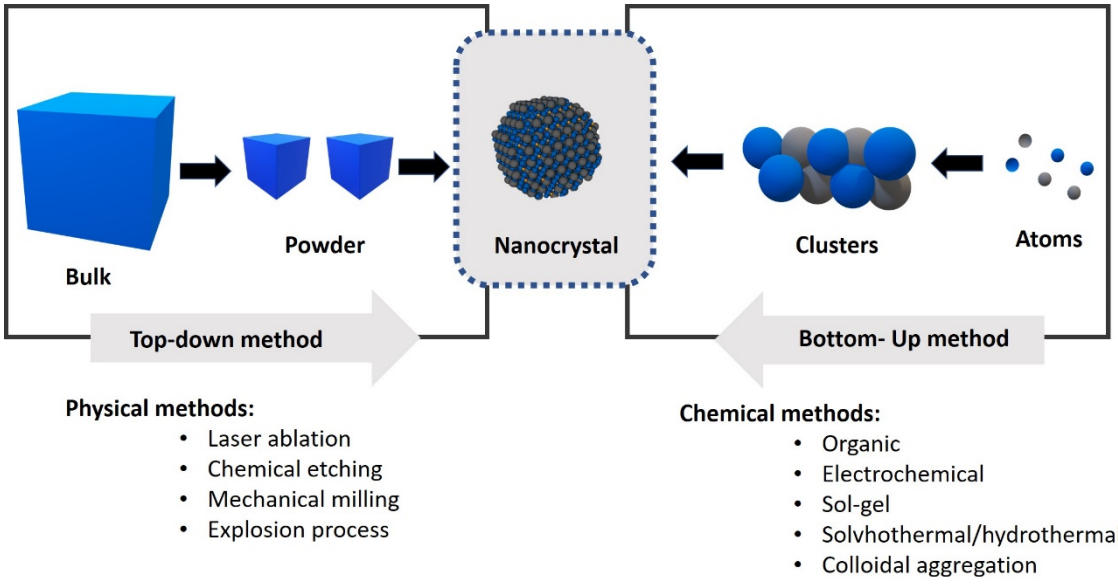

Figure1.3. Schematic representation of top-down and bottom-up synthesis approaches.

Bottom-up approach uses chemical precursors to produces nanoparticles using chemical reactions from atoms, molecules and clusters and build-up a nanoscale system. Moreover, this approach allows a better manipulation and control over the final NCs by using a chemical synthesis based methods (*i.e.,* Sol-gel, solvothermal, colloidal aggregation). This way we have the possibility to tailor-designed a novel strategy for synthesis a material. Among the different reported routes, the most representative for synthesis of $BaMO_3$ nanocrystals are; sol-gel,[52–54] solid-phase synthesis,[55] solvothermal and microwave routes.[56–58]

Solid-phase process requires high temperatures and has a deficiency on the control over the sizes and morphology of the solid NCs. Besides, they are showing difficulties regarding impurities formation, chemical homogeneity or the formation of a not desired intermediate phase.

In the case of the sol-gel method when introducing oxide precursors in to a solvent, an oxide network is formatted via inorganic polymerization reaction

forming the well-known gel.[59–61] This methodology allows a kinetic control of size and morphology of the NCs. Moreover, it uses low temperature leading to the possibility of achieving both non-crystalline and crystalline particles. The drawback is that the products often show a lack of crystallinity, needing a posterior heat treatment to finally reach a nanocrystal.

Concerning the reaction time, solvothermal and microwave are the most highlighted and promising methods for obtaining a nanoscale system reducing the reaction times and leading to a promising NCs without the need of a posterior heat treatment.[62]

1.2.3.1 Sol-gel

Sol-gel process is centered on the conversion of a precursor solution to oxide nanoparticles by chemical reaction.[59,63] The precursors can be either inorganic salts (chloride, nitrate, acetate, etc..) or metal organic species (*i.e.,* alkoxides). Aqueous sol-gel is based on hydrolysis and condensation/dehydration of the chemical precursors, forming an inorganic polymer by the hydrolysis step and transforming it to a crosslink solid (gel).[61,63,64]

To reach the final solid particles, the whole sol-gel process has proved to be very complex depending on numerous parameters like i) pH, ii) precursors iii) order of mixing the reagents, iv) temperature, v) caping ligand, vi) solvents vii) concentration.

Metal alkoxides are one of the most used compounds on sol-gel approach,[54,59,61,65] due to, their high stability in organic solvent. Beside it is easy to convert them in the corresponding oxides and most of the alkoxides compounds are commercially available. Alkoxides reactivity in front hydrolysis have a direct dependency with the electronegativity of the metal, coordination number and the length of the alkoxo chain.[59,61] This means that the reaction rate decreases in the this order : $M(OMe)_4 > M(OEt)_4 > M(OPr)_4 > M(OBu)_4$.

The sol-gel process involving alkoxide precursors can be defined by Equation 1.1-1.3. The water molecule through a nucleophilic attack to the alkoxo group (OR), replaces the alkoxo group for a hydroxylated species (OH). The key point is to hydrolyze the alkoxo compounds (Equation 1.1) to link two hydrolyzed molecules together forming the resulting bridge between M-O-M. This will trigger the polymer formation (Equation 1.2-1.3). Condensation reaction between two hydroxide metal compounds entails to a M-O-M with the release of water (oxalation) seen in Equation 1.2. In the case of the reaction between an alkoxide

and hydroxyl metal compounds an alcohol (alkoxolation) will be released (Equation 1.3).

Hydolysis:

$$M(OR)_n + x\ H_2O \longrightarrow M(OH)_x(OBu)_{n-x} + x\ R\text{-}OH \quad (1.1)$$

Condensation/dehydratation:

$$OH\text{-}M(OR)_3 + OH\text{-}M(OR)_3 \longrightarrow (OR)_3M\text{-}O\text{-}M(OR)_3 + H_2O \quad (1.2)$$

$$M(OR)_4 + OH\text{-}M(OR)_3 \longrightarrow (OR)_3M\text{-}O\text{-}M(OR)_3 + ROH \quad (1.3)$$

Although the sol-gel process has been deeply investigated for decades, the fast hydrolysis and condensation reactions lead to a variety of different species which, even nowadays, is not yet fully controllable.

1.2.3.2 Hydro/solvothermal methodologies

The classical heating process is often carried out in systems where the temperature is usually determined by the boiling point of the used solvent (*i.e.,* reflux system). For that reason, many of the classical reactions take a quite long time (*i.e.,* overnight, days, weeks). An alternative procedure to reduces the reaction time is the hydro/solvothermal method where the solution is filled in a steel vessel and heated to high temperature, even beyond the boiling point. The hydro/solvothermal synthesis is a strategy based on the use of water "hydrothermal" or any other organic or inorganic solvents (*i.e.,* alcohols) as the "solvothermal" reaction. The temperature and pressure generated inside facilitate the dissolution of the chemical precursor and the production of the crystalized products.[66] Following this system, the reaction time could be decreased from days to hours.

Using this technique, the formation of NCs consists mainly in two steps: crystal nucleation and the subsequent growth. This process has a high control over the size, morphology, and crystallinity of the NCs. due to a tight control of the: i) pH ii) temperature iii) reactant concentration iv) solvents v) capping ligands. The phenomena to control the final nanocrystals formation, thus the size and morphology, resides on the nucleation and the growth rate which are in a close dependence with the supersaturation process.[67,68]

The fundament to understanding the complexity of NCs evolution to form a final nucleus release by homogeneous nucleation proceed according the LaMer model.[69]

When the concentration of free monomer [C_s] is raised above the critical point [$C_{min}^{nucleation}$] (Figure 1.4) the nucleation, formation of the first crystalline nucleus, occurs. This point is when the solution gets supersaturated.[70] During the nucleation, the concentration of the monomers decreases and drops to [C_s] reducing the nucleation step and increasing the number of solid particles. Afterwards these particles are grown until the point of solubility is reached. The fact of having fast/slow nucleation rates has a direct role on the final particles formation. In the case of a fast nucleation rate the monomers concentration sharply reduces, which will generate small NCs. However slower rates of nucleation lead to slow monomers concentration reduction bestowing a large final NCs.[71,72]

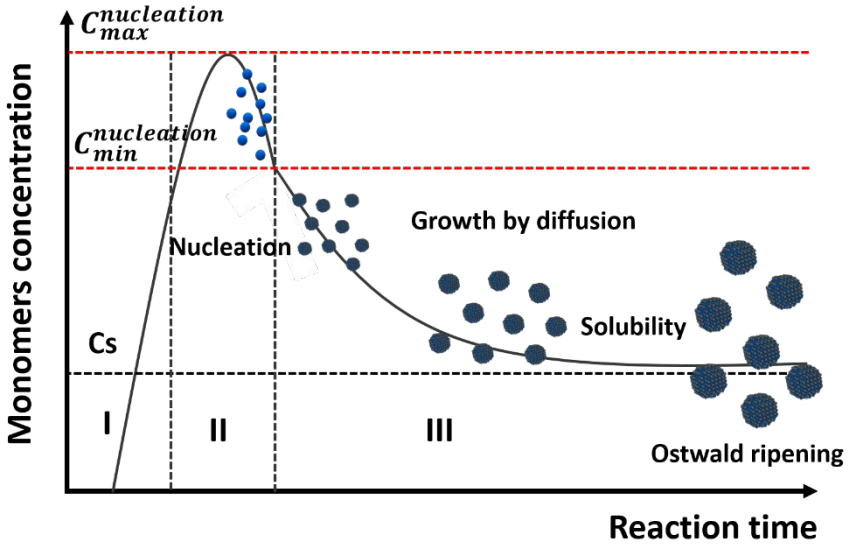

Figure 1.4. Schematic diagram illustrating LaMer model by a representation of three stages. (I) the generation of atoms. (II) Nucleation. (III) growth process towards the reaction time.

Moreover exposing the NCs at high temperature for long times during the growth process could lead to NCs coarsening by Ostwald ripening phenomenon,[73] where the smallest NCs redissolve and get redeposited by material diffusion onto the large crystals, resulting in bigger NCs. For this reason, a high control over the temperature and time in the thermal routes is mandatory to achieve a tight control of the final size and the homogeneity of the NCs.

Most of the NCs have a strong tendency to agglomerate in the colloidal solution during the growth process due to the high surface free energy, forming precipitates. To solve this problem, the implementations of capping ligand and additives seems to be an excellent pathway to manipulate the NCs surface. Among the different process to manipulate the NCs surface one methodology called polyol

route[74–77] has been emerged as a versatile route to synthesized high-quality nanomaterials. The polyol route was reported for the first time in 1989 by Fievet, Lagier and Figlarz.[78,79] They performed a liquid-phase synthesis by dissolving the precursors (*i.e.,* oxides, hydroxides, salts) in polyols to finally achieve oxide NCs. This process involves different types of polyol, where the most representative are, ethylene glycol (EG), diethylene glycol (DEG), triethylene glycol (TREG) and so up to polyethylene glycol (PEG). In addition, this route can be performed in many methodologies as hydro/solvothermal method, thermal methods, etc.

1.2.3.3 Microwave synthesis

Although thermal methods have been proved to be efficient for the synthesis NCs, the interest on this field for scaling up and achieve higher yields, homogeneous crystals, and tight control over temperature and pressure rates lead to a new pathway for the synthesis of the NCs: the assisted microwave radiation.[62,80] Microwave-assisted is based on two main mechanisms: dipole rotation (the ability of a substance to generate heat after being irradiated by microwave radiation and align the dipoles with the oscillating fields coming from the microwaves) and ionic conduction (collision between the ions present in the solution, generating friction and thus, increasing the temperature).[81]

Comparing these two cases, hydro/solvothermal and microwave assisted radiation the main difference is the heating process. Conventional methodologies (hydro/solvothermal) use an indirect heating process where the energy is transferred through convection and radiation between the external part of the vessel and the solution (Figure 1.5). The microwave reaction transfers directly the energy to the solution through the vessel leading to a more homogeneous heating. Thus the reaction time is reduced from hours or days to minutes.[62]

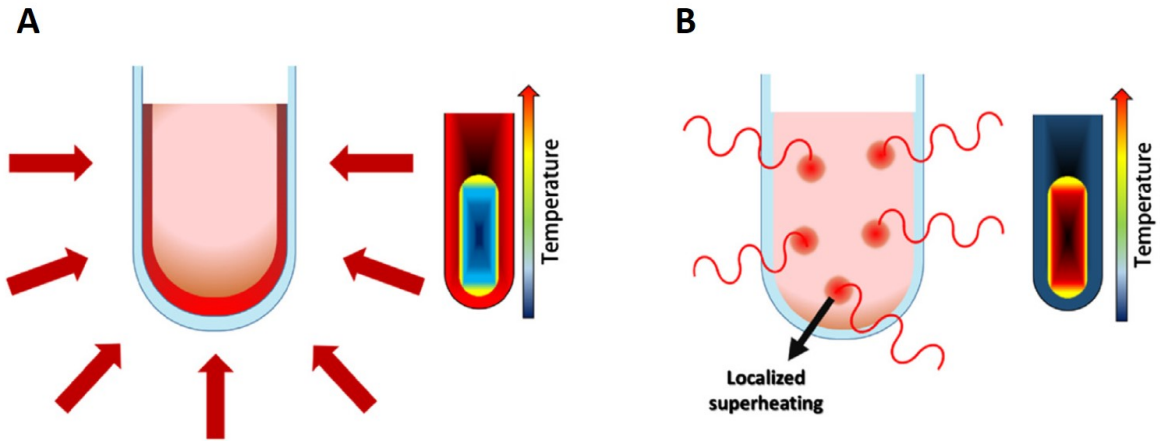

Figure 1.5. Scheme of the difference between heating via (A) conventional solvothermal method and (B) microwave-assisted solvothermal method. [82]

In addition, the implementation of microwave-assisted provides an excellent control over the reaction parameters (*i.e.,* pressure, time and temperature) by monitoring the full reaction.

1.3 Superconducting nanocomposite

1.3.1 From nanocrystals synthesis to application

The incorporation of the nanostructures into the superconductive matrix has been extensively reported in literature,[8,12,83,84] and the methods used could be generally divided in physical and chemical processes. The physical processes are using techniques such as: hot pressing gas[85] pressure sintering[86] or spark plasma sintering process. Nonetheless, these methods require long fabrication times, and have a high cost and scale-up manufacturing limitations.

Currently, chemical deposition techniques are gaining importance to fabricate the superconductor nanocomposites, highlighting the vacuum deposition[84] and the chemical solution deposition (CSD).[14,16,19,21,87] However, vacuum deposition brings some drawbacks as a lack in scalability and cost/effectiveness. The CSD has been rising as a promising deposition technique for its high yield, versality and low investment cost.

In this thesis, we will be focused on CSD methodology applied for different REBCO precursor solutions in order to reach REBCO nanocomposites. There are two main strategies to achieve REBCO nanocomposites, as observed in Figure 1.6. On one hand, the spontaneous segregation, where NCs are formed during the growth process of REBCO layers. In this case the precursors salts of the desired NCs at the desired concentration are added directly in the precursor solution of the desired REBCO phase. The second approach relies on adding the preformed NCs to the precursors solution of the REBCO. In this case the NCs are previously synthesised with a tight control over the size, shape, homogeneity and concentration.[14,15,19,88]

For the spontaneous segregation methodology a variety of oxide nanocrystals such as $BaZrO_3$, Ba_2YTaO_6, $BaHfO_3$[14,15,19,88] have been studied. Even though, the achieved nanocomposites have shown an enhanced of the superconducting properties this approach has some limitations: poor control on NCs size, difficult control of the distribution of NCs in REBCO matrix and high tendency of agglomeration. All these limitations lead to poor reproducibility of the results.[16,22,89,90]

The preformed NCs approach seems not to have the above-mentioned limitations, since the NCs are previously synthesised with very good control of NCs sizes and shape.

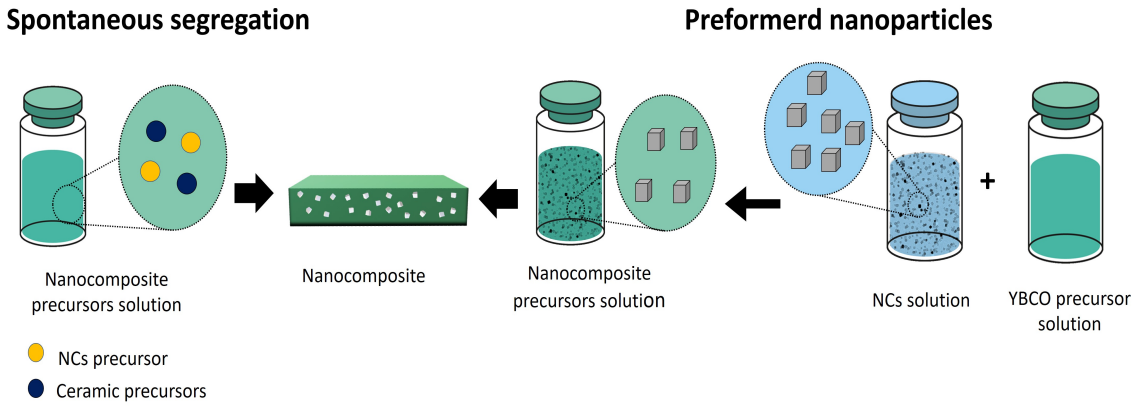

Figure 1.6. Scheme of a chemical solution deposition (CSD). On the left a spontaneous segregation methodology. On the right the preformed nanoparticles approach.

In this work, we presented the implementation of the preformed NCs colloidal solution into the REBCO precursor solution. For this, the precursor solution chosen was $YBa_2Cu_3O_{7-\delta}$ (YBCO) containing yttrium, barium and copper salts and methanol as solvent. It is important that the preformed NCs have a high stability in the REBCO precursor solution. This will lead to homogeneously distributed NCs in the REBCO matrix after the growth process of the nanocomposite. Once the stability of the NCs is achieved, the nanocomposite precursor solution is deposited onto a substrate and subjected to two heat treatments (pyrolysis and growth) and converted into crystalline YBCO nanocomposite. The incorporation of the NCs leads to an increment of the final critical current under high magnetic fields.

During this Thesis the NCs application in superconducting field has been performed with the collaboration of Superconducting Materials and Large Scale Nanostructures (SUMAN) group from ICMAB. The synthesis and characterization of the BMO_3 NCs, as well as the stability study of the NCs with the YBCO precursors solutions and some pyrolyzed samples has been performed by us. The optimization of nanocomposite growth process and the physicals measurements from the nanocomposite has been performed in collaboration with researchers from SUMAN group. The BMO_3 NCs implemented in superconducting fields has been also reported in Zi Liang Li Thesis,[91] Julia Jareño Thesis[92] and B. Villarejo Thesis.[93]

In order to understand the role of the NCs into the superconducting matrix a brief explanation about superconductivity is exposed in the following sections.

1.3.2 Basic principles in superconductivity

A superconductor is a material that shows zero resistance against to electrical current below a certain conditions. This material has a direct dependency with temperature, the temperature where the electrical resistance of the materials drops to zero is called critical temperature T_c (Figure 1.7A). In the case of non-superconduct material this behaviour is not observed.

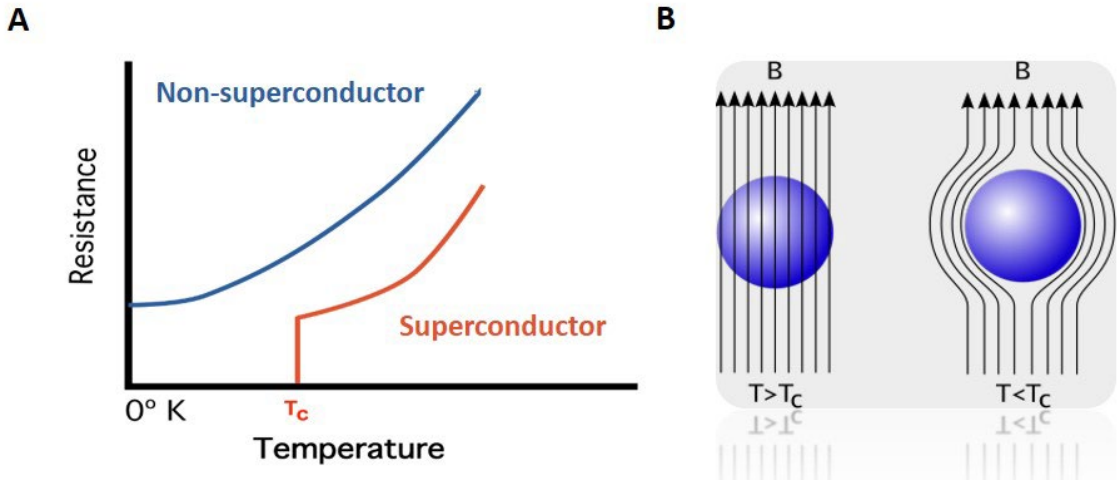

Figure 1.7. (A) graph representation of resistance vs temperature on a superconductor material and non-superconductor material. (B) The Meissner effect shows a superconductor's magnetic flux above critical temperature (left) and below critical temperature (right).

One of the most unique features that superconductors exhibit is the Meissner effect,[20] where the material shows a perfect diamagnetic behaviour. This effect is based on the ability to expel the magnetic field from the interior of the material at a temperature below the T_c (which provides the material with the ability to "levitate" on a magnetic field) (Figure 1.7B). Moreover, the magnetic field is also directly affecting the superconductor states. The magnetic field used to break down the superconductivity is known as Critical Magnetic Field (H_c). The critical magnetic field is temperature dependent as observed in the Equation 1.4, where H_o is the magnetic field at 0K.

$$H_c = H_o \left(1 - \left(\frac{T}{T_c}\right)^2\right) \quad (1.4)$$

The maximum current that can pass through a superconductor material, without deteriorating its superconductive state is called the critical current (I_C). Instead of use I_c is more suitable to use the critical current density (J_c) which is no depending on the dimensions of the material. $J_c = (I_c/A)$.

Therefore, the three conditions that can break the superconductivity of the materials are: i) critical magnetic field (H_c) ii) critical temperature (T_c) iii) critical current density (J_c).

1.3.3 Types of superconductors

Superconductors materials are classified depending on their critical temperature: in low temperature superconductors (LTS) and high temperature superconductors (HTS) and depending on their behaviour under magnetic field in type I and type II.

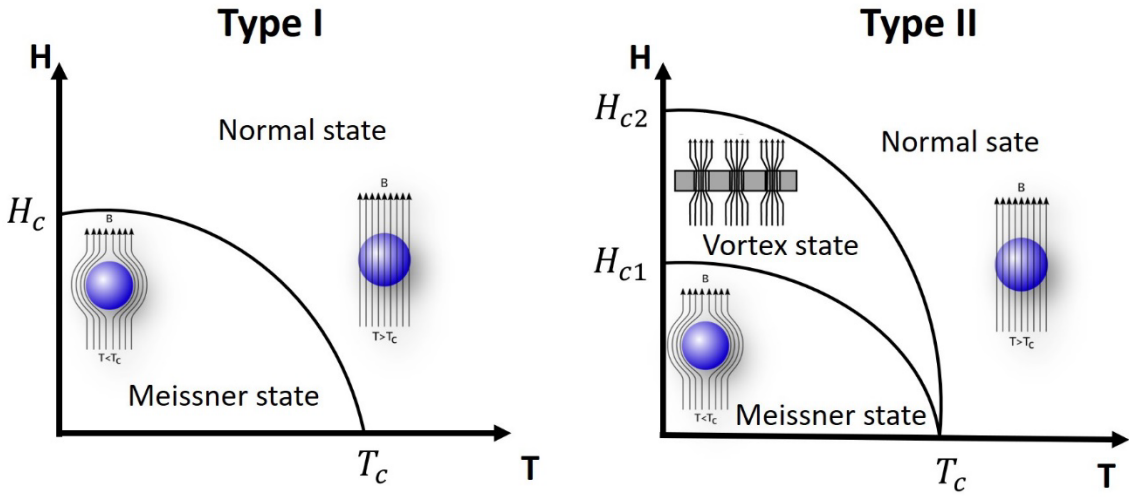

Figure 1.8. Schematic diagram of type I (left) and type II (right) superconductors.

Type I are those superconductors that have the ability to expel the magnetic field from the inside of the material when they are below the T_c and critical magnetic field (H_c), giving rise to the Meissner state.[20] Therefore, when they are above the T_c and H_c, the magnetic field penetrates the material and the superconductor state is lost. (Figure 1.8).

Type II, differs from the previous one because they have a new mixed state,[94,95] defining a new mixed region between them with two different critical magnetic field, called H_{c1} and H_{c2} (Figure 1.8). The materials show the same properties as type I when the materials are below T_c and H_{c1}, thus expelling the magnetic field out of the superconductor (Meissner state). However, in the mixed state created between H_{c1} and H_{c2}, the magnetic field can penetrate into the material without breaking down the superconductivity forming magnetic vortices.

The other classification of the superconductors mentioned above distinguishes between low-temperature superconductor (LTS) and high-temperature

superconductors (HTS). LTS comprises those with a superconductor transition at T_c below 20 K, and HTS those with at Tc above 20 K.

1.3.4 $YBa_2Cu_3O_{7-\delta}$ superconducting material

$YBa_2Cu_3O_{7-\delta}$ commonly termed as YBCO, is a type II superconducting material, described as a triple perovskite. YBCO was discovered in 1987,[96] and belongs to high-temperature superconductor (HTS) with a T_c of 92 K.

The unit cell $YBa_2Cu_3O_{7-\delta}$ displayed in Figure 1.9 is composed by three cubes, one central $YCuO_3$ cube and two adjacent cubes of $BaCuO_3$ above and below, the structure shows some anion deficiency (*i.e.,* oxygen vacancies). The crystal structure and properties of the YBCO depend on the oxygen vacancies, which are related to δ.[97] For $\delta < 0.5$ the YBCO structure is tetragonal (*i.e.,* without superconductivity propierties). While for $0.5 < \delta < 1$ the crystalline structure has orthorhombic symmetry providing YBCO with superconducting properties.[97]

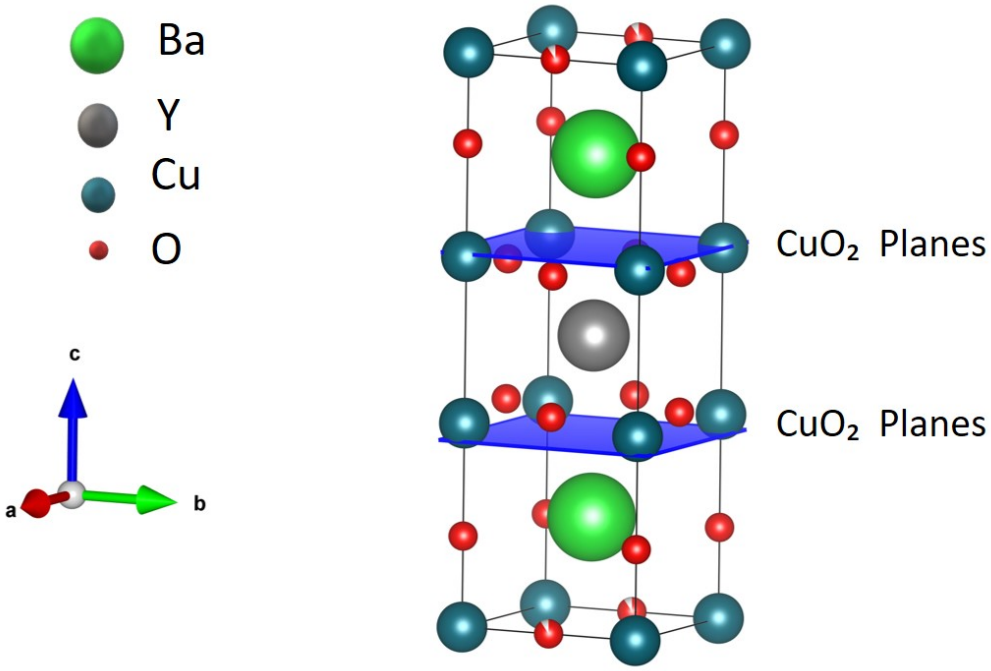

Figure.1.9. Unit Cell of $YBa_2Cu_3O_{7-\delta}$ orthorhombic structure

There is an anisotropy on this material, based on the different current flow going through the a-b planes and the c-planes. This phenomenon is created because the conductivity is confined along the CuO_2 planes, parallel to the a-b planes. They are called conducting planes. At the same time, the charges transport is significantly reduced on the c-axis.[98] Consequently, it is of great importance

having a perfect growth orientation of the YBCO layer along the c-axis, in order to increment the current flow density on the a-b planes.[17,99,100]

1.3.5 Vortex pinning

Type II superconductor allows the flow of the magnetic field through the material when it is working under the conditions of the mixed state (*i.e.,* H_{c1} and H_{c2} see Figure 1.8) below T_c. However, the magnetic field does not cross uniformly through the superconductor material, but in a vortex direction.[101] In the case of the superconductor material, a vortex core is surrounded by superconducting current and the magnetic flux in the vortex itself (Figure 1.10).

When a current is introduced in the superconductor, these vortices start to move due to the Lorentz force (F_L). This process causes energy dissipation, equivalent to resistance and hence loss of superconductivity.[102] However, if the vortices are pinned at a fixed position, the material remains in its superconductive state. To prevent this motion, the arrangement of vortices in a fixed position will create a pinning force (F_p) opposed to the Lorentz force, enabling dissipation free current through the material as long as the pinning force is stronger than the Lorentz-force. The limit of zero resistance current flow in the mixed state is at $F_p=F_L$. For this standpoint the F_p can be defined as Equation 1.5, when the driving forces are equal. The corresponding current density is defined as the critical current density J_c, and it represents the maximum current density that can flow through the superconductor without energy loss. The value of F_p is determined by the type of the pinning centres in which the vortices are pinned.

$$F_p = F_L = J_c \, x \, B \tag{1.5}$$

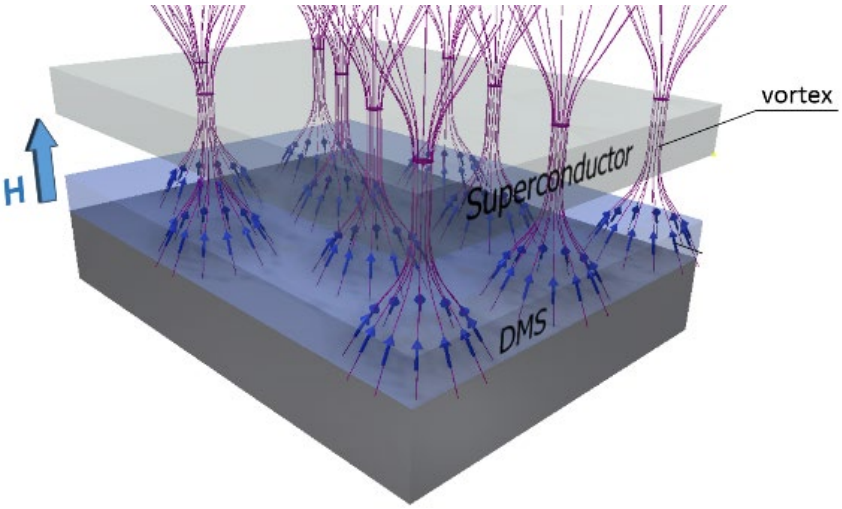

Figure 1.10. Schematic representation of the pinning centre onto the superconductor matrix. Showing the magnetic field flux through vortex created by the pinning centres[103].

The superconductor material itself shows some local defects, impurities, secondary phases, crystalline defects and/or other irregularities that can act like pinning centres. The defects can be naturally induced during the growth process on the superconducting matrix as mentioned previously (*i.e.,* impurities, secondary phases, crystalline defects) or they can artificially be introduced (artificial pinning centre, APC) to the superconducting matrix (*i.e.,* nanocolumns, nanocrystals).[19,104,105]

1.3.6 Artificial pinning centers

YBCO layer must ensure the higher current flow attempting to reduce the amount of energy dissipation. A superconductor nanocomposites takes advantages on the defects created on the YBCO matrix, allowing an increment on the final current.[19,21,106] The natural defects induced on the YBCO matrix are difficult to control in size and distribution. For this reason, the addition of NCs into the YBCO precursor solution has been rising interest in the last decades.[14,19,21,88]

In this work we will focused on study and implementation of preformed NCs (APC) into YBCO precursors solution via CSD.

Nonetheless, the implementation of this NCs into the superconductor matrix must accomplish some requirement to properly increase the final critical current:

i) The dimension of APC needs to be smaller of <15 nm, to avoid large NCs which could create defects on the lattices, acting as the opposite of pinning centers.
ii) Preserving a stable colloidal solution of the NCs with the YBCO precursor solution.
iii) Homogeneous distribution of the NCs during the deposition and thermal processes avoiding any possible agglomeration.
iv) NCs must show high crystallinity.

1.4 Objectives and Outline

The objective of this PhD study is to obtain homogeneous and stable BMO_3 (M = Ti^{4+}, Zr^{4+} and Hf^{4+}) NCs using an easy, fast and reproducible method. We have used a general hybrid solvothermal methodology to synthesise perovskite BMO_3 nanocrystals with tunable sizes and long-time stability. As far as we know, our hybrid method is used successfully for the first time to synthesise BMO_3 (M = Ti^{4+}, Zr^{4+} and Hf^{4+}) NCs.

The current interest of these NCs remains in their applicability, acting as pinning centres on superconductive thin and thick films. We envisage the synthesis of monodispersed NCs to incorporate them in an inorganic matrix of YBCO to increase the critical current.

Thanks to the better understandings of the insights concerning the mechanisms, tuneability of sizes and the ability to exchanges cations to synthesise new compounds these NCs can reach a new range of applications.

In consequence, with the main objective explained above, this thesis will be divided in two main blocks; the first one which comprise chapter 3 and chapter 4 is focused on the synthesis of perovskites NCs. The second one, which include chapter 5, deals with the applicability of the NCs to YBCO nanocomposites.

In Chapter 2, the experimental procedures and methodology is detailed for NCs and YBCO precursor solutions, as well as the procedure for the implementation of NCs into the YBCO matrix. Moreover, a brief explanation of the different characterization techniques required for both NCs and nanocomposite is presented.

Chapter 3, exposes the synthesis and optimization of $BaZrO_3$ NCs by the combination of aqueous sol-gel and solvothermal methodologies. This hybrid methodology has been successful for achieving NCs with high crystallinity, agglomeration-free and small sizes. Moreover, we evidence the role of water in the hydrolytic step of a sol-gel process as the key parameter to tune the final size of the NCs. This allowed us to obtain a wide range of NCs sizes from (4 to 30 nm).

Chapter 4, is focused on the study of a general route to obtain a new range of perovskites from the same BMO_3 family. It consists in the replacement of B or M sites for others divalent or tetravalent cations by following the hybrid methodology reported in Chapter 3. This synthetic procedure has been expanded to the other metals from the same periodic group (IV), where M = Ti^{4+} and Hf^{4+} obtaining $BaTiO_3$ and $BaHfO_3$ NCs. Also, the divalent cation was exchanged from Ba^{+2} to Sr^{+2} and studied.

In chapter 5 the applicability of the NCs synthesised on the previous chapters is presented. In this chapter the effort has been focused in generating a nanocomposite of YBCO superconducting layer by embedding the $BaMO_3$ (M= Zr^{4+} and Hf^{4+}) NCs into the YBCO precursors solution. The NCs stability onto the YBCO precursors solution was demonstrated. The final YBCO nanocomposites have been fully characterized and their superior performances compared with the pristine YBCO layers have been proven.

1.5 References

1 S. K. Kulkarni, *Nanotechnology - Principles and Practices 3rd ed (Springer, CP, 2015).pdf*, 2014.

2 P. I. Kattan, *Nat. Nanotechnol.*, 2016, **11**, 575.

3 Z. Chai, X. Hu, F. Wang, X. Niu, J. Xie and Q. Gong, *Adv. Opt. Mater.*, 2017, **5**, 1600665.

4 D. Astruc, *Chem. Rev.*, 2020, **120**, 461–463.

5 J. P. F. Feighan, A. Kursumovic and J. L. MacManus-Driscoll, *Supercond. Sci. Technol.*, 2017, **30**, 123001.

6 D. A. Barzinjy, *Eurasian J. Sci. Eng.*, 2018, **4**, 82–98.

7 J. Hári and B. Pukánszky, in *Applied Plastics Engineering Handbook*, ed. M. Kutz, Elsevier, Oxford, 2011, pp. 109–142.

8 R. Mishra and J. Militky, in *Nanotechnology in Textiles*, eds. R. Mishra and J. Militky, Elsevier, 2019, pp. 263–310.

9 D. Shi, Z. Guo and N. Bedford, in *Nanomaterials and Devices*, eds. D. Shi, Z. Guo, et al., William Andrew Publishing, Oxford, 2015, pp. 293–315.

10 K. NIIHARA, *J. Ceram. Soc. Japan*, 1991, **99**, 974–982.

11 K. Niihara, K. Suganuma, A. Nakahira and K. Izaki, *J. Mater. Sci. Lett.*, 1990, **9**, 598–599.

12 R. Mishra and J. Militky, in *Nanotechnology in Textiles*, eds. R. Mishra and J. Militky, Woodhead Publishing, 2019, pp. 263–310.

13 S. Stankovich, D. A. Dikin, G. H. B. Dommett, et al., *Nature*, 2006, **442**, 282–286.

14 J. Gutiérrez, A. Llordés, J. Gázquez, et al., *Nat. Mater.*, 2007, **6**, 367–373.

15 S. V. Samoilenkov, O. V. Boytsova, V. A. Amelichev and A. R. Kaul, *Supercond. Sci. Technol.*, 2011, **24**, 055003.

16 P. Cayado, K. De Keukeleere, A. Garzón, et al., *Supercond. Sci. Technol.*, 2015, **28**, 124007.

17 N. F. Heinig, R. D. Redwing, I. F. Tsu, et al., *Appl. Phys. Lett.*, 1996, **69**, 577–579.

18 M. Miura, B. Maiorov, M. Sato, et al., *NPG Asia Mater.*, 2017, **9**, e447–e447.

19 A. Llordés, A. Palau, J. Gázquez, et al., *Nat. Mater.*, 2012, **11**, 329–336.

20 W. Meissner and R. Ochsenfeld, *Naturwissenschaften*, 1933, **21**, 787–788.

21 K. Matsumoto and P. Mele, *Supercond. Sci. Technol.*, 2010, **23**, 014001.

22 K. De Keukeleere, P. Cayado, A. Meledin, et al., *Adv. Electron. Mater.*, 2016, **2**, 1–9.

23 H. Rijckaert, G. Pollefeyt, M. Sieger, et al., *Chem. Mater.*, 2017, **29**, 6104–6113.

24 M. Johnsson and P. Lemmens, *J. Phys. Condens. Matter*, 2008, **20**, 264001.

25 M. H. K. Rubel, T. Takei, N. Kumada, et al., *Inorg. Chem.*, 2017, **56**, 3174–3181.

26 Z. Song, J. Zhao and Q. Liu, *Inorg. Chem. Front.*, 2019, **6**, 2969–3011.

27 R. N. Singh, T. Sharma and A. Singh, *J. New Mater. Electrochem. Syst.*, 2007, **10**, 105–111.

28 R. Mouta, R. X. Silva and C. W. A. Paschoal, *Acta Crystallogr. Sect. B Struct. Sci. Cryst. Eng. Mater.*, 2013, **69**, 439–445.

29 C. J. Bartel, C. Sutton, B. R. Goldsmith, et al., *Sci. Adv.*, 2019, **5**, 1–10.

30 F. S. GALASSO, in *Structure, Properties and Preparation of Perovskite-Type Compounds*, Elsevier, 1969, pp. 79–114.

31 W. Cai, C. Fu, J. Gao, Q. Guo, X. Deng and C. Zhang, *Phys. B Condens. Matter*, 2011, **406**, 3583–3587.

32 P. C. Reshmi Varma, in *Perovskite Photovoltaics*, Elsevier, 2018, pp. 197–229.

33 J. B. Goodenough, *Reports Prog. Phys.*, 2004, **67**, 1915–1993.

34 A. von Hippel, R. G. Breckenridge, F. G. Chesley and L. Tisza, *Ind. Eng. Chem.*, 1946, **38**, 1097–1109.

35 N. A. Benedek and C. J. Fennie, *J. Phys. Chem. C*, 2013, **117**, 13339–13349.

36 N. Nuraje and K. Su, *Nanoscale*, 2013, **5**, 8752–8780.

37 W.-J. Yin, Y. Yan and S.-H. Wei, *J. Phys. Chem. Lett.*, 2014, **5**, 3625–3631.

38 Y. Dong, Y. Zhao, S. Zhang, et al., *J. Mater. Chem. A*, 2018, **6**, 21729–21746.

39 M. B. Smith, K. Page, T. Siegrist and A. Et, *J. Am. Chem. Soc.*, 2008, **130**, 6955–6963.

40 K. P. Goetz, A. D. Taylor, F. Paulus and Y. Vaynzof, *Adv. Funct. Mater.*, 2020, **30**, 1910004.

41 H. Amorín, M. Algueró, R. Del Campo, et al., *Sci. Technol. Adv. Mater.*, 2015, **16**, 16001.

42 M. K. Kim, J. Y. Moon, S. H. Oh, D. G. Oh, Y. J. Choi and N. Lee, *Sci. Rep.*, 2019, **9**, 5456.

43 M. Segev-Bar and H. Haick, *ACS Nano*, 2013, **7**, 8366–8378.

44 L. E. Woodard, C. L. Dennis, J. A. Borchers, et al., *Sci. Rep.*, 2018, **8**, 1–13.

45 M. Mahmoudi, M. Yu, V. Serpooshan, et al., *Nat. Nanotechnol.*, 2017, **12**, 845–855.

46 S. A. Bonke, A. M. Bond, L. Spiccia and A. N. Simonov, *J. Am. Chem. Soc.*, 2016, **138**, 16095–16104.

47 Q. Jia, S. Ghoshal, J. Li, et al., *J. Am. Chem. Soc.*, 2017, **139**, 7893–7903.

48 A. Noori, M. F. El-Kady, M. S. Rahmanifar, R. B. Kaner and M. F. Mousavi, *Chem. Soc. Rev.*, 2019, **48**, 1272–1341.

49 R. R. Salunkhe, Y. V. Kaneti and Y. Yamauchi, *ACS Nano*, 2017, **11**, 5293–5308.

50 M. E. Franke, T. J. Koplin and U. Simon, *Small*, 2006, **2**, 36–50.

51 N. Patel, R. Abhinav, B. Srinivasan and R. Srinivasan, in *12th International Symposium on Process Systems Engineering and 25th European Symposium on Computer Aided Process Engineering*, eds. K. V Gernaey, J. K. Huusom, et al., Elsevier, 2015, vol. 37, pp. 2387–2392.

52 I. Bilecka, L. Luo, I. Djerdj, et al., *J. Phys. Chem. C*, 2011, **115**, 1484–1495.

53 M. Niederberger, 2007, **40**, 793–800.

54 M. Niederberger and G. Garnweitner, *Chem. - A Eur. J.*, 2006, **12**, 7282–7302.

55 N. Pinna, G. Garnweitner, M. Antonietti and M. Niederberger, *Adv. Mater.*, 2004, **16**, 2196–2200.

56 K. De Keukeleere, J. De Roo, P. Lommens, J. C. Martins, P. Van Der Voort and I. Van Driessche, *Inorg. Chem.*, 2015, **54**, 3469–3476.

57 K. De Keukeleere, J. Feys, M. Meire, et al., *J. Nanoparticle Res.*, 2013, **15**, 2074.

58 M. Niederberger, G. Garnweitner, N. Pinna and M. Antonietti, *J. Am. Chem. Soc.*, 2004, **126**, 9120–9126.

59 U. Schubert, in *The Sol-Gel Handbook*, Wiley-VCH Verlag GmbH & Co. KGaA, Weinheim, Germany, 2015, pp. 1–28.

60 E. Kemnitz and J. Noack, *Dalt. Trans.*, 2015, **44**, 19411–19431.

61 A. Vioux, *Chem. Mater.*, 1997, **9**, 2292–2299.

62 I. Bilecka and M. Niederberger, *Nanoscale*, 2010, **2**, 1358.

63 A. E. Danks, S. R. Hall and Z. Schnepp, *Mater. Horizons*, 2016, **3**, 91–112.

64 L. John and P. Sobot, in *Ceramic Materials*, Sciyo, 2010.

65 J. Oliver, in *Climate Change 2013 - The Physical Science Basis*, ed. Intergovernmental Panel on Climate Change, Cambridge University Press, Cambridge, 2013, vol. 53, pp. 1–30.

66 R. I. Walton, *Chem. Soc. Rev.*, 2002, **31**, 230–238.

67 J. Van Embden, A. S. R. Chesman and J. J. Jasieniak, *Chem. Mater.*, 2015, **27**, 2246–2285.

68 M. M. Lencka and R. E. Riman, *Chem. Mater.*, 2002, **5**, 61–70.

69 V. K. LaMer and R. H. Dinegar, *J. Am. Chem. Soc.*, 2002, **72**, 4847–4854.

70 C. N. R. Rao, A. Müller and A. K. Cheetham, *Nanomaterials Chemistry*, Wiley, 2007.

71 L. Bahrig, S. G. Hickey and A. Eychmüller, *CrystEngComm*, 2014, **16**, 9408–9424.

72 J. Polte, *CrystEngComm*, 2015, **17**, 6809–6830.

73 P. W. Voorhees, *J. Stat. Phys.*, 1985, **38**, 231–252.

74 F. Fi, R. Brayner, F. Chau, et al., *Chem. Soc. Rev.*, 2018, **47**, 5187–5233.

75 E. M. Hotze, T. Phenrat and G. V. Lowry, *J. Environ. Qual.*, 2010, **39**, 1909–1924.

76 Z. Wu, S. Yang and W. Wu, *Nanoscale*, 2016, **8**, 1237–1259.

77 R. A. S. and W. J. Parak, *Phil. Trans. R. Soc. A*, 2010, **368**, 1333–1383.

78 F. Fievet, J. P. Lagier and M. Figlarz, *MRS Bull.*, 1989, **14**, 29–34.

79 F. FIEVET, J. LAGIER, B. BLIN, B. BEAUDOIN and M. FIGLARZ, *Solid State Ionics*, 1989, **32–33**, 198–205.

80 A. Verma, R. Dwivedi, R. Prasad and K. S. Bartwal, *J. Nanoparticles*, 2013, **2013**, 1–11.

81 C. O. Kappe, *Angew. Chemie Int. Ed.*, 2004, **43**, 6250–6284.

82 D. Nunes, A. Pimentel, L. Santos, et al., in *Metal Oxide Nanostructures*, eds. D. Nunes, A. Pimentel, et al., Elsevier, 2019, pp. 21–57.

83 E. Omanović-Mikličanin, A. Badnjević, A. Kazlagić and M. Hajlovac, *Health Technol. (Berl).*, 2020, **10**, 51–59.

84 P. H. C. Camargo, K. G. Satyanarayana and F. Wypych, *Mater. Res.*, 2009, **12**, 1–39.

85 A. Goyal, S. Kang, K. J. Leonard, et al., *Supercond. Sci. Technol.*, 2005, **18**, 1533–1538.

86 T. Ohnishi, J.-U. Huh, R. H. Hammond and W. Jo, *J. Mater. Res.*, 2004, **19**, 977–981.

87 S. Engel, T. Thersleff, R. Hühne, L. Schultz and B. Holzapfel, *Appl. Phys. Lett.*, 2007, **90**, 2005–2008.

88 J. L. Macmanus-Driscoll, S. R. Foltyn, Q. X. Jia, et al., *Nat. Mater.*, 2004, **3**, 439–443.

89 L. Soler, J. Jareño, J. Banchewski, et al., *Nat. Commun.*, 2020, **11**, 344.

90 Z. Li, M. Coll, B. Mundet, et al., *Sci. Rep.*, 2019, **9**, 5828.

91 Ziliang Li, *Growth and Characterization of Nanocomposite YBa2Cu3O7-x - BaMO3 (M= Zr, Hf) thin films from colloidal solutions. PhD thesis, Universitat Autonoma de Barcelona*, 2018.

92 J. Jareño, *Growth of YBCO nanocomposite films through TLAG. PhD thesis, Universitat Autonoma de Barcelona*, 2020.

93 B. Villarejo, *Synthesis of defect free YBa2Cu3O7–x films over 1μm by CSD using Inkjet Printing, Universitat Autonoma de Barcelona.*, 2018.

94 R. H. Koch, V. Foglietti, W. J. Gallagher, G. Koren, A. Gupta and M. P. A. Fisher, *Phys. Rev. Lett.*, 1989, **63**, 1511–1514.

95 M. P. A. Fisher, *Phys. Rev. Lett.*, 1989, **62**, 1415–1418.

96 M. K. Wu, J. R. Ashburn, C. J. Torng, et al., *Phys. Rev. Lett.*, 1987, **58**, 908–910.

97 V. Breit, P. Schweiss, R. Hauff, et al., *Phys. Rev. B*, 1995, **52**, R15727--R15730.

98 R. A. Sinton and A. Cuevas, *Appl. Phys. Lett.*, 1996, **69**, 2510–2512.

99 D. Dimos, P. Chaudhari, J. Mannhart and F. K. LeGoues, *Phys. Rev. Lett.*, 1988, **61**, 219–222.

100 D. M. Feldmann, J. L. Reeves, A. A. Polyanskii, et al., *Appl. Phys. Lett.*, 2000, **77**, 2906–2908.

101 M. Gunzburger and J. Peterson, in *Vortex Dominated Flows*, WORLD SCIENTIFIC, 2005, pp. 67–85.

102 J. Bardeen and M. J. Stephen, *Phys. Rev.*, 1965, **140**, A1197–A1207.

103 G. Shaw, S. B. Blanco Alvarez, J. Brisbois, et al., *Metals (Basel).*, 2019, **9**, 1022.

104 P. Mele, K. Matsumoto, T. Horide, et al., *Supercond. Sci. Technol.*, 2008, **21**, 32002.

105 J. Gutiérrez, T. Puig and X. Obradors, *Appl. Phys. Lett.*, 2007, **90**, 162514.

106 X. Obradors and T. Puig, *Supercond. Sci. Technol.*, 2014, **27**, 044003.

2

Experimental methodologies

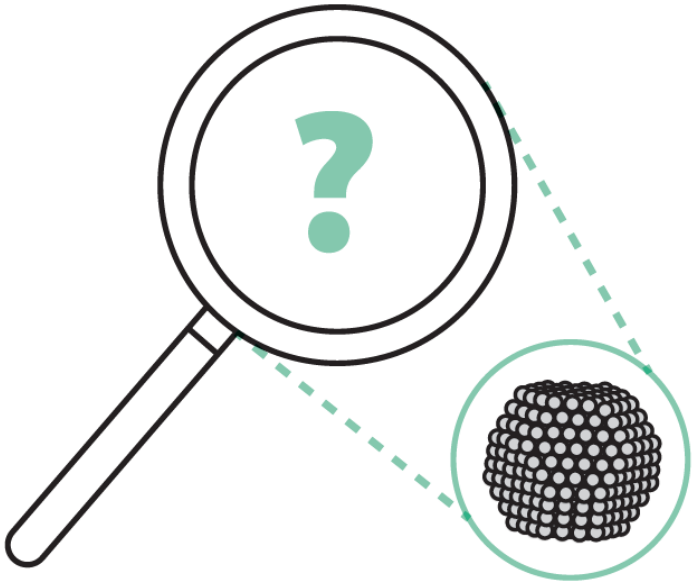

In this chapter, the experimental procedures and characterization techniques used during this thesis will be explained in detail. The first part of the chapter is developed to explain the synthesis of the NCs exposed during the thesis, as well as the synthesis of the different superconducting nanocomposites precursors solutions. Also, the preparation process of thin and thick nanocomposite films is included in this section.

The second part deals with the different characterization technique employed to study the properties of the as-synthesised NCs (*i.e.,* morphology, crystallinity, etc.), and to characterize the nanocomposite films achieved with these NCs.

2.1 Nanocrystals synthesis procedures

❖ **BMO_3 solvothermal route**

In a standard procedure, 1.24 mL (2.8 mmol) of $Zr(OC_4H_9)$ or 2.8 mmol of the desired n-butoxide precursor (M = Ti^{4+}, Zr^{4+} and Hf^{4+}) was added to 10 mL of absolute ethanol at room temperature under N_2 atmosphere. After 5 min. of vigorous stirring, barium hydroxide octahydrate, $Ba(OH)_2{\cdot}8H_2O$, 1.104 g (3.5 mmol) was added. The solution was stirred until a homogeneous solution was formed (approx. 10 min.). Then, 6 mL of triethylene glycol (TREG) and 1 mL of NH_3 30% v/v solution (or alternatively the corresponding mmol of water as detailed later in the thesis) were added under continuous stirring at room temperature, resulting in a milky solution (5 min.). The final suspension was transferred into a steel autoclave equipped with a Teflon-line and heated up to 180 °C under constant stirring for 1 hour. Afterwards the resulting suspension was slowly cooled down to room temperature. The resulting, orange-coloured suspension was washed as follows. Firstly, 10 mL of ethyl acetate as added to the suspension. The resulting mixture was sonicated for 10 min. and then centrifuged at 10.000 rpm for another 10 min. Secondly, supernatant was discarded and 10 mL of ethyl acetate: ethanol (4:1) were added. The mixture was sonicated until total dispersion of the pellet and later centrifuged at 10.000 rpm for 10 min. (this washing procedure was repeated twice). In the final step, the pellet was dispersed into absolute ethanol. To ensure a homogenous size distribution of the NCs an extra-step of centrifugation of 10 min at 7.000 rpm was performed, discarding the pellet and keeping the supernatant.

❖ **Microwave method**

Microwave (MW) synthesis was performed in 30 mL glass microwave tube by following the same procedure as in solvothermal reaction. In some cases, the NH_3 30% v/v solution was replaced with the corresponding amount of water as detailed later in the thesis (added in the same step). After the mixing, the resulting milky solution was transferred to the MW Teflon and heated with a ramp of 36 °C/min until 180 °C for the $BaMO_3$ (M = Zr^{4+} and Hf^{4+}) and 100 °C for $BaTiO_3$, holding the corresponding final temperature for 5 minutes. Afterwards, 3 centrifugation cycles were done with ethyl acetate (3 cycles x 10 mL per cycle) and finally the NCs were dispersed into absolute ethanol. A microwave profile used on $BaZrO_3$ synthesis is illustrated in Figure 2.1.

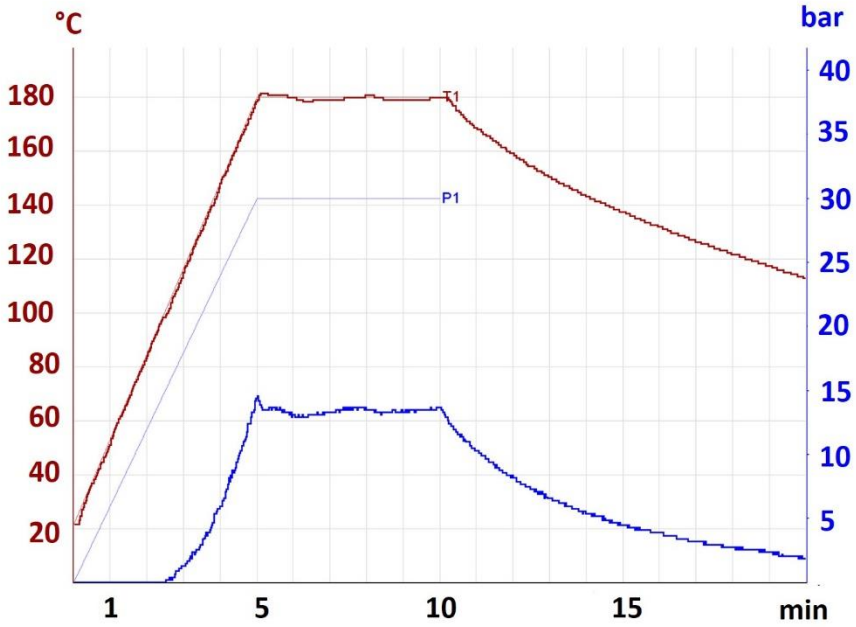

Figure 2.1. $BaZrO_3$ microwave profile (temperature and pressure), synthesised with a ramp of 36 °C/min and dwell during 5 minutes at 180 °C.

❖ $SrMO_3$ Synthesis

2.8 mmol of the desired n-butoxide precursor (M = Ti^{4+}, Zr^{4+} or Hf^{4+}) was added to 10 mL of absolute ethanol at room temperature, and vigorously stirring for 5 min. Then $Sr(OH)_2{\cdot}8H_2O$, 0.930g (3.5 mmol) was added under continuous stirring. After approx. 10 min., when the solution is homogeneous, 6 mL of TREG and 55 mmol of water were added, resulting in a milky solution after 5 min. of stirring. The final suspension was transferred into a steel autoclave equipped with a Teflon-line and heated up at 180 ˚C, under constant stirring, for 1 hour, then slowly cooled down to room temperature. Afterwards, 3 centrifugation cycles were done with ethyl acetate (3 cycles x 10 mL per cycle) and the final dispersion into absolute ethanol.

❖ $BaZrO_3$ doped with Y^{+3}

The doped process differs only on the first step of the standard procedure of $BaZrO_3$ solvothermal synthesis, which consist on varying the concentration of $Zr(OBu)_4$ and the addition of $Y(OiPr)_3$.

Doped NCs at 5% Y^{3+}: Starting at room temperature, 2.66 mmol of the $Zr(OBu)_4$ and 0.14 mmol $Y(OiPr)_3$ precursors were added to 10 mL of ethanol absolute and vigorously stirred for 5 min.

Doped NCs at 10% Y^{3+}: Starting at room temperature, 2.52 mmol of the Zirconium n-butoxide and 0.28 mmol $Y(OiPr)_3$precursor are added to 10 mL of absolute ethanol and stirred vigorously.

The posterior part of the process follows the same procedure for a typical $BaZrO_3$ synthesis.

2.2 Nanocomposite procedures

2.2.1 YBCO solution precursors

❖ **TFA-YBCO solution**

The synthesis of the TFA-YBCO solution used in this thesis was optimized by Roma et al.[1] The synthesis starts by mixing the YBCO powder (YBa_2Cu_3O) in an excess of trifluoroacetic anhydride, a small quantity of trifluoroacetic acid (Sigma Aldrich 99%) as catalyst and recently distilled acetone as solvent. The mixture is stirred for 72 hours at constant temperature (50 °C). The resulting solution is composed by TFA salts of $Ba(CF_3COO)_2$, $Cu(CF_3COO)_2$ and $Y(CF_3COO)_3$. The as-synthesised solution is then filtrated for removing any remaining powder and evaporated using a rotavapor. The mixture obtained is dissolved in anhydrous methanol up to a total metal ion concentration of 1-1.5 M. This solution is stored in sealed vials, in an inert atmosphere.

❖ **Low Fluorine-YBCO solution**

The Low fluorine solution is prepared by following the recipe proposed by X. Palmer et al.[2] The $Ba(CH_3COO)_2$ salt are mixed with methanol for about 15–20 minutes. Afterwards, propionic acid is added to completely dissolve the Ba precursor. After we make sure that the Barium acetate is completely dissolved, we add $Cu(CH_3COO)_2$ and stir until complete dissolution. Then $Y(CF_3COO)_3$ is added bestowing a final stoichiometric amount of Y:Ba:Cu=1:2:3. The solution is prepared with a continuous stirring under Ar atmosphere to reduce to the minimum the water absorption from the atmosphere. When all the precursors are completely dissolved, the last step is the addition of the necessary quantity of methanol in order to achieve the desired volume and concentration. The as-prepared solution is filtered and kept in a controlled humid atmosphere.

In the case of using YBCO-LF for ink-jet printing, just before the deposition a 6% v/v of an additive polymer compound (Kao Chimigraf, Barcelona, Spain) and 5% mol $Ag(CF_3COO)$ are dissolved in the low-fluorine solution.

❖ **Fluorine Free-YBCO solution**

The FF-YBCO solution was described by Laia Soler[3] and Julia Jareño[4] in their thesis. Following this methodology all three salts, barium, copper and yttrium are acetates. The preparation was carried out by mixing the three acetates salts in propionic acid under nitrogen atmosphere during 4 hours at 50 °C. The solution is called the "mother solution" (final concentration around 2 M from all the metals) stable on storage up to 4 weeks. For the final solution 50% of the mother solution is mixed with MeOH (1/1) at the desired concentration. Sometimes a small amount of additive triethanolamine (TEA) 5% in weight is added to increase the viscosity of the solution which will increase the thickness of the film.

2.2.2 Preparation of YBCO colloidal precursor solutions

The YBCO colloidal solution was synthesised by taken 1 mL of YBCO solution and 1 mL of NCs solution with the desired concentration (*i.e.,* 6, 12, 20 mol%). In this thesis the YBCO precursors solution used were TFA-YBCO, LF-YBCO and FF-YBCO. After achieving a stable NCs in ethanol media, they were mixed with the YBCO precursor solution forming a colloidal solution. An important step is to calculate the volume of the NCs colloidal solution needed to obtain the desire concentration of the NCs into the YBCO colloidal precursor solution. To do this step it is necessary to take into account the molarity of the NCs initial colloidal solution and the molarity of YBCO precursor solution.

Equation 2.1. is an example of the calculation required to obtained a final volume of the colloidal precursors solution of 2 mL.

$$\frac{[\mathrm{NCs}]\cdot(\mathrm{V_{NCs}})}{[\mathrm{YBCO}]\cdot(\mathrm{V_{TFA}})} = \%\ \mathrm{mol\ (Ncs)} \qquad (2.1)$$

Where [NCs] is the concentration of the nanocrystals batch (*i.e.,* ,80 mM), [YBCO] is the concentration YBCO solution (*i.e.,* 0.25 M respect the Y) and (V_{TFA}) is the volume of YBCO used, which is 1 mL. (V_{NCs}) is the value we are looking for, which corresponds to the volume of the NCs batch needed to arrive to the final mol% of the NCs. For instance, in the case of a NCs batch of 80 mM, the volume of NCs needed for reach 12 mol% is 0.37 mL.

Finally, the (1-V_{NCs}) mL of MeOH are mixed with the previous calculated (V_{NCs}) mL of the NCs leading to a total volume of NCs + MeOH of V_T= 1 mL. This volume is added as last step to YBCO (= 1 mL) resulting on a final total volume of 2 mL, thus a modifying the final concentration of YBCO.

2.2.3 Deposition technique via CSD

The deposition technique used for the deposition of nanocomposite films in this thesis were: spin-coating[5] deposition and ink-jet printing deposition (IJP)[6]. Spin-coating is a simple procedure for depositing thin films in one deposition (Figure 2.2A). In order to increase the thickness of the films using this technique multidepositions have to be performed. Regarding IJP, this methodology allows to obtain in one single deposition a higher thicker layer, moreover, is suitable for long length production or pattering (Figure 2.2B).

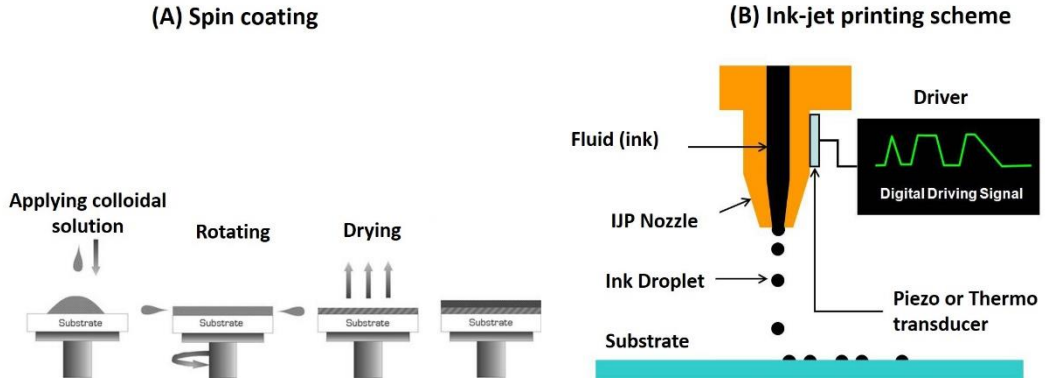

Figure 2.2 Illustration of (A) spin-coating deposition[7] and (B) ink-jet printing [8]

2.2.3 1 Spin-coating

A drop ~ 15 µl of the solution is deposited onto 5x5 mm substrate and spin at 6000 rpm for 2 minutes. After spinning, the sample is placed on a hot plate and heated at 70°C for 5 minutes to evaporate the solvents excess, resulting in a flat, uniformed and dense solid onto the substrate. This whole process was done under a nitrogen atmosphere ensuring a humidity level below 10%, to avoid the incorporation of water in our films. The final homogeneity and thickness of the layer are closely related with the acceleration, holding time, spin rotation and composition of the solution. [7,9]

2.2.3.2 Ink-jet printing

IJP methodologies relays on a drop by drop solution deposition on the substrate. The deposition is made by a piezoelectric single nozzle which responds to a pulse vibration by an electrical current. With this technique there is a tight control on the drop disposition (volume and frequency of the drop) as well as a pattern desire shape.[6,10] In our specific case, the nozzle is static while the substrate

is moving in two perpendicular direction. The procedure is made under glove box nitrogen flow to keep a lower amount of humidity on the environment.

2.2.3.3 Substrate treatment

The choice of the suitable substrate relays on materials compatible with the crystalline structure of YBCO (triple perovskite).The use of another perovskites as $LaAlO_3$ (LAO) or $SrTiO_3$(STO) shows a low mismatch value compared with YBCO lattice parameters. LAO with a mismatch (<-1.56) produce a compressive strain, while the STO (>1.56) a tensile strain.

Table 2.1. Lattice parameters of the substrates compared with the YBCO structure.

	Structure	a-parameter (Å)	Mismatch (%)
LAO	cubic	3.79	-1.56
STO	cubic	3.91	1.56
YBCO	orthorhombic	3.85	0

Therefore, LAO and STO are suitable substrate to work with and commercially available. The substrates must be meticulously clean to ensure no impurities remain on their surface. The cleaning process is performed using sonification in methanol and acetone. After the substrates are clean, they undergo a thermal treatment at high temperature (900 °C) in oxygen, in order to ensure an atomically flat surface.

2.2.4 Nanocomposites thermal process

After the deposition onto the substrate there is an entire challenging process where many parameters must be studied and optimized in order to achieve high performance superconducting films. This process consists in two thermal treatments: one at low temperature (pyrolysis) and one at high temperature (growth). The steps to achieve superconducting YBCO nanocomposites from the deposition until growth are resumed in Figure 2.3 and Figure 2.4A.

The pyrolysis process is performed usually between 300 °C and 500 °C in a humid oxygen atmosphere. During this treatment, the organic part of the films is decomposed, and the intermediate crystalline phases are formed. The pyrolysis process of TFA-YBCO is represented in Figure 2.4B. The growth process is performed at high temperatures (>800 °C) in humid oxygen and nitrogen. During this process, the final crystalline phase is formed (YBCO).

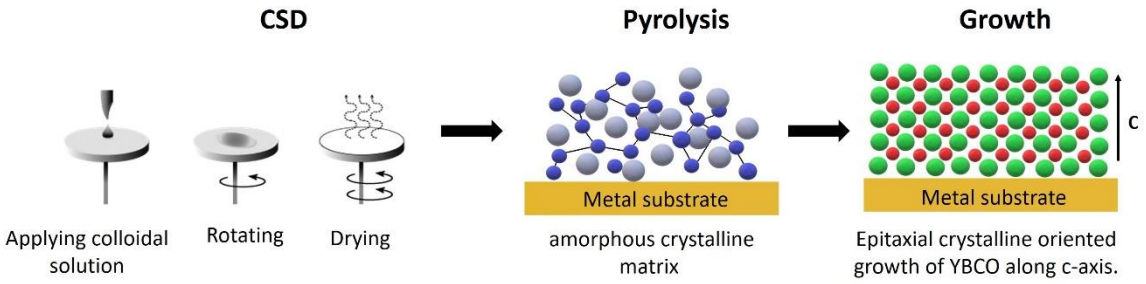

Figure 2.3 Scheme from the different steps before obtained the nanocomposite. Starting by the CSD by spin coated onto the substrate. Secondly, showing the pyrolysis procedure by applying temperature (300-500 °C) and finally growth process with a complete crystallized matrix.

After YBCO is completely crystallized an oxygenation process is performed (at 450 °C – 550 °C) on the cooling ramp after the growth. This growth process is called Conventional Thermal Annealing (CTA) and it is represented in Figure 2.4C.

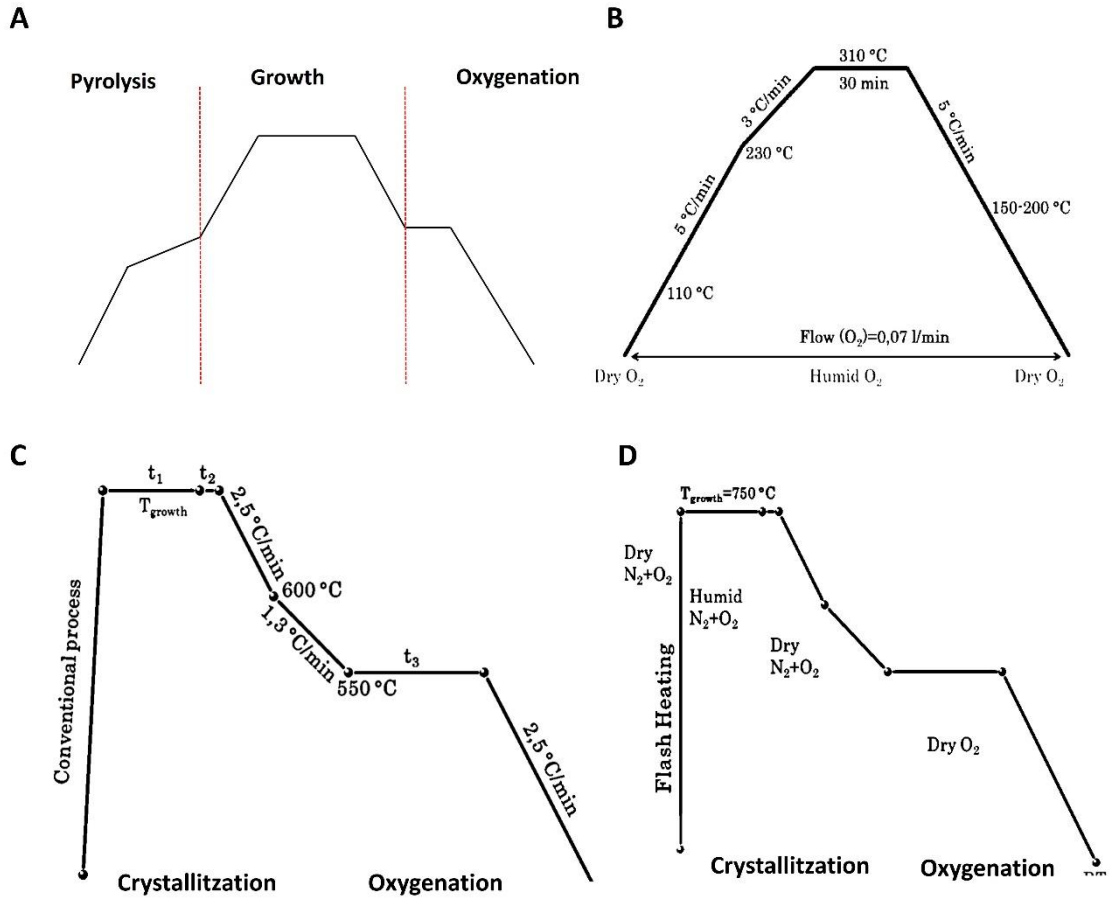

Figure 2.4. General scheme of the thermal process to generate YBCO layers, the two main parts: Pyrolysis and Growth jointly with the oxygenation process.(B) Representation of the standard pyrolysis process for TFA-YBCOA route, (C) and (D) are a standard growing process for TFA-YBCO route by Conventional Thermal Annealing process and Flash Heating respectively.

In this thesis another growth treatment was performed: Flash Heating (FH Figure 2.4D). The difference between the CTA process and the FH process is the heating rate up to the growth temperature. In the FH process the sample is introduce in the furnace directly at the growth temperature, meanwhile in CTA the sample is heated to the growth temperature with a rate on 25 °C /min. The rest of the FH process is identical with CTA.

2.3 Characterization techniques

Once the NCs are synthesised it is of main importance to completely characterise them. This way we can have an overview of the system created (i.e., sizes, crystallinity, morphology, homogeneity, etc.). For that reason, the selection of the most appropriate techniques to characterize the samples is necessary.

Commonly, when we focus on the NCs characterization, the information taken from the surface chemistry can be divided into three categories: (i) entire particle, (ii) shell and (iii) crystal. The division is a useful strategy to studied separately different parameters of the NCs. Firstly, we focus on the overall system, compose by the core and the shell (*i.e.,* hydrodynamic diameter), secondly on the shell surrounding the NCs (i.e., ligands) and finally on the core itself (*i.e.,* crystallinity, crystal size, core composition). In Figure 2.5 these three categories are represented with the different characterization techniques applied to understand the insight of each category.

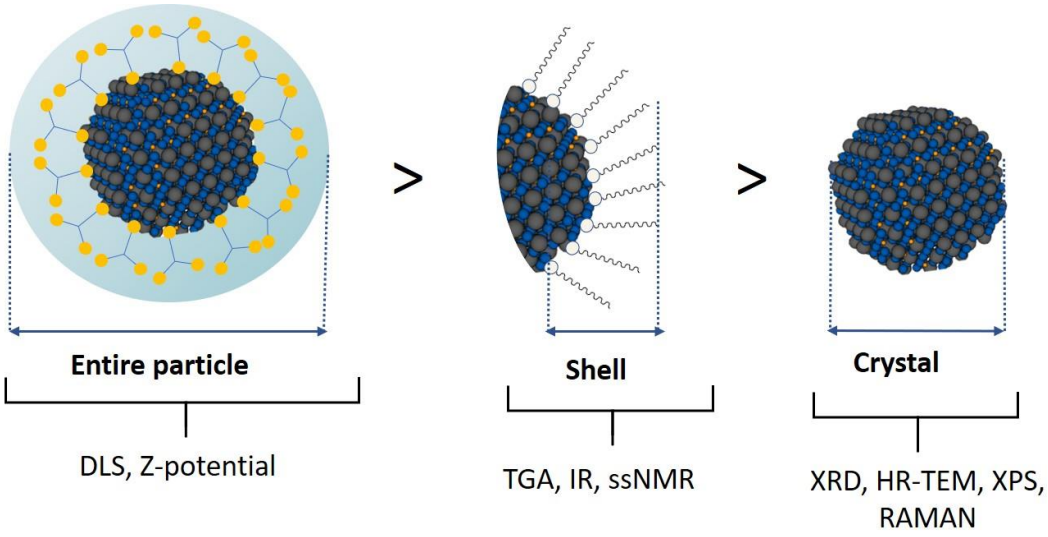

Figure.2.5. Scheme of the different techniques to full characterization the chemistry surface of the NCs. Division made by comparing the radius of the particles, firstly the largest radio of the particle (entire particles), secondly the ligand attached on the NCs surface and finally the nanocrystal core.

First category includes the information about the entire particle which is comprehended as the core and organic/inorganic shell. A perfect tool to unravel the hydrodynamic diameter of the NCs is the Dynamic Light Scattering (DLS). This tool shows the whole diameter (*i.e.,* core and shell) of the NCs. The NCs shell can be studied by different techniques, among them: Solid-state Nuclear Magnetic Resonance (ssNMR) and Infrared Spectroscopy (IR) were implemented in order to study the organic/inorganic molecules attached onto the NCs surface. Also, a quantitative analysis of the organic/inorganic shell could be done via Thermal Gravimetric Analysis (TGA). The final category is based on the core study of the particle, looking for the size without organic/inorganic shell and studying the NCs core morphology by the implementation of High Resolution Transmission Electron Microscopy (HR-TEM), and the crystallinity by both HR-TEM and X-ray Diffraction (XRD). Information about the lattice can also be obtain performing Raman spectroscopy. Besides X-ray Photoelectron Spectroscopy (XPS) measurements were used to observe the chemistry composition onto the NCs surface.

Regarding the applications of the NCs into superconductor matrix, the main characterizations presented in this thesis are divided in three sections observed in Figure 2.6: i) stability NCs into YBCO matrix, ii) Pyrolysis homogeneity, and iii) characterization of the grown film.

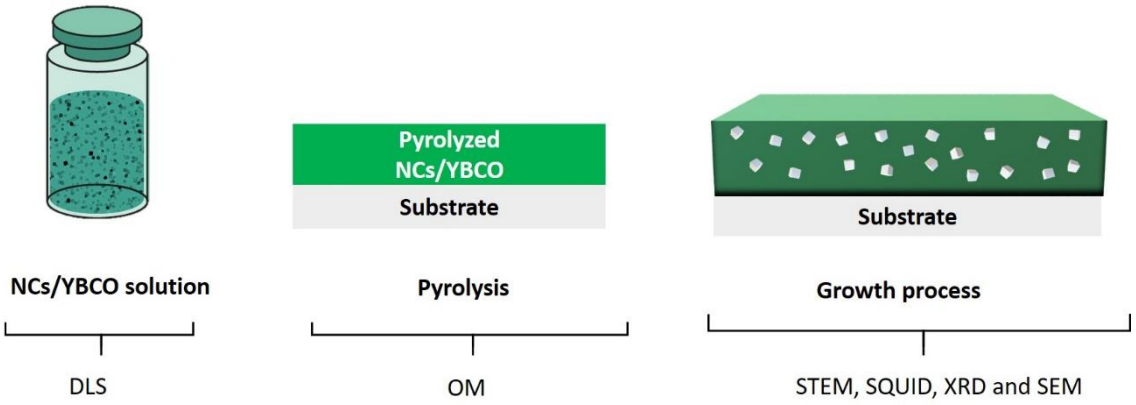

Figure.2.6. Scheme of different characterization techniques of NC/YBCO solution until achieving a successful nanocomposite. Divided, firstly on the stabilization of NCs into YBCO matrix. Secondly, checking the pyrolysis process. Finally the growing process by testing the physical property and proving the presence of the NCs into the YBCO matrix.

First section is focused on the study of the colloidal solution stability between the NCs colloidal solution and the YBCO precursor solution. Dynamic light scattering (DLS) is a good tool not only for studying the size of the NCs but also to monitoring the colloidal stability of the NCs into the YBCO solution precursors. Using this technique, it can be proving a non-agglomeration or precipitate tendency. After the pyrolysis process, it must be checked the homogeneity layer of NCs/YBCO onto the substrate by using an optical microscope (OM). After the

growth process, the scanning transmission electron microscopy (STEM) is used for checking the random deposition of the NCs onto the matrix, as well as looking for defects on the matrix growths. Besides an XRD is performed to corroborate; the presence of the NCs onto the nanocomposites and the epitaxial growth of YBCO. Finally, in this last section a physical characterization of superconducting properties is measured by commercial superconducting quantum interference device (SQUID).

2.3.1 Dynamic light scattering

Dynamic light scattering (DLS) is a technique used to determine the mean size of a particle and their approximate distribution, working in a range of 1-1000 nm. Basically, consist of the measurement and interpretation of light scattering data induced on a colloidal solution. The particles are illuminated with a laser and the feedback is analyzed on microsecond time scale.[11,12]

DLS is based on Brownian motion. For a system of particles undergoing Brownian motion, smaller nanoparticles move or diffuse more quickly and large particles diffuse more slowly. The Brownian motion rate is quantified as the translation diffusion coefficient (D) by using an autocorrelation function. The goal of the DLS technique is to determine the mean sizes of the particle which is obtained by using Stoke-Einstein equation (equation 2.2)[12,13]

$$D = \frac{K_b T}{6\pi\eta_s D_H} \qquad (2.2)$$

where D is the diffusion coefficient, K_b is Boltzmann's constant, η the viscosity of the solvent we are using and D_H the hydrodynamic radius of the particle. The equations show a dependency with a viscosity (η) and temperature (T). The results obtained correspond to the final diameter of the particles, called the hydrodynamic diameter (D_H).

The detected light scattered can be plotted in several ways: (i) intensity, (ii) volume and (iii) number. The intensity distribution is weighted according to the scattering intensity of each particle fraction or family. The particle scattering intensity is proportional to the square of the molecular weight. Nonetheless the intensity result can be overly sensitive to very small numbers of aggregates or dust, which can dominate the distribution. However, if the measurement shows substantial tail on the analysis or more than one peak, then Mie theory[14] should be applied. Mie theory describe the relative proportion of multiple components in the sample based on their volume or number of the particles rather than based on their weight.

In this work, we have been using volume distribution, which give us a smooth correlation function to detect the most accurate hydrodynamic diameter of the NCs.

In addition, other important term in DLS measurements is the parameter called Z-average. The Z-average is derived from Cumulant analysis. This parameter is based on the intensity overall average particle size, thus focusing on weight distribution.[15,16] This may not be the actual size value of the nanoparticle as there may be aggregates. But it can show us an overall of the system. In Figure 2.7A is an example representation of a DLS measurement for the same sample of size distribution by intensity (black) and volume (red) distribution, showing in both cases same Z-average corresponding to 36.4 nm.

Another important use of DLS technique, is the measurement of ζ-Potential by using the same instrumentation.[17] ζ-Potential measure the electrophoretic mobility, which is related to the net surface charge that nanoparticles have and quantified the repulsion between the particles in suspension aiding stability studies. ζ-Potential is defined as the voltage at the edge of the slip plane.

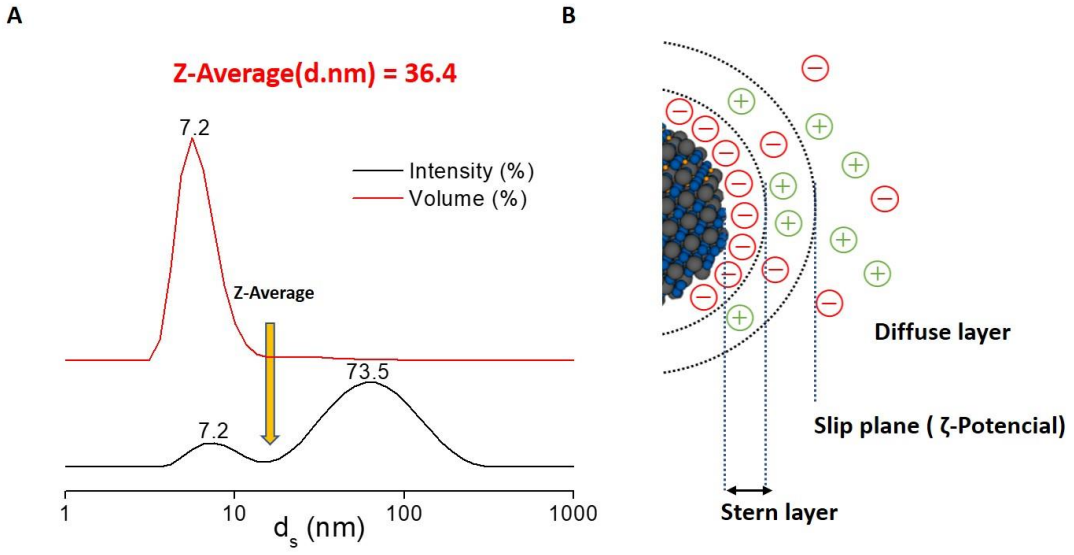

Figure 2.7.(A) Example of a representation of DLS measurement from the same sample by using sizes distribution in intensity and volume %. Showing a Z-Average on the intensity graph and pointing the total value of Z-average in both cases. (B) Scheme of the ζ-Potential measurement.

In order to ensure good stable colloidal solution, the values of ζ-potential must be on the rage of ζ-potential ≤ -30 or +30 ≤ ζ-potential, in this specific scenario they will not agglomerate due to repulsive electrostatic forces between the particles.

The DLS and ζ-Potential measurements in this thesis were done with a Zetasizer Nano (Malvern Instruments) equipment by following the Smoluchowski equation with measurement range of 0.3 nm – 10.0 μm and sensitivity of 0.1 mg/mL.

2.3.2 Spectroscopy

2.3.2.1 Raman spectroscopy

Raman spectroscopy has become an attractive technique to analyses the structural composition providing information about the lattice structure, oxygen vacancies and structure distortion of the solid NCs. In this thesis we used Raman as an alternative technique to XRD in order to corroborate the crystal structure of $BaTiO_3$, and see if the lattice has suffered some distortion. The Raman technique use vibrational spectroscopy, based on the inelastic scattering of monochromatic laser light through a sample, and it is used to detect vibrations, rotational and other low-frequencies modes in the system.[18,19] The Raman scattering can be though as two photons process and take place due to inelastic collision between photons and electrons. Photons of the laser light are absorbed by the sample and then reemitted. The difference in energy between incident photon and emitted photon generates Raman lines. Depending on the emitted frequency, the lines generated can be called Stokes lines, if their frequency are less than incident frequency of photons. In the case that frequency of emitted photons are greater than incident frequency, the lines are called Anti/stokes lines. The Raman spectra give a molecular fingerprint and it is different for different molecules.

The instrument used for measure Raman spectroscopy was Micro-Raman performed in backscattering geometry at room temperature using the 5145 Å line of Argon-ion laser with a XploRA PLUS Raman spectrometer from Horiba, attached to an Olympus microscope and equipped with CCD detector.

2.3.2.2 Energy Dispersive X-Ray Analysis

Energy Dispersive X-Ray Analysis (EDX) is X-ray technique incorporated in electron microscopy instruments (TEM and SEM). It is used to identify the elemental composition of the bulk material. EDX is capable to show the peaks corresponding to the elements, providing the true composition of the sample, being qualitative, semi-quantitative and quantitative analysis.[20,21] The position of a peak in the spectrum is related with the energy of each element, identifying the element; the area under the peak is proportional to the number of atoms of the element in the irradiated area. X-rays are also produced when the electron beam is

slowed by the electrostatic fields of the atomic nuclei of elements present in the specimen.

During this thesis, this technique was performed in order to ensure the detection of Yttrium in the Y^{3+} doped $BaZrO_3$ NCs and to study the real composition of the main metals (Ba^{2+}, Zr^{4+}) in the sample. The measurements were performed with a HRTEM equipped with a detector EDS Oxdord Instruments X-max. Resolution energy 136 eV.

2.3.2.3 X-ray Photoelectron Spectroscopy

X-ray Photoelectron Spectroscopy (XPS) is a sensitive spectroscopy technique used to study the chemical composition of the NCs. The technique is based on the photoelectric effect described by Einstein in 1905, using in this case as a light source coming from X-ray beans. [22-24] The detector can measure the kinetic energy of the emitted electron from the NC surface, so it is possible to extract the binding energy of a particular electron by following the Equation 2.3.

$$E_{binding} = E_{photon} - (E_{Kinetic} - \phi) \quad (2.3)$$

where ϕ is the work function for the specific surface and the spectrometer. Every element emits electrons at different binding energies, being this signal a footprint of each material. For this reason, by scanning a wide range of binding energies, it is possible to identify all the elements present in the NC surface.

The XPS in this thesis have been useful to corroborate the presence of ammonia in the NCs surface. The XPS measurements were performed with a Phoibos 150 analyser.

2.3.2.4 Infrared Spectroscopy

Infrared Spectroscopy (IR) becomes an attractive tool for study the surface properties and conformation of NCs.[25] IR is a rapid and cheap measurement, based on the interaction of infrared radiation with the solid sample in all the IR spectrum. The sample selectively absorbs the radiation of specific wavelength changing the dipole moment of the sample molecules, which makes a vibration energy transfer from the ground state to an excited state. This transition energy corresponds to many functional groups which are found in the mid infrared region (4000 - 400 cm^{-1}), therefore the appearance of an absorption band in this region suggests the presence of a specific functional group exist on the sample. Most of the measured

absorbance bands are associated with stretching and bending vibrations, which gives an important key to understanding what is on the surface.

The measurement with this technique has been done by Infrared spectroscopy (IR) analyses have been carried out in the Servei d'Anàlisi Química with the Bruker spectrophotometer IR Tensor 27.

2.3.3 Thermal Gravimetric Analysis

Thermal gravimetric analysis (TGA)[26,27] measures the weight loss of the material surrounding the NCs. The analysis is based on heating the sample to high temperatures, making that one or some of the components decompose. During the whole process, the changes in weight in relation to a temperature are measured under controlled atmosphere. Contrary to the techniques expose previously, this is also a quantitative tool. It gives valuable information about the amount of organic ligand which remains on the nanoparticle surface and the thermal decomposition of this ligand.

The measurement of TGA made in this thesis were performed at a heating ramp of 5 °C/min from room temperature to 800 °C in air atmosphere. The equipment used was a NETZSCH STA 449C analyser from ICMAB.

2.3.4 Microscopy techniques

Microscopy technique is a very wide field which encompasses different detection methods as well as different instruments depending which characteristics we want to study on a sample.

2.3.4.1 Optical Microscopy

Optical Microscopy (OM) gives a closer view of a sample through a magnifying lens by using visible light. Therefore, the resolution of this microscopes is limited to a wavelength between 400 nm and 700 nm. This technique was used to check the homogeny and the good texture of the YBCO nanocomposite films after the pyrolysis (application of the NCs into the superconductive field). This is an important step used to the identify any defect that could appear on the film surface, determining the suitability of the pyrolyzed films for the next growth process.

In this thesis the optical microscope images were acquired with a Leica DM 1750 M optical microscope from ICMAB.

2.3.4.2 Transmission Electron Microscopy

Transmission electron microscopy (TEM) is an enormously powerful tool for the characterization of the NCs.[28] TEM equipment use an electron beam that bombards the previously prepared samples. A representation of different parts of a TEM microscope is found in Figure 2.8.

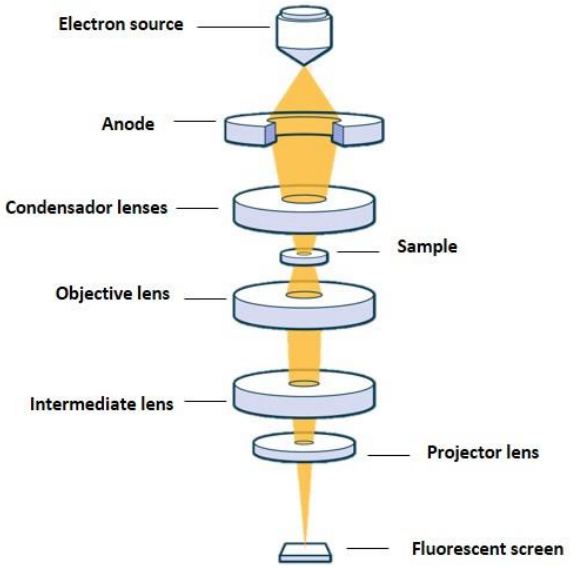

Figure 2.8 Scheme from the different parts of the TEM microscope

A electron beam travel among a column under high vacuum from the electron source and get detected by a digital camera.(Figure 2.8) The beam goes through the sample creating an image that details the sample's (i) morphology, (ii) composition and (iii) crystal structure. The samples must be thinner, less than 150 nm to facilitate to the electron beam pass through it and finally creating a 2D image. To increase the TEM resolution the High-Resolution Transmission Electron (HRTEM) was implemented. With this technique it is possible to achieve resolution at atomic scale. This is especially useful when analysing the structural lattice of the NCs.

The TEM characterization in this thesis have been done by: Transmission electron microscopy (TEM) micrographs on a 120 kV JEOL 1210 TEM, which has a resolution point of 3.2 Å from ICMAB. Transmission Electron Microscopy (TEM) analysis by a CM200 LaB6 Philips microscope with an operation voltage of 200 kV, equipped with an energy dispersive X-ray (EDX) elemental analysis system from Humboldt university from Berlin. In the case of High-Resolution Transmission

Electron Microscopy (HRTEM) micrographs obtained on a 200 kV JEOL 2011 TEM, with a resolution point of 1.8 Å at 200 kV from Servei de Microscòpia of UAB. The samples were prepared for TEM analysis by spreading a drop of as-prepared NC diluted dispersion on amorphous carbon-coated grids and then dried in air.

The YBCO nanocomposite films were also analysed using TEM, but in this case Scanning Transmission Electron Microscope (STEM) was used. Through this analysis many useful information about the films features were obtained. We could be observed in great detail the NCs size, their distribution in the superconductor matrix and also their orientation. The STEM analysis was performed on a FEI Titan 60-30 microscope equipped with X-FEG gun, a CETCOR probe corrector and Gatan TRIDIEM 866 ERS energy filter operated in STEM mode 300 kV.

2.3.4.3 Scanning Electron Microscopy

Scanning Electron Microscopy (SEM) follows almost the same principles as TEM. Using this technique the images are obtained from the signals that result from the interaction between the accelerated electron beam with the atoms situated at different depths of the sample (Figure 2.9). This interaction generates different types of signal: secondary electrons, backscatter electrons, X-rays, transmitted electrons, etc. Each signal has a different detector. The resulting image is a 3D map, which entails a sample's topography and element composition.

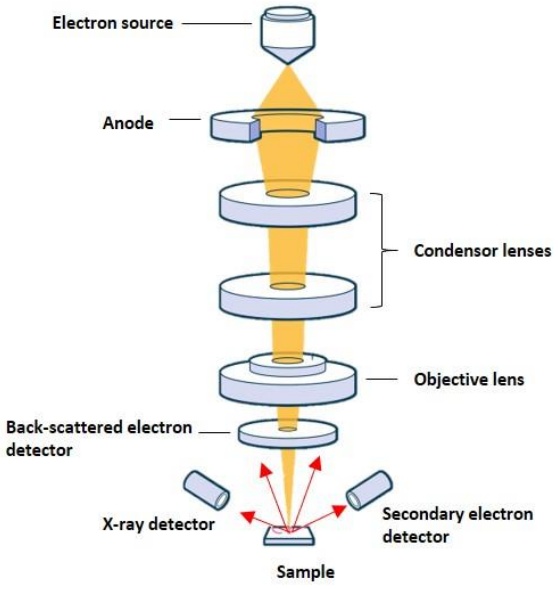

Figure 2.9. Scheme from the different parts of the SEM microscope

In this thesis SEM was used to characterize the YBCO nanocomposite layers. SEM images were taken using FEI Quanta 200 FEG SEM of FEI CompanyTM.

2.3.5 X-ray Diffraction

X-ray Diffraction (XRD) is a nondestructive technique used to characterized crystalline materials. This technique provides information on the crystalline structure, crystalline phases, preferred crystal orientation and others structural parameters that could be extract from the data as: average grain sizes, crystallinity, lattice parameters, etc.

XRD is based on the Bragg's law[29] (Equation 2.4), which stablish the relationship describing the angle at which a beam of X-rays of a particular wavelength diffracts from a crystalline surface.

$$n\lambda = 2\, d\, sin\theta \tag{2.4}$$

where the "n" is an integer number, d is the interplanar distance, λ is the wavelength of the incident wave and θ is the Bragg angle. Figure 2.10 is a representation of the X-ray diffraction. Generally, XRD are operating at a known voltage and current using a fixed wavelength (*i.e.,* Cu, Fe, Mo, etc.).

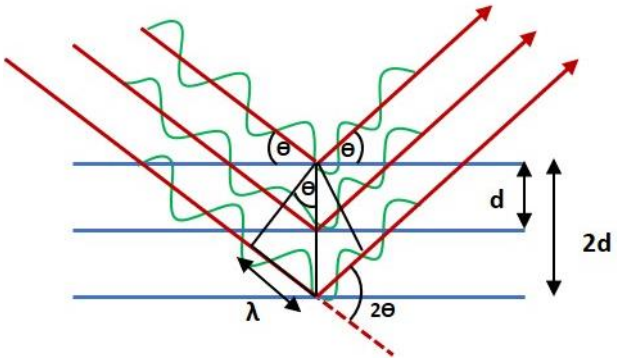

Figure 2.10. Schematic representation, showing the incident and diffracted waves on the crystal surface according to the Bragg's Law equation.

By scanning the sample through 2θ angles, the diffraction waves intensity is collected by a detector for each incident angle to build the so-called diffraction pattern. This pattern is the fingerprint of the periodic atomic arrangements in a giving material. Additionally, from the XRD pattern some information related with the crystalline coherence domain of a NCs can be collected and calculated using Scherrer Equation[30] (Equation 2.5).

$$\tau = \frac{K\lambda}{\beta cos\theta} \tag{2.5}$$

where τ correspond to the main grain sizes of the NCs, K is a constant dimensionless shape factor, λ the X-ray wavelength, β is the value of the broadening at half of the maximus intensity peak also called FWHM, θ is the Bragg angle. Therefore, a broad peak means high values of β and small NCs size. Using the Scherrer equation it is possible to calculate the crystalline sizes of the nanoparticle being useful as a complementary alternative with TEM technique to corroborate the sizes of the nanoparticle.

The XRD equipment used was a Phillips X Pert diffractometer equipped with a two circle diffractometers and Cu tube. In some specific cases XRD patterns were recorded with a STOE MP diffractometer in transmission configuration using Mo Kα radiation (λ=0.07093 nm).

For the nanocomposite layers a two-dimensional diffractometer was used. The 2D diffraction pattern of the YBCO layers was integrated using GADDS and Origin software and transformed to a conventional XRD spectra. The films were analysed using the Bruker-AXS General Area Detection Diffraction System in ICMAB.

2.3.6 Solid-state Nuclear Magnetic Resonance

Solid-state Nuclear Magnetic Resonance (ss-NMR)[31,32] method has emerged as a powerful technique to provide structural and dynamic information of the NC surface, improving the sensitivity and resolution in NMR techniques. This technique used solid powder of the sample, thus removing any trace of interaction with the solvent as could happened by using NMR. In contrast ssNMR spectra are much road than the NMR, due to the internuclear distance between them and the anisotropy or orientation-dependent interactions of the chemical shift. In order to enhance the spectra resolution, and sharply the peaks to a better definition, one of the most used methodology is the technique called magic angle spinning(MAS).[33,34] MAS entails a rapidly rotation of the sample about an axi oriented at probe angle corresponding to 54.74° with respect to the external magnetic field, generating a significant narrowing of the line width in the spectrum

The ss-NMR used in this Thesis was recorded in Humboldt university of Berlin by Bruker spectrometer 4 mm MAS 1H/19.

2.3.7 Select Area Diffraction Pattern

Select Area Diffraction Pattern (SAED) technique is used to studying the crystal structure and the crystal defects of the sample.[35] It is similar to XRD but it

allows the examination of smaller areas. SAED is usually performed in TEM and SEM instruments.

To analysis SAED patterns we combine the Bragg's Equation (2.4) and geometric relationship in the reciprocal space. Therefore, we can calculate the d-spacing for the spots on the SAED pattern by following Equation 2.6

$$D = D/(\lambda L) \tag{2.6}$$

where D is the distance between spots on the SAED, L is the camera length for the machine used and λ is the wavelength of electron beam used. Every spot in the SAED pattern corresponds to lattice planes of a certain miller index in single crystal. The diffraction pattern is completely dependent on the d-spacing and on the composition of the crystal sample analysed. The radii of the rings are inversely proportional to the interplanar spacings dhkl of a lattice planes of crystals, which obeys the relationship that mentioned previously. In other words, the diffraction pattern could be regarded as a fingerprint for a certain crystal.

Therefore, if the sample is amorphous or the grain size is extremely small, the ring disappears leading to a bright spot in the centre (Figure 2.11A). A single crystal sample as the one display in Figure 2.11B has a high degree of order in which the crystal lattice of the entire sample is continuous with no grain boundaries.

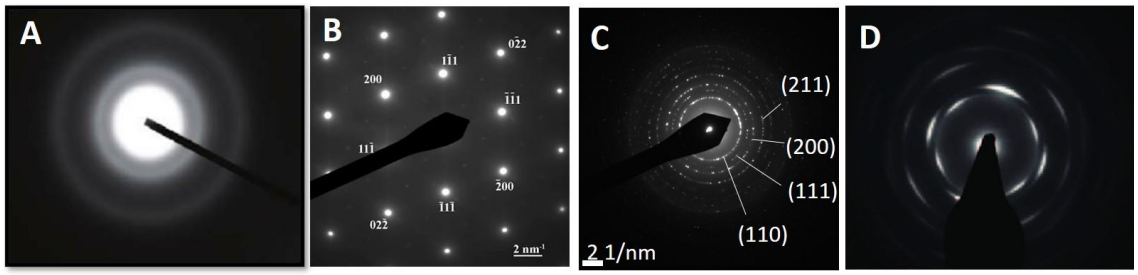

Figure 2.11. Selected area electron diffraction (SAED) patterns obtained from (A) amorph sample, (B)monocrystal sample, (C) polycrystalline sample amd (D) crystal sample oriented in a favoured direction.

In Figure 2.11C every ring in SAED pattern corresponds to a group of lattice planes of the same miller index family in a polycrystalline sample. In the case of Figure2.11D the grain in the sample is oriented in a favoured direction, the diffraction pattern is shown as an intermediate between diffraction in single crystal and polycrystalline.

2.3.7 Physical characterization of superconducting properties

A superconducting quantum interference device (SQUID) is a magnetometer[36,37] used to measure electromagnetic response of superconducting YBCO films. The information obtained by the evolution of the magnetic moment with temperature or magnetic field provides information about superconducting properties such as T_c, J_c or the behaviour of the material when some external magnetic field is applied.

During this thesis m(H) measurements were carried out for the nanocomposite layers using an (H//c) configuration to observe the evolution of the critical current at increasing the magnetic field. In order to determine the J_c values, the Bean model[38] for a square shape superconductor was applied (Equation 2.7):

$$J_c = \frac{3m}{\pi r^3 t} \tag{2.7}$$

where J_c is the value of critical current for a square layer with thickness "t" and "r" as the area of the layers. To present the results usually a quadrant plot in a log-log scale is used. In Figure 2.12 is displayed an example of this measurement. The films with better performances are those for whom the $\mu_0 H^*$ is pushed towards higher magnetic fields.

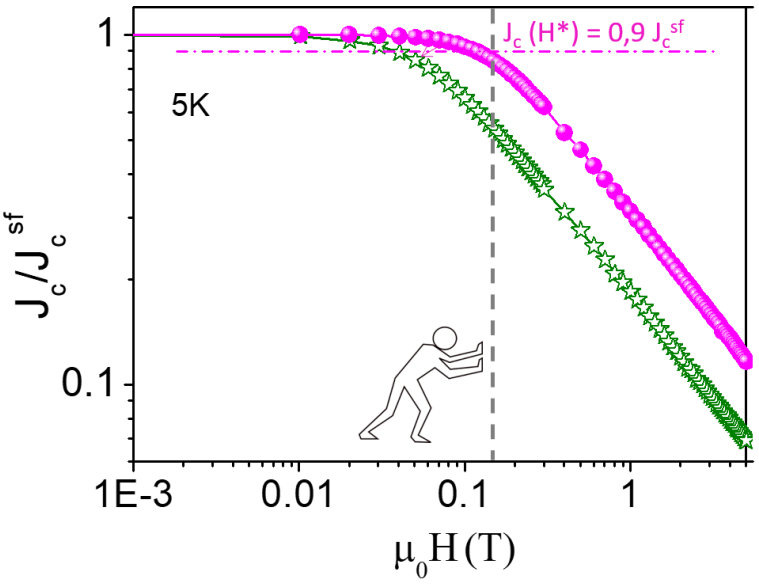

Figure 2.12. An example of log-log scale $J_c(H)$ plot showing the degradation of J_c exposed to magnetic field. Besides the definition of $\mu_0 H^*$ using the criteria of $J_c(\mu_0 H^*)=0.9\ J_c^{sf}$.

In this thesis, the SQUID was used to analyse the differences behaviour between the nanocomposites and the pristine films, in order to demonstrate the efficiency of the NCs embedded on YBCO matrix as a pinning centre.

2.4 References

1 N. Roma, S. Morlens, S. Ricart, et al., *Supercond. Sci. Technol.*, 2006, **19**, 521–527.

2 X. Palmer, C. Pop, H. Eloussifi, et al., *Supercond. Sci. Technol.*, 2016, **29**, 024002.

3 L. Soler, *Liquid-assisted ultrafast growth of superconducting films derived from chemical solutions. PhD thesis, Universitat Autonoma de Barcelona.*, 2019.

4 J. Jareño, *Growth of YBCO nanocomposite films through TLAG. PhD thesis, Universitat Autonoma de Barcelona.*, 2020.

5 M. V Kelso, N. K. Mahenderkar, Q. Chen, J. Z. Tubbesing and J. A. Switzer, *Science (80-.).*, 2019, **364**, 166–169.

6 B. Derby, *Annu. Rev. Mater. Res.*, 2010, **40**, 395–414.

7 L. A. Dobrzanski and Szindler, *J. Achiev. Mater. Manuf. Eng.*, 2012, **52**, 7–14.

8 V. Bansal, P. Poddar, A. Ahmad and M. Sastry, *J. Am. Chem. Soc.*, 2006, **128**, 11958–11963.

9 R. W. Schwartz, *Chem. Mater.*, 1997, **9**, 2325–2340.

10 M. Vilardell, X. Granados, S. Ricart, et al., *Thin Solid Films*, 2013, **548**, 489–497.

11 J. Stetefeld, S. A. McKenna and T. R. Patel, *Biophys. Rev.*, 2016, **8**, 409–427.

12 J. Lim, S. P. Yeap, H. X. Che and S. C. Low, *Nanoscale Res. Lett.*, 2013, **8**, 1–14.

13 P. J. Patty and B. J. Frisken, *Appl. Opt.*, 2006, **45**, 2209–2216.

14 Q. Fu and W. Sun, *Appl. Opt.*, 2001, **40**, 1354–1361.

15 D. E. Koppel, *J. Chem. Phys.*, 1972, **57**, 4814–4820.

16 J. C. Thomas, *J. Colloid Interface Sci.*, 1987, **117**, 187–192.

17 S. Bhattacharjee, *J. Control. Release*, 2016, **235**, 337–351.

18 R. S. Das and Y. K. Agrawal, *Vib. Spectrosc.*, 2011, **57**, 163–176.

19 G. S. Bumbrah and R. M. Sharma, *Egypt. J. Forensic Sci.*, 2016, **6**, 209–215.

20 M. S. I. Khan, S.-W. Oh and Y.-J. Kim, *Sci. Rep.*, 2020, **10**, 2368.

21 M. Scimeca, S. Bischetti, H. K. Lamsira, R. Bonfiglio and E. Bonanno, *Eur. J. Histochem.*, 2018, **62**, 2841.

22 D. Briggs, *Handb. Adhes. Second Ed.*, 2005, 621–622.

23 M. Aziz and A. F. Ismail, in *Membrane Characterization*, eds. N. Hilal, A. F. Ismail, et al., Elsevier, 2017, pp. 81–93.

24 G. Greczynski and L. Hultman, *Prog. Mater. Sci.*, 2020, **107**, 100591.

25 M. A. Mohamed, J. Jaafar, A. F. Ismail, M. H. D. Othman and M. A. Rahman, in *Membrane Characterization*, Elsevier, 2017, pp. 3–29.

26 S. Loganathan, R. B. Valapa, R. K. Mishra, G. Pugazhenthi and S. Thomas, in *Thermal and Rheological Measurement Techniques for Nanomaterials Characterization*, eds. S. Thomas, R. Thomas, et al., Elsevier, 2017, pp. 67–108.

27 D. I. Donato, G. Lazzara and S. Milioto, *J. Therm. Anal. Calorim.*, 2010, **101**, 1085–1091.

28 P. S. Kumar, K. G. Pavithra and M. Naushad, in *Nanomaterials for Solar Cell Applications*, eds. S. Thomas, E. H. M. Sakho, et al., Elsevier, 2019, pp. 97–124.

29 W. H. Bragg and W. L. Bragg, *Proc. R. Soc. London. Ser. A, Contain. Pap. a Math. Phys. Character*, 1913, **88**, 428–438.

30 F. T. L. Muniz, M. A. R. Miranda, C. dos Santos and J. M. Sasaki, *Acta Crystallogr. Sect. A*, 2016, **72**, 385–390.

31 T. O. Niinikoski, in *The Physics of Polarized Targets*, Cambridge University Press, 2020, pp. 199–244.

32 P.-H. Chien, K. J. Griffith, H. Liu, Z. Gan and Y.-Y. Hu, *Annu. Rev. Mater. Res.*, 2020, **50**, 493–520.

33 P. T. Judge, E. L. Sesti, E. P. Saliba, et al., *J. Magn. Reson.*, 2019, **305**, 51–57.

34 T. Polenova, R. Gupta and A. Goldbourt, *Anal. Chem.*, 2015, **87**, 5458–5469.

35 S. H. I. Honglong, Z. Guling, Z. O. U. Bin, L. U. O. Minting and W. Wenzhong, 2013, **647**, 641–647.

36 R. Kleiner, D. Koelle, F. Ludwig and J. Clarke, *Proc. IEEE*, 2004, **92**, 1534–1548.

37 C. Granata and A. Vettoliere, *Phys. Rep.*, 2016, **614**, 1–69.

38 C. P. Bean, *Phys. Rev. Lett.*, 1962, **8**, 250–253.

3

Hybrid approach to obtain high-quality $BaZrO_3$ perovskite nanocrystals

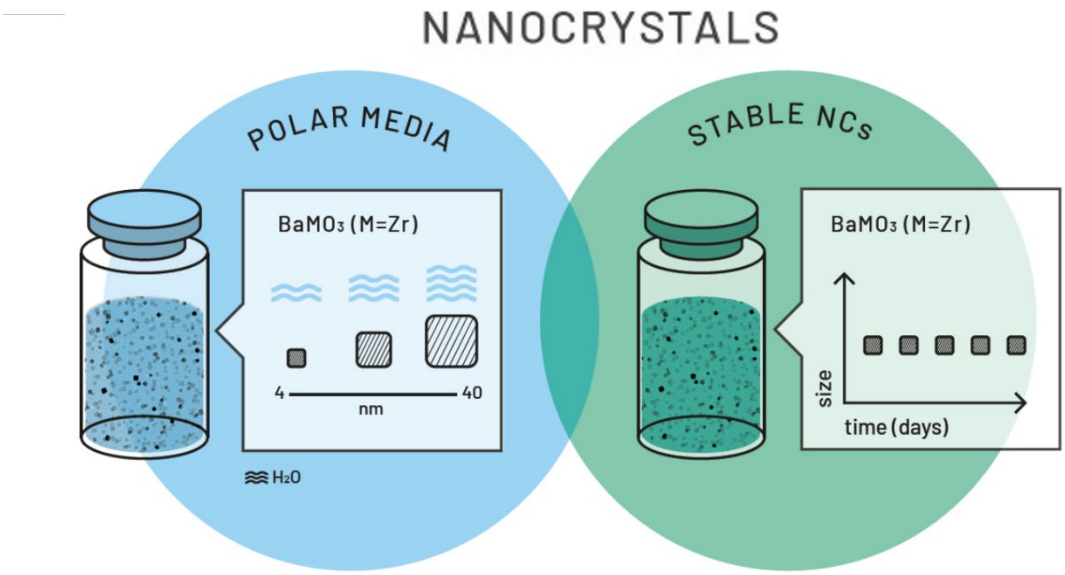

In this chapter, we present a hybrid solvothermal approach (*i.e.,* sol-gel and solvothermal) to synthesise $BaZrO_3$ nanocrystals with tunable sizes and long-time stability. The purpose was to obtain homogeneous and stable $BaZrO_3$ nanocrystals using an easy, fast and reproducible method. There is no suitable $BaZrO_3$ nanocrystals synthesized strategy to achieve non-agglomerated and stable nanocrystals in a non-aqueous media described in the literature. In contrast with commonly reported methodologies, the combination of aqueous sol-gel and solvothermal treatments not only allowed the successfully production of these particles but also a high tunable control of their size and homogeneity. In addition, by using this technique, we evidence the role of water in the hydrolytic step as the key parameter to tune the final size of the nanocrystals. The control of this parameter allowed us to obtain sizes from 4 to 30 nm, adapting these nanocrystals to a wide range of applications.

Adapted from: N. Chamorro, J. Martínez-Esaín, T. Puig, et al., *RSC Adv.*, 2020, **10**, 28872–28878.

3.1 Introduction

One of the applications of nanocrystals (NCs) that have awaken a lot of interest lately is superconductivity.[1–4] In superconductivity the NCs can be combined with REBCO (RE= rare earth) leading to very interesting superconductive properties at high magnetic fields. Taken this into account, in this chapter we will present the methodology of synthesis for $BaZrO_3$ NCs to better adapt the final material to this application. In order for this to happen the NCs have to accomplish with the next requirements:

- ✓ Small sizes < 15 nm
- ✓ High crystallinity
- ✓ Long stability on polar media
- ✓ Concentrations up to 80mM
- ✓ ≤ 0.5% content of water
- ✓ Low-cost route
- ✓ Stable during the growth process of REBCO matrix (no agglomeration, no coarsening, no reactivity, etc.)

Among the different methodologies to synthesise oxide nanocrystals, two main strategies are highlighted: (i) sol-gel aqueous processes and (ii) non-aqueous solvothermal treatments.

Sol-gel process is a well-known method to obtain NCs oxides, studied for decades.[5–8] Aqueous sol-gel methods are based on the fast hydrolysis and posterior condensation of the precursors obtaining a gel-based precursor oxide as the previous step.[9–11] The issue with this method is that the reactions can lead to complex compounds, that can be difficultly identified. Therefore, the sol-gel process is even nowadays still not fully controlled. Also, the NCs obtained with this method show poor crystallinity, requiring high thermal treatments in order to overcome this issue.

Several advantages such as high crystallinity, controlled crystal growth and homogeneous NC dispersions[12,13] made the non-aqueous solvothermal treatment to be of high interest to researchers in the field. However, this methodology shows two main drawbacks: long reaction times and the need to use high temperatures during the process[14–16] which could lead to high costs.

In this chapter we firstly chose the solvothermal method, however, the need to optimize the $BaZrO_3$ NCs parameters in order to reach the requirements stated before, lead us to reveal the use of a hybrid method between solvothermal and sol-gel.

3.2 Barium Zirconate synthesis

3.2.1 Previous Experiments

The synthesis of BMO_3 perovskite family *(i.e.,* $BaTiO_3$, $PbCrO_3$, $LiNbO_3$, etc.) has been widely studied.[12,17–21] However, in the case of $BaZrO_3$ NCs there is still a lack of knowledge on its synthetic pathway to overcoming some issues like: agglomeration, size control, crystallinity and reaction time.[22–27] In order to make these NCs attractive for the application these issue need to be solved.

At first, we chose the solvothermal method because it best suited our needs: achieve high crystalline NCs and be able to work with organic solvents (*i.e.,* alcohol media). Initially we tested three different methods. Method 1 and method 2 were based in two previous works by K. Nakashima, et. al.,[25] and H. W. Lee, et.al.,[28] respectively. Method 3 was related to our previous experience in the laboratory by using a polyol route in the synthesis of metal oxide nanocrystals.[29] Thus, we aimed to use a modified polyol route and make it extensible to the $BaZrO_3$ perovskite NCs.

The conditions and the precursors used for all three methods are summarized in Table 3.1.

Table 3.1 An overview of different methodologies trials and the parameters needed for the synthesis of $BaZrO_3$ NCs. The main drawbacks and achievements of the methodologies are exposed in the issue's column.

Method	Precursors (mmol)		Solvents (mL)		Temp./time	Issues
1			EtOH	10	230 °C/18 h.	Agglomeration
	$Zr(OBu)_4$	3.5	2-methoxyethanol	6		Polydisperse
	$Ba(OH)_2{\cdot}8H_2O$	3.5	H_2O	0.27		Precipitate
			NH_3	1		Crystalline
2			EtOH	10	200 °C /48 h.	Amorphous
	$Zr(OBu)_4$	2.5	Triethanolamine	5		Agglomeration
	$Ba(OH)_2{\cdot}8H_2O$	3.5	H_2O	-		
			NH_3	2.5		
3			EtOH	10	210 °C /24 h.	Agglomeration
	$Zr(OBu)_4$	3.5	Triethylene glycol	6		Polydisperse
	$Ba(OH)_2{\cdot}8H_2O$	3.5	H_2O	-		Crystalline
			NH_3	1		

The main data obtained from the methodology 1 was a Transmission Electron Microscopy (TEM) image (Figure 3.1 A) showing a $BaZrO_3$ NCs without a defined shape. Nonetheless, the Selected area Electron Diffraction (SAED) pattern from the TEM indicates a polycrystalline structure. The planes observed (110), (111),

(200), (211) corresponds with $BaZrO_3$ NCs structure as checked the planes in the international centre for diffraction data with a reference pattern of (00-006-0399).

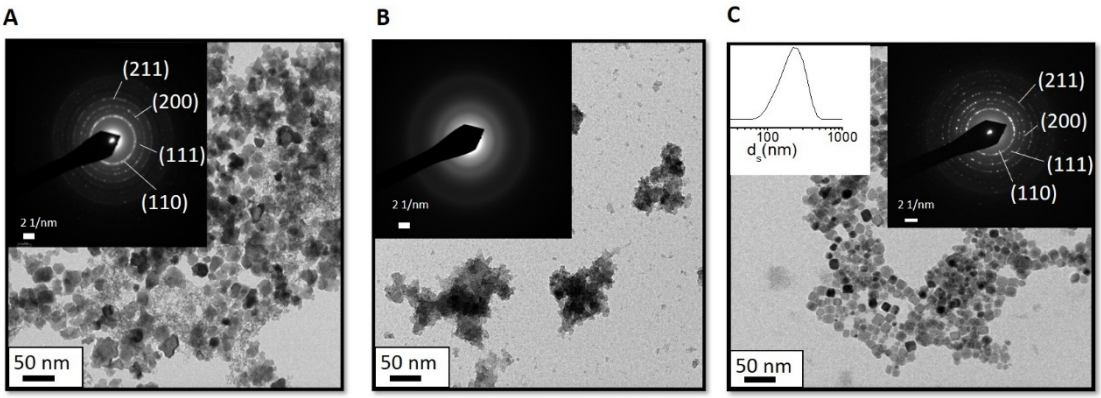

Figure 3.1 TEM and SAED of the (A) method 1, (B) method 2 and (C) method 3. This last method shows a DLS measuremt of the colloidal soltuion.

Hence, the $BaZrO_3$ NCs are obtained, but the tendency of agglomeration is so high that the NCs do not remain in a colloidal state (immediate precipitation). Using methodology 2, no $BaZrO_3$ NCs can be observed in the TEM image (Figure 3.1B). Additionally, SAED shows no crystalline planes and thus confirms that the material is amorphous. Both methodologies fail in obtaining an accurate control of the final material properties. Moreover, both methods require a long reaction time and high temperature, what will increase cost and time.

Finally, by using the third methodology we tried to overcome the issues encountered in the first two methodologies. The result obtained by TEM analysis (Figure 3.1C) using methodology 3 shows a successful achievement of $BaZrO_3$ NCs with a square-like shape and an average size of 12 ± 3.4 nm. Nonetheless, the dynamic light scattering (DLS) in Figure 3.1C point out to agglomerated NCs in solution with a hydrodynamic diameter of d_H = 250 nm. Figure 3.1C shows a SAED pattern where the lattice distance measured from the diffraction rings are in perfect agreement with the cubic phase of $BaZrO_3$ NCs perovskites structure, showing a polycrystalline system.

Although it was a first approximation and it must be optimised, this result suggested a promising system with suitable choice of the precursors (concentration to be optimised) and solvents (amount to be optimised). The parameters we need to improve are: the stability on the media and reducing the large agglomerations of the NCs. The use of $Ba(OH)_2{\cdot}8H_2O$ compound as starting material has been proved in many methodologies giving promising results,[24,27,28] as well as the addition of aqueous ammonia.[25,28] Additionally, the alkoxide precursors had been studied widely for the preparation of oxide materials.[6,30,31] However, they must be studied separately under acidic or basic conditions. It has been reported

than the alkoxides reacts more efficiently in alkaline media than in acidic one.[7,10] This finding evidenced that using the modified polyol route (method 3) is a promising choice to synthesise the $BaZrO_3$ NCs.

3.2.2. The optimization of $BaZrO_3$ NCs synthesis

After assessing method 1, 2 and 3 and finding out that the latter might be useful for the final obtention of $BaZrO_3$ NCs a screening of the reaction condition for method 3 was performed to achieve optimal condictiones. Several parameters as different amount of TREG (*i.e.,* 4, 6, 8 and 10 mL), differentiation ratio molar of the Zr^{4+} and Ba^{2+} (*i.e,* 1:1 and 1:1.25) and temperature from 210 to 180 °C were studied. Finally, the optimal condition were found to be by using a ratio molar of the Zr^{4+} and Ba^{2+} to 1:1.25 and the optimization of the amount of the TREG to 44.90 mmol (6 mL). The reaction took place at 180 °C for 24 hours and the result was a white-transparent colloidal solution. The synthesis is described in detail in experimental methodologies in Chapter 2.

The implementation of the new condition led to achieve of homogeneous square-like shape NCs, suggesting an isotropic growth Figure (3.2 A). Moreover, High-Resolution Transmission Electron Microscopy (HRTEM) technique allowed identifying NCs with a narrow size distribution range and an average size of 8.8 ± 1.7 nm. The interplanar distance observed was 2.94 Å (Figure 3.2.C), that being corroborated with the [110] $BaZrO_3$ which is the main crystalline plane from

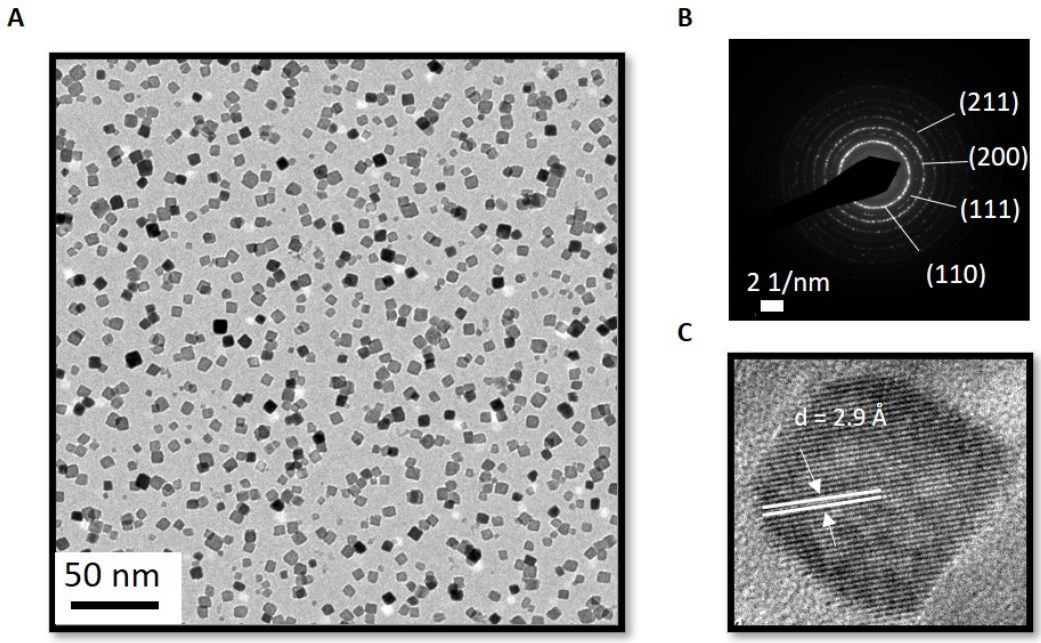

Figure 3.2.(A) HRTEM image of the $BaZrO_3$ NCs.(B) The corresponding SAED and (C) the magnefication of one isolted crystal on HRTEM showing equivalence lattice of (110) at 2.9 Å.

$BaZrO_3$ cubic phases structure. The lattice distance measured from the diffraction rings on the SAED (Figure 3.2.B) are in perfect agreement with the cubic phase of $BaZrO_3$. The planes in X-ray diffraction (XRD) pattern indicates a cubic structure with a Pm-3m space group (Figure 3.3). The crystalline diameter of these NCs obatined from Scherrer equation[32,33] was of 8.5 nm. The calculated value agrees with those obtained by TEM.

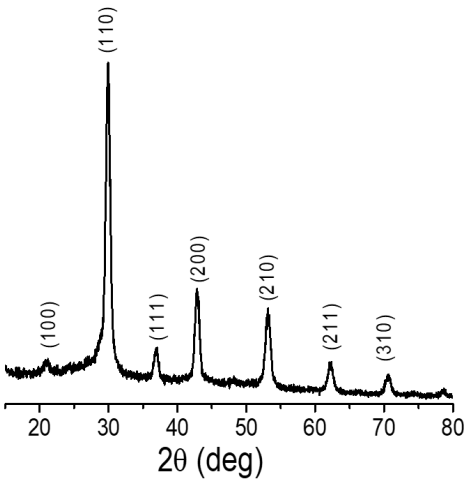

Figure 3.3. XRD pattern of $BaZrO_3$ sample which corroborate the cubic structure assigned with the reference pattern of (00-006-0399) of the internation centre for diffraction data.

3.2.3 Homogeneity and stability of the $BaZrO_3$ NCs colloidal solution

Although the NCs samples are colloidally stable, the DLS measurements show a high degree of polydispersity of the colloidal solution in Figure 3.4A. The polydispersity could come from the presence of different families (large NCs) or any precipitates, impurity or large aggregation on the colloidal solution. The TEM image in Figure 3.4C shows us different sizes of NCs present in the colloidal solution with an average size of 10.5 ± 3.8 nm, explaining the broad peaks in the DLS measurement. For the chosen applications it is very important the small size of the NCs, the purity of the colloidal solution and the complete lack of agglomeration. Therefore, a good monodisperse colloidal solution is mandatory for the later application.[1,3,34,35]

In order to ensure a narrow monodispersed NCs in the whole colloidal solution we implemented an extra-step after the cleaning process. This extra-step is based on a successful separation between small and large NCs and is performed by using a centrifugation technique. The centrifugation consists in spinning the vessel with the NCs colloidal solution at 7.000 rpm during different times (from 5 to 20 min).

After the centrifugation the eventual agglomerates and impurities will remain at the bottom of the vessel, meanwhile the small NCs will remain in suspension in the colloidal solution. Figure 3.4A illustrate the DLS measurement of the NCs average size after different times of centrifugation. What we can conclude is that after 10 minutes of centrifugation the DLS measurements show us a monodispersed colloidal solution, without a broader peak or tail in the peak.

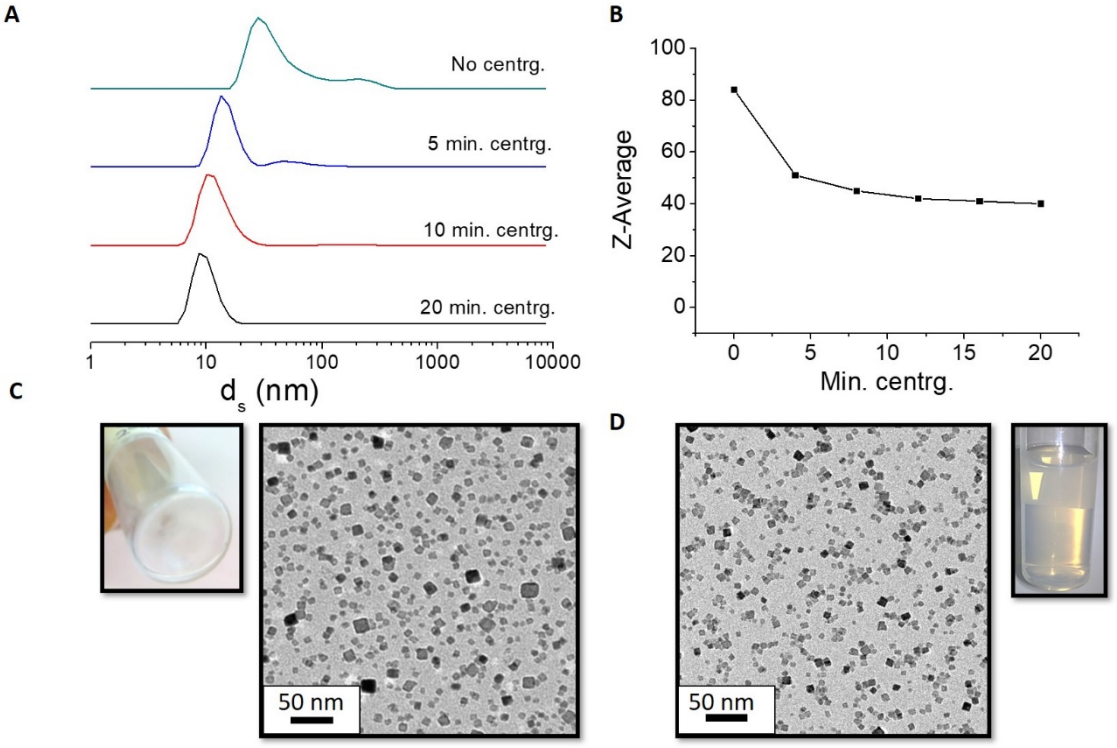

Figure 3.4. (A) DLS measurements after applying 7000 rpm during 0, 5, 10, 15 and 20 minutes under centrifugation (centrg), the measurement were performed in volume %. (B) Z-average parameter taken from DLS to compare the average sizes of total colloidal solution on the batch. (C) TEM image, and a picture of the respective batch solution showing some precipitation without the use of extra-step and (D) TEM image and picture of the respective batch by the implementation of the extra-step.

The average size of the NCs remaining in the colloidal solution is around d_H = 10 nm. This average size does not change even after 20 minutes of centrifugation. The Z-average values (Figure 3.4B) emphasise again the importance of the centrifugation. We can observe that after 5 minutes of centrifugation the stability of the NCs in the colloidal solution improves drastically. Moreover, the Z-average values corroborated that after 10 minutes of centrifugation the stability remains unchanged. In order to better see the size of the NCs and to ensure the lack of any small agglomeration we performed TEM analysis on the colloidal solution centrifuged after 10 minutes of centrifugation. The TEM image presented in Figure

3.4D confirms us the small size of the NCs 8.8 ± 1.7 nm. Moreover, no tendency of further agglomeration was observed.

The implementation of this procedure not only affects the dispersity of the colloidal solution, but also has a directed impact on the final yield. A study of the yields at different times of centrifugation is presented in Table 3.2. A reduction of yield is observed with the increment of centrifugation time. For 10 minutes of centrifugation we still obtained around 40-60 % yield.

Table 3.2. Overview of the impact of increasing the centrifugate time by ana1ºlysed: DLS measurements sizes in volume %, DLS measurament sizes in Z-average and the yield %.

Extra-centrg.	DLS (nm)	Z-average(nm)	TEM (nm)	Yield (%)
0 min.	40	84	10.3 ± 3.4	65-80
10 min.	10	45	8.8± 1.7	40-60
20 min.	9	40	8.3 ± 1.0	35-50

It is observed that applying more than 5 minutes of centrifugation we obtained similar NCs sizes via DLS measurements. However, increasing the time of centrifugation the NCs yield decrees. Therefore, we decided to apply 10 minutes as an optimum centrifugation time.

The stability of these centrifuged NCs was studied after 6 months. From the DLS measurement presented in Figure 3.5 we can see a slight shift of the d_H from 9 to 11 nm, confirming a very high stability of these NCs in spite of the centrifugation process.

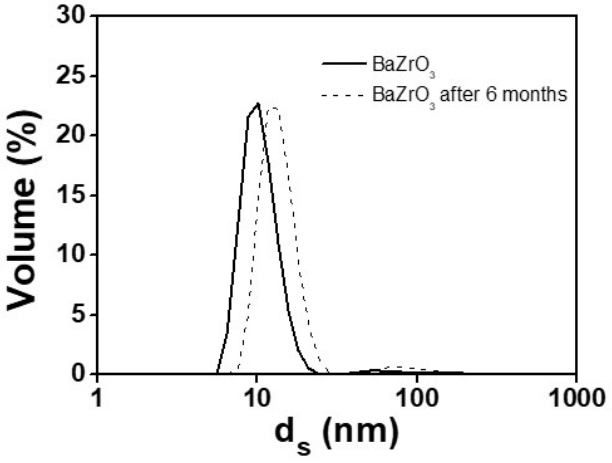

Figure 3.5. DLS stability study of the $BaZrO_3$ NCs during 6-month in ethanol media.

Moreover, there was not observed any sedimentation of large aggregates during this period by either DLS data or visual inspection, confirming the aforementioned high stability of the system.

3.2.4 IR and 13 C solid NMR spectra of $BaZrO_3$ NCs

The hybrid solvothermal synthesis of $BaZrO_3$ NCs uses TREG as stabilizing agent so it is expected to be present on the NC surface. The Infrared Spectroscopy (IR) spectrum of $BaZrO_3$ NCs shown in Figure 3.6A a characteristic TREG absorptions at the bands at 3320 (O-H stretching), 2872 (C-H stretching) and 1057 cm^{-1} (C-O-C bending).[36–38]

It should be pointed out the presence of two intense absorptions at 1554 and 1412 cm^{-1} corresponding to ν(OCO) stretching bands. The most probable origin of these bands is the presence of CO_3^{2-} carbonate anions on the NC surface formed in the handling of the $Zr(OBu)_4$ or $Ba(OH)_2$.

Metal alkoxides shows high reactivity when they are exposed to air conditions. The atmospheric CO_2 reacts with them easily giving rise the formation of carbonates[39]. On the other hand it is common the presence of $Ba(CO_3)$ impurification in $Ba(OH)_2$ reactions. Carbonate anions can act as terminal monodentate or bidentate ligands as well as bridging ligands. In protonic media it can been also found as bicarbonate[39–42] (Table 3.3). C, Morterra et al,[43] and J. R. Copeland et al.,[41] found the chemisorption of CO_2 onto several metals (*i.e.,* Al, Zr, Ti, Ce, Mg). In their studies, they assigned pair of IR bands at 1600-1320 peaks to carbonate species.

Table 3.3 Comparing of the principle band of carbonates. By analyzing the peaks on the ν_{asym}OCO, ν_{sym}OCO and δCOH (all frequencies in cm^{-1})

bicarbonate			bidentate carbonate		unidentate	
ν_{asym}	ν_{sym}	δOH	ν_{asym}	ν_{sym}	ν_{asym}	ν_{sym}
~1650	~1480	~1220	1670-1530	1330-1287	1530-1470	1370-1300

To complement the IR results a ^{13}C MAS Solid-state Nuclear Magnetic Resonance (MAS ssNMR) of $BaZrO_3$ NCs was performed (Figure 3.6B). Firstly the ssNMR shows a broad peak at 171 ppm which is consistent with carboxylic compounds,[44] although this signal could be also related to the presence of any organic carboxylate group it have been dismissed after several experiments due to the formation of carbonate anion in the synthesis of NCs synthesis seems more probable.

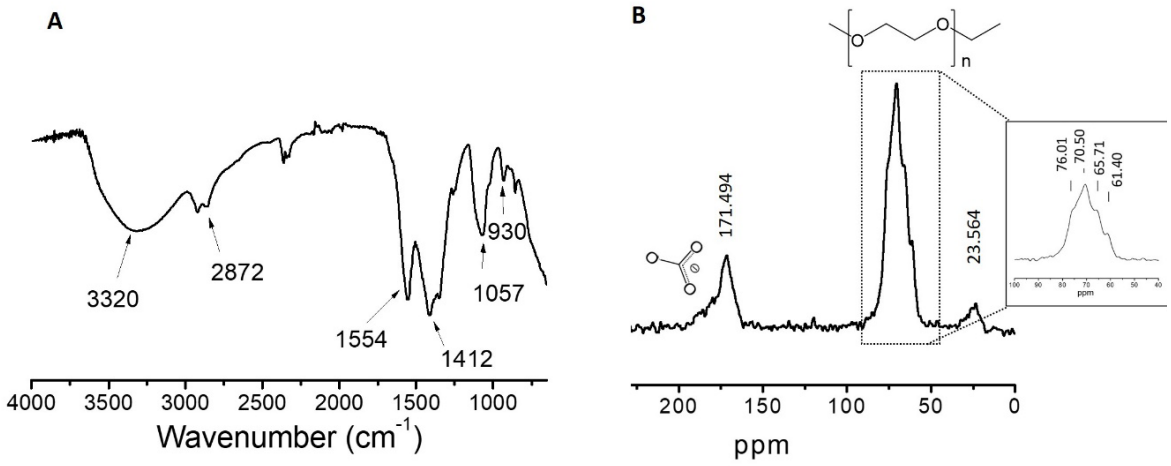

Figure 3.6. (A) IR spectra from $BaZrO_3$ powder (B)^{13}C MAS ssNMR spectra (12 kHz) of powder $BaZrO_3$ and a magnification of the region between 100 and 40 ppm.

Secondly, the broad peak at ≈70 ppm is consistent with aliphatic carbons bonded to an oxygen atom[44–47] which confirms the presence of the TREG chain (CH_2-O-CH_2) on the NCs surface.

These results may suggest the presence of carbonates on the NCs surface as well as the presence of the TREG attached on the NCs surface. However, this hypothesis is still being studying and needs complementary studies to confirm the real characteristics of the NCs surface.

3.2.5 Importance of the stoichiometry ratio on $BaZrO_3$ NCs synthesis

This study explores the advantages of working at non-stoichiometry precursors concentration of (Zr:Ba). Many perovskite NCs from this family have been synthesised using stoichiometric amounts of M:Ba (1:1), even though the resulting NC systems are not homogeneous enough nor well dispersed.[23,48,49] Nonetheless, it has been demonstrated that the excess of hydroxide compounds could lead to an increment on homogeneity and NC sizes, as well as, a better defined NCs shape.[27,28] To ensure an optimal result, the synthesis in both conditions was performed (*i.e.,* stoichiometric and non-stochiometric Zr:Ba) in order to study the effects on the resulting $BaZrO_3$ NCs. As shown in Figure 3.7A, the use of stoichiometric Zr:Ba (1:1) ratio produced a non-homogeneous NC dispersion with agglomeration observed via TEM and corroborated with DLS measurements. Using a non-stoichiometric Zr:Ba (1:1.25) leads to a monodisperse NCs with no agglomeration effect. DLS measurements show a d_H = 10 nm.

However, both NC dispersions show the same cubic phase and crystallinity in powder XRD (Figure 3.7C).

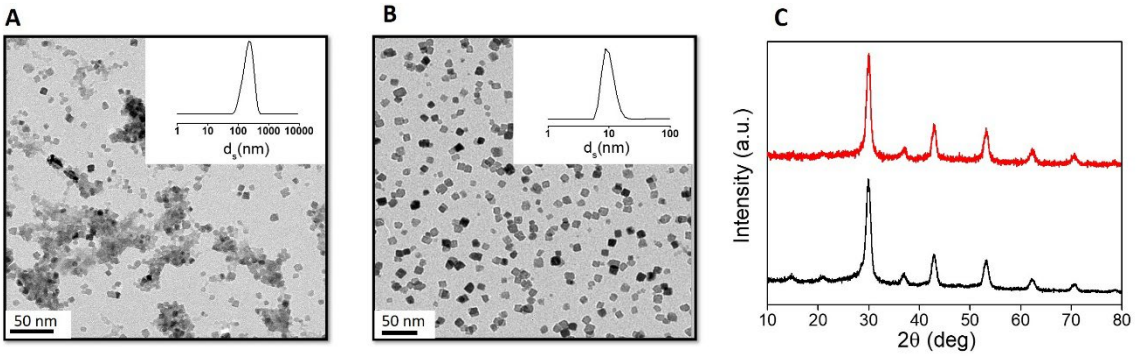

Figure 3.7. TEM and DLS mesuraments of $BaZrO_3$ NCs at (A) stoichiometric Ba:Zr (1:1) and (B) non-stoichiometric Ba:Zr (1:1.25), (C) XRD pattern for stoichiometric (red) on the graph and non-stoichiometric (black), without showing any different phases or impurities.

ζ-potential study on the NCs surface reveals a positive value of +40mV via Smoluchowski approximation. Regarding the ζ-potential, to ensure good stable colloidals solution the values must be on the rage of ζ-potential ≤ -30 or +30 ≤ ζ-potential. If the sample exhibits these values it means that the colloidal solution is stable in the media due to repulsive electrostatic forces between the particles.[50] Although the role of using non stoichiometric approach is not still clear, it seems to be closely related to a surface stabilization. We postulate a surface effect on the stabilisation of the NCs, allowed for an excess of Ba^{2+} ions on the NCs surface.

Energy dispersive X-ray analysis (EDX) measurements for $BaZrO_3$ NCs are displaied in Figure 3.8. We notice an excess of Ba^{2+} compared with Zr^{4+}. EDX results provide further support for the hypothesis of being the barium cations the stabilizers on the NCs surface, confirming a higher amount of Ba^{2+} of 60 atomic% compared with a 40 atomic. % of Zr^{4+}.

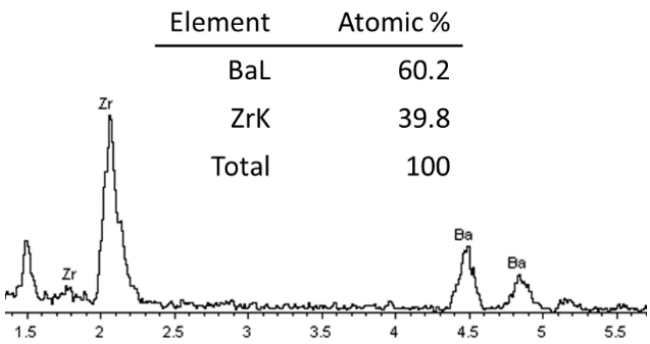

Figure 3.8. EDX analyses from a $BaZrO_3$ sample

3.3. Tuning the synthesis parameters

With the optimized synthetic conditions for synthesis succesfully $BaZrO_3$ NCs, from now on we focused our attention to unravel how to manipulate the size and shape of the NCs. Much attention has been addressed to manipulate these parameters as a way to tune the physical and chemical properties of the NCs.[51,52] These properties can be tuned by modifying several factors such as: i) time,[53] ii) temperature,[54,55] iii) starting precursors,[56,57] iii) surfactants,[58–61] iv) precursors ratio[27] and/or v) solvents.

3.3.1 Effect of the temperature

It is known that temperature and time have a direct effect on the size, shape and crystallinity of the final colloidal dispersions.[62] By using the solvothermal methodology, we are inducing a certain temperature and pressure that will trigger the nucleation of the crystals and a posterior growth of these nuclei to mature crystals. We performed a study of temperature and time to observe the correlation of these parameters with the final NCs characteristics (*i.e.,* sizes, shape, crystallinity).

The first experiment was done by keeping constant the concentration of precursors, solvents and the reaction time (24 hours), while the temperature in the solvothermal reactor was increased from 100 to 210 °C. As seen in the TEM images presented in Figure 3.9A, at 100 °C $BaZrO_3$ NCs are not crystallized yet. The XRD analysis show a broad peak with a non-definite cubic phase, where the main presence are impurities coming from the *$BaCO_3$. This suggests that the temperature is not high enough to induce the complete crystallization of the NCs. Increasing the temperature to 180 °C we observe that the NCs are well-crystallized with a typical square-like shape. The average size is 8.8 ± 1.7 nm, as revealed by the TEM analysis (Figure 3.9B). This is confirmed by XRD patterns at 180 °C showed in Figure 3.9D where we can appreciate sharp peaks suggesting a high crystallinity of the $BaZrO_3$ NCs. Increasing even more the temperature (210 °C) we cannot see changes neither in sizes or shape of the NCs, nor in the crystallinity of these NCs. The TEM image in Figure 3.9C show again monodispersed NCs with an average size of 8.2 ± 1.4 nm. Also, the XRD pattern for 210 °C is almost identical to the XRD pattern for 180 °C. In both temperatures the diameter of the NCs, calculated with Scherrer equations, show a similar average NCs size of 8 nm.

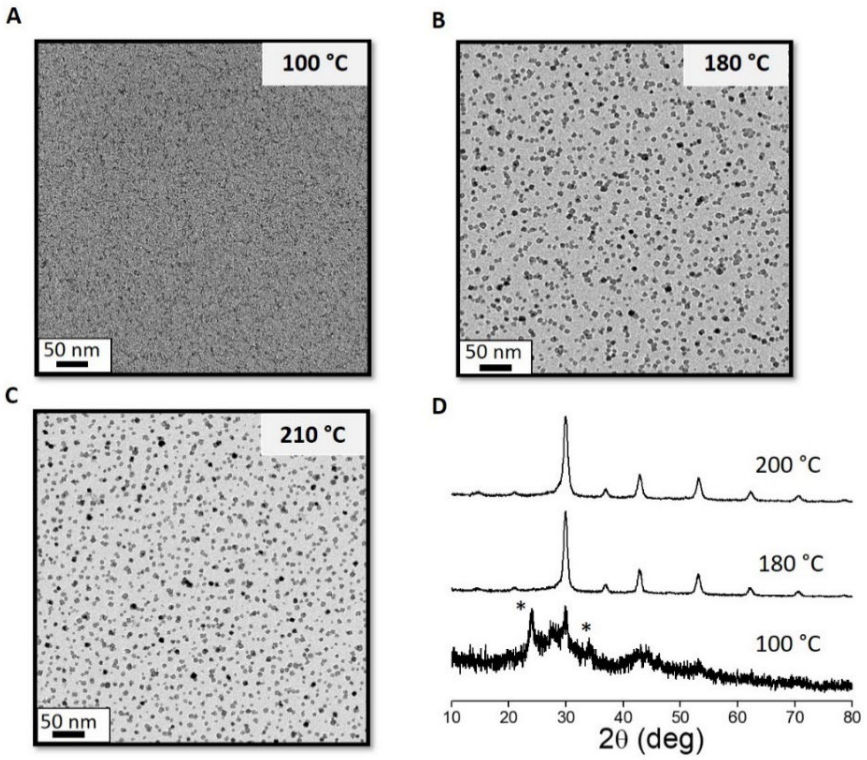

Figure.3.9. TEM images of $BaZrO_3$ synthesised at different temperatures (A) 100 °C, (B) 180 °C and (C) 210 °C using in all cases 24 hours of reaction. (D) XRD patterns of the $BaZrO_3$ synthesised at different temperatures.

For clarity all these data are summarized in Table 3.4. The optimum reaction temperature chosen for us was 180°C.

Table 3.4. $BaZrO_3$ at different temperature and the sizes by Scherer and TEM average.

Temperature (°C)	TEM (nm)	Scherrer (nm)
100	-	-
180	8.8 ± 1.7	8.5
210	8.2 ± 1.4	7.8

3.3.2 Effect of the reaction time

According to the literature, the reaction time needed to achieve $BaZrO_3$ NCs with the solvothermal method is around 18-48 hours.[22,25,27] In order to understand the growing process, exhaustive measurement at different times were done and the results are reported in table 3.5. While the reaction temperature was kept at 180°C different reaction times were assessed: 1 hour, 8 hours, 24 hours and 72 hours.

The NCs obtained at different reaction times were subjected to TEM and XRD analysis to investigate their sizes, shape and crystallinity. Figure 3.10A shows successful achieve of $BaZrO_3$ NCs with a drastically reduction of time from 24 hours to 1 hour without show any variation in crystallinity or sizes. For the 1 hour synthesis the NCs show a square-like shape with an average size of 8.6 ± 1.5 nm as revealed by TEM images and summarized in Table 3.5. The XRD pattern evidence the crystallinity of $BaZrO_3$ NCs. Moreover, when increasing the reaction time to 72 hours, no substantial difference was found on the NCs main size, shape and crystallinity, refusing the possibility of the NCs to suffers grain growth caused by Ostwald ripening effect.[54,63] Both TEM images and XRD data corroborated it.

Table 3.5. Sizes of the obtained NCs at different synthetic time by TEM and Scherrer

Time (h)	Size by Scherrer	Size by TEM
72	7.8 nm	8.1 ± 1.5 nm
24	8.5 nm	8.8 ± 1.7 nm
8	8.2 nm	8.4 ± 1.3 nm
1	7.7 nm	8.6 ± 1.5 nm

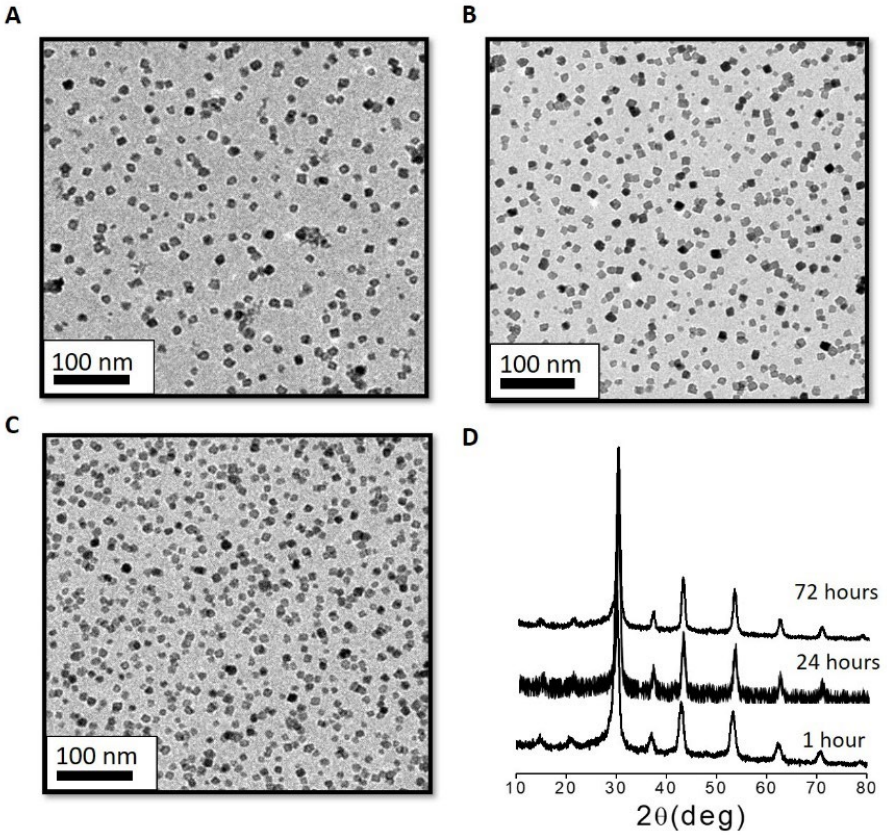

Figure 3.10. TEM images of $BaZrO_3$ synthesised at 1 hour (A), 24 hours (B) and 72 hour (C) at 180 °C. (D) XRD powder from $BaZrO_3$ in their cubic phase without any significant changes.

To conclude, one-hour reaction time seem to be the optimal reaction time to achieve a high degree of crystallinity for $BaZrO_3$ NCs with size and shape suitable for our needs. This leads to important energy cost and time reduction without compromising the quality of the $BaZrO_3$ NCs.

3.3.3. Concentration and polyol type effect

The polyols have emerged as a particular useful compound, especially when we are talking about the synthesis of oxide nanoparticles. The use of polyols in the synthesis of NCs lead to so-called polyol route.[58,60,64,65] The introduction of the polyol compound allow excellent control of the particle sizes, morphology and agglomeration.[58,59,64]

The role of using different types of polyol was studied to assess their effect in our system. Firstly, the experiments were performed by using different type of polyols such as diethylene glycol (DEG) and tetraethylene glycol (TEG). A polyol-free synthesis was also performed in order to compared with the other polyols. For the synthesis made with TREG an optimum % v/v was found. As a first approach to synthesise with DEG and TEG we maintained the % v/v in the reaction.

When using DEG (6 mL) no NCs were observed in the TEM image (Figure 3.11A), which show only the presence of some organic matter. This does not happen in the case of TEG where $BaZrO_3$ NCs are clearly formed (Figure 3.11B). The main drawback when using this amount of TEG is that the NCs have no definite shape

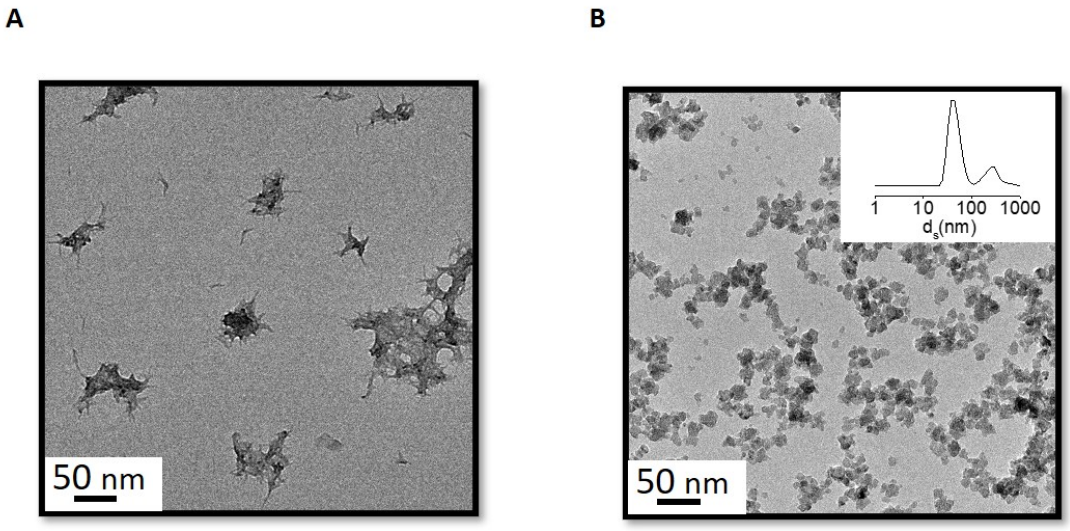

Figure 3.11. TEM images of $BaZrO_3$ synthesized by varying the type of polyol from the standard methodology, without modified the final % v/v in solution. (A) using DEG and (B) using TEG at 180 °C for 1 hour. And showing in the case of TEG the DLS in order to study the stability. DLS (A) was avoided due to the lack of NCs formation.

and seem to have tendency of agglomeration. The average size measured by TEM is 11.5 ± 3.1 nm. The DLS measurements show a polydisperse system, corroborating the TEM analysis.

An optimization study of these two polyols was performed. Different % v/v were tested until the optimum amount to obtained agglomeration-free NCs was found. In the case of DEG we found that using 1.5 mL leads to a monodispersed colloidal solution of $BaZrO_3$ NCs with an average size of 4.9 ± 0.8 nm (Figure 3.12B). We notice that with less amount of DEG not only we are able to achieve highly crystalline NCs but also the sizes of the NCs are quite small. The shape of these NCs are spherical when using DEG. On the other hand, the optimum amount of TEG was found to almost double (11 mL). In this case the size of the NCs is around 11.1 ± 1.7 nm as observed in TEM image (Figure 3.12D). The DLS measurements, in this case, corroborate the TEM analysis showing a monodisperse colloidal solution with a similar d_H of the NCs. XRD pattern shows in both cases high crystallinity of the NCs, with a broader peak in the case of DEG suggesting smaller NCs size compared with the sharper peak in the case of using TEG.

To emphasis the role of the polyol additive in the characteristics of the NCs we have synthesised $BaZrO_3$ NCs without adding any type of polyol. The results can be appreciated in Figure 3.12A, where high agglomeration of $BaZrO_3$ are observed, with a lack of homogeneity and an average size of 52.0 ± 15.9 nm. As a consequence of an uncontrolled growth process, it can be seen different family sizes and large agglomeration, resulting in a not stable solution that precipitates after a minute of being dispersed on the ethanol media. The XRD pattern in Figure 3.12 reveals the formation of crystalline $BaZrO_3$ NCs even without the use of any poloyol.

For clarity all these studies are resumed in Table 3.6. The results of the standard methodology using TREG is also included in order to better comparison.

Table 3.6 Amount of the different polyols use it, follow by the TEM average sizes and the Scherrer sizes of each one.

Polyol	Chemistry composition	Label	Amount (mmol)	TEM size (nm)	Scherrer size (nm)
No polyol	-	A	0	52.0 ± 15.9	21.4
Diethylene glycol	$C_4H_{10}O_3$	B	15.80	4.9 ± 0.8	4.8
Triethylene glycol	$C_6H_{14}O_4$	C	44.90	8.6 ± 1.5	8.2
Tetraethylene glycol	$C_8H_{18}O_5$	D	63.71	11.1 ± 1.7	10.7

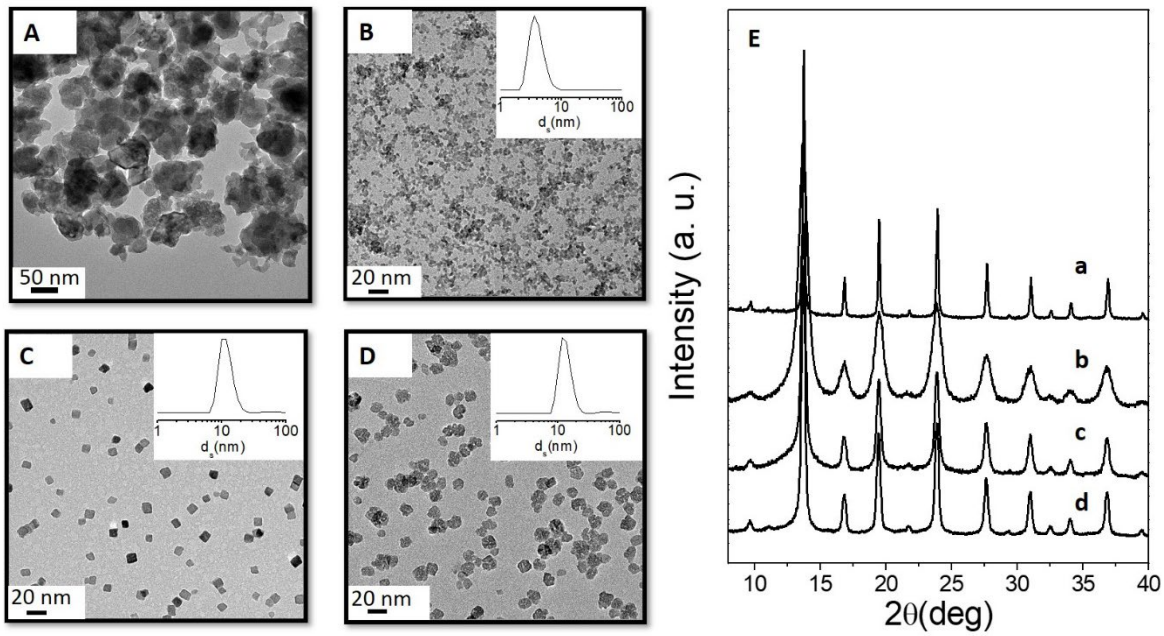

Figure 3.12. TEM image and its respective DLS measurements for (A) without using any amount of polyol. (B) 1.5 mL of diethylene glycol (C) 6 mL triethylene glycol and (D) 11 mL of tetraethylene glycol. The reaction was made at 180 ° C for 1 hour. The DLS in the case of polyol free was not displayed due to the fast precipitation on ethanol media. (E) shows the XRD powder diffraction from $BaZrO_3$ NCs synthesized with a different kind of polyols, the label corresponding to each one could be followed on table 3.6. In this case XRD diffractometer was used with a transmission configuration using Mo Kα.

In the cases of polyol free synthesis, the DLS measurement could not be performed because this NCs are incapable of remaining in suspension, therefore the need of polyol additive is clear.

Besides the necessity of polyol what we can also conclude is that higher the polyol chain, higher the amount needed for a stable monodisperse colloidal solution. Moreover the type of polyol is related with the sizes and shape of the NCs.[64,66,67]

3.3.4 Concentration effect on NCs sizes and shape

The concentration is known as a parameter that could influence the final size and shape of the NCs.[27] In order to study this effect a series of colloidal solutions with different amount of metal precursors were prepared, keeping the same molar ratio in all the synthesis. An amount ranges from 1.6 mmol of Zr^{4+} to 4 mmol of Zr^{4+} were employed. The reaction time remained 1 hour, the reaction temperature 180°C, the solvent EtOH, aqueous ammonia and the polyol, TREG, remain equal for the entire

study. In Figure 3.13A-B we can see that the shape and size of the $BaZrO_3$ NCs remain the same independently of the precursor amount.

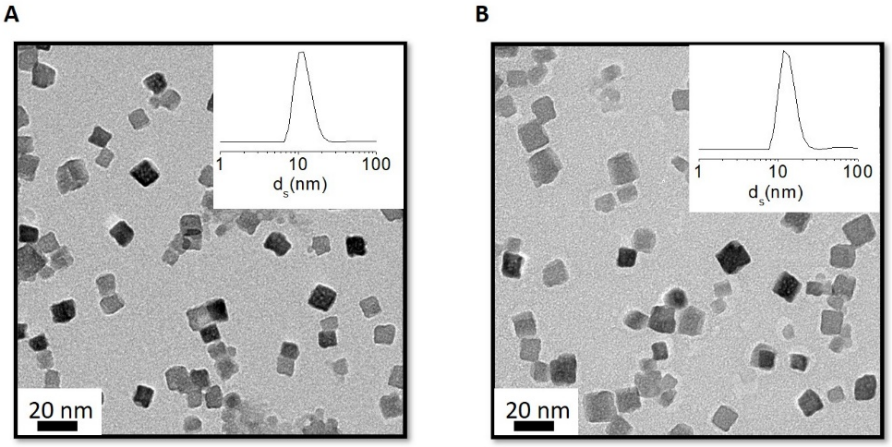

Figure 3.13. TEM image of $BaZrO_3$ synthesis by keeping all the parameters equals and changing the metal precursors amount to reduce the concentration of the metals. (A) used 1.6 mmol of Zr^{4+} and (B) increase the concentration by using 4 mmol of Zr^{4+}. Each case showing the respective DLS measurement.

When lowering the concentration of precursor the NCs sizes is around 9.1 ± 1.4 while upon increasing of the concentration the average size is 9.3 ± 1.8 nm. Furthermore, both cases show a stable colloidal solution, which suggests that the increment or reduction of metal precursors do not have a direct impact on the final agglomeration, size or morphology.

3.4 Microwave methodology

It is well known that microwave activation provides numerous advantages in comparasion to conventional heating procedures (*i.e.,* solvothermal, hydrothermal).[68–70] One of the major advantages is an excellent control over the reaction parameters (*i.e.,* pressure, temperature, etc.) by monitoring the full reaction, besides of high heating rates and homogenous heat through the sample. Microwave route has another important advantage over the solvothermal route in terms of reaction times.[70,71] What solvothermal route can take some hours or days in microwave route can take a few minutes or hours.

Although in our case we were able to achieve short times via solvothermal route, the following question arised. If we used the microwave route, how much faster could the $BaZrO_3$ NCs be synthesised? To answer this question, we have synthesised $BaZrO_3$ NCs using the microwave route. The microwave treatment was performed by using the same initial precursor solution (*i.e.,* same precursors amount and same amount of solvents) transferring the solution into 30 mL

microwave vessel. The reaction took place at 180 °C for 5 minutes at a pressure of 15 bars. The microwave profile is displaied in Chapter 2. The time used is significantly reduced compared to the solvothermal treatment (1 hour). The NCs synthesised by both procedures can be analysed in Figure 3.14. The TEM analysis reveals in both cases square-like shape and similar average size for the $BaZrO_3$ NCs. The average size of $BaZrO_3$ NCs via microwave route is 7.8 ± 1.2 nm, meanwhile the ones obtained via solvothermal method exhibits an average size of 8.6 ± 1.5 nm.

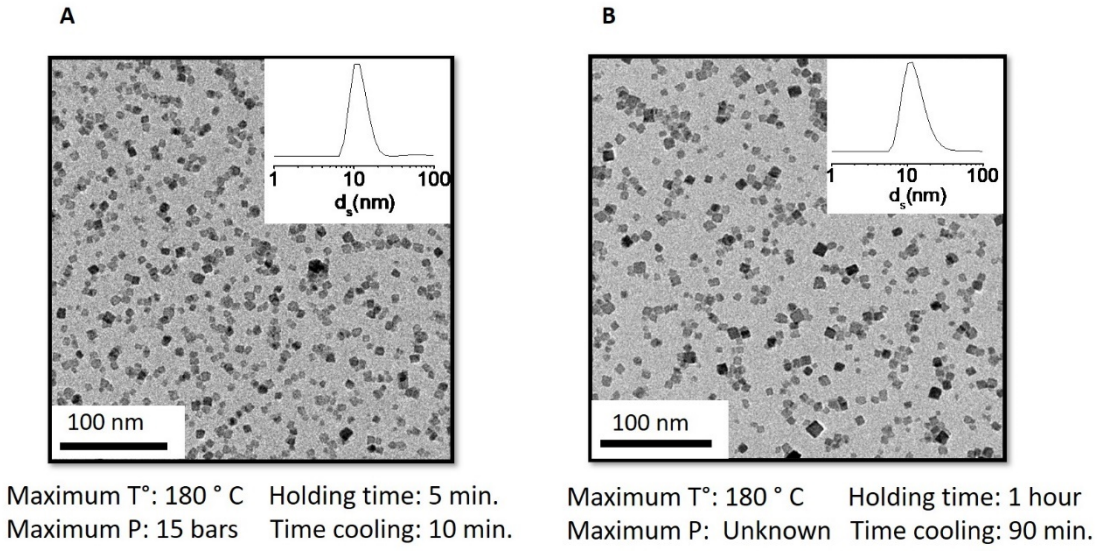

Figure 3.14. TEM image of $BaZrO_3$ synthesis by using (A) microwave route and (B) solvothermal route both with the corresponding synthetic information below.

ζ-potential measurements reveal values of +40 mV in both processes. This shows similar stability of the $BaZrO_3$ NCs in the colloidal solutions. Moreover, the DLS measurements are displayed showing by both methodologies a $d_H \approx 10$ nm. In Figure 3.15 the crystallinity of the NCs is confirmed by the XRD analysis, in which the cubic phase is recognized in both cases, showing similar patterns. No other crystalline phase except $BaZrO_3$ can be identified, showing high purity in both cases.

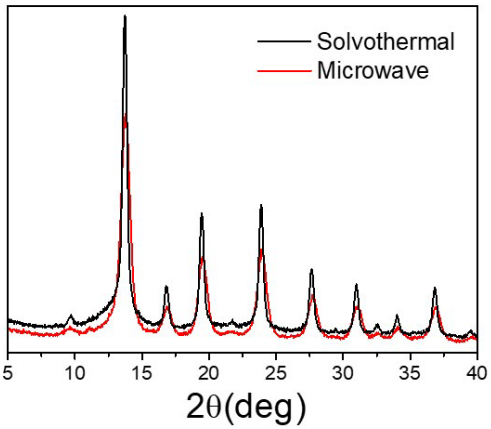

Figure 3.15 XRD of the NCs synthesised by using the solvothermal and microwave routes. The XRD patter was performed in transmission configuration using Mo Kα radiation.

We can conclude that both routes (solvothermal and microwave) are more than suitable to achieve high crystalline, small sizes and square-like shape $BaZrO_3$ NCs. However, due to the short reaction time needed to obtain $BaZrO_3$ NCs and higgher homogenity at heatting the microwave route is highly recommended.

3.5 Hybrid solvothermal method

In this section we will show you step by step, how we came to realized that our methodology is governed by both sol-gel and solvothermal reactions. This conclusion became clear during the study of the effect of aqueous ammonia in the synthesis of the $BaZrO_3$ NCs.

3.5.1 What is the role of ammonia?

The role of a aqueous ammonia in the reaction was not clear, due to its ability to act as a base or as a cationic stabilizer on the NC surface (*i.e.*, as ammonium cation stabilizing the system).[72] Using the standard methodology for $BaZrO_3$ synthesis, 1 mL of aqueous NH_3 at 30% v/v% is necessary to obtain the final NCs solution. In order to understand the role of the ammonia and its influence in the final nanoscale system, X-ray photoelectron spectroscopy (XPS) of the nitrogen element was performed (Figure 3.16). XPS is revealing the absence of nitrogen compounds onto NCs surface. That concludes that ammonia/ammonium cation has no role in the stabilization of the NCs.

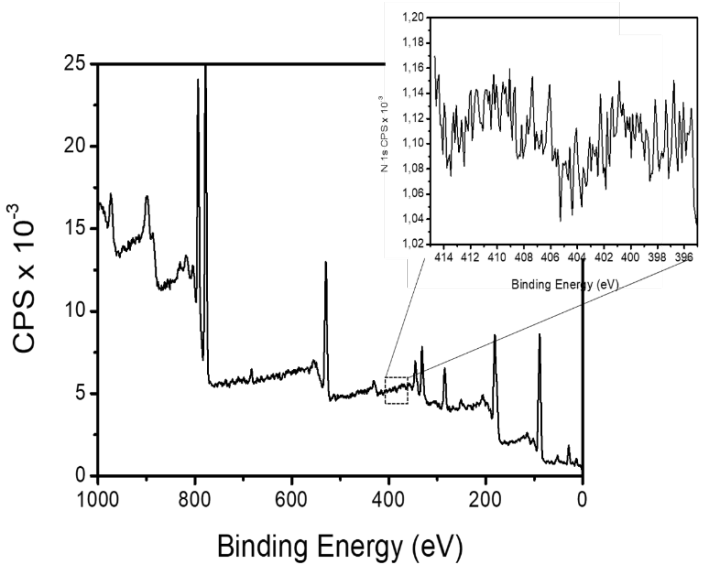

Figure 3.16. XPS analysis of $BaZrO_3$ synthesized with ammonia showing the lack of nitrogen presence on the NC surface.

There are several options to consider to understand the role of ammonia, among them, we hesitated whether ammonia had no role, but the water amount coming from the ammonia did influence the synthesis. We used NH_3 at 30% v/v which means that the rest 70% v/v is composed by water. Considering this possibility, to evaluate the role of NH_3, we compared three different synthesis: firstly one made by using 1 mL NH_3 at 30% v/v, secondly one made with 0.7 mL of water (the equivalent amount of water from 1 mL of NH_3 at 30% v/v) and finally, without using ammonia or water at all (Figure 3.17). The first thing we observe is that without using ammonia or water the $BaZrO_3$ NCs are poorly formed. This is also confirmed by the XRD pattern where the main peaks observed are the ones corresponding to $BaCO_3$. The TEM images (Figure 3.17) show a similar NCs formation between the use of 1 mL ammonia 30% v/v or directly using its equivalent amount of water (0.7 ml of water).

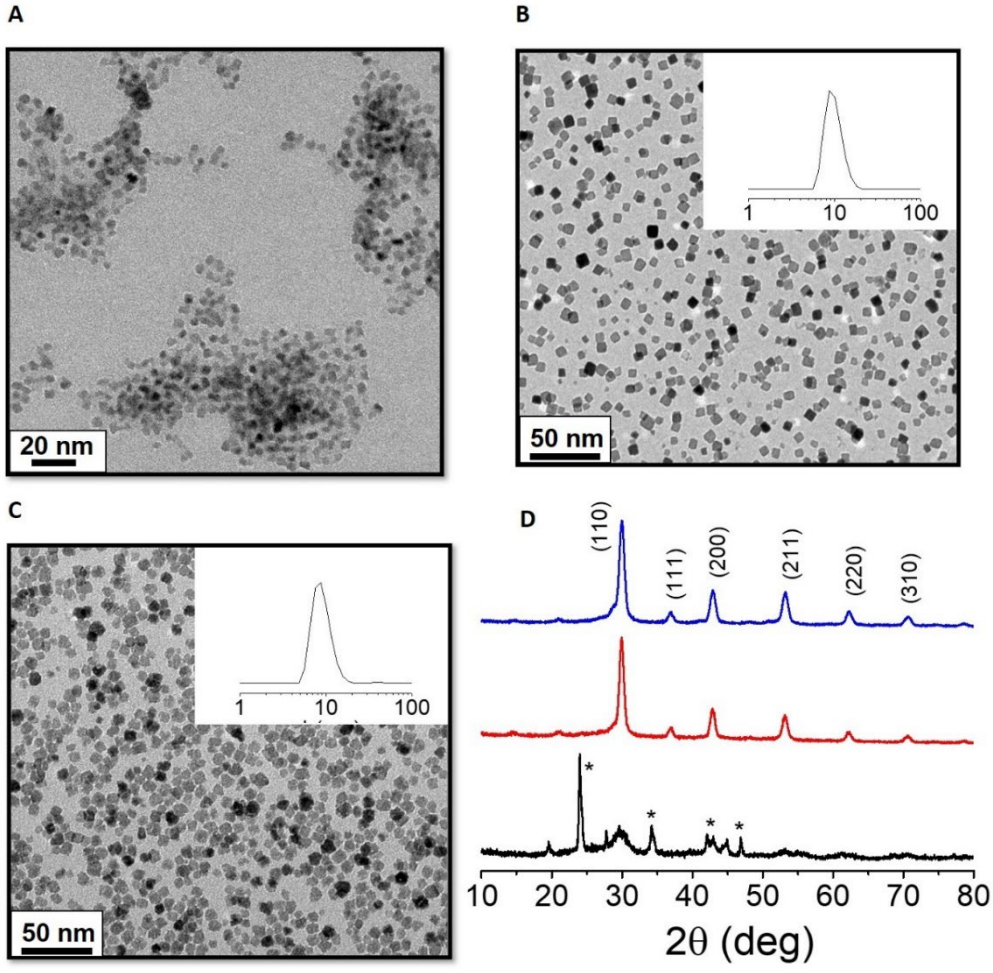

Figure 3.17. (A) TEM of $BaZrO_3$ NCs synthesized via standard procedure without using any amount of water or aqueous ammonia at 180 °C for 1 hour (B) TEM of $BaZrO_3$ NCs synthesized via standard procedure by using 0.7 mL of water instead of ammonia at 180 °C for 1 hour. (C) TEM of $BaZrO_3$ NCs synthesised via standard procedure by using 1 mL of ammonia 30% v/v (i.e. 0.3 mL and 0.7 mL water) at 180 °C for 1 hour. (D) the respective XRD cubic pattern from (A) black and (B) red and (C) blue.

A homogeneous dispersion with square-like NCs shape is revealed. We observe from the XRD analysis a narrow size and a cubic phase pattern with a coherent crystal domain of 8.54 nm obtained by Scherrer equation.

This evidence, in addition with the XPS analysis, suggest that ammonia did not play any additional role in our methodology, being just the amount of water coming from the ammonia solution who govern the NC formation. Thus, ammonia was further suppressed from the synthesis methodology being replaced by the equivalence amount of water.

3.5.2 Importance of water

Previously, it was proved that the addition of water on the system triggers the final formation of NCs. For this standpoint, it is interesting to pay attention to the kinetic control of the reaction by the addition of water.

To study the specific role of water a series of reaction with different quantities of water (from 0 mmol to 139 mmol) was performed in order to test which is the pivotal role from the water in the system (summarised in Table 3.7). The most striking result emerging from this data is how an incrementation of water amount (0, 27, 55, 83, 111 and 139 mmol) produces a continuous increment in size: 4, 7, 11, 16, 26 and 31 nm of the NCs respectively. This is observed in the TEM images (Figure 3.18). All of the $BaZrO_3$ NCs obtained with water content from 28 mmol to 139 mmol exhibit a square-like shape.

Table 3.7. Summary of the TEM and Scherrer sizes for all NCs obtained by using different amount of water on the synthesis reaction.

Water amount (mmol)	TEM size (nm)	Scherrer size (nm)
0	-	-
28	7.0 ± 1.2	7.4
55	11.9 ± 1.8	11.8
83	14.7 ± 3.5	14.1
111	25.8 ± 7.5	25.0
139	32.6 ± 9.8	29.0

Firstly, a test without adding water in the media using the standard protocol as before (180 °C and 1 hour in autoclave) evidence the initial seed formation of NCs (Figure 3.18). Moreover XRD pattern (Figure 3.19) showed a high presence of $BaCO_3$ as the main product, suggesting that the water amount in the $Ba(OH)_2$

$8H_2O$ is not enough to initiate the nucleation process, or the conditions are not still suitable to obtain the desired final NCs.

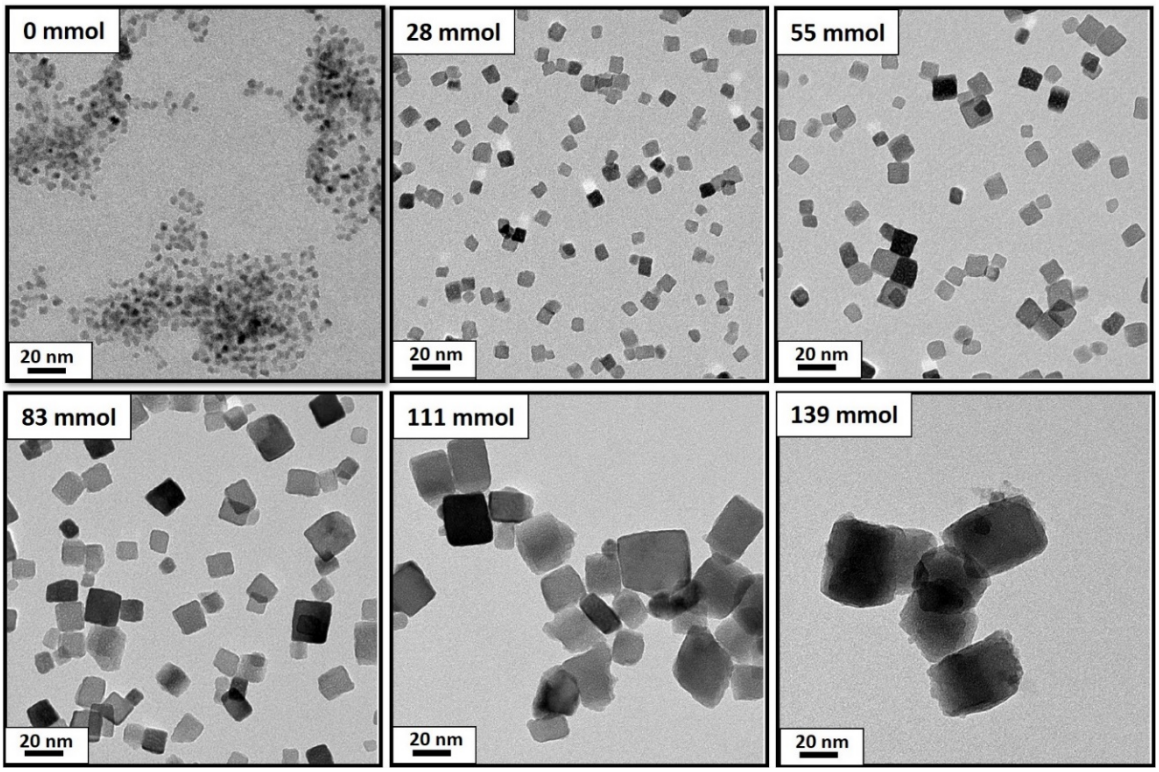

Figure 3.18. TEM images of $BaZrO_3$ NCs using different additional water concentrations during the synthetic process (from 0 to 139 mmol) increasing the concentration of water in the synthesis, from 28 mmol (0.5 mL H_2O) to 139 mmol (2.5 mL H_2O) as is shown in Table 3.7.

The final formation of $BaZrO_3$ confirms the postulation of being the water the decisive factor for controlling the size of NCs rather than the temperature or time as it was checked previously. In addition, by using this approximation, we evidence the role of water as the hydrolytic step to tune the size of the final nanocrystals. This allowed us to obtain a wide range of sizes from 4 to 30 nm of the NCs. Many efforts have been invested in reducing the crystal sizes of the structure of this perovskite families, even though most of the previous reported papers showed a non-defined shape and large aggregation.[15,24,26,73] The findings in this study suggest a controlled size and shape by the manipulation of the hydrolytic step.

3.5.3 Monodispersity and crystallinity

At this point, we realised that the effect of water is not only related with the increase of size but also in the polydispersity of the final colloidal systems. In Figure 3.19A XRD of the NCs at different amount of water are displayed. Without adding water in the media, the XRD evidence initial seed formation of NCs (Figure

3.18A). The broadest peaks on XRD correspond to 28 mmol amount of water. This is explained by the smaller average sizes of the NCs. The latest results of XRD are appreciated as sharper peaks since larger NCs are formatted.

Moreover, the standard deviation in TEM histograms increases with the size of the NCs too, in other words, the use of more water in the reaction allows obtaining big and more polydisperse NCs (Figure 3.19B). This effect could be explained by the hydrolysis step in which the amount of water in the first step of the reaction starts the hydrolysation process hence, affects the kinetics of the reaction, making the nucleation step faster. From a kinetic point of view, if the nucleation process is increased without modifications on the thermodynamics, the system becomes polydisperse and with poor control on the stabilization (*i.e.,* we are increasing the concentration of water with the same amount of polyol TREG). DLS as it is observed in figure 3.19C corroborate with TEM average sizes. It is observed with the increment of water the hydrodynamic radii increases too. The smallest NCs size is shown by the ones obtained with less quantity of water (27 mmol – 7 nm), and the biggest NCs size is exhibit by the ones obtained using 139 mmol (40 nm).

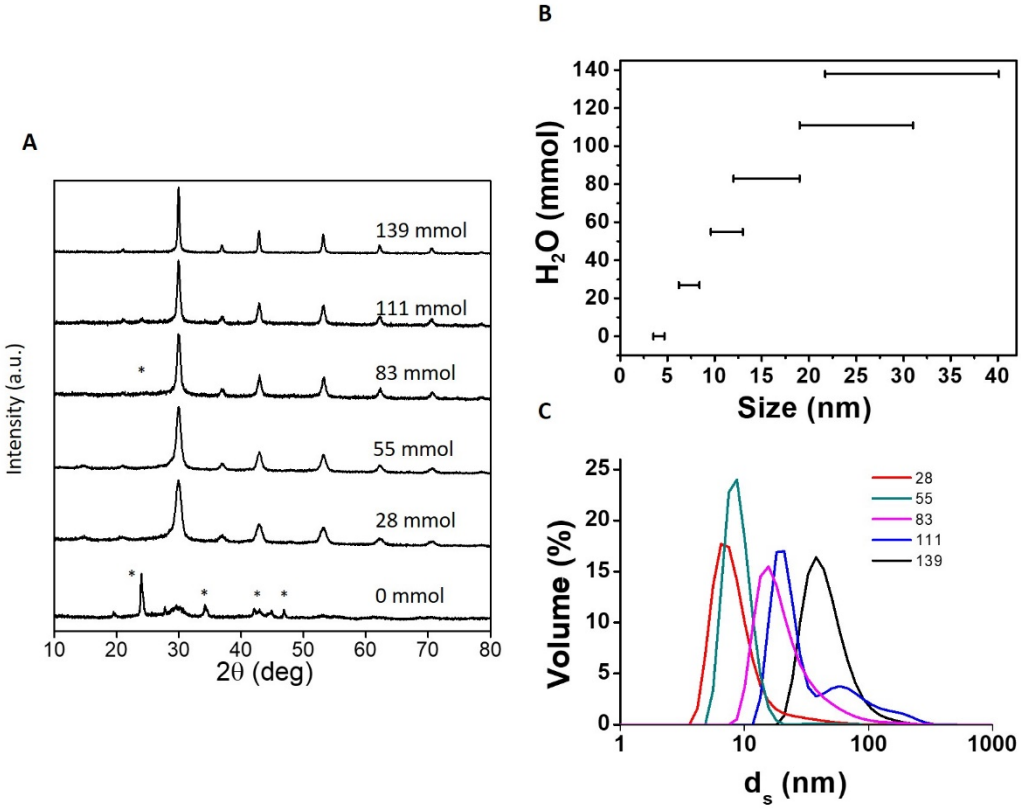

Figure 3.19 (A) XRD pattern corresponding to the NCs for the different amounts of water from 0 mmol to 139 mmol. XRD at 0 mmol also includes the main peaks of *$BaCO_3$ as the main impurity of this synthesis. 111 mmol pattern also shows a subtle *$BaCO_3$ peak suggesting an impurity quantification of 4% from $BaCO_3$. (B) the standard deviations of TEM histograms are showed to note the polydispersity when increasing water concentration. (C) DLS measurements of the different $BaZrO_3$ NCs (avoiding the ones at 0 mmol due to its partial aggregation on TEM).

Although NC size is tuned with the addition of different amounts of water, other properties are nearly similar in terms of shape, homogeneity and crystallinity. Concerning their crystalline structure, all NCs present a cubic structure with a Pm-3m space group (Figure 3.19A), in which Scherrer sizes match with the obtained via TEM and DLS (Table 3.7).

3.5.4 Unraveling the mechanism insight

Our starting precursors are alkoxides, and even the hydrolysis of metal alkoxide has been widely studied,[6,10,11] there are still some controversial aspects concerning the full mechanism reaction.[8,30] The method of synthesis described in this chapter is based on the advantages of the hydrolysis step of metal alkoxides which is the basis for a sol-gel process. Precisely, the reaction we are presenting, shows the kinetic control over the hydrolysis of metal alkoxides by the addition of water. As it is well known, the sol-gel process is based on the hydrolysis and polycondensation steps (Equations 3.2-3.4) and it has been extensible as the main step to synthesise many oxide nanoparticles.[7,10,11,74]

In an ethanol medium, the stabilisation of the alkoxide into the solvent is considered the first step forming the intermediate $M(OBu)_{4-x}(OEt)_x$ as shown in Equation 3.1. Alkoxides are extremely sensitive to water, so the addition of $Ba(OH)_2{\cdot}8H_2O$ plays a double role: (i) firstly the addition of the binary cation for the perovskite structure and (ii) secondly as a source of -OH groups and water which will trigger the hydrolysis reaction (Equation 3.2). This will also trigger the formation of intermediate hydroxide species group $M(OH)_x(OBu)_{n-x}$.[75] The following steps described in Equations 3.3 and 3.4, corresponded to polycondensations of hydroxyl-alkoxide intermediates, where it is forming a M-O-M framework, being a critical point for the further formation of final $BaZrO_3$ NCs. The concentration of -M-OH species in our reaction media is controlled with the addition of water, allowing the formation of large -M-O-M chains (polycondensation), producing bigger NCs.

$$M(OBu)_4 + xEtOH \rightarrow M(OBu)_{4-x}(OEt)_x + x\ BuOH \qquad (3.1)$$

$$M(OBu)_n + xH_2O \rightarrow M(OH)_x(OBu)_{n-x} + x\ BuOH \qquad (3.2)$$

$$\text{-M-OH} + \text{H-O-M} \rightarrow \text{-M-O-M-} + H_2O \qquad (3.3)$$

$$\text{-M-OH} + \text{Bu-O-M} \rightarrow \text{-M-O-M-} + BuOH \qquad (3.4)$$

The hydrolysis and condensation reactions presented in Equation 3.1 to 3.4 are founded in the initial step of our reaction (*i.e.,* before the solvothermal approach). These reactions are aimed to be an extremely fast process, being reported as a reaction of milliseconds after mixing the reagents.[5,6,10,76,77] Hu. M.Z. et al.[76] proved the rapid hydrolysis and condensation of zirconium n-butoxide in ethanol leading to a 100 millisecond reaction time. Consequently, we are dealing in our system with an extremely fast process governed by the hydrolytic step leading to a final tuneability of the NCs sizes.

3.6. Conclusions

In this chapter, we present the synthesise and optimization of $BaZrO_3$ NCs. It has been demonstrated a well-defined $BaZrO_3$ NCs, with small sizes and stable in alcoholic colloidal solution in high concentration (up to 110 mM). Concerning the synthetic methodology, we reported a hybrid method based on the advantages of sol-gel method and the solvothermal treatment.

Considering previous approximations where $BaZrO_3$ NCs needs long times reactions and high temperatures, we have demonstrated the synthesis of a crystalline shape-defined $BaZrO_3$ NCs in 1 hour via autoclave and 5 minutes in microwave activation. Therefore reducing drastically the actual time for the synthesis of this $BaZrO_3$ NCs.

We studied the influence of the different synthetic parameters (*i.e.,* concentrations, solvents, time, temperature) to optimize the synthesis and unravel which is the factor to tune the NCs sizes. The replacement of ammonia for water suggests us a new insight to unravel the mechanism in the synthetic approximation. The combination of aqueous sol-gel and solvothermal treatments not only allowed the successfully production of these particles, but also a high tuneable control of their sizes. The role of the water amount in the hydrolytic step of a sol-gel process easily tune the size of the final NCs from 4 to 30 nm without decreasing the crystallinity and affecting the shape appearance. In this approach, the controlled addition of increasing quantities of water allows to tune the M-O-M chain which trigger the formation of bigger NCs.

Finally, the NCs shows a high stability in ethanol media, revealing a long time (*i.e.,* 6 months) stable NC colloidal solutions. This allows their use in a full range of applications without any issues in the solution storage.

3.7 References

1 H. Rijckaert, G. Pollefeyt, M. Sieger, et al., *Chem. Mater.*, 2017, **29**, 6104–6113.

2 A. Llordés, A. Palau, J. Gázquez, et al., *Nat. Mater.*, 2012, **11**, 329–336.

3 P. Cayado, K. De Keukeleere, A. Garzón, et al., *Supercond. Sci. Technol.*, 2015, **28**, 124007.

4 J. Gutiérrez, A. Llordés, J. Gázquez, et al., *Nat. Mater.*, 2007, **6**, 367–373.

5 L. L. Hench and J. K. West, *Chem. Rev.*, 1990, **90**, 33–72.

6 U. Schubert, in *The Sol-Gel Handbook*, Wiley-VCH Verlag GmbH & Co. KGaA, Weinheim, Germany, 2015, pp. 1–28.

7 A. E. Danks, S. R. Hall and Z. Schnepp, *Mater. Horizons*, 2016, **3**, 91–112.

8 A. Vioux, *Chem. Mater.*, 1997, **9**, 2292–2299.

9 C. N. Chervin, B. J. Clapsaddle, H. W. Chiu, A. E. Gash, J. H. Satcher and S. M. Kauzlarich, *Chem. Mater.*, 2006, **18**, 1928–1937.

10 In *The Chemistry of Metal Alkoxides*, Kluwer Academic Publishers, Boston, 2006, pp. 107–125.

11 J. Oliver, in *Climate Change 2013 - The Physical Science Basis*, ed. Intergovernmental Panel on Climate Change, Cambridge University Press, Cambridge, 2013, vol. 53, pp. 1–30.

12 N. Pinna, *J. Mater. Chem.*, 2007, **17**, 2769–2774.

13 N. Pinna, G. Garnweitner, M. Antonietti and M. Niederberger, *J. Am. Chem. Soc.*, 2005, **127**, 5608–5612.

14 M. Niederberger, G. Garnweitner, N. Pinna and M. Antonietti, *J. Am. Chem. Soc.*, 2004, **126**, 9120–9126.

15 Z. Lu, Y. Tang, L. Chen and Y. Li, *J. Cryst. Growth*, 2004, **266**, 539–544.

16 J. De Roo, K. De Keukeleere, J. Feys, P. Lommens, Z. Hens and I. Van Driessche, *J. Nanoparticle Res.*, 2013, **15**, 1778.

17 M. Niederberger, *Acc. Chem. Res.*, 2007, **40**, 793–800.

18 R. Deshmukh and M. Niederberger, *Chem. - A Eur. J.*, 2017, **23**, 8542–8570.

19 D. Caruntu, T. Rostamzadeh, T. Costanzo, S. Salemizadeh Parizi and G. Caruntu, *Nanoscale*, 2015, **7**, 12955–12969.

20 A. Pucci and N. Pinna, *Zeitschrift fur Naturforsch. - Sect. B J. Chem. Sci.*,

2010, **65**, 1015–1023.

21 D. Yang, M. Cao, Q. Zhong, P. Li, X. Zhang and Q. Zhang, *J. Mater. Chem. C*, 2019, **7**, 757–789.

22 M. Niederberger, N. Pinna, J. Polleux and M. Antonietti, *Angew. Chemie Int. Ed.*, 2004, **43**, 2270–2273.

23 T. Charoonsuk, W. Vittayakorn, N. Vittayakorn, P. Seeharaj and S. Maensiri, *Ceram. Int.*, 2015, **41**, S87–S94.

24 A. Yoko, M. Akizuki and Y. Oshima, *J. Nanoparticle Res.*, 2014, **16**, 1–9.

25 K. Nakashima, T. Goto, S. Iwatsuki, M. Kera, I. Fujii and S. Wada, *IOP Conf. Ser. Mater. Sci. Eng.*, 2011, **18**, 92049.

26 K. De Keukeleere, J. Feys, M. Meire, et al., *J. Nanoparticle Res.*, 2013, **15**, 2074.

27 K. Kanie, Y. Seino, M. Matsubara, M. Nakaya and A. Muramatsu, *New J. Chem.*, 2014, **38**, 3548–3555.

28 H. W. Lee, S. Moon, C. H. Choi and D. K. Kim, *J. Am. Ceram. Soc.*, 2012, **95**, 2429–2434.

29 E. Solano, L. Perez-Mirabet, F. Martinez-Julian, et al., *J. Nanoparticle Res.*, 2012, **14**, 1034.

30 L. John and P. Sobota, in *Ceramic Materials*, ed. W. Wunderlich, IntechOpen, Rijeka, 2010.

31 D. C. Bradley, *Chem. Rev.*, 2002, **89**, 1317–1322.

32 F. T. L. Muniz, M. A. R. Miranda, C. dos Santos and J. M. Sasaki, *Acta Crystallogr. Sect. A*, 2016, **72**, 385–390.

33 I. V Krasnikova, I. V Mishakov and A. A. Vedyagin, in *Carbon-Based Nanofillers and Their Rubber Nanocomposites*, eds. S. Yaragalla, R. K. Mishra, et al., Elsevier, 2019, pp. 75–137.

34 K. De Keukeleere, P. Cayado, A. Meledin, et al., *Adv. Electron. Mater.*, 2016, **2**, 1–9.

35 K. De Keukeleere, S. Coucke, E. De Canck, et al., *Chem. Mater.*, 2017, **29**, 10233–10242.

36 A. León, P. Reuquen, C. Garín, et al., *Appl. Sci.*, 2017, **7**, 49.

37 D. Philip, *Spectrochim. Acta Part A Mol. Biomol. Spectrosc.*, 2009, **73**, 650–653.

38 D. Philip, *Spectrochim. Acta Part A Mol. Biomol. Spectrosc.*, 2010, **75**, 1078–1081.

39 M. Piumetti, S. Bensaid, D. Fino and N. Russo, *Appl. Catal. B Environ.*, 2016, **197**, 35–46.

40 P.-Y. Wu, Y.-P. Jiang, Q.-Y. Zhang, Y. Jia, D.-Y. Peng and W. Xu, *New J. Chem.*, 2016, **40**, 2878–2885.

41 J. R. Copeland, I. A. Santillan, S. M. Schimming, J. L. Ewbank and C. Sievers, *J. Phys. Chem. C*, 2013, **117**, 21413–21425.

42 J. I. Di Cosimo, V. K. Díez, M. Xu, E. Iglesia and C. R. Apesteguía, *J. Catal.*, 1998, **178**, 499–510.

43 C. Morterra, A. Zecchina, S. Coluccia and A. Chiorino, *J. Chem. Soc.{,} Faraday Trans. 1*, 1977, **73**, 1544–1560.

44 M. J. Simpson and A. J. Simpson, in *Encyclopedia of Spectroscopy and Spectrometry*, Elsevier, 3rd edn., 2017, pp. 170–174.

45 H. Yasunaga, M. Kobayashi and S. Matsukawa, in *Studies in Physical and Theoretical Chemistry*, Elsevier B.V., 1998, vol. 84, pp. 737–769.

46 J.-C. Daigle, A. Arnold, A. Vijh and K. Zaghib, *Magnetochemistry*, 2018, **4**, 13.

47 G. E. Maciel, in *Studies in Physical and Theoretical Chemistry*, Elsevier B.V., 1998, vol. 84, pp. 923–984.

48 M. Veith, S. Mathur, N. Lecerf, et al., *J. Sol-Gel Sci. Technol.*, 2000, **17**, 145–158.

49 M. L. Moreira, J. Andrés, V. R. Mastelaro, J. A. Varela and E. Longo, *CrystEngComm*, 2011, **13**, 5818–5824.

50 S. Bhattacharjee, *J. Control. Release*, 2016, **235**, 337–351.

51 C. Burda, X. Chen, R. Narayanan and M. A. El-Sayed, *Chem. Rev.*, 2005, **105**, 1025–1102.

52 Y. Jun, J. Choi and J. Cheon, *Angew. Chemie Int. Ed.*, 2006, **45**, 3414–3439.

53 Y. Wang, Y. Zheng, C. Z. Huang and Y. Xia, 2013, **135**, 1941–1951.

54 F. Wang, V. N. Richards, S. P. Shields and W. E. Buhro, *Chem. Mater.*, 2013, **26**, 5–21.

55 J. van Embden, A. S. R. Chesman and J. J. Jasieniak, *Chem. Mater.*, 2015, **27**, 2246–2285.

56 J. Polte, *CrystEngComm*, 2015, **17**, 6809–6830.

57 C. N. R. Rao, A. Müller and A. K. Cheetham, *Nanomaterials Chemistry*, Wiley, 2007.

58 Z. Wu, S. Yang and W. Wu, *Nanoscale*, 2016, **8**, 1237–1259.

59 R. A. S. and W. J. Parak, *Phil. Trans. R. Soc. A*, 2010, **368**, 1333–1383.

60 F. Fi, R. Brayner, F. Chau, et al., *Chem. Soc. Rev.*, 2018, **47**, 5187–5233.

61 E. M. Hotze, T. Phenrat and G. V. Lowry, *J. Environ. Qual.*, 2010, **39**, 1909–1924.

62 J. Van Embden, A. S. R. Chesman and J. J. Jasieniak, *Chem. Mater.*, 2015, **27**, 2246–2285.

63 N. T. K. Thanh, N. Maclean and S. Mahiddine, *Chem. Rev.*, 2014, **114**, 7610–7630.

64 H. Dong, Y. C. Chen and C. Feldmann, *Green Chem.*, 2015, **17**, 4107–4132.

65 R. Hachani, M. Lowdell, M. Birchall, et al., *Nanoscale*, 2016, **8**, 3278–3287.

66 B. Lim and Y. Xia, *Angew. Chemie - Int. Ed.*, 2011, **50**, 76–85.

67 A. J. Biacchi and R. E. Schaak, 2011, **5**, 8089–8099.

68 C. O. Kappe, *Angew. Chemie Int. Ed.*, 2004, **43**, 6250–6284.

69 K. De Keukeleere, J. De Roo, P. Lommens, J. C. Martins, P. Van Der Voort and I. Van Driessche, *Inorg. Chem.*, 2015, **54**, 3469–3476.

70 I. Bilecka and M. Niederberger, *Nanoscale*, 2010, **2**, 1358.

71 K. De Keukeleere, J. Feys, M. Meire, et al., *J. Nanoparticle Res.*, 2013, **15**, 2074.

72 J. Martínez-Esaín, J. Faraudo, T. Puig, et al., *J. Am. Chem. Soc.*, 2018, **140**, 2127–2134.

73 M. Niederberger, N. Pinna, J. Polleux and M. Antonietti, *Angew. Chemie - Int. Ed.*, 2004, **43**, 2270–2273.

74 M. Niederberger and G. Garnweitner, *Chem. - A Eur. J.*, 2006, **12**, 7282–7302.

75 G. W. Scherer, *J. Ceram. Assoc. Japan*, 1987, **95**, 31-54-.

76 M. Z.-C. Hu, J. T. Zielke, C. H. Byers, J. S. Lin and M. T. Harris, *J. Mater. Sci.*, 2000, **35**, 1957–1971.

77 N. V Golubko, M. I. Yanovskaya, I. P. Romm and A. N. Ozerin, *J. Sol-Gel Sci. Technol.*, 2001, **20**, 245–262.

4

General hybrid approach to synthesise BMO_3 perovskite nanocrystals

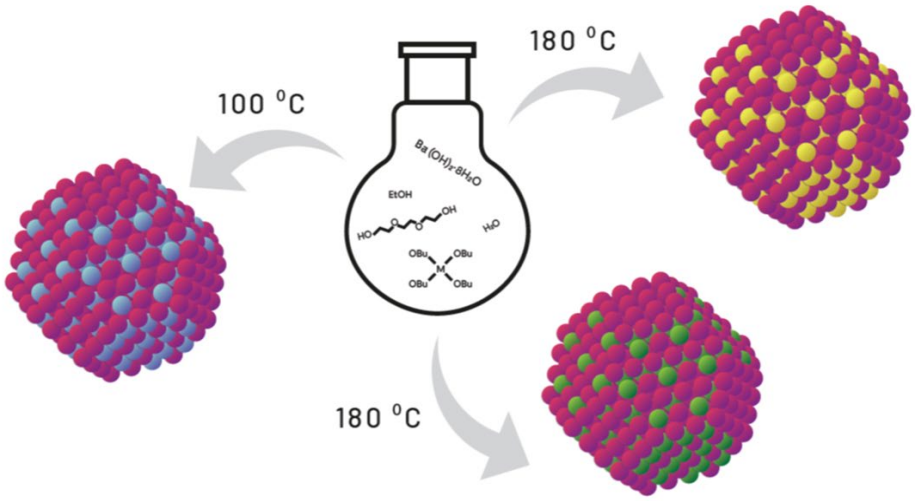

Here, we present a whole general route to successfully synthesise high-quality BMO_3 nanoscale compounds. By the implementation of the hybrid methodology exposed in the previous chapter, we proved the effectiveness for synthesis of new perovskite-type materials.

Our results demonstrate that it is possible to selectively exchange the tetravalent cation, resulting in a successful synthesised BMO_3 (M= Ti^{4+}, Zr^{4+} and Hf^{4+}) NCs. The chemistry of the Hf^{4+} shows similar behaviour than Zr^{4+}. Besides their specific synthetic parameters, both ions show remarkable similarities. In contrast, Ti^{4+} cation shows a different behaviour: at the growing process and the ability to tailor the NC sizes. Additionally, the ex-change of the divalent cation (B-site) using Sr^{2+} instead of Ba^{2+} was studied. This exchange leads to modification of the lattice's structure which has a direct effect on the final NC formation. We will show that our method to synthesise BMO_3 NCs only works if the finals crystalline structure of the NCs is cubic. In addition, in this Chapter we have studied the doping of the $BaZrO_3$ NCs with Y^{3+} cation up to 10%.

Adapted from: (A) N. Chamorro, J. Martínez-Esaín, T. Puig, et al., *RSC Adv.*, 2020, **10**, 28872–28878. **(B)** N. Chamorro, T. Puig, X. Obradors, et al.,**In preparation**

4.1. Introduction

Concerning the general trends of the family of BMO_3 perovskite, the ideal structure has a space group P*m-3m*, where the B cations are on the edges of the cubic structure and the M cation are octahedrally coordinated by the anions in the centre of the cell.[1–3] BMO_3 perovskite type structure NCs are of great importance because their properties can be tailored by the substitution of different elements into their crystal lattices. The perovskite structures are enormously tolerant at incorporate ions of various size and charge showing a great flexibility of composition.[2,4–6] Not all the perovskites have an ideal cubic structure, some can suffer from partial distortion on their lattice structure.

The tolerance factor (t), proposed by V. M. Goldschmidt at 1926, is an empirical measure that relates the structure stability of BMO_3 perovskites with the radii of each element by following the Equation 4.1.[1,7–9]

$$t = \frac{(r_B + r_o)}{\sqrt{2}(r_M + r_o)} \tag{4.1}$$

where r_B is the ionic radius of B, r_M the ionic radius of the M and r_O the ionic radius of oxygen.

This equation has a direct dependence on the ionic radii of each element of the perovskite's crystal structure. Besides is a useful tool to measure the degree of distortion of the crystal lattice. In the case of a tolerance factor with a value t=1 or values close to the unity, the B and M cations are ideally coordinated. Therefore, a cubic structure is predicted to be stable. If the tolerance factor is in the range of 0.8-1.06 then the perovskites are stable but not necessarily with a cubic phase. When t≠1 it implies the possibility of a new lattice structure showing as the most representatives phases: orthorhombic, rhombohedral, tetragonal, monoclinic, etc.[1,3,7,8,10]

4.2 Changing the tetravalent cation

To demonstrate the effectiveness of this dual-based synthetic approach, we are going to changes the tetravalent cation from Zr^{4+} to Ti^{4+} and Hf^{4+}, thus making it extendable through the other two metal from the same periodic group (IV). As a result of changing the tetravalent cation, a $BaTiO_3$ and $BaHfO_3$ NCs are obtained. Zr^{4+} and Hf^{4+} show remarkable similarity on chemical properties[11] with an oxidation state of +4 and an ionic radius similar 0.72 Å in the case of Zr^{4+} and 0.71 Å in the case of Hf^{4+}. Ti^{4+} on the other hand, could lead to different physicals properties. Its reduced ionic radii 0.61 Å could drive to different crystalline structure than the others two.

Although, $BaTiO_3$ has been widely studied compared with the other two materials, and it is much well known,[12–15] it has been never synthesised by using the hybrid solvothermal approach. Herein we focus on a general route to synthesise the three perovskites ($BaZrO_3$, $BaTiO_3$ and $BaHfO_3$) using the same methodology.

4.2.1 $BaMO_3$ (M= Ti^{4+}, Zr^{4+}, Hf^{4+}) synthesis

Initially, the synthesis was performed by following the standard approach. $M(OBu)_4$, reagents where M = (Ti^{4+}, $Zr^{4+}$and Hf^{4+}) and $Ba(OH)_2{\cdot}8H_2O$ were dissolved in absolute ethanol and finally mixed with aqueous ammonia and TREG. The first results were done by using 1 mL of aqueous ammonia and heating the vessel with the mixture up to 180 °C for 1 hour. The implementation of the standard synthesis was carried out with ammonia in order to study step by step the NCs formation and to unravel the insight of the mechanisms from these materials.

The versatility for this approach is reflected in Figure 4.1 by observing a successfully synthesis for the three perovskites using the same hybrid methodology. The HRTEM show that the three type of NCs exhibit high crystallinity (isolated particles and its respective planes). The shape is well-defined in the case of $BaZrO_3$ showing a square-like shape NCs compared with $BaTiO_3$ and $BaHfO_3$, which present a spherical shape (Figure 4.1). Table 4.1 report the average sizes of each compound analysed via TEM and XRD.

Table 4.1. Summary of average size (Scherrer and TEM), morphology and ζ-potential from the obtained nanocrystals.

NCs	Scherrer size	TEM size	Morphology	ζ-potential (mV)
$BaTiO_3$	7.8 nm	8.3 ± 1.4 nm	Spherical	+31.7
$BaZrO_3$	8.2 nm	8.6 ± 1.5 nm	Square-like	+40.2
$BaHfO_3$	6.8. nm	7.0 ± 1.2 nm	Spherical	+38.6

This is further supported by the implementation of the Scherrer equation to calculate the crystalline domain which evidence a smallest NCs in the case of $BaHfO_3$ with a crystalline domain of 6.8 nm, followed by $BaTiO_3$ with 7.8 nm and finally the $BaZrO_3$ with 8.2 nm size. The XRD of the three perovskites NCs show typical diffraction peaks of cubic structure and are indicative of a high crystallinity.

The three synthesis have a similar yield (40-60 %) after applying the extra-step after the cleaning process. The results are pearl-white solutions for all the NCs colloidal solution which after drying the sample led to white powders in all the cases.

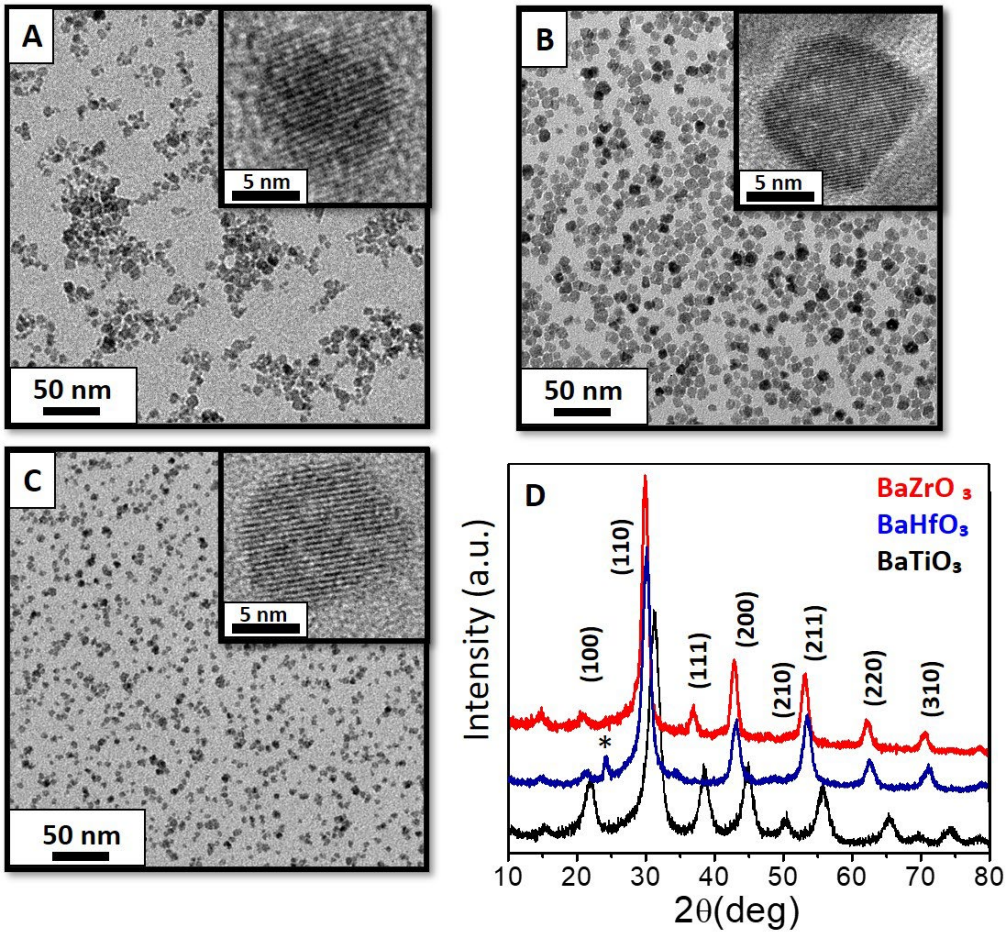

Figure 4.1. TEM image of (A) $BaTiO_3$ (B), $BaZrO_3$ and(C) $BaHfO_3$ by using the hybrid solvothermal reaction at 180 ^{0}C and 1 hour, shown their corresponding HRTEM and the planes of isolated NCs of each one. (D) The index miller of the principal peaks by XRD has been assigned into the diffractogram to confirm the cubic structure. On $BaHfO_3$ appears an *$BaCO_3$ peak suggesting a 5% of impurity on the pattern. $BaTiO_3$ pattern used from data base ICSD file number 01-075-0210. $BaHfO_3$ patter with reference code 00-022-0084

In the case of $BaHfO_3$, the presence of an impurity peak which was determined to be *$BaCO_3$ has been observed. It has low intensity and it have been quantified to be 5% traces. The three NCs show a positive ζ-potential, $BaZrO_3$≈ +40 mV, $BaHfO_3$≈ +39 mV, $BaTiO_3$≈ +34 mV, thus, pointed out that there is a positive charge in the NCs surface.

Assessing the NCs stability and homogeneity in alcoholic solution the DLS analysis revealed in Figure 4.2 show that the NCs remain well dispersed and stable in ethanol up to 6 months. The DLS measurements also shown a d_H = 7-10 nm, in close agreement with the results obtained by TEM and XRD. This results once again promote an exceptional storage property in high concentration and for long times.

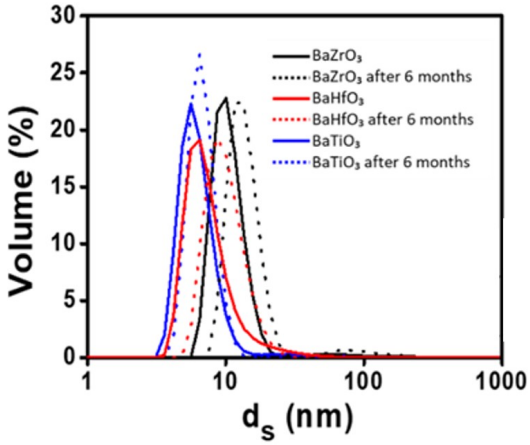

Figure 4.2. A stability study by using DLS for monitoring the stability of the nanocrystals ($BaTiO_3$, $BaZrO_3$ and $BaHfO_3$ synthesised at 180 °C for 1 hour) from the moment of the synthesis to 6 months, all of them in ethanol media.

Regarding the crystal structure stability of each compound, the Goldschmidt tolerance factor (t) equation (Equation 4.1) was implemented. In the case of M = Zr^{4+} and Hf^{4+} shown a tolerance factor of t = 1 which is considered as the ideal cubic structure, where the ions are in a perfect cubic lattice (Table 4.2).

Table 4.2. Overview of the radii from each element of the different perovskites, all radii data has been taken from R.D Shannon.[16] Ionic radius of O^{2-} is 1.40 Å. The number on the parenthesis correspond to the coordination of the ion into the perovskite structure.

Perovskites BMO_3	Ionic radius [Å]				Tolerance factor
	Cation B^{2+}		Cation M^{4+}		
$BaZrO_3$	Ba^{2+}(XII)	1.61	Zr^{4+} (VI)	0.72	1.00
$BaHfO_3$	Ba^{2+}(XII)	1.61	Hf^{4+} (VI)	0.71	1.00
$BaTiO_3$	Ba^{2+}(XII)	1.61	Ti^{4+}(VI)	0.61	1.06

Applying Equation (4.1) to the $BaTiO_3$, a value of t > 1.05 is obtained due to a smaller size of Ti^{4+} cations. This might cause distortion on the lattice structure which could entail a phase transition from cubic to tetragonal.[12,13,17] $BaTiO_3$ with tetragonal phase is well known due to it's ferroelectric behaviour leading to a new range of applications for this material.[12,17,18] A deeper study of $BaTiO_3$ to ensure the crystal

structure and the possibility to show a phase transition will be presented in the next sections.

4.2.2 Tuning synthetic parameters

As we have already studied the synthetic parameters for $BaZrO_3$ we are going to analyse in the same way the parameters for $BaTiO_3$ and $BaHfO_3$. Consequently, a study by varying temperature and time parameters is exposed, as well as which is the key parameter to control the size tuneability.

4.2.2.1 Temperature and time

From the knowledge acquired from $BaZrO_3$, a new outcome comes at extrapolate the study of temperature and time reaction for the $BaTiO_3$ and $BaHfO_3$ synthesis. In accordance with this standpoint, two main experiments were performed. Firstly, keeping the time constant (1 hour) and varying the temperature (100 and at 180 °C). Secondly, we keep the temperature constant and studied different reaction times, 1 hour and 24 hours.

The TEM images in Figure 4.3 displayed the three perovskites NCs synthesised at 100 °C. The results provide a successful achievement of $BaTiO_3$ NCs, with a final average sizes of 8.2 ± 1.6 nm at 100°C. In contrast, this experimental data differs from $BaZrO_3$ and $BaHfO_3$ NCs, where TEM images evidence that at 100 °C the NCs are not completely formed. These results suggest that a $BaTiO_3$ needs a much lower temperature to crystallize. In order to confirm the crystall structure XRD (Figure 4.3D) were performed. $BaTiO_3$ shows a cubic phase pattern with a crystalline domain of 7.4 nm which agrees with the TEM values. However, $BaZrO_3$ and $BaHfO_3$ shows a lack of crystallinity evidenced by broad peaks, where the main presence is proved to be impurities of $*BaCO_3$. (Figure 4.3D). In addition, once the reaction is performed at 180°C all three perosvkites ($BaTiO_3$, $BaZrO_3$ and $BaHfO_3$) NCs have been successfully synthesized (Figure 4.4). We can notice that after 1 hour of reaction at 180°C, the size of $BaTiO_3$ NCs (8.3 ± 1.4 nm) are extremely similar with the ones obtained at 100°C. This difference in growth conditions could be driven by a faster supersaturation point and different surface energy by using Ti^{4+} instead of Zr^{4+} or Hf^{4+} precursors.[19]

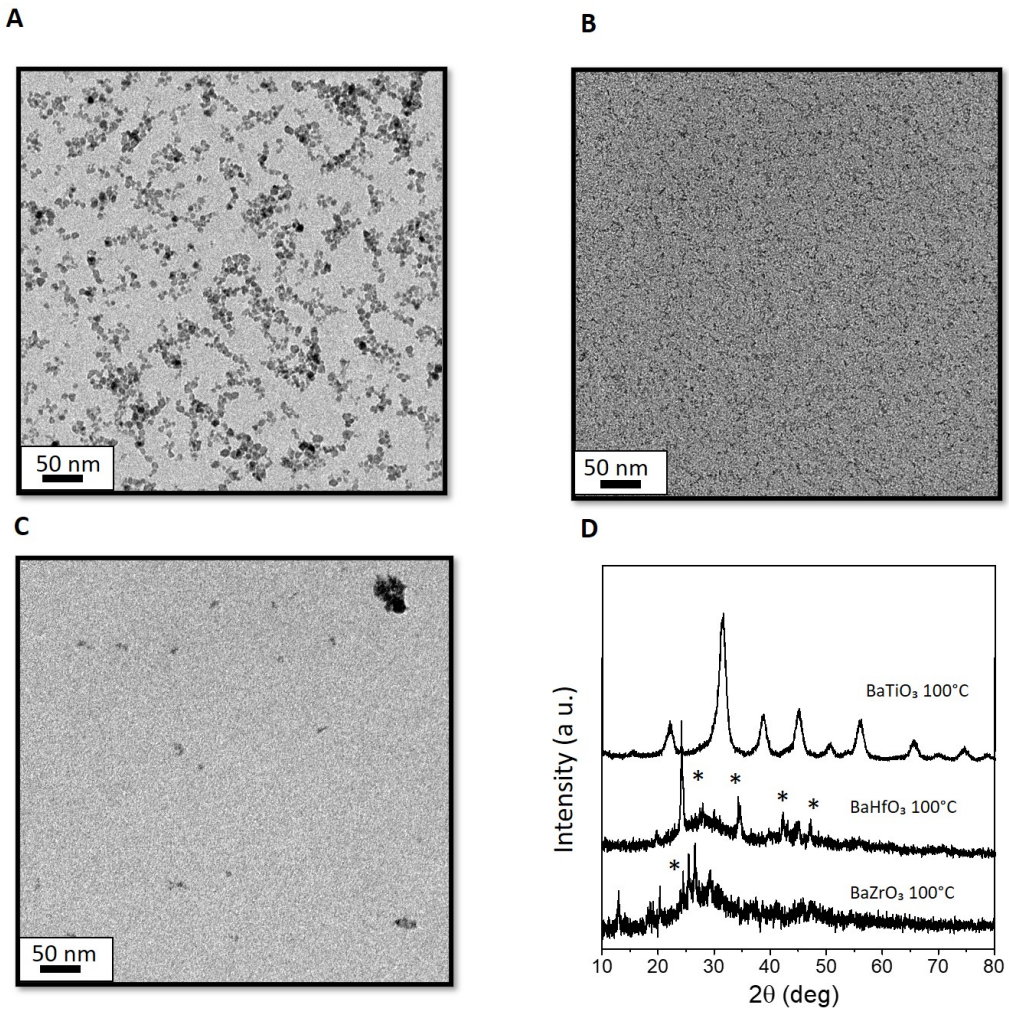

Figure 4.3. TEM images of (A) $BaTiO_3$, (B) $BaZrO_3$ and (C) $BaHfO_3$ synthesised at 100 °C for 1 hour. (D) XRD pattern of $BaZrO_3$, $BaHfO_3$ and $BaTiO_3$ synthesized via standard procedure by using 1 mL of aqueous ammonia for 1 hour at 100 °C. In the case of $BaMO_3$ (M = Zr^{4+} and Hf^{4+}) at 100 °C without a final crystal formation, and showing a main peak coming from the presence of *$BaCO_3$ impurities.

Consequently, even we prolong the reaction time to 24 hours and the NCs do not show any changes on the crystallinity, NCs size or dispersibility (Figure 4.4). This study indicates that by keeping the NCs for long time at the reaction temperatures they do not suffer grain growth (Oswald ripening) process, leading to a constant size towards long times reactions. Therefore, 1 hour is enough for the NC formation, and keeping the reaction 24 hours at the same temperature did not affect the crystallinity or a possible grain growth of the NCs.

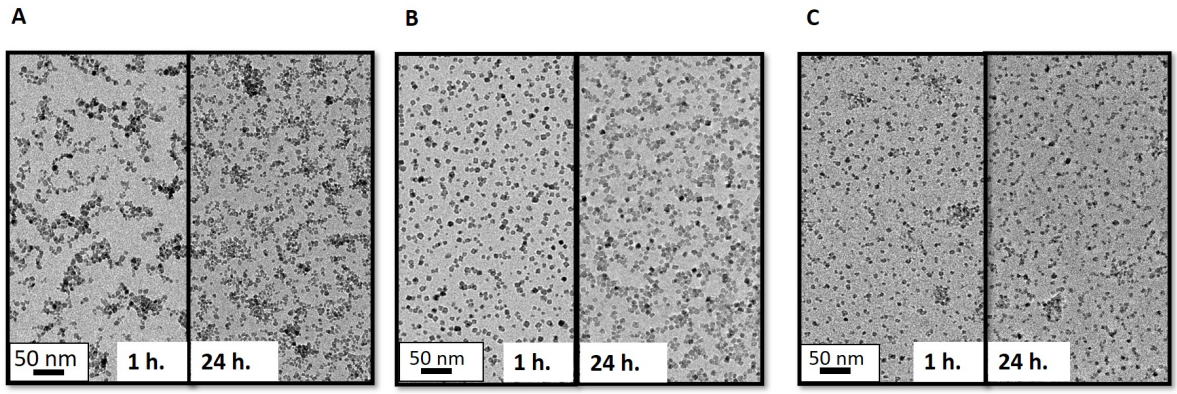

Figure 4.4. TEM images of (A) $BaTiO_3$, (B) $BaZrO_3$ and (C) $BaHfO_3$ synthesised at 180 °C for 1 hour and 24 hours of reaction.

Table 4.3 sums up the sizes of the NCs obtained via TEM and Scherrer equation, both at 100 and 180 °C and 1 hour and 24 hour of reaction time.

Table 4.3. Summary sizes (TEM and Scherrer equation) of $BaZrO_3$, $BaHfO_3$ and $BaTiO_3$ at different temperatures 100 °C and 180 °C. Inn al three cases it was study different time reaction at 1 hour and 24 hours.

NCs	Temp.(°C)	Time (hours)	TEM sizes (nm)	Scherrer size (nm)
$BaTiO_3$	100	1	8.2 ± 1.6	7.4
		24	7.8 ± 1.7	7.2
	180	1	8.3 ± 1.4	7.8
		24	8.0 ± 1.3	7.5
$BaZrO_3$	100	1	-	-
		24	-	-
	180	1	8.5 ± 1.5	8.2
		24	8.8 ± 1.70	8.5
$BaHfO_3$	100	1	-	-
		24	-	-
	180	1	7.0 ± 1.2	6.8
		24	6.7 ± 1.4	6.4

Considering the XRD, the patterns do not reveal any evidence of difference at crystallinity or size (*i.e.,* via Scherrer equation). It seems that the nucleation rate of the NCs is almost instantaneous once they are subjected to an adequate combination of pressure and temperature in the autoclave, without changing the morphology or crystallinity of the NCs. Some aspect related to the different behaviour between this three metals has been reported by previous research using M (Ti^{4+}, Zr^{4+} and Hf^{4+}) shown that the reactivity strongly depends on the radii and the metal itself.[20,21]

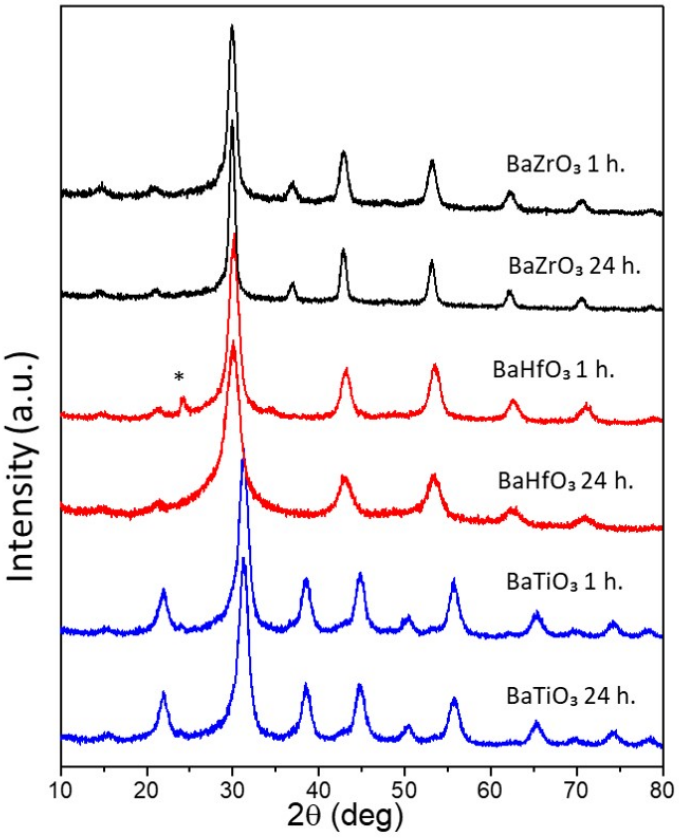

Figure 4.5. XRD diffraction patterns from $BaZrO_3$, $BaTiO_3$ and $BaHfO_3$ NCs at 180 °C synthesised via standard procedure by using 1 mL of aqueous ammonia for 1 hour and 24 hours. $BaHfO_3$ at 180 °C shows a *$BaCO_3$ peak suggesting a 5% of impurity.

The use of different metals can result in a conflict on the synthetic pathway to reach the final NCs. Each metal has different chemical and physical properties.[11] Even though, we choose three metals from the same periodic group, we should remark the similar characteristics between Zr^{4+} and Hf^{4+} very closely indeed with only minor differences in such properties as solubility and volatility, showing almost identical radii compared with titanium.[11,22,23]

4.2.2.2 Water effect

Regarding the strategy discussed for $BaZrO_3$ (Chapter 3), the hydrolytic steps is claimed to be the one who govern the NCs sizes by controlling the water amount in the synthesis. Since we already proven that the reaction temperature is different for $BaTiO_3$ we want to see if the water amount has the same role in the synthesis of these NCs ($BaTiO_3$ and $BaHfO_3$).

For both cases, $Ti^{4+}$and Hf^{4+} the synthetic methodology follows the standard procedure, adding $M(OBu)_4$ into absolute ethanol at room temperature followed by the addition of $Ba(OH)_2{\cdot}8H_2O$, TREG and different amounts of water (28 and 111 mmol). The solutions were transferred to an autoclave and heat up until 180 °C in the case of $BaHfO_3$ and 100 °C in the case of $BaTiO_3$.

$BaHfO_3$ NCs size shows a water-dependency. Figure 4.6A-B reveals an average size of 4.2 ± 0.7 nm by the addition of 28 mmol of water and 14.8 ± 3.4 nm.by the addition of 111 mmol amount of water. Therefore, $BaHfO_3$ shows a similar behaviour than $BaZrO_3$, as it was expected, due to, the close similar properties that these two elements have in common (Table 4.4). In the case of $BaTiO_3$ TEM images in Figure 4.6C-D shows a non-size variation of NCs independently of the amount of water used. In both cases the average sizes is around 9 nm.(Table 4.4).

Table 4.4. Summary for $BaHfO_3$ and $BaTiO_3$ by the addition of different quantity of water.

NCs	Water (mmol)	TEM sizes (nm)	Scherrer size (nm)
$BaHfO_3$	28	4.6 ± 0.7	4.4
	111	14.8 ± 3.4	14.3
$BaTiO_3$	28	8.7 ± 2.6	8.5
	111	9.2 ± 2.1	9.0

The mechanism insight to unravel the tuneability of NC sizes is related with the hydrolysis rate, thus a kinetical control on the reactions by the addition of water. $BaZrO_3$ and $BaHfO_3$ corroborated this postulation, both NCs follow the equations (3.1 to 3.4) exposed on Chapter 3. These equations described the hydrolysis and condensation process of a sol-gel reaction, being the water the one who triggers the formation of M-O-M chains leading to bigger NC formation.

Based on this relationship with the water amount, the average particle sizes were plotted in function of "h" value (h= $[H_2O]/[M(OR)_4]$) observed in Figure 4.6E. According to Figure 4.6E the particle sizes have an almost linear relationship on Zr^{4+}

and Hf^{4+} compounds by increasing the sizes while the amount of water is raising. However, in the case of Ti^{4+}, the $H_2O/Ti(OR)_4$ ratio keeps equal towards the addition of more quantity of water. This conclusion is supported by the previous work of R. Azouni, et al.,[24] and S. Labidi, et al.,[25] which reported the kinetics formation of titanium-oxo-alkoxy and zirconium-oxo-alkoxy respectively in a sol-gel process by controlling the "h" ratio. This work is based on varying the "h" from 1. to 2.7 to study the size evolution in these ranges showing some divergence between Ti^{4+} and Zr^{4+}.

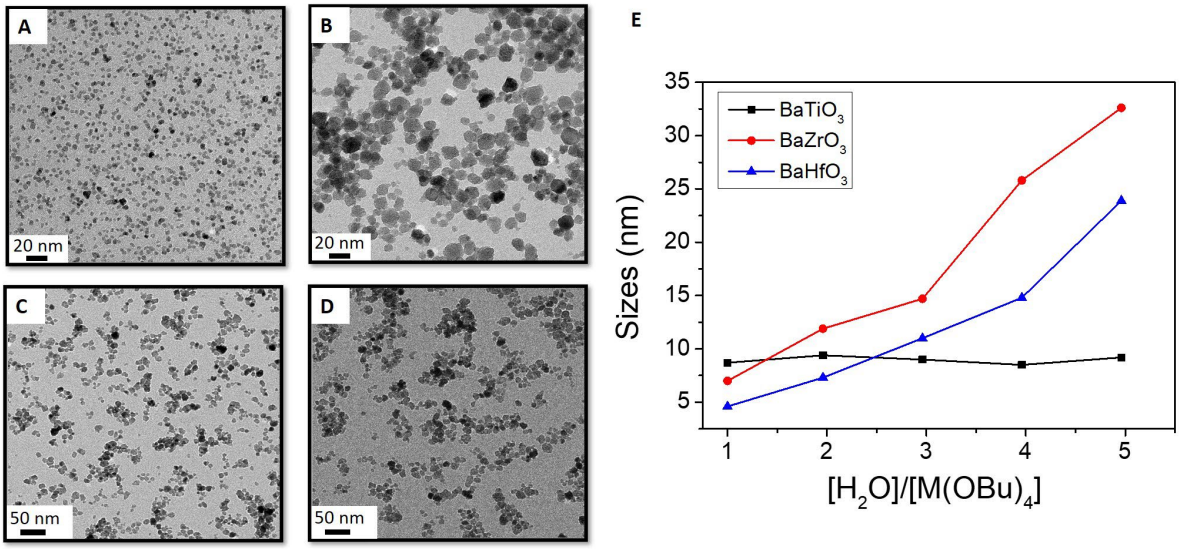

Figure 4.6. TEM image of $BaHfO_3$ by the addition of 28 mmol (A) and 111 mmol (B) of water. TEM image of $BaTiO_3$ by the addition of 28 mmol(C) and 111 mmol (D) of water. (E) relationship between water and metal alkoxide ratio "h" and the particles mean sizes of $BaMO_3$ (M= Ti^{4+}, Zr^{4+} and Hf^{4+}).

Even though there is an inconsistency when we talk about the $BaTiO_3$, a possible explanation for the different behaviour of the Ti^{4+}, can start from the behaviour of the alkoxide precursors in solution, as well as their tendency to polymerise. We should consider the sophistication for the alkoxides precursors on solution as well as the tendency to polymerise creating coordination polymers $[M(OR)_x]_y$ (where "y" is the degree of polymerization) which determine the final product of the crystal. Moreover, the degree of polymerisation has a direct dependency with the physicals properties off the metals i) radius of the metal ($Ti^{4+} < Zr^{4+}$, Hf^{4+}) ii) coordination number iii) sizes of group R on the alkoxide. Thereby a high metal radius entails a higher polymerization degree.

Here, we need to consider the analogy between coordination chemistry and NC surface as the well-known covalent bond classification (CBC).[26,27] CBC is mainly based in the direct comparison between coordination chemistry and the surface of NC, in which each metallic cation center could be considered as a coordination complex. In our case, it seems that titanium cations exposed in the surface are less favorable to the NC growth. Regarding the other two metals, the hydrolysis process triggers the formation of M-O-M chains and therefore, the favorable growth of nanocrystals. This hypothesis is supported by previous publications related to studies in coordination chemistry in which the authors found significant differences between the reactivity of titanium and zirconium alkoxides against hydrolysis and/or coordination.[22,28–30]

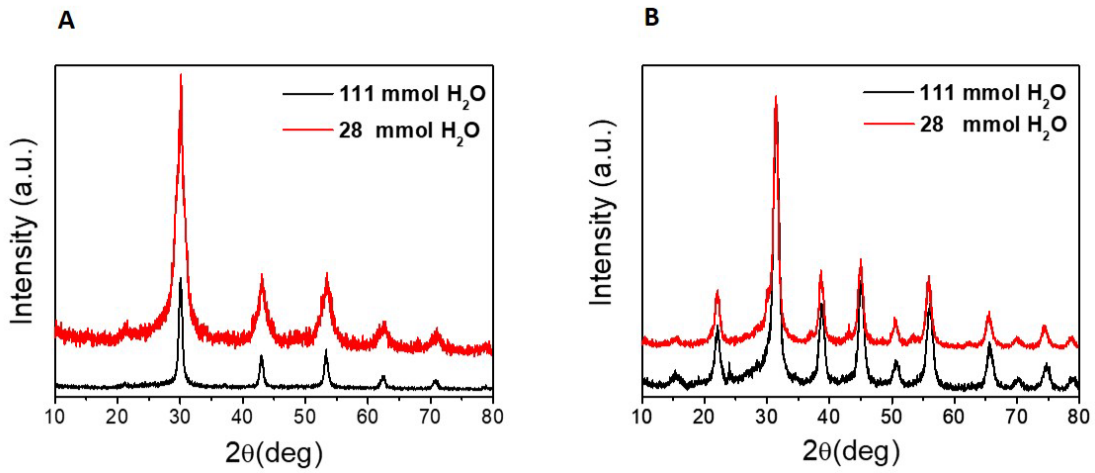

Figure 4.7. XRD diffraction patterns for (A) $BaHfO_3$ and (B) $BaTiO_3$ NCs synthesised via standard procedure by adding 28 and 111 mmols of water instead of aqueous ammonia at 180 °C ($BaHfO_3$) and at 100 °C ($BaTiO_3$).

Once again, the XRD show evidence about the different behaviour between the two precursors ($Ti^{4+} \neq Hf^{4+}$) and proves the size variation between both cases. $BaHfO_3$ show a broad diffraction peak pointing to small size by adding 28 mmol of water, and a narrow peak at increasing the amount of water to 111 mmol (Figure 4.7A). On the other hand, $BaTiO_3$ shows a similar peak width at increasing the amount of water (from 28 to 111 mmol) without significance differences (Figure 4.7B). XRD shows a cubic phase, for both NCs type. Table 4.4 presents the size of the NCs calculated with Scherrer equation which corroborates the NCs sizes calculated by TEM.

4.2.3 The different behaviour of $BaTiO_3$ NCs

The emphasis to investigate $BaTiO_3$ NCs comes from it's excellent dielectric and electrochemical properties.[12,18,31,32] It has been successfully applied on; ion water splitting,[33] energy conversion,[18] thin-film capacitors[34] and multiferroics materials.[32,35–37] Since it behaves differently than $BaZrO_3$ and $BaHfO_3$, $BaTiO_3$ NCs have been studied in more detail to see which parameters influence the size and shape and what is these NCs crystalline structure.

4.2.3.1 Control of size and shape of $BaTiO_3$ NCs

We have shown that water has no influence in the sizes of $BaTiO_3$ NCs. For this standpoint we focus on this element to try to unravel the growing process of the NCs. As it has been reported on many occasions beyond the different parameters that can influence the final achievement of NCs[38,39] we can find i) metal precursors concentration, ii) capping ligand and iii) temperature and time reaction. The preliminary studies revealed that reaction time, temperature or water amount have not affected the morphology, crystallinity or sizes. Considering the parameters exposed above, we focused to study how the metal precursors concentration can affect the final NCs by varying the amount of the $Ti(OBu)_4$ and $Ba(OH)_2{\cdot}8H_2O$.

The experiment was performed at different amount of $Ti(OBu)_4$ and $Ba(OH)_2{\cdot}8H_2O$, always keeping the same molar ratio of Ti^{4+}:Ba^{2+} (1:1.25). The amount of $Ti(OBu)_4$ was varied as follows: 2.8 mmol, 3.5 mmol and finally to 6.5 mmol. The amount of the other reagents as water and the polyol was kept constant. The solution was transfer to an autoclave vessel and heated up to 100 °C for 1 hour.

Initially the use of lower precursors amount (2.8 mmol of $Ti(OBu)_4$) leads to an average size of 8.3 ± 1.4 nm of $BaTiO_3$ NCs with undefined shape.(Figure 4.8). At increasing the amount of $Ti(OBu)_4$ to 3.5 mmol the synthesised NCs have a more defined shape with a final size of 10.2 ± 1.9 nm. Finally, when using 6.5 mmol of $Ti(OBu)_4$ the NCs show sort of hexagonal morphology with an average size of 13.2 ± 1.8. nm. These results can be followed in table 4.5.

The HRTEM image of individual isolated NCs shows several lattice planes, confirming a high degree of crystallinity. It is interesting to see how at increasing the amount of the precursors, a hexagonal morphology starts appearing with more clarity (Figure 4.8). This outcome suggests a different crystal growth on the $BaTiO_3$ surface, compared with the square-like shapes of $BaZrO_3$ NCs. This shows a different crystal habit from the same space group (XRD pattern shown on next section).

Table.4.5. Sum up of TEM sizes and Scherre sizes by varying the amount precursors, being represented the modification of $Ti(OBu)_4$ amount, on a standard reaction of 1 hour at 100 °C.

$Ti(OBu)_4$ (mmol)	TEM sizes (nm)	Scherrer Sizes (nm)
2.8	8.3 ± 1.4	7.8
3.5	10.2 ± 1.9	9.1
6.5	13.2 ± 1.8.	11.9

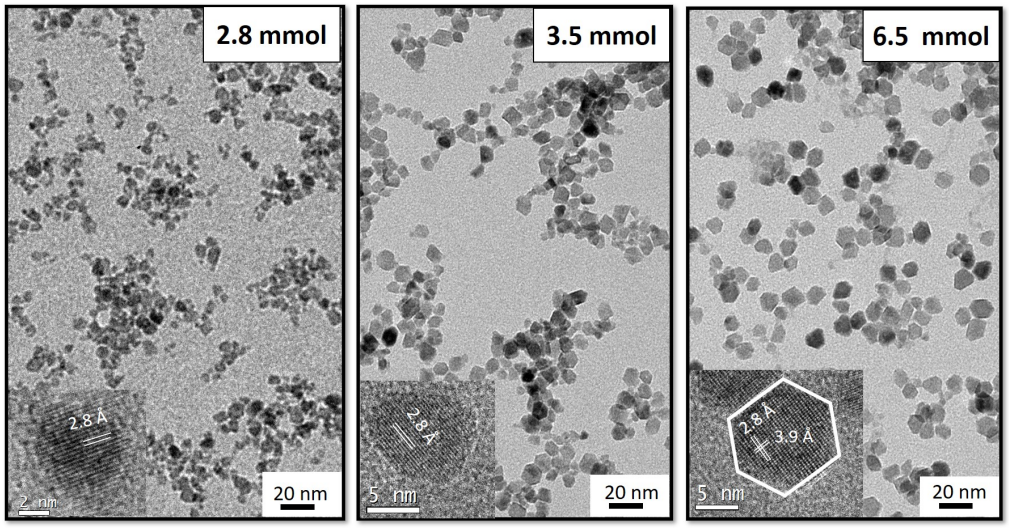

Figure 4.8. (A) HRTEM images from synthesis $BaTiO_3$ at different concentration of $Ti(OBu)_4$, on a standard reaction of 1 hour at 100 °C. Showing a d-spacing of 3.9 and 2.8 Å corresponding to the (001) and (110) planes of $BaTiO_3$ respectively.

Regarding the process of crystal growth, it is well known the correlation between the growth rate along the crystallographic orientation and the surface energy.[40,41] According to the crystal growth theory,[42,43] crystal facets with the most bonded atoms are the most stable in the process of crystal growth.[44] The facets with lowest surface energy grow the most slowly. The modification of a crystal morphology during the growth process is driven by decreasing the surface energy, thus limiting the growth of the final NCs.[40,44] Such process is apparently related to the modification of some parameters such as; initial reagents concentration, solvent and ligands, temperature and pressure, which during the growth environment may provide flexible conditions to tailor the shape of the crystal.

The crystal shape evolution during the growth process could explain the different crystal habit of $BaTiO_3$ compared with the square-like shape from the $BaZrO_3$ NCs. Keke. H, et al.[44] summarized in a review the recent progress of research in crystal facet tailoring in perovskite oxides by discussing the principles of the facet tailoring mechanism. Moreover, Hongquan Z. et al.[45] studied precisely the morphology of $BaTiO_3$ NCs in the presence of polyethylene glycol to finally obtained dodecahedral crystals. They postulated a selective absorption of the polyol to {110} facets, decreasing the surface energy, thus, limiting the growing process and promoting the dodecahedral morphology.

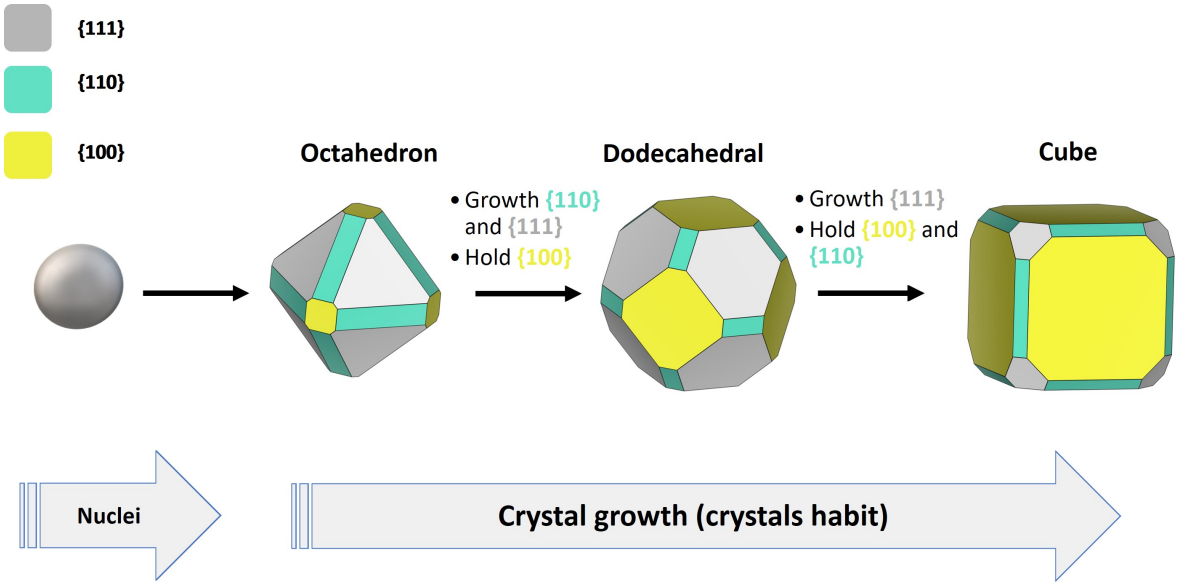

Figure 4.9. Representation for the proposed growth process for BMO_3. Crystals facets representation by using VESTA software

Figure 4.9 illustrates the shape evolution model for a typical cubic structure perovskite. The different colours represent different facets. Initially Figure 4.9 shows a primary particle (grey sphere) by undetermined facets. Posteriorly the particle growth to an octahedron shape dominantly encloses by {111} facets and a posterior growth to a dodecahedral shape. The dodecahedral morphology shows 12 {110} facets, and the crystal is limited by {111} and {100} facets. Finally, the, most common shape of these structures is square-like shape as $BaZrO_3$ perovskite NCs which is mainly enclosed by {100}.

Therefore, one explanation for our case $BaTiO_3$ NCs could be, due to the {111} facets are coordinated, thus limiting the growth through this facet leading to final dodecahedral shape.

4.2.3.2 $BaTiO_3$ structure

The tolerance factor equation (4.1), $BaTiO_3$ shows a t>1, thus bestowing the possibility to suffers a lattice distortion due to the small radius of Ti^{4+}. This is characterized by the switching from paraelectric cubic phase (Pm-3m) to ferroelectric tetragonal phase (P4mm), which means a distortion on c-axis lattice (a=b≠ c) from the crystal structure.[12,13,32]

To verify the possibility of tetragonal phase, XRD diffraction could show some limitation since both, cubic and tetragonal phase, may coexist together. An evidence of tetragonality by using XRD would be observed by a split peak over 2θ = 45° position. In the paraelectric phase 2θ = 45° correspond to (200) $BaTiO_3$ peak. In the tetragonal phase this peak split in two: (002) $BaTiO_3$ and (200) $BaTiO_3$ at the same 2θ values. Figure 4.10A evidence $BaTiO_3$ XRD pattern at different amount of $Ti(OBu)_4$ as reported on previous section, all of them corresponding to cubic phase, showing an individual peak on the position 2θ = 45°. However, the assignation cannot be fully attributed to cubic phase as a consequence of working at such reduced sizes (8 nm), limiting the XRD detection.

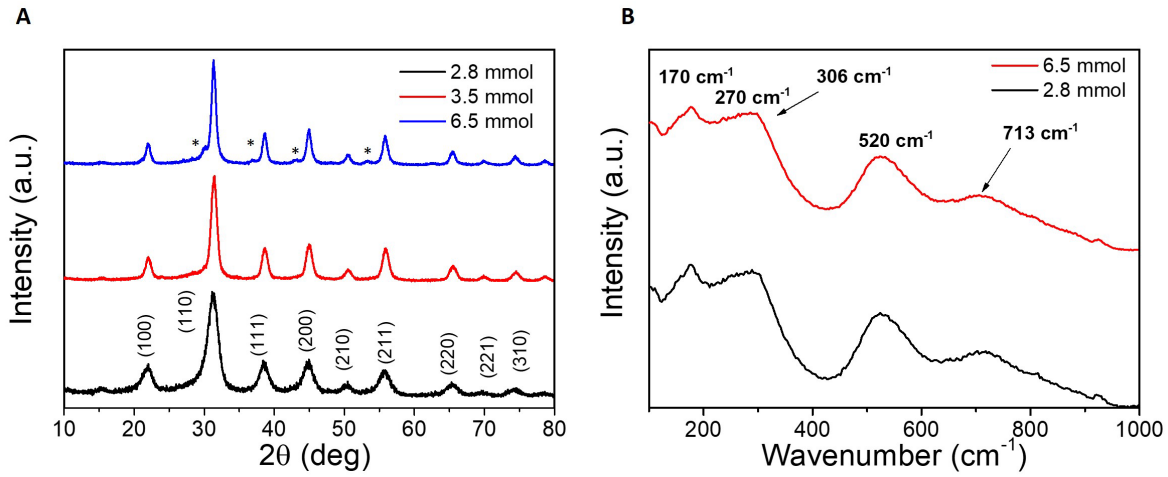

Figure 4.10. (A) XRD pattern of the three powder samples 2.8, 3.5 and 6.5 mmol of $Ti(OBu)_4$. (B) Raman spectroscopy of $BaTiO_3$ powder at room temperature from 2.8 and 6.5 mmol of $Ti(OBu)_4$. In XRD the peak of 6.5 mmol shows some traces of BCO_3 impurities, suggesting an 8% of $BaCO_3$.

For that reasons, to complete the study on the phase transition a complementary analysis using a Raman spectroscopy was performed (Figure 4.10B). The local tetragonality in Raman spectroscopy is distinguished by two actives bands. The inactive bands present on paraelectric cubic phase (176, 270 and 520 cm^{-1}) become active on the transition to tetragonal phase[12,13,46,47] at 306 cm^{-1} (sharp peak) and 713 cm^{-1} with a well-defined and high intensity peaks. These peaks are the footprint to

determine the tetragonally. $BaTiO_3$ powder at room temperature was analysed observing in both cases (2.8 and 6.5 mmol of $Ti(OBu)_4$) an absence of a sharp peak at 306 cm^{-1}. The spectra show a broad peak on 208 cm^{-1} coming for the inactive bands from cubic phase, and a subtle broad peak on 713 cm^{-1}. This case suggests a non-dominant tetragonal phase on the crystal which lead to cubic perovskite postulation.

4.2.4 Microwave methodology

Microwave activation was proved to be successful regarding both syntheses of NCs ($BaTiO_3$ and $BaHfO_3$). Using microwave activation, we will have tight control over the induced temperature and pressure created inside the vessel.

The NCs were synthesised by microwave activation at 180 °C ($BaZrO_3$ and $BaHfO_3$) and 100 °C ($BaTiO_3$) for 5 minutes and using 28 mmol amount of water for each case. The microwave reaction in the case of $BaZrO_3$ and $BaHfO_3$ lead to a maximum pressure of 15 bars and in the case of $BaTiO_3$ lead to 4 bars. The images observed by TEM (Figure 4.11A-C) show in all three cases, the successful formation of NCs. Also, it is evidenced an average size for $BaZrO_3$, $BaHfO_3$ and $BaTiO_3$ of 5.8 ± 1.2, 4.5 ± 0.8 and 6.3 ± 1.1 respectability.

Concerning the crystallinity of these NCs obtained by microwave activation, XRD measurements of all powder samples were performed (Figure 4.14D). The pattern shows a typical cubic phase as those obtained by solvothermal method. The sizes of NCs synthesised by microwave activation are calculated with Scherrer equation and confirmed by TEM analysis (Table 4.6).

Table 4.6. Sum up of the size (TEM and Scherrer) from the synthesis for 5 minutes at 100 °C for $BaTiO_3$ and 180 °C to $BaZrO_3$ and $BaHfO_3$. The synthesis was made with 28 mmol amount of water.

NCs	Size TEM (nm)	Scherrer sizes (nm)
$BaZrO_3$	5.8 ± 1.2	5.3
$BaHfO_3$	4.5 ± 0.8	4.1
$BaTiO_3$	6.3 ± 1.1	5.9

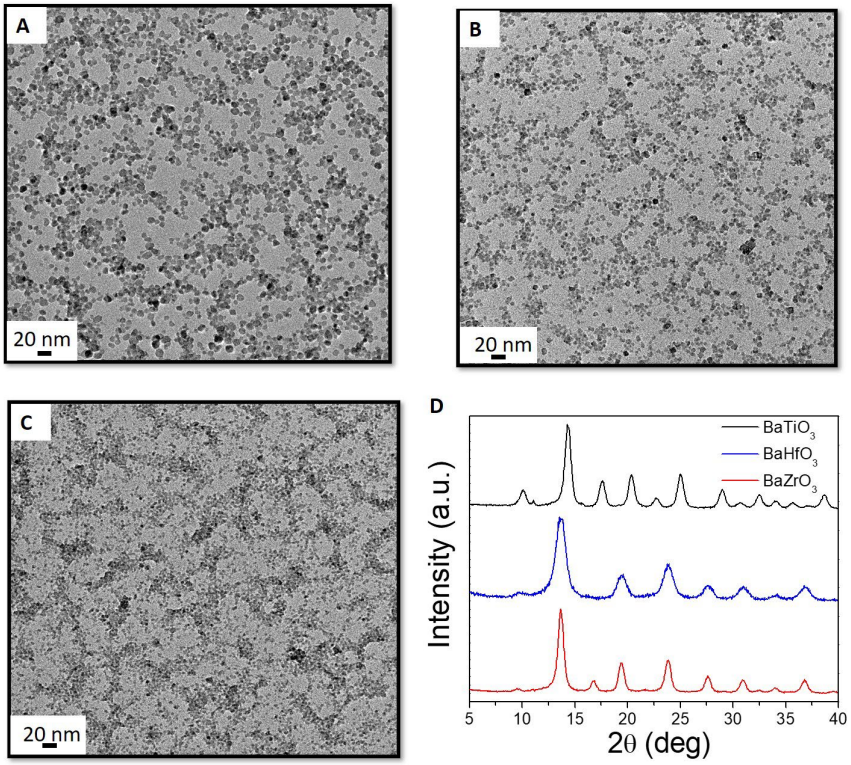

Figure 4.11. TEM images of $BaTiO_3$ (A), $BaZrO_3$ (B) and $BaHfO_3$ (C) NCs synthesised by using microwave activation, with a ramp of 36 °C/min and dwell during 5 minutes at 180 °C ($BaZrO_3$, $BaHfO_3$) and 100 °C ($BaTiO_3$). The methodology was made using 28 mmol of H_2O (D) the XRD patterns from the respective NCs.

After these results, both methodologies microwave and solvothermal show similar results regarding to size and crystal structure of NCs. The main difference is the reaction time, allowing a fast synthesis in microwave treatment in all three cases of 5 minutes.

4.3 Changing the divalent cation

Following the ability to exchanges the tetravalent cation from the perovskite structure, we aimed to prove the effect of changing the divalent cation using Sr^{2+} instead of Ba^{2+}.

By modifying this cation, it could lead to a distortion of the crystal structure, bestowing a new crystal phase. This effect appears as previously mention by the dependence of the crystal lattice with the ionic radii from each element. There is a reduction of the ionic radii from Ba^{2+}= 1.61 Å to Sr^{2+}= 1.44 Å, for that reason following the Equation (4.1) we can expect a distortion on the crystal structure. The Goldschmidt tolerance factor (t) in these cases, shows a $SrZrO_3$ and $SrHfO_3$ with a t= 0.95 (Table 4.7). This structure leads away from the ideal perovskite structure.

Nonetheless, the reduction of the ionic radius size in the case of $SrTiO_3$ perovskite makes a perfect match between the radius of Sr^{2+} and Ti^{4+} resulting on an ideal cubic structure with a tolerance factor of t= 1.

Table.4.7. Overview of the radii from each element of the different perovskites. all radii data has been taken from R.D Shannon.[16] The number on the parenthesis correspond to the coordination of the ion into the perovskite structure. Ionic radius of O^{2-} (IV) is 1.40 Å

Perovskites BMO_3	Ionic radius [Å]				Tolerance factor
	Cation B^{2+}		Cation M^{4+}		
$SrZrO_3$	Sr^{2+} (XII)	1.44	Zr^{4+} (VI)	0.72	0.95
$SrHfO_3$	Sr^{2+} (XII)	1.44	Hf^{4+} (VI)	0.71	0.95
$SrTiO_3$	Sr^{2+} (XII)	1.44	Ti^{4+} (VI)	0.61	1.00

The synthetic procedure followed was the same hybrid methodology, thus a $M(OBu)_4$ where (M = Ti^{4+}, Zr^{4+} and Hf^{4+}) was dissolved in absolute ethanol, then $Sr(OH)_2{\cdot}8\ H_2O$ was added and stirred until an homogeneous solution was formed. Finally, we add TREG and H_2O to the solution (water amount of 38 mmol). The mixed solution is transfer to a vessel and heated up to 100 °C for the $SrTiO_3$ and 180 °C for $SrZrO_3$ and $SrHfO_3$. In all three cases the temperature was kept for 1 hour.

4.3.1 $SrTiO_3$ NCs

We proved previously the successful achievement of NC formation following a cubic phase structure, in the case of $BaTiO_3$, $BaZrO_3$ and $BaHfO_3$. The crystal structure coincides with the cubic phase calculated for SrTiO in Table 4.7. A tolerance factor of t= 1 lead us to expect a successful achievement of SrTiO NCs by the implementation of the hybrid methodology.

The stable structure of $SrTiO_3$ is reflected in TEM images (Figure 4.12A), where it is shown a well-defined square-like shapes with an average size of 11.7 ± 2.4 nm and high crystallinity. In Figure 4.12B the HRTEM shows an isolated NC where it is easy to distinguish the planes, confirming the high crystallinity. The lattice distance measured from the diffraction rings with the SAED are in perfect agreement with the cubic phase (Pm-3m) of $SrTiO_3$ observed on XRD. It should be noticed the presence of some impurities identified as $SrCO_3$. These peaks suggest a 10% of impurity and it is identified with (*). Moreover, we obtained a monodisperse as-synthesized sample that remains stable on ethanol media for a long time. After 6 months there is no proof of agglomeration tendencies. The study of the stability is displayed in Figure 4.12C

showing a minimal shift on the DLS between the $SrTiO_3$ NCs as-synthesised and after 6 months.

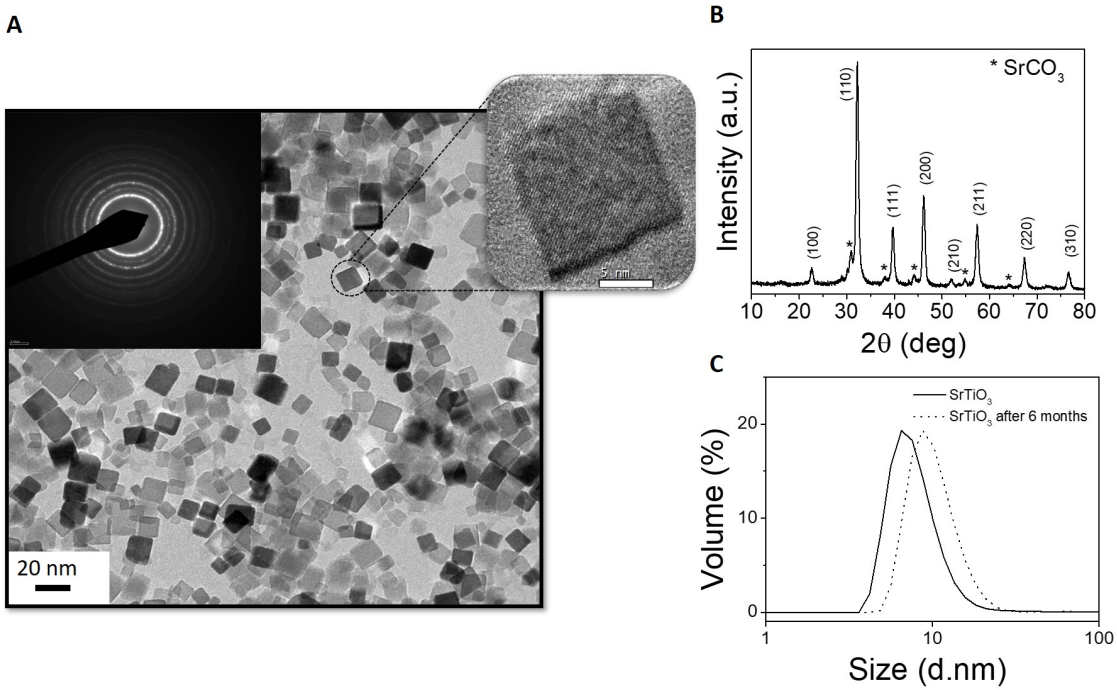

Figure 4.12. (A). TEM image of cubic-like shape $SrTiO_3$, SAED and a HRTEM image of an isolated particle. (B) XRD cubic patter of the $SrTiO_3$ where the * represents $SrCO_3$ peak suggesting a 10% of impurity. (C) DLS measurement, showing an stables NCs on ethanol for 6 months. $SrTiO_3$ pattern used from data base 00-005-0634.

4.3.2 $SrZrO_3$ and $SrHfO_3$ NCs

Contrarily, $SrZrO_3$ and $SrHfO_3$ show a tolerance factor t = 0.95, suggesting the possibility of some distortion in the lattice.

Analysing the $SrHfO_3$ sample by TEM analyisis we observe a sort of roods-like shape (Figure 4.13). However the XRD analysis show only evidence of $SrCO_3$.[48–51] This outcome suggests the formation of orthorhombic $SrCO_3$ NCs with roods-like shape instead of $SrHfO_3$ NCs.[48–51] The TEM analysis of the $SrZrO_3$ NCs (Figure 4.13) evidence an amorphous sample covered mostly by rests of organic remains on the sample. The XRD measurements shows an amorphous structure which confirms the findings of the SAED analysis. The substitution of divalent cation site, in this case, lead to a change in symmetry and crystalline phase. The synthetic route applied may not be efficient enough to deal with this distortion. Therefore, we are not able to synthesise these NCs using the hybrid methodology without more optimization. However, these

methodology shows to be compatible with those NCs who follow an ideal cubic phase structure (*i.e.,* $SrTiO_3$).

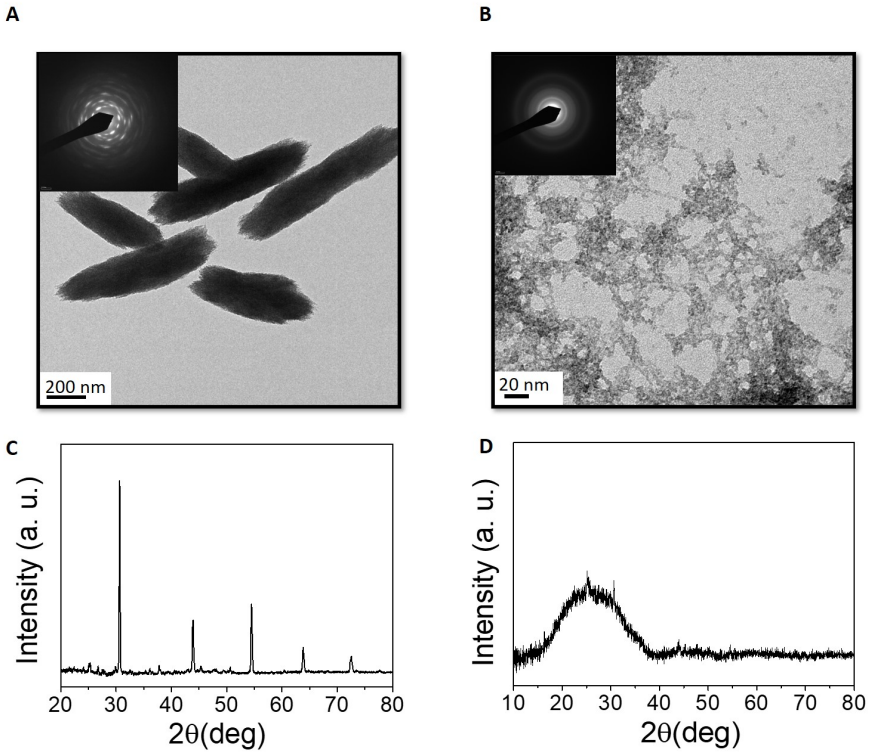

Figure 4.13. TEM image by the implementation of the hybrid methodology. (A) $SrHfO_3$ and (B) $SrZrO_3$ with their respective SAED. Below the XRD patterns from (C) the $SrHfO_3$ NCs and (D) $SrZrO_3$ NCs

4.4 Doped Barium Zirconate

Doping has been considered as a promising way to control the electronic, magnetic and optical properties of NCs.[52–57] The efficiency of the doping methodology has been reported mostly with transition metals ion and lanthanides.[53,54,58] Since $BaZrO_3$ NCs have been completely optimized, we have chosen these NCs to study the effect of Yttrium doping.

The increasing interest on the doped $BaZrO_3$ NCs relays especially on the application of these NCs in superconductivity. Nanocomposite superconductor films (Chapter 5) are made by a superconductor matrix and BMO_3 NCs as a secondary phase. In our case as you can further see in Chapter 5, the superconductor nanocomposite films are mostly formed by a ceramic matrix of $YBa_2Cu_3O_7$ and the BMO_3 NCs. Most of the studies were made using $BaZrO_3$ NCs, and what we have notice is that during the growth process of the nanocomposites the $BaZrO_3$ NCs seem to increase their size. One of the theories is that Y^{3+} from the $YBa_2Cu_3O_7$ matrix could

enter in the perovskites structure of the $BaZrO_3$ NCs, thus expanding the final sizes. As a solution to this issue we propose to dope the $BaZrO_3$ NCs with Y^{3+} up to 10%.

Doping $BaZrO_3$ is not new thing and it has proven to be promising when using Y^{3+} ions.[58,59] It has been shown that Y^{3+} ions compete for Zr^{4+} sites.[60,61] The doping of $BaZrO_3$ NCs with Y^{3+} was carry out by using the hybrid methodology. However, in this case the first step of the synthesis was to mix $Y(OiPr)_3$ and $Zr(OBu)_4$ in absolute ethanol, followed by the addition of $Ba(OH)_2{\cdot}8H_2O$ and stirring vigorously until complete homogenization of the solution. Finally, a posterior addition of TREG and water was added. The mixture is transferred to an autoclave and heat it up to 180 °C for 1 hour. To investigate the doping effect of Y^{3+}, different amount of of Y^{3+}respect to Zr^{4+} were used: 0, 5 and 10 % weight of Y^{3+} cation (Table 4.8).

Table 4.8. Composition of Y^{3+} an Zr^{4+} content on the doping as well as the diameter sizes of the NCs by TEM and Scherrer equation. Moreover, the lattice position of a (Å) is indicated.

$Y(OiPr)_3$ (mmol)	$Zr(OBu)_4$ (mmol)	Y^{3+}(%)	Size TEM (nm)	Scherrer size (nm)	a/ Å
-	2.80	0%	8.5 ± 1.2	8.2	4.205
0.14	2.66	5%	12.3 ± 2.4	11.5	4.230
0.28	2.52	10%	14.12 ± 3.9	14.0	4.244

According to TEM measurements (Figure 4.14), in all three cases we observed well formed NCs with a square-like shape. The average size of the NCs found by TEM measurements are: 8.5 nm, 12.3 nm and 14.12 nm in the case of doping with 0%, 5% and respectively 10% Y^{3+}. These results evidence a correlation between the sizes and the amount of Y^{3+} incorporated into the NCs structure.

To study the doping efficiency of Y^{3+} cations on the structure, an EDX spectra was performed (Figure 4.14). In the images E and F we can observed the Y^{3+} peaks by EDX measurements. Contrary, the D image represents the lack of Y^{3+} in the $BaZrO_3$ NCs structure. The EDX measurements and TEM analysis confirms the successful synthesis of Y^{3+} doped $BaZrO_3$ NCs. EDX show the peak of the Y^{3+} which starts appearing at doping the sample, getting more representative in those with more amount of Y^{3+}. With an effective atomic % percentage of Y^{3+} increasing on the EDX measurements while the doping amount increase.

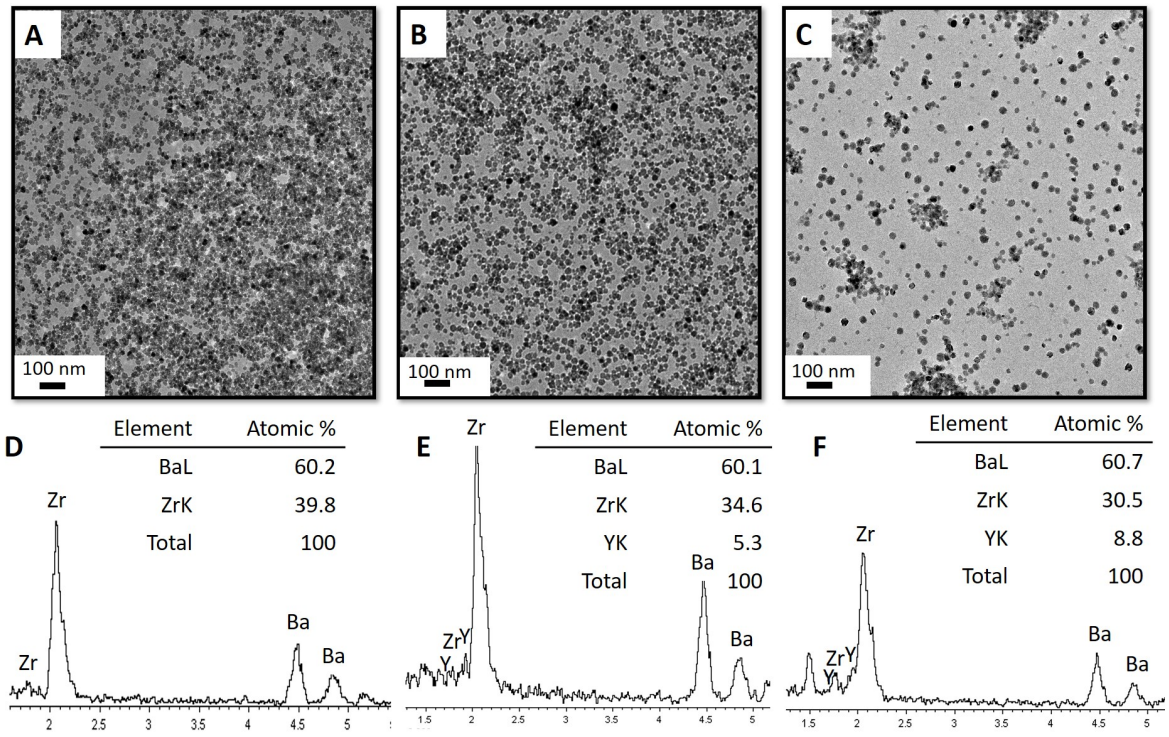

Figure 4.14. (A) $BaZrO_3$ non-doped (B) $BaZrO_3$ doped with 5% of $Y(OiPr)_3$ (C) $BaZrO_3$ doped with 10% weight of $Y(OiPr)_3$. Below EDX spectrums of each nanocrystal, showing the % atomic of each element. (D) NCs non-doped, (E) with a 5% of Y^{3+} and (F) doping with a 10% of Y^{3+}.

The XRD measurements are displayed in Figure 4.15. The patterns confirm the same cubic structure for all three samples and the increment on the NCs sizes as the amount of Y^{3+} increases. Undoped $BaZrO_3$ shows a lattice parameter of a = 4.205 Å and average NCs sizes of 8.2 nm. The lattice parameter increases to a = 4.229 Å after doping with 5% of Y^{3+}, and to a= 4.240 Å in the case of doping with 10% of Y^{3+}. The average crystal size calculated with Scherrer equation can be also found in Table 4.8.

A general trend can be notices by an increment of the Y^{3+} content, the lattice parameter *a, b, c* is increasing. This variation on the lattice parameters (Figure 4.15B) could be driven by various factors: an increment or decrement of the lattice structure (modifying the sizes) or the substitution of a Zr^{+4} atom for Y^{3+}atom. Zr^{4+} has an ionic radius of 0.73 Å while Y^{3+}has value of 0.9 Å. Consequently, the accommodation of Y^{3+} cation within the $BaZrO_3$ structure reflects in a lattice expansion, thus an increment of the lattice parameters.

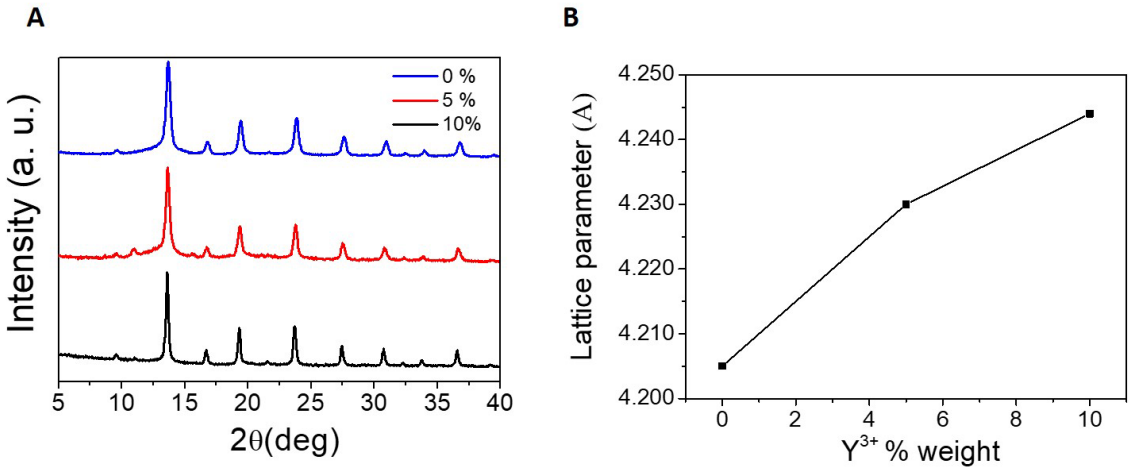

Figure 4.15. (A) Powder XRD pattern in all three cases, by doping at 0, 5 and 10 % amount of Y^{3+}. (B) evolution of the lattice parameters at increasing the Y^{3+}amount. XRD measurements have been done at Mo Kα radiation.

4.5 Conclusions

In summary, we not only present a suitable synthetic methodology for a group of NCs but also a general route that allow accurate control of the NC size of high-quality systems. This synthetic procedure has been expanded to the three tetravalent cations (*i.e.*, Ti^{4+}, Zr^{4+} and Hf^{4+}), as to the divalent cation (*i.e.*, Ba^{2+} to Sr^{2+}). This methodology shows an outstanding possibility to synthesise a wide range of materials from BMO_3 perovskite family, obtaining quality NCs.

Consequently, by changing the tetravalent cation we obtained $BaTiO_3$ and $BaHfO_3$ NCs, with a cubic structure in both cases, high crystalline, small sizes and monodisperse NCs. The temperature and time effect on the reaction suggest a similar behaviour between Zr^{4+} and Hf^{4+} with an optimal temperature of 180 °C. Contrarily, $BaTiO_3$ shows a different reaction temperature (100 °C) suggesting a different growth process compared with the other two perovskites.

To study how to control the NC sizes of these perovskite NCs, we focus on the $BaZrO_3$ postulation, where NC sizes are tailored by controlling the amount of water (hydrolytical step). $BaHfO_3$ follows this approximation showing a linear dependence with the water amount of the final NC sizes. This result corroborates the hydrolysis-polycondensation process on the sol-gel reaction as the main parameter to control the NCs size. In contrast, $BaTiO_3$ does not support this outcome. Independently of the amount of water used, the NCs size remains constant.

In the case of $BaTiO_3$ the parameter that controls the sizes of the NCs has turn out to be the precursors amounts. In order to clarify the final cubic crystal structure

of $BaTiO_3$ we evidenced the lack of tetragonal phase by using a complimentary analysis of XRD via RAMAN spectrometry.

Concerning the divalent cations, the exchange of Ba^{2+} with Sr^{2+} can lead to changes in the final crystalline structure. In the case of $SrTiO_3$ with a tolerance factor of t= 1, the synthesis was successfully achieved showing an ideal cubic phase with high crystallinity, sizes of 12 nm and high stability in ethanol media. Nonetheless, these results differ in the case of $SrZrO_3$ and $SrHfO_3$. In these cases, more optimization is needed. These experimental data suggest a better efficiency for our hybrid methodology to those systems that show an ideal cubic structure, rather than those showing a lattice distortion.

In addition, Y^{3+}doped $BaZrO_3$ NCs synthesized by our hybrid methodology has proved to be a success up to 10%. The next step is to use these doped NCs in the growth of nanocomposites. This promising finding brings us the possibility of doping the perovskites with a new range of ions (lanthanides, metals, etc.) bestowing new promising materials with new physicals and chemistry properties.[53,54]

4.6 References

1 C. J. Bartel, C. Sutton, B. R. Goldsmith, et al., *Sci. Adv.*, 2019, **5**, 1–10.

2 D. I. Woodward and I. M. Reaney, *Acta Crystallogr. Sect. B Struct. Sci.*, 2005, **61**, 387–399.

3 P. C. Reshmi Varma, *Low-dimensional perovskites*, Elsevier Inc., 2018.

4 J. B. Goodenough, *Reports Prog. Phys.*, 2004, **67**, 1915–1993.

5 M. H. K. Rubel, T. Takei, N. Kumada, et al., *Inorg. Chem.*, 2017, **56**, 3174–3181.

6 J. Luo, M. Hu, G. Niu and J. Tang, *ACS Appl. Mater. & Interfaces*, 2019, **11**, 31575–31584.

7 M. A. Peña and J. L. G. Fierro, *Chem. Rev.*, 2001, **101**, 1981–2018.

8 R. Mouta, R. X. Silva and C. W. A. Paschoal, *Acta Crystallogr. Sect. B Struct. Sci. Cryst. Eng. Mater.*, 2013, **69**, 439–445.

9 B. Jiang, J. Iocozzia, L. Zhao, et al., *Chem. Soc. Rev.*, 2019, **48**, 1194–1228.

10 N. F. Atta, A. Galal and E. H. El-Ads, in *Perovskite Materials*, eds. L. Pan and G. Zhu, IntechOpen, Rijeka, 2016.

11 N. N. GREENWOOD and A. EARNSHAW, Eds., in *Chemistry of the Elements (Second Edition)*, Butterworth-Heinemann, Oxford, Second Edi., 1997, pp. 954–975.

12 M. B. Smith, K. Page, T. Siegrist and A. Et, *J. Am. Chem. Soc.*, 2008, **130**, 6955–

6963.

13 D. Caruntu, T. Rostamzadeh, T. Costanzo, S. Salemizadeh Parizi and G. Caruntu, *Nanoscale*, 2015, **7**, 12955–12969.

14 S. Adireddy, C. Lin, B. Cao, W. Zhou and G. Caruntu, *Chem. Mater.*, 2010, **22**, 1946–1948.

15 M. Niederberger, G. Garnweitner, N. Pinna and M. Antonietti, *J. Am. Chem. Soc.*, 2004, **126**, 9120–9126.

16 R. D. Shannon, *Acta Crystallogr. Sect. A*, 1976, **32**, 751–767.

17 N. A. Benedek and C. J. Fennie, *J. Phys. Chem. C*, 2013, **117**, 13339–13349.

18 S. S. Parizi, A. Mellinger and G. Caruntu, *ACS Appl. Mater. Interfaces*, 2014, **6**, 17506–17517.

19 J. Van Embden, A. S. R. Chesman and J. J. Jasieniak, *Chem. Mater.*, 2015, **27**, 2246–2285.

20 R. R. Schrock and G. W. Parshall, *Chem. Rev.*, 1976, **76**, 243–268.

21 Y. D. Wu, Z. H. Peng, K. W. K. Chan, X. Liu, A. A. Tuinman and Z. Xue, *Organometallics*, 1999, **18**, 2081–2090.

22 U. Schubert, in *The Sol-Gel Handbook*, Wiley-VCH Verlag GmbH & Co. KGaA, Weinheim, Germany, 2015, pp. 1–28.

23 A. Vioux, *Chem. Mater.*, 1997, 9, 2292–2299.

24 R. Azouani, A. Soloviev, M. Benmami, K. Chhor, J.-F. Bocquet and A. Kanaev, *J. Phys. Chem. C*, 2007, **111**, 16243–16248.

25 S. Labidi, Z. Jia, M. Ben Amar, K. Chhor and A. Kanaev, *Phys. Chem. Chem. Phys.*, 2015, **17**, 2651–2659.

26 J. Owen, *Science (80-.).*, 2015, **347**, 615–616.

27 M. A. Boles, D. Ling, T. Hyeon and D. V. Talapin, *Nat. Mater.*, 2016, **15**, 364.

28 U. Schubert, E. Arpac, W. Glaubitt, A. Helmerich and C. Chau, *Chem. Mater.*, 1992, **4**, 291–295.

29 A. Kumar, S. De, A. G. Samuelson and E. D. Jemmis, *Organometallics*, 2008, **27**, 955–960.

30 In *The Chemistry of Metal Alkoxides*, Kluwer Academic Publishers, Boston, 2006, pp. 107–125.

31 N. Nuraje and K. Su, *Nanoscale*, 2013, **5**, 8752–8780.

32 V. Bansal, P. Poddar, A. Ahmad and M. Sastry, *J. Am. Chem. Soc.*, 2006, **128**, 11958–11963.

33 N. Artrith, W. Sailuam, S. Limpijumnong and A. M. Kolpak, *Phys. Chem. Chem. Phys.*, 2016, **18**, 29561–29570.

34 P. N. Nikolarakis, I. A. Asimakopoulos and L. Zoumpoulakis, *J. Nanomater.*, 2018, **2018**, 7023437.

35 M. Acosta, N. Novak, V. Rojas, et al., *Appl. Phys. Rev.*, 2017, **4**, 41305.

36 D. Popovici, M. Okuyama and J. Akedo, in *Ferroelectrics*, ed. M. Lallart, IntechOpen, Rijeka, 2011.

37 M. M. Vijatovic Petrovic, J. D. Bobic and B. D. Stojanovic, in *Magnetic, Ferroelectric, and Multiferroic Metal Oxides*, ed. B. D. Stojanovic, Elsevier, 2018, pp. 545–557.

38 C. Burda, X. Chen, R. Narayanan and M. A. El-Sayed, *Chem. Rev.*, 2005, **105**, 1025–1102.

39 Y. Jun, J. Choi and J. Cheon, *Angew. Chemie Int. Ed.*, 2006, **45**, 3414–3439.

40 S. Haussühl, *Berichte der Bunsengesellschaft für Phys. Chemie*, 1974, **78**, 1276.

41 G. Dhanaraj, K. Byrappa, V. Prasad, M. Dudley and K. Schmetzer, *Springer Handbook of Crystal Growth*, 2010, vol. 39.

42 K. A. Jackson, in *Changes of State*, ed. N. B. Hannay, Springer US, Boston, MA, 1975, pp. 233–282.

43 J.-P. Andreassen and A. E. Lewis, in *New Perspectives on Mineral Nucleation and Growth: From Solution Precursors to Solid Materials*, eds. A. E. S. Van Driessche, M. Kellermeier, et al., Springer International Publishing, Cham, 2017, pp. 137–154.

44 K. Huang, L. Yuan and S. Feng, *Inorg. Chem. Front.*, 2015, **2**, 965–981.

45 H. Zhan, X. Yang, C. Wang, et al., *Cryst. Growth & Des.*, 2012, **12**, 1247–1253.

46 H. Hayashi, T. Nakamura and T. Ebina, *J. Phys. Chem. Solids*, 2013, **74**, 957–962.

47 G. Yang, Z. Yue, T. Sun, J. Zhao, Z. Yang and L. Li, *Appl. Phys. A Mater. Sci. Process.*, 2008, **91**, 119–125.

48 B. J. Kennedy, C. J. Howard and B. C. Chakoumakos, *Phys. Rev. B - Condens. Matter Mater. Phys.*, 1999, **60**, 2972–2975.

49 M. Karmaoui, E. V. Ramana, D. M. Tobaldi, et al., *RSC Adv.*, 2016, **6**, 51493–51502.

50 P. De La Presa, R. E. Alonso, A. Ayala, et al., *J. Phys. Chem. Solids*, 1999, **60**, 749–757.

51 P. De La Presa and A. L. García, *J. Korean Phys. Soc.*, 1998, **32**, 1–3.

52 Y. Yang, Y. Jin, H. He, et al., *J. Am. Chem. Soc.*, 2010, **132**, 13381–13394.

53 G. Pan, X. Bai, D. Yang, et al., *Nano Lett.*, 2017, **17**, 8005–8011.

54 K. Kanie, Y. Seino, M. Matsubara, M. Nakaya and A. Muramatsu, *New J. Chem.*, 2014, **38**, 3548–3555.

55 G. Nedelcu, L. Protesescu, S. Yakunin, M. I. Bodnarchuk, M. J. Grotevent and M. V. Kovalenko, *Nano Lett.*, 2015, **15**, 5635–5640.

56 B. Zhou, B. Shi, D. Jin and X. Liu, *Nat. Nanotechnol.*, 2015, **10**, 924–936.

57 P. Ayala, R. Arenal, M. Rümmeli, A. Rubio and T. Pichler, *Carbon N. Y.*, 2010, **48**, 575–586.

58 Y. Yamazaki, R. Hernandez-Sanchez and S. M. Haile, *J. Mater. Chem.*, 2010, **20**, 8158–8166.

59 Y. Yamazaki, F. Blanc, Y. Okuyama, et al., *Nat. Mater.*, 2013, **12**, 647–651.

60 M. S. Islam, P. R. Slater, J. R. Tolchard and T. Dinges, *Dalt. Trans.*, 2004, **3**, 3061–3066.

61 Y. Yamazaki, F. Blanc, Y. Okuyama, et al., *Nat. Mater.*, 2013, **12**, 647–651.

5

Nanocomposites of $YBa_2Cu_3O_{7-\delta}$ layers

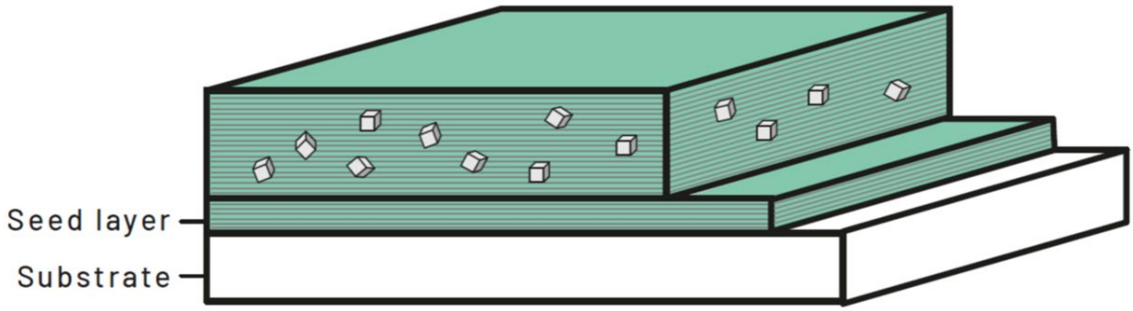

This chapter is focused on the applicability of the as-synthesised NCs, $BaZrO_3$ and $BaHfO_3$, obtained as described in the previous chapters. Using these NCs we have successfully achieved high quality $YBa_2Cu_3O_{7-\delta}$ nanocomposites.

In order to ensure a stable and well dispersed $YBa_2Cu_3O_{7-\delta}$ nanocomposite precursor solutions, the influence of concentration of NCs (from 12% - 20%mol), size of the NCs (between 5 nm–10 nm) and the composition ($BaMO_3$; M= $Zr^{4+,}$ Hf^{4+}) have been thoroughly studied. Once the precursor solutions meet all the requirements, we proceed to the deposition and growth of $YBa_2Cu_3O_{7-\delta}$ nanocomposites. Our results show a homogeneous distribution of the NCs among the $YBa_2Cu_3O_{7-\delta}$ matrix, preserving their sizes and shape. The $YBa_2Cu_3O_{7-\delta}$ nanocomposites are highly epitaxial and no proof of reactivity between NCs and $YBa_2Cu_3O_{7-\delta}$ matrix was found. Moreover, by using these types of NCs we have achieved $YBa_2Cu_3O_{7-\delta}$ nanocomposites with enhanced superconducting properties.

Adapted from: (A) X. Obradors, T. Puig, Z. Li, et al., *Supercond. Sci. Technol.*, 2018, **31**, 044001. Z. **(B)** Li, M. Coll, B. Mundet, et al., *Sci. Rep.*, 2019, **9**, 1–14. **(C)** L. Soler, J. Jareño, J. Banchewski, et al., *Nat. Commun.*, 2020, **11**, 344.

5.1 Introduction

As already mentioned in the introduction (Chapter 1) by adding NCs to the REBCO (RE = rare earths) matrix we can enhance the superconducting properties which make them quite attractive for power system applications.[1,23] Different oxide NCs have been reported to be exceptional candidates for this purpose. [4–6] The implementation of the NCs into the superconductor matrix is a challenging process, because of the necessity to have a tight control of the size, reactivity and distribution in the REBCO matrix.[6,7] However, most of the common oxide NCs previously tested suffer reactivity or instability in the REBCO matrix (*i.e.,* CeO_2, ZrO_2 and $CoFe_2O_4$).[6,8,9] Nonetheless, it has been reported that binary perovskites like $BaZrO_3$ and $BaHfO_3$ or ternary perovskites such as Ba_2YTaO_6 and Ba_2YNbO_6 seem to be suitable candidates because they do not react during the formation of the REBCO ceramic matrix.[4–6]

Chemical Solution Deposition (CSD) has become one of the most useful methods to obtain REBCO superconducting layers. CSD highlights are due to their low capital investment and low-cost production leading to more scalable and quicker process compared with other physical and chemical deposition methods. In addition, this method has proved to be also very compatible with the formation of REBCO nanocomposites.[6,9–11] The CSD is divided in two main processes: spontaneous segregation approach and preformed NCs approach (Figure 1.6). In the spontaneous segregated process, the NCs precursors are added to the REBCO precursors solution. The NCs are formed during the growth process of REBCO nanocomposites. However, the spontaneous segregation lacks control over the sizes, sizes distribution and the stoichiometry the NCs. All these limitations lead to poor reproducibility of the results.[6,9,10,12] In this work, we follow the preformed NCs approach. Since the NCs are previously synthesised with very good control on the NCs sizes and shape.

The schematic illustration in Figure 5.1 shows the different stages of CSD nanocomposite process. The first stage consists in the addition of the NCs to the REBCO salt precursors solution. It is important that the preformed NCs have a high stability in the REBCO precursors solution. This will lead to homogeneously distributed NCs in the REBCO matrix after the growth process of the nanocomposite. (Figure 5.1 stage I). Second, the colloidal solution is deposited onto a substrate. Different deposition techniques can be used to produce the nanocomposite layers. Among them the used techniques in our laboratories are spin-coating and inkjet printing. Spin-coating allows us a fast and easy deposition at lab scale. The thickness of the nanocomposite layers will depend on the rheological properties and concentration of the colloidal solution, the rotation

speed of the spinner and the time of spinning used.[13,14] This methodology usually allows us to achieve a thickness of around 150 nm. Using spin coating deposition, thick layers of around 350 nm can be also produced by multiple deposition approach. On the other hand, Ink-jet Printing (IJP) is suitable to obtain thicker films of around 1 μm from one single deposition.[15,16]

Once the solution has been successfully deposited, two heat treatment are used to achieve the orthorhombic structure of REBCO nanocomposite layers. The first heat treatment is called pyrolysis and it is performed at low temperatures (max. 500 °C). During the pyrolysis the organic part is decomposed and the oxide and fluorine or carbonate phases are formed. After the pyrolysis, a second heating treatment at high temperatures (~800 °C) was performed where the sample is grown and oxygenated. The optimization of these processes (*i.e.*, temperature, pressure, oxygenation) is mandatory to ensure a highly epitaxial nanocomposite REBCO layer with good superconducting properties.

Following this approach, we achieve nanocomposites layers with high epitaxy, with the NCs randomly oriented, homogeneously distributed in the REBCO matrix.

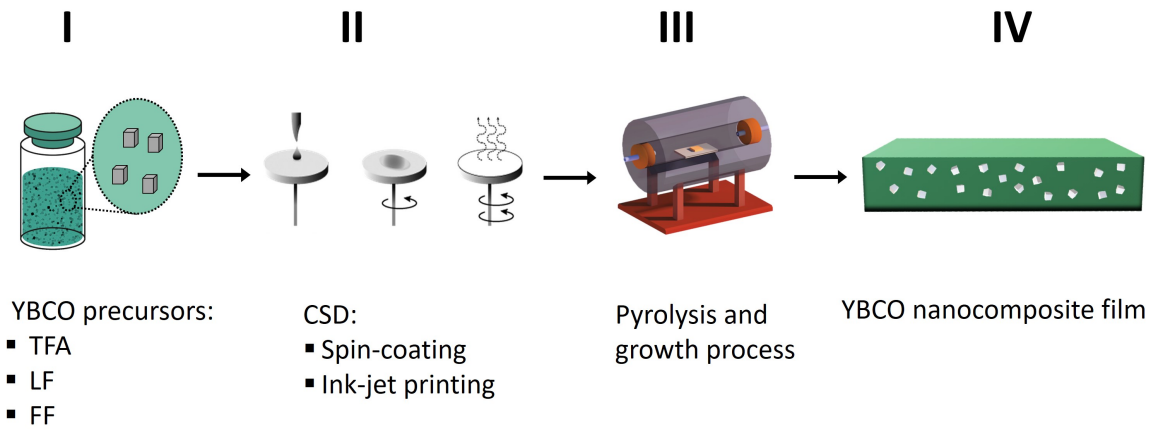

Figure 5.1 Schematic illustration of the different stages for the fabrication of REBCO nanocomposite film. Stage (I) NCs stabilization on the REBCO precursor solution. Stage (II) chemical solution deposition in a substrate via spin-coated or ink-jet printing. Stage (III) thermal treatment to crystallize REBCO/NCs by a pyrolysis and posterior growing process to obtain the final REBCO nanocomposite film (Stage IV).

In this thesis, the NCs that we have chosen are $BaZrO_3$ and $BaHfO_3$. These perovskites have been previously tested using the methodology of spontaneous segregation approach,[3,5,17–19] suggesting promising results. However, the lack of control over the NCs limits the possibility to enhance the superconducting properties. For that reason, applying the preformed NCs approach could bring outstanding progress in this field.

The main optimization of this work (the optimization of the growth process and the physical measurements) has been carrying out with the collaboration of the SUMAN group from ICMAB lead by Prof. Dr T. Puig.

5.2 Stability of the NCs onto YBCO precursor solution

The REBCO chosen for this work is $YBa_2Cu_3O_{7-\delta}$ (YBCO). The NCs have been mixed with three different YBCO precursor solutions; Trifluoroacetate precursor solution (TFA), Low Fluorine (LF) and Fluorine free (FF).

The most used YBCO precursor solution so far was the TFA-YBCO precursor solution.[20] The precursor salts are yttrium, barium and copper trifluoroacetates.[21,22] Due to the high toxicity of the HF formed during the decomposition and growth process of the YBCO nanocomposites, different approaches with lower amount of fluorine have been developed.[23–25] LF-YBCO reduces drastically the amount of fluorine by using yttrium trifluoroacetate as the only source of fluor. The other two precursor salts were Cu^{2+} and Ba^{2+} acetates. Recently promising results have been achieved using fluorine free precursor solutions. This type of solutions has zero content of fluorine, therefore there are no toxic fluorinated by-products.[11,24,26]

In Chapter 3 and 4, it was reported the synthesis of $BaMO_3$ (M= Zr^{4+}, Hf^{4+}) showing the control over the sizes and crystal structure. In this incoming section, the homogeneity and stability of the NCs in solution are studied.

As mentioned in Chapter 4, the stability of the NCs ($BaZrO_3$ and $BaHfO_3$) in ethanol were monitored by DLS for 6 months (Fig 4.2). The data emerging from these measurements confirms a stable solution for long time, showing a slight shift of the DLS peak (from a hydrodynamic diameters d_H=9 nm to d_H= 11 nm in the case of $BaZrO_3$, and a shift from d_H= 8 nm to d_H= 10 nm in the case of $BaHfO_3$). During this period, it was not observed any sedimentation of large aggregates by either DLS data or visual inspection.

DLS analysis reveals that the NCs remain highly dispersible and stable in alcohol media for long periods of time even in concentrations up to 110 mM. As an example, in Figure 5.2B is presented the TEM image of these $BaZrO_3$ NCs in EtOH after 6 months. TEM analysis confirms the sizes of the NCs with 8.8 ± 1.7 nm revealed by DLS measurement and also shows not changes from the standard as-prepared NCs. Therefore, no agglomeration of the NCs is detect after 6 months.

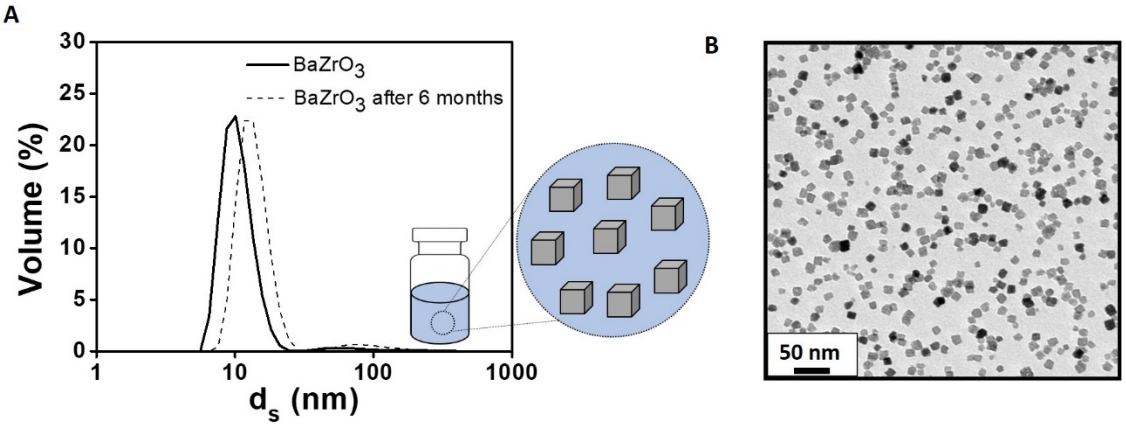

Figure 5.2 (A) DLS stability study of the as-synthesized $BaZrO_3$ NCs on the first day after the synthesis and 6-month post-synthesis in ethanol. (B) TEM image of $BaZrO_3$ solution in ethanol media after 6 months.

5.2.1. TFA-YBCO precursor solution

The stability study of colloidal YBCO precursors solution was focused on the influence of; (i) nanocrystals sizes (5-10 nm), (ii) concentration (12-25 mol%) and (iii) nanocrystals composition ($BaZrO_3$ and $BaHfO_3$).

In the case of TFA-YBCO precursor solutions both $BaZrO_3$ and $BaHfO_3$ have been studied. The solution consisted of a mixture of Y^{3+}, Ba^{2+} and Cu^{2+} trifluoroacetates in concentrations of around 1.5 M (∑ Metals) and with methanol as solvent. We next present in detail the results obtained using $BaZrO_3$ NCs and then we compare with the results obtained using $BaHfO_3$.

Different concentrations (*i.e.*, 12 and 25 mol%) of $BaZrO_3$ NCs with an average size of 10 nm were mixed with the as-prepared TFA-YBCO precursors solution.

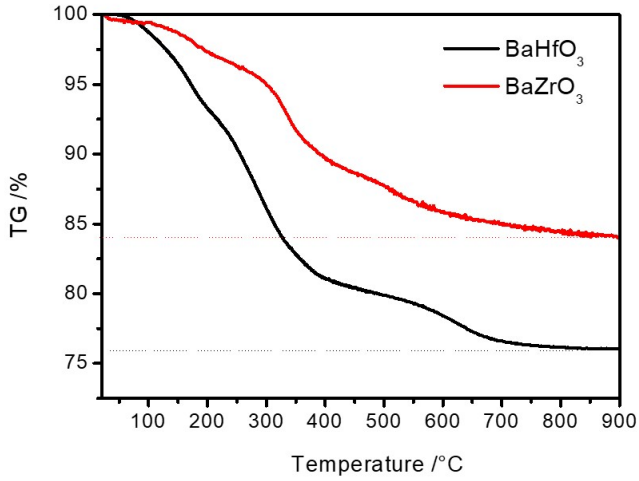

Figure 5.3. TGA measurement from the organic matter of $BaZrO_3$ and $BaHfO_3$ powered.

Previously a thermogravimetric analysis (TGA) was performed to quantify the organic matter on the NCs surface. The TGA analysis was performed under air atmosphere up to 900 °C with a heating rate of 10 °C/min. The results in Figure 5.3 show a different organic loss for the two perovskites. $BaHfO_3$ show a weight loss of 25% and the $BaZrO_3$. has a weight loss of 15%. These results were used to recalculate the final concentration of the NCs to be used in the preparation.

Figure 5.4A represents the steps taken to prepare the TFA-YBCO colloidal precursor solution. The result is a colloidal YBCO precursor solution with stable NCs. The stability was checked in time by means of TEM and DLS analysis. In our particular case, the stability study consists in: a study of the colloidal system in highly salt content environments like YBCO precursor solution (Figure 5.4A).

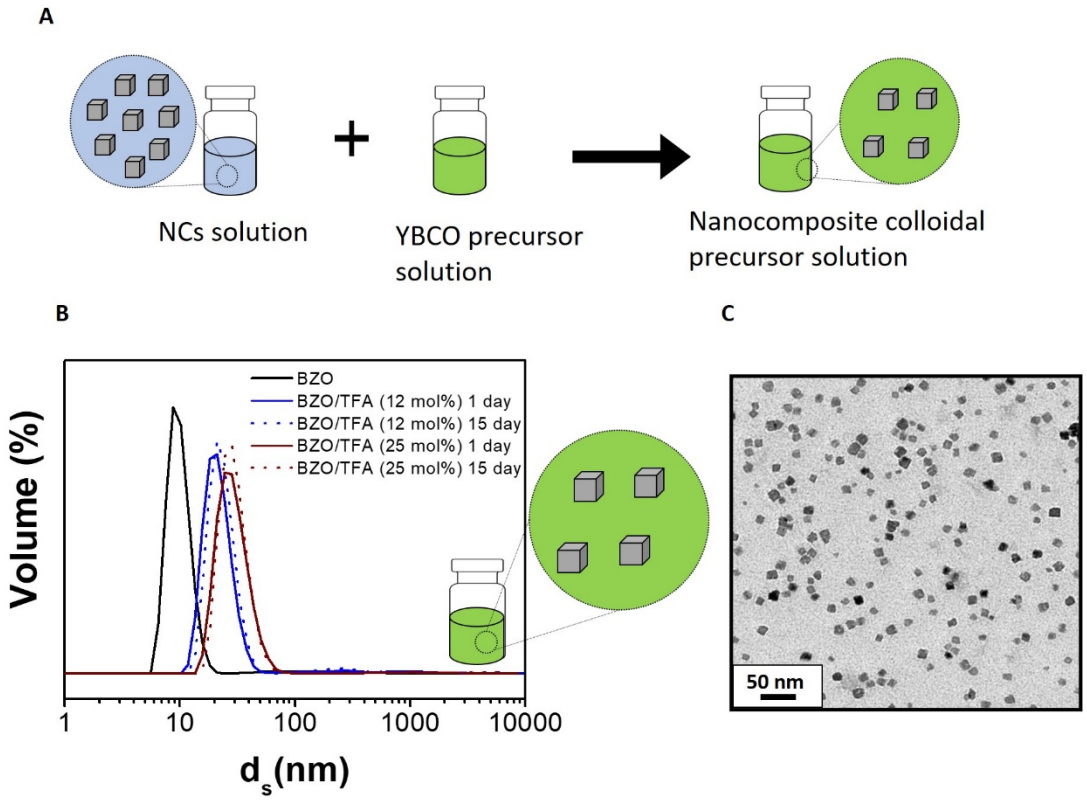

Figure 5.4. (A) Schematic representation in which solution of NCs ($BaZrO_3$ and $BaHfO_3$) in ethanol are introduced to the YBCO precursor solution (metallic salts dissolved in methanol) to finally obtaining the nanocomposite colloidal precursor solution. (B) DLS measurement at 12 and 25 mol% of $BaZrO_3$ (BZO) (10 nm) on TFA -YBCO precursors solution showing a stable colloidal solution for 15 days in both cases. (C) TFA-YBCO solution with $BaZrO_3$ NCs showing a TEM image of the solution $BaZrO_3$ NCs/TFA-YBCO (10 nm NCs at 12 mol% and 25 mol%)

In TFA colloidal solution the DLS is presented in Figure 5.4B. Initially shows d_H =9 nm of the NCs ethanolic solution, the measurement shift to higher $d_H \approx 20$ nm when mixing 12 mol% NCs with TFA precursor solution, and to $d_H \approx 24$ nm

when mixing 25 mol% YBCO precursor solution. This can be explained by the presence of yttrium, barium and cooper salts in the YBCO precursor solution. The increase of salt concentration can produce an increase of the hydrodynamic diameter of the NCs (*i.e.,* ionic molecules interacting with the NCs surface). The TEM image confirms that the NCs stability is very high even after 15 days and no changes in size are detected independently of the concentration of NCs. Showing an average size of 9.1 ± 1.7 nm. Besides no agglomeration of NCs were found even after 15 days. This demonstrate that DLS shift to bigger size is only produced by the salt environment interactions and not for agglomeration of the NCs.

Similar results have been obtained in the case of $BaHfO_3$ as it can be seen in Figure 5.5. $BaHfO_3$ NCs at sizes of 10 nm in 12 and 25 mol% leads to a slight shift from the d_H=9 nm to d_H=28 nm.

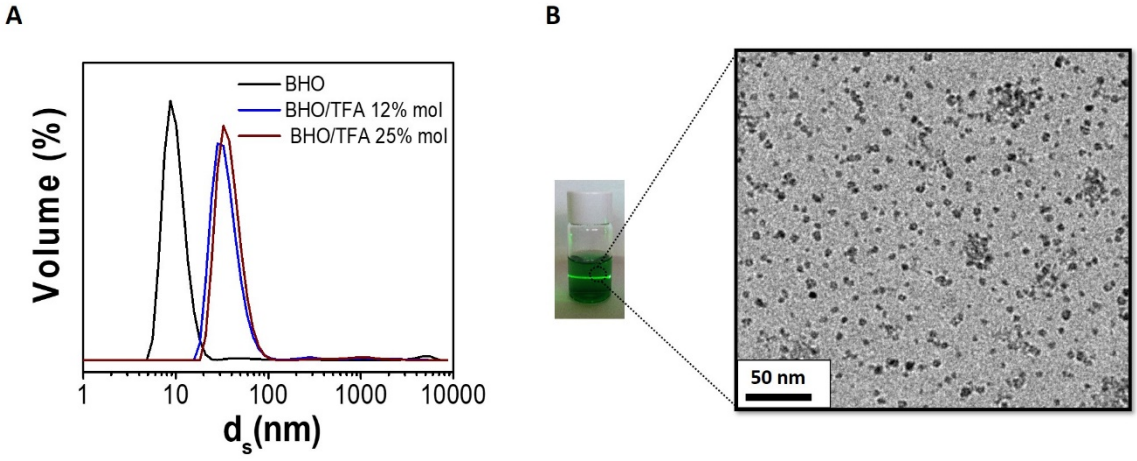

Figure 5.5. DLS measurement at different concentration of NCs 12 and 25 mol% after 15 days of mixing; $BaHfO_3$ (BHO) NCs with a sizes of 10 nm mixed with YBCO-TFA precursors solution and (B) YBCO colloidal solution showing a typical Tyndall effect confirming the presence of NCs onto the YBCO precursor solution and the corresponding the TEM image of the solution $BaHfO_3$/YBCO-TFA (10 nm NC at 12 mol%).

Since the ability to tailoring the NCs sizes was demonstrated in previous chapters, a parallel study of the NCs with the sizes of 5 nm was performed in order to verify if the size could be a factor of the NCs stability in the YBCO colloidal precursor solution. The stability was checked over 15 days after the preparation of the colloidal YBCO precursor solution. The stability study was done with $BaZrO_3$ NCs showing an average sizes of 5 nm (Figure 5.6A). Two concentration of $BaZrO_3$ NCs were used 12 mol% and 25 mol%. From Figure 5.6A we can conclude that neither the concentration or reducing the size of the NCs affects the stability through time of the TFA-YBCO colloidal precursor solutions. The DLS peak in this case shifts from 5 nm to 20 nm both for 12 mol% and 25 mol%. The reason why the hydrodynamic diameter of the NCs seem to be bigger in YBCO colloidal solution

was previously explained. Independently of the $BaZrO_3$ NCs concentration in the YBCO colloidal solutions we cannot detect any agglomeration tendencies with time. The stability was studied also for the $BaHfO_3$ with an average sizes of 5 nm using the same concentrations as in the case of $BaZrO_3$ NCs. A shift from d_H = 4 nm to d_H = 21 nm is observed in the DLS spectra for both concentrations of NCs. TEM measurements corroborated a non-increment in NCs sizes after mixing the NCs with the YBCO precursors solution with a values of 5.4 ± 1.2 nm in the case of $BaZrO_3$ NCs and 4.6± 0.8 nm in the case of $BaHfO_3$ NCs.

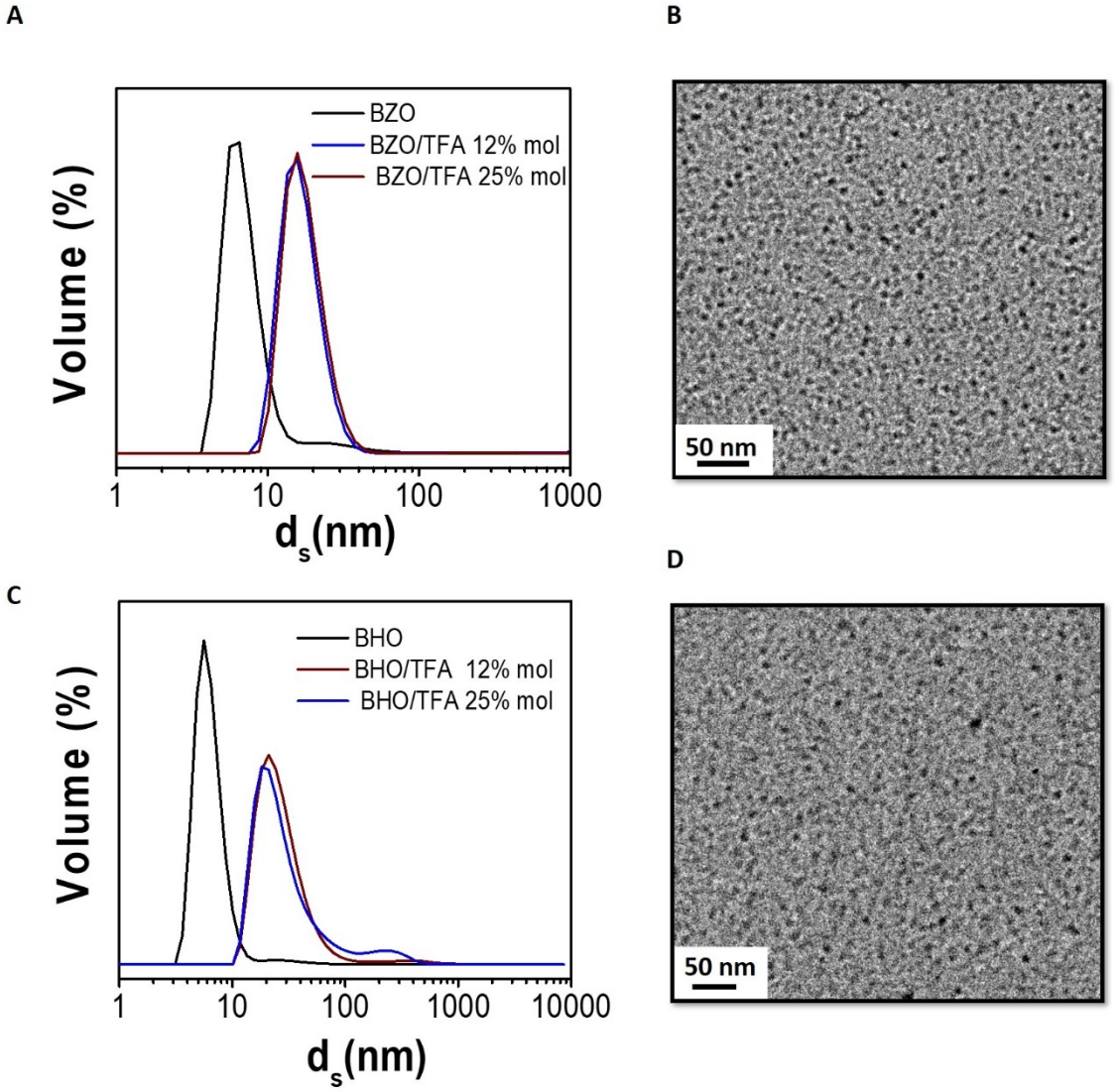

Figure 5.6. DLS measurement at different concentration of NCs 12 and 25 mol% after 15 days of mixing; (A) $BaZrO_3$ (BZO) NCs with an average sizes of 5 nm mixed with TFA-YBCO precursors solution, (B) TEM image of the previous solution mentioned.(C) $BaHfO_3$ (BHO) NCs with a sizes of 5 nm mixed with TFA-YBCO solution precursors and (D) TEM image of $BaHfO_3$ (BHO) NCs with a sizes of 5 nm mixed with TFA -YBCO solution precursors.

In consequence, we can conclude that neither the concentration (up to 25 mol%) or the smaller size of the NCs have a significant influence on the stability through time of NCs in the TFA-YBCO colloidal precursor solution.

Moreover, a graph with the Z-average values was displayed in Figure 5.7. The plot shows initially Z-average values ~40 nm corresponding to the NCs, $BaZrO_3$ and $BaHfO_3$ in ethanol media. After mixing the NCs with the YBCO precursor solutions a very rapid increment in Z-average value appears due to the influence of the YBCO precursor salts in the media. The Z-average value start to drop with time (hours) revealing an increase in stability of the NCs in the YBCO colloidal precursor solution (Figure 5.7).

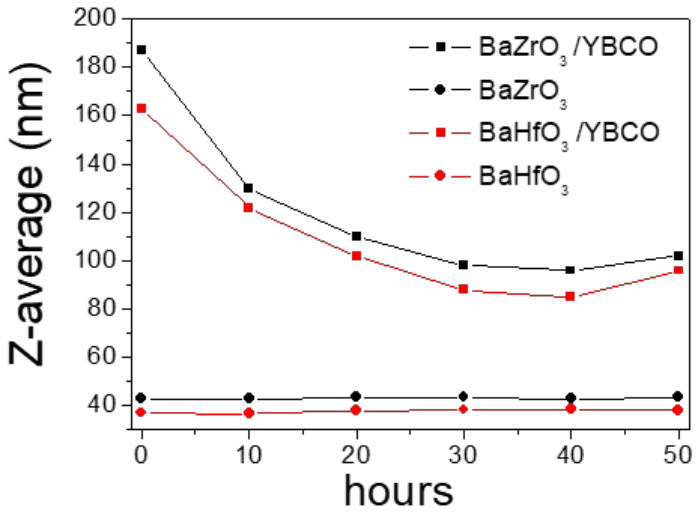

Figure 5.7. Feedback Z-average values during 50 hours of $BaZrO_3$ (5 nm) and $BaHfO_3$ (5 nm) in ethanol media and after mixed 12 mol% of NCs into TFA-YBCO precursor solution.

In order to achieve the best results, we have decided that after the preparation of the YBCO colloidal solution it is best to use the colloidal solution after some hours rest when maximum stability is reached (*i.e.,* 20-30 hours).

5.2.2 LF-YBCO and FF-YBCO precursors solution

YBCO Low Fluorine and Fluorine free solutions were studied in our laboratories to develop a more environmentally friendly and less toxic solutions, thus better suited for industrial production.[11,24,26]

The initial solutions consisted of a mixture of Y^{3+} trifluoroacetate, and Ba^{2+} and Cu^{2+} acetates in concentrations of around 1.5 M (of all the metals) for the Low Fluorine (LF) and with a mixture of methanol and propionic acid (70/30) as solvents. For the FF-YBCO Y^{3+}, Ba^{2+} and Cu^{2+} acetates are used with a similar mixture of solvents and similar concentrations.

The replacement of $Cu(CF_3COO)_2$ for $Cu(CH_3COO)_2$ salts affects the final colour of the colloidal precursors solution, leading to a blue colour solution. DLS

is a light-scattering tool, and in this precise case show some limitation with wavelength of the blue colour from the colloidal solution. The wavelength of blue colour interferes with the wavelength of the equipment that could lead to errors in detection. For solving this problem instead of using copper salt it was substituted by zinc salts to keep the ionic environment on the solution similar and be able to check the stability through DLS measurements.

Furthermore, the implementation of these two approaches of YBCO precursors solution defers from TFA-YBCO on the use of propionic acid and some additives: ethanolamine (EA) and triethanolamine (TEA). The new solutions have different pH that can affect the NCs surface. This could lead to changes in the stability of the NCs in the new YBCO colloidal precursor solutions.

For these reasons, stability studies have been performed in the case of LF-YBCO colloidal precursor solution and FF-YBCO colloidal precursor solution. DLS measurements were performed for 15 days. The results can be seen in Figure 5.8. We can observe a similar behaviour as in the case of TFA-YBCO colloidal solution.

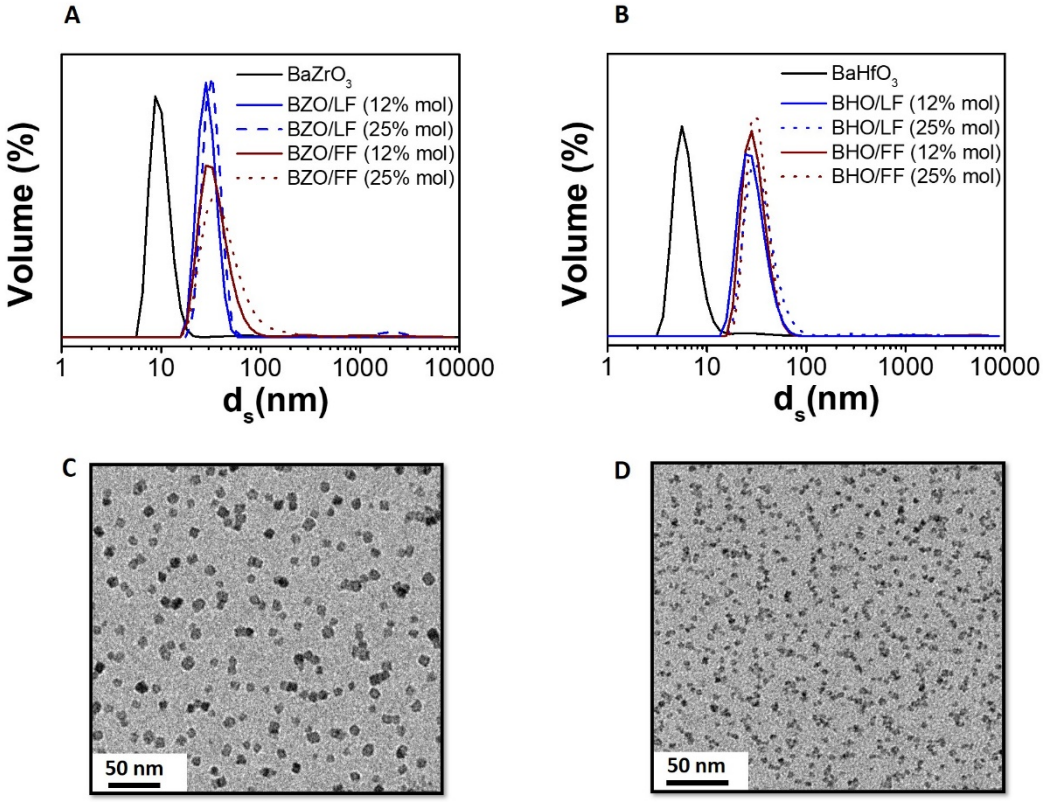

Figure 5.8. DLS measurement by compering (A) $BaZrO_3$ (BZO) with a concentration of 12 and 25 mol% , measured with an average sizes of 10 nm for $BaZrO_3$ mixed with LF-YBCO precursor solution and FF-YBCO precursors solution after 15 days of being mixed. (B) TEM image of $BaZrO_3$ NCs (10 nm) into FF-YBCO precursors solution (C) $BaHfO_3$(BHO) with a concentration of 12 and 25 mol% and an average size of 5 nm $BaHfO_3$ with LF-YBCO precursor solution and FF-YBCO precursors solution after 15 days of being mixed. (D)TEM image of 5 nm of $BaHfO_3$ NCs mixed with FF-YBCO precursor solution.

The peaks shift from d_H = 10 nm to d_H = 28 nm and from d_H = 4 nm to d_H = 21 nm in the case of $BaZrO_3$ NCs and $BaHfO_3$ NCs respectively. We only display the stability study for the NCs with specific sizes of 10 nm in the case of $BaZrO_3$ and 5 nm in the case of $BaHfO_3$. For each NCs the stability was studied with concentrations of 12 and 25 mol%. No evidences of agglomeration has been observed taking into account that the shift of these peaks are attributed to the changes in the environment of the YBCO colloidal precursors solutions (new precursors salts and the presence of propionic acid).

These conclusions can be drawn for both used concentration of NCs. TEM. These results suggest that even changing the YBCO precursors solution the stability of the final colloidal YBCO precursor solution has been achieved.

The Z-Average of NCs solutions displayed in Figure 5.9 shows the same behaviour as the TFA-YBCO colloidal solution. The mixture of NCs with the YBCO precursor solution leads to an increase of the Z-average values, that decrease after several hours showing again an increase in stability of the NCs in the LF-YBCO and FF-YBCO colloidal precursors solutions.

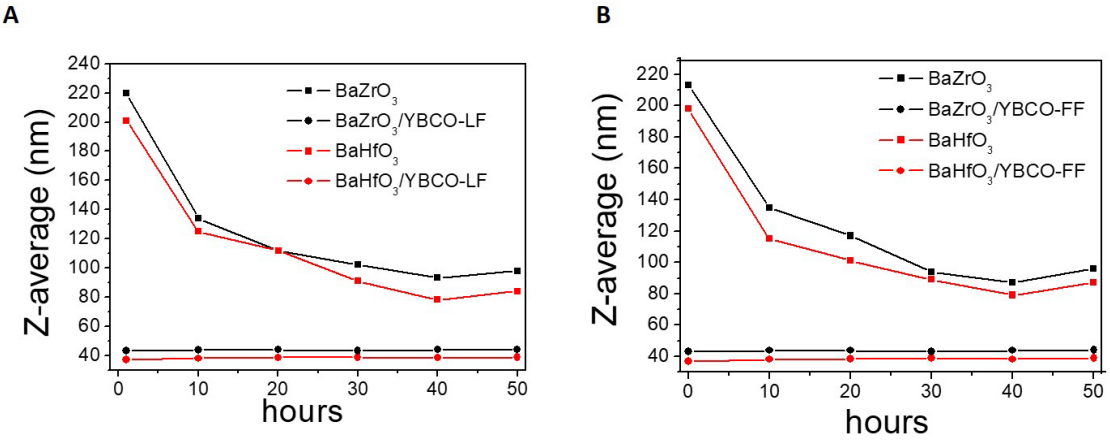

Figure 5.9. Z-average measurements of NCs $BaZrO_3$ and $BaHfO_3$ in ethanol media and compared with(A) LF-YBCO and (B) FF-YBCO precursors solution.

Therefore, the $BaZrO_3$ and $BaHfO_3$ NCs have a high stability for 15 days, independently of the type of YBCO precursors solution used.

5.3 YBCO nanocomposites

In the previous section we already proved that preformed NCs can be used to prepare stable YBCO colloidal precursor solutions. These solutions can be a very promising way to grow YBCO nanocomposites allowing us to control the sizes and the tendency of agglomeration of the NCs in the final YBCO matrix. We know that the NCs embedded in the YBCO matrix can act like artificial pinning centres (APC)

either by themselves or producing strain in the ceramic matrix. [8,27–29] Therefore, the control of NCs sizes is quite important when growing YBCO nanocomposites. Also, another important factor is the possible reaction between the NCs and YBCO. In our case the use of $BaZrO_3$ and $BaHfO_3$ NCs avoid any possible reactions due to the fact that these NCs are non-reactive.[6,9,11,30]

In Figure 5.10 all the steps needed to ensure good quality YBCO nanocomposites are illustrated. The initial step is the addition of preformed NCs (secondary phases) into the YBCO precursor solution. After YBCO colloidal precursor solution has rested for several hours the solution is then deposited, either by spin-coating or ink-jet printing onto a single crystalline substrate. If the deposition process is successful in terms of homogeneity the as-deposited layer is subjected to a low temperature treatment (pyrolysis).

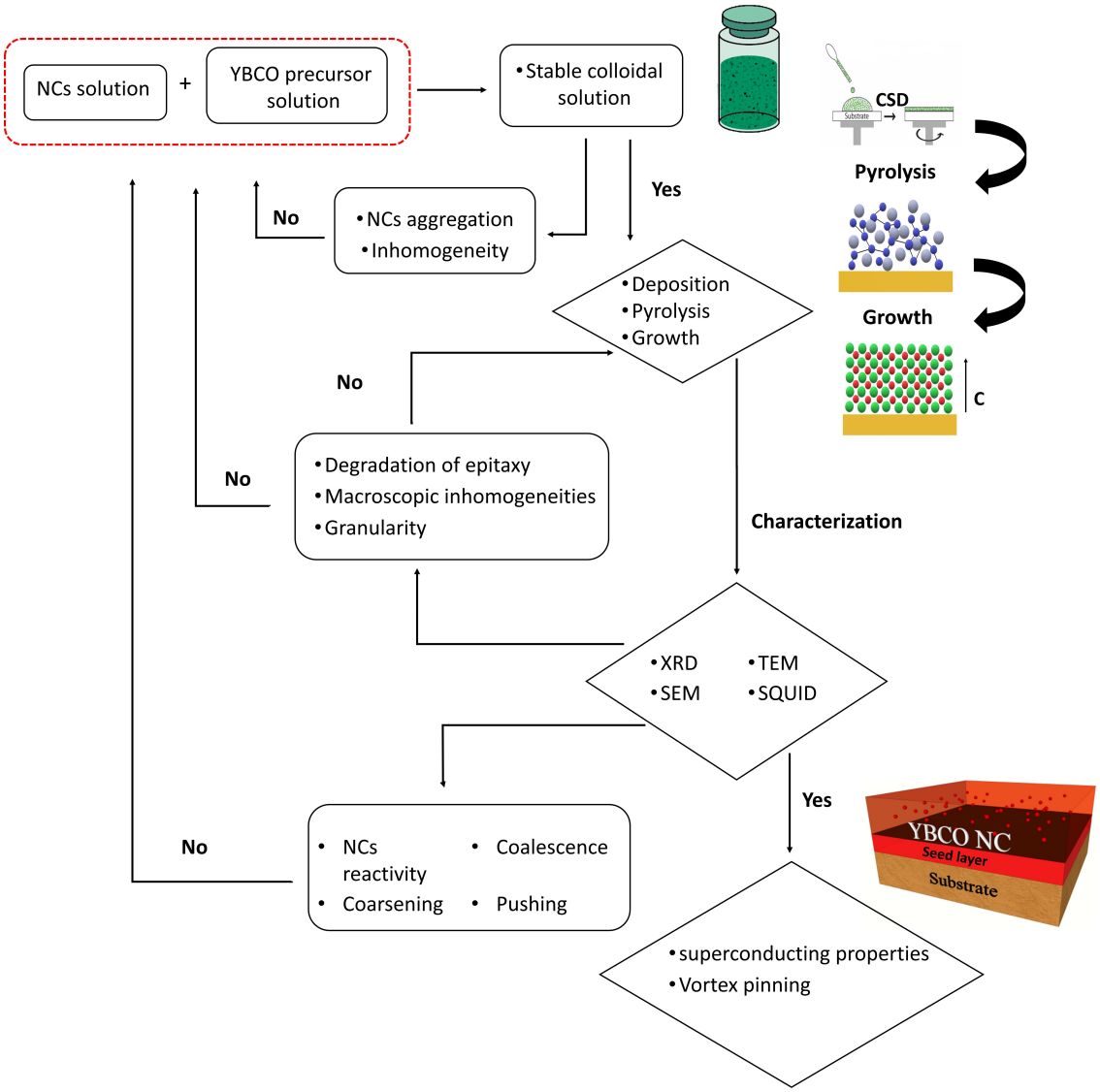

Figure 5.10. Scheme of the different stage involving CSD by the implementation of preformed NCs onto YBCO precursor solution. Highlighting the drawbacks to face with during the whole process. Besides to show the optimum path to to achieve a good nanocomposited with high superconductor properties.

The pyrolyzed layer is then checked by optical microscope (MO) to ensure that the presences of inhomogeneities or cracks are not detected. If the quality of the pyrolyzed layer is acceptable we subject the layers to the growth and oxygenation process. The grown process reaches temperatures of around 800 ºC and the oxygenation process is performed during the cooling ramp usually between 450 and 550 ºC. The grown YBCO nanocomposite layers are then analysed by means of XRD, SEM, TEM and SQUID.

Until now we have focused on the stability of the YBCO colloidal solutions, being this the first important step to achieved high quality YBCO nanocomposite. Another important factor to achieve this goal is the behaviour of the NCs during the growth process of the nanocomposites. There are different phenomena that can drastically affect the nanostructure and therefore the superconducting properties of the nanocomposites (Figure 5.11). These phenomena are:

i) *NCs reactivity:* Depending on the type of the NCs used to obtained nanocomposites, these can react with the YBCO. We already establish that our NCs are non-reactive so in this work this phenomena does not happen.[6,9]

ii) *Pushing and trapping effects*. We have emphasized that the sizes of the NCs is of great importance for obtaining good quality nanocomposites, this effect is one of the main reasons. If the NCs are to small (bellow 2 nm) during the growth of the nanocomposite they can be pushed to the surface of the layer.[6] This way the NCs lose their purpose as APC. On the other hand, if the NCs exceed a certain diameter they can be trapped at the interface between the substrate and the forming YBCO. In this case, YBCO will nucleate on the surface of the NCs instead of the substrate and the nucleation will be random.[31–34] Besides the control of the NCs sizes another important factor to avoid this effects is the growth rate of YBCO nanocomposites.

iv) *Coarsening and coalescence effects* NCs become larges according to the Ostwald ripening theory not being favourable to obtain high critical current.

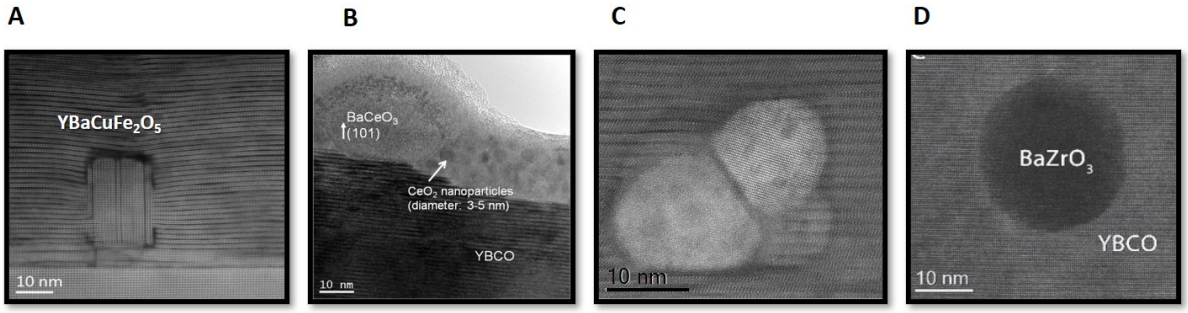

Figure 5.11. Illustration of the phenomes which could lead to a degradation of a proper vortex pinning, such; (A) reactivity of $MnFe_2O_4$ to $YBaCuFeO_5$,[35] (B) pushing effects from the CeO_2 NCs to the top part of the matrix,[6] (C) coalescence and (D) coarsening effect.[9]

All these phenomena have to be avoided in order to achieve high performance YBCO nanocomposites. The efficiency of $BaZrO_3$ and $BaHfO_3$ will be demonstrated in the next pages in case of TFA-YBCO, LF-YBCO and FF-YBCO nanocomposites. The deposition methods used were spin-coating and ink-jet printing.

5.3.1 TFA-YBCO nanocomposites

5.3.1.1.The pyrolysis process

The stable colloidal solution of NCs/TFA (0.125 M with respect Y) was deposited onto the LAO substrate by using spin-coating (≈ 15 μL) and then pyrolyzed using the standard pyrolysis process, reported on Methodologies Chapter 2. The pyrolyzed layers were visualized through optical microscopy in order to identify the possible defects presents. In figure 5.12A we can observe a standard image of the pyrolyzed layers that comply with a good quality pyrolyzed YBCO nanocomposites layers. A homogeneous and continuous layer is revealed with no cracks or buckling present. Examples of pyrolysis samples with defects as cracks (Figure 5.12B) and buckling films (Figure 5.12C) are also presented.

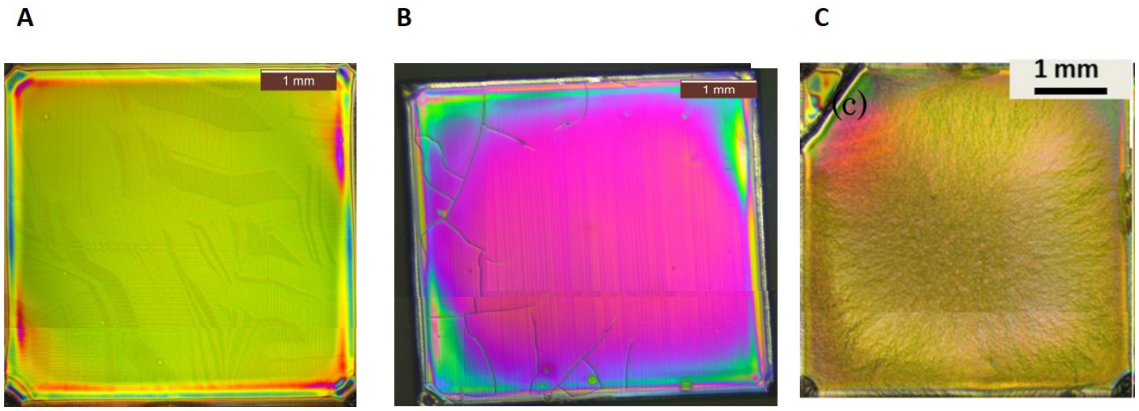

Figure 5.12. Optical microscopy images of pyrolyzed samples of $BaZrO_3$/TFA-YBCO (A)Homogeneous film deposition of $BaZrO_3$/ TFA-YBCO colloidal solution with 12 mol% of NCs. (B) an example of cracked sample and (C) buckled film after the conventional pyrolisi process.

After the pyrolysis the YBCO nanocomposite films were grown by following the standard TFA growth process.[25,36] Nonetheless, it was observed that increasing the concentration of the NCs can lead to the degradation of YBCO texture. This issue was previously studied by P. Cayado,[37] for CeO2 and ZrO2 NCs. They show that when using higher concentrations of NCs in the YBCO nanocomposites during the thermal processes the NCs agglomerate in the interface of the LAO (Figure 5.13A). This leads to an incorrect nucleation of YBCO due to the high mismatch

between YBCO and $BaZrO_3$. To overcome this problem, they propose the addition of a 50 nm seed layer of pyrolyzed YBCO pristine in the top of the substrate before the deposition of NCs/YBCO.

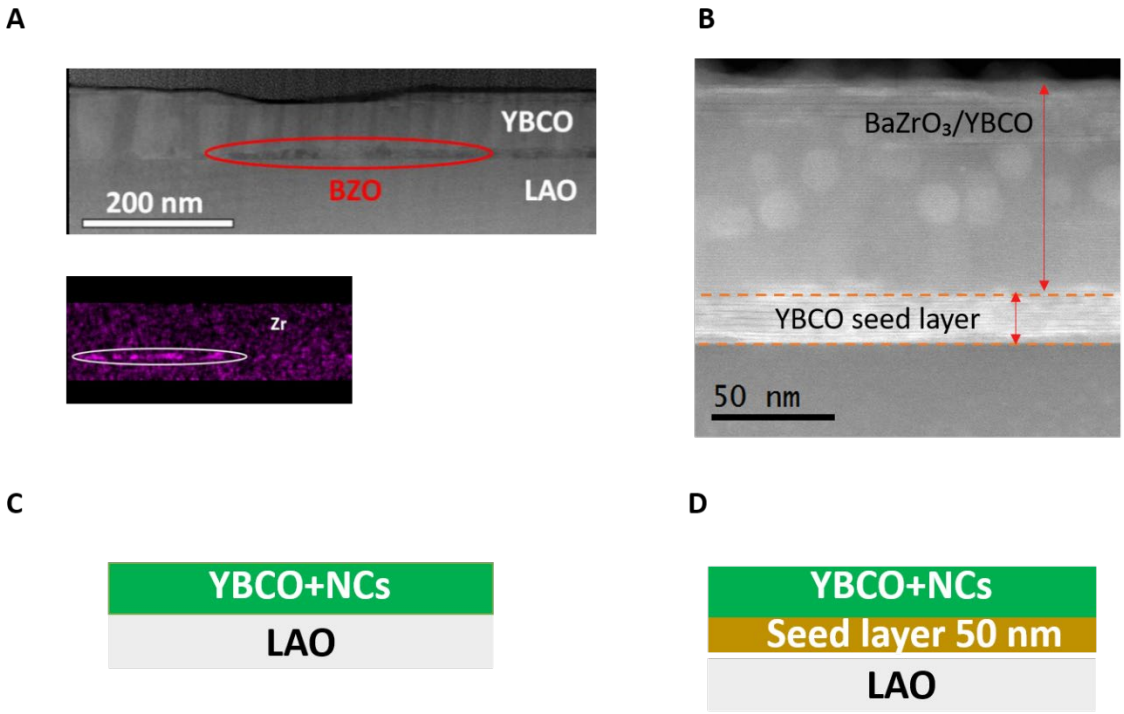

Figure 5.13. TEM images (A) ZrO_2/YBCO at 1 mol% pyrolyzed without the use of seed layer. The $BaZrO_3$ NCs formed are deposited at the interface of the substrate. Below it is shown the EDX of Zr confirming the presences of Zr accumulation in the interface, therefore $BaZrO_3$ on the top of the substrate.[37] (B) TEM images after growing process by firstly pyrolysis a seed layer and afterwards pyrolyzed a $BaZrO_3$/YBCO 20 mol %. (C) and (D) corresponds to an illustration of a pyrolysis film without using seed layer onto the top of the substrate and using a seed layer respectively.

Figure 5.13 illustrate the mentioned issues: without using a seed layer (C) and using a seed layer (D). In the case of using pyrolyzed seed layer we deposit the YBCO colloidal precursor solution with the desired concentration of NCs in the top of the pyrolyzed seed. After pyrolysis and growth, the total thickness of the YBCO nanocomposite layer will be around 150 nm. In the Figure 5.13B we can appreciate the benefits of using the YBCO pyrolyzed seed layer. As it can be seen the concentration of NCs in the nanocomposites can be increased up to 20 mol% without any degradation of the texture and keeping a uniform distribution of these NCs in the YBCO matrix.

In the Figure 5.14 we can observe the changes in the YBCO morphology when we use 6 mol% (A), 12 mol% (B) concentration of NCs without using a YBCO seed layer. For YBCO at 6 mol% $BaZrO_3$ NCs the SEM image reveals a standard morphology of YBCO with some CuO precipitates on the surface.[38] The YBCO at

12 mol% of $BaZrO_3$ NCs surface is full of needle-like formation indicating an incorrect texture and nucleation of YBCO. Nevertheless, when a 50 nm YBCO seed layer is prior deposited and pyrolyzed the upper YBCO nanocomposite layer can include up to 20 mol% of NCs without any texture and morphology degradation (Figure 5.14C).

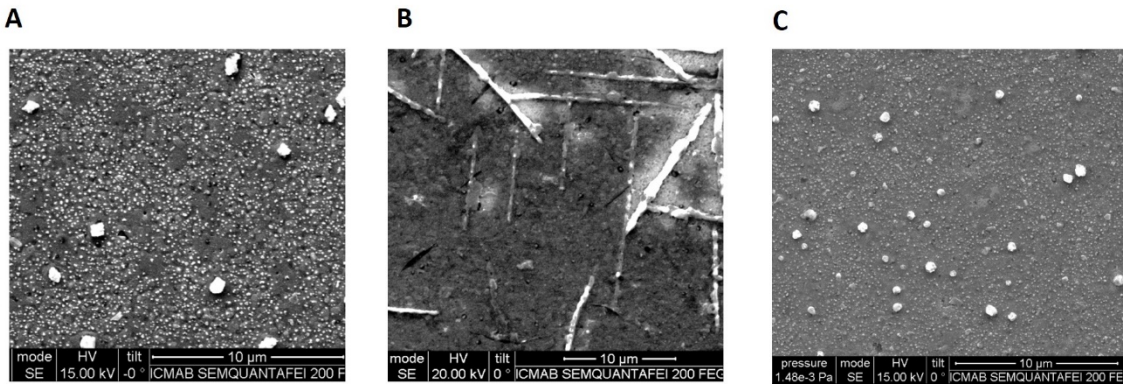

Figure 5.14 SEM images after the growing process. Direct colloidal samples deposition of $BaZrO_3$/YBCO-TFA into the substrate (A) with a 6 mol% NCs(B) with 12 mol% NCs. (C) SEM image after growing process, by firstly deposition of a seed layer and posterior pyrolysed of $BaZrO_3$/TFA-YBCO at 20 mol% layer.

Acknowledging the advantages of the YBCO pyrolyzed seed layer we have decided to conduct all our nanocomposite studies independently of the NCs concentration used, applying this approach.

5.3.1.2 Growing process via convectional thermal annealing

Recently, a deep study of the growth conditions of YBCO nanocomposite layers synthesized from TFA colloidal solutions were studied in the PhD Thesis of Zi Liang Li.[39] What we will present here are some of these results made in collaboration that confirms the good behaviour of the preformed approach to YBCO nanocomposite layers and the different strategies to enhance the performances by tuning the nanoparticles size content and the rate growth of the synthesis.

The conventional thermal annealing growth process is the standard process for TFA-YBCO already described in Chapter 2. The CTA growth process was also used to achieve YBCO nanocomposites using the spontaneous segregation methodology.[5,22,38,40] The behaviour of $BaZrO_3$ and $BaHfO_3$ in YBCO nanocomposites are compared. The concentration of NCs used is 20 mol% and the size of the NCs is 10 nm in both cases.

The grown YBCO nanocomposite layers were analysed by means of scanning transmission electron microscopy (STEM) presented in Figure 5.15. In Figure 5.15A we can see that YBCO has grown epitaxially and the NCs of $BaZrO_3$ are distributed through the YBCO matrix. There is a slight tendency of the migration of NCs at the interface with the substrate and at the top of the grown YBCO layer. The shape of the NC appears to remain the same after growth, meanwhile the size of the $BaZrO_3$ NCs is the range of 10-20 nm. The increment in size of some of the NCs is prove of a slight coarsening taking place during the growth process.

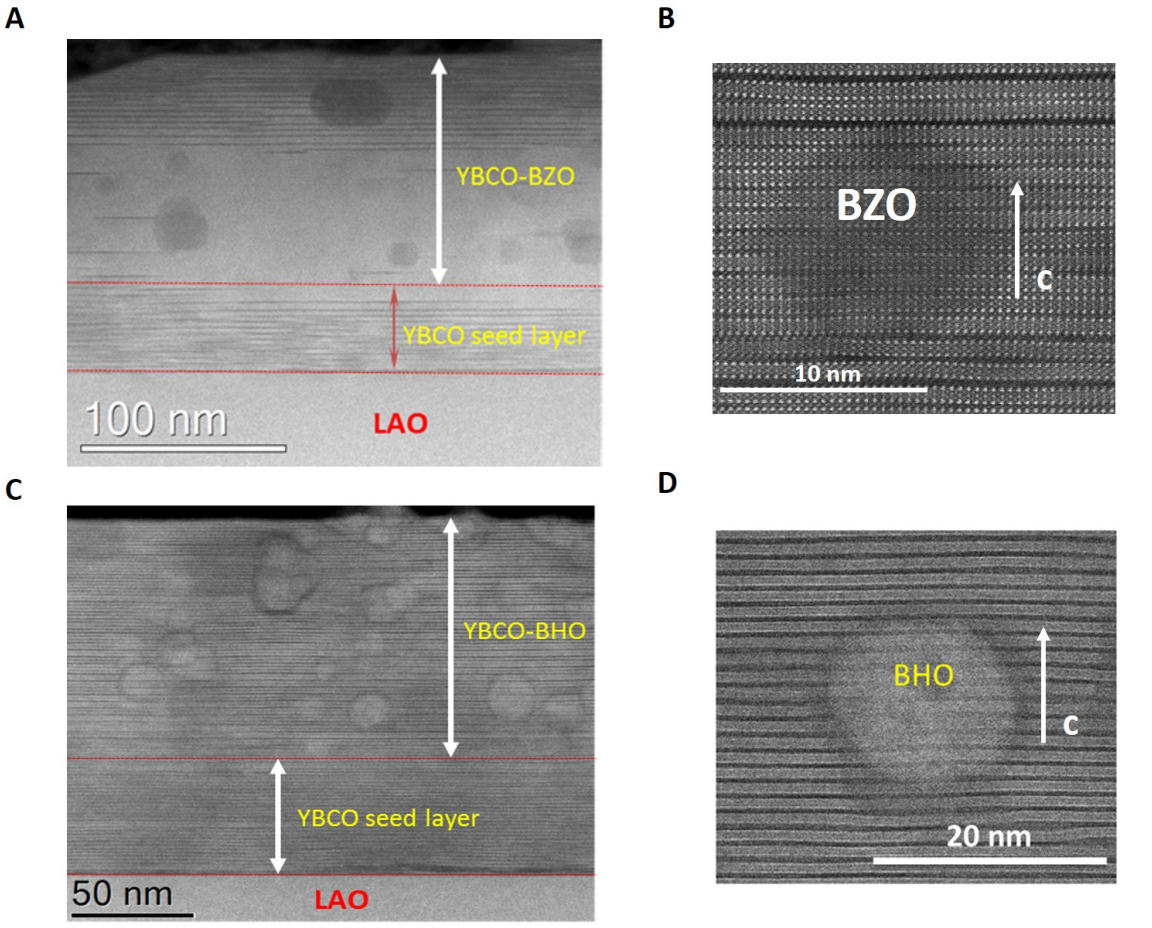

Figure 5.15. STEM and HRSTEM images of 10 nm at 20 mol% $BaZrO_3$ (BZO) at (A) and (B) respectively. STEM and HRSTEM images of 10 nm at 20 mol% $BaHfO_3$ (BHO) at (C and D) showing an epitaxial growth of YBCO.

Similar behaviour was found for $BaHfO_3$ NCs. The STEM in Figure 5.15C-D image shows more uniform distribution of these NCs in the YBCO matrix than for $BaZrO_3$ NCs. There is also, a slight increment of some of the $BaHfO_3$ from 10 nm to 15 nm, lower than in the case of $BaZrO_3$.

SQUID measurements have been used to evaluate the superconducting properties of the YBCO nanocomposites. The behaviour of the critical current density (J_c) with magnetic field can give us important clues of the performance of the NCs embedded in the YBCO matrix. Figure 5.16 compares the behaviour of critical current density with magnetic field for YBCO nanocomposite (both with $BaZrO_3$ and $BaHfO_3$ NCs) with a pristine YBCO. We can observe that regarding the nanocomposite films there is a smoother critical current decay with a magnetic field that in the case of YBCO pristine layers. When comparing the $BaZrO_3$/YBCO nanocomposites with $BaHfO_3$/YBCO nanocomposites we can appreciate slightly higher performances at both 5 K and 77 K.

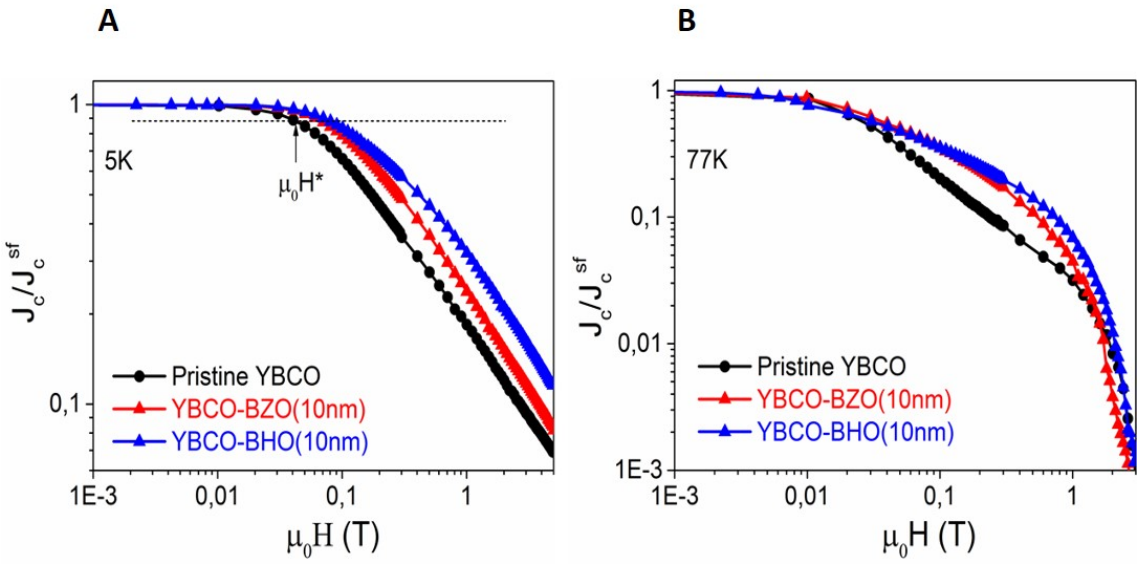

Figure 5.16 Normalized J_c(H) dependence with magnetic field at 5 and 77 K in (A) and (B) respectively. In (A) show $BaZrO_3$ and $BaHfO_3$ at same sizes and concentration (10 nm at 20 mol%) at 5 K. (B) $BaZrO_3$ and $BaHfO_3$ (10 nm at 20 mol%) at 77 k. The horizontal dashed line in (A) marks the criterion to determine the μ_0H* value J_c (μ_0 H) = 0, 9 J_c^{sf}.

In order to compare the effect of the concentration of the NCs both in the case of spontaneous segregation methodology and in the case of preformed NCs, $BaZrO_3$ was chosen. What we can observed in Figure 5.17 is the behaviour of critical current density at different NCs concentration. In the case of spontaneous segregated NCs it is appreciated that after adding more than 5 mol% and 10 mol% of NCs the J_c at 5 K and 77 K respectively suffers a drastic decay. This is attributed to the lack of control of the NCs sizes during the growth process. On the other hand, when using the preformed NCs we can increase the concentration up to 20 mol% without degrading the performances at 5 K and even up to 25 mol% without any significant changes in performances at 77 K.

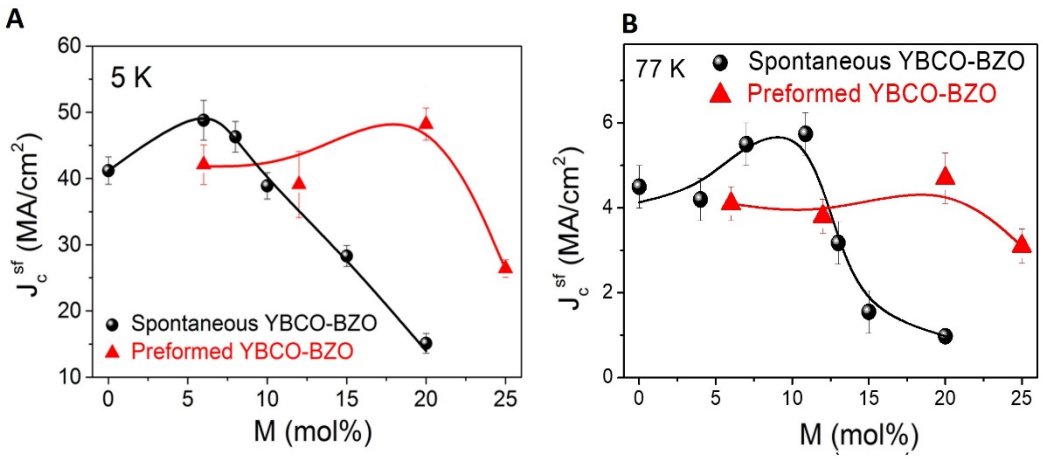

Figure 5.17. Dependence of J_c^{sf} self at (A) 5 K and (B) 77K respect NCs amount (mol%) from $BaZrO_3$-YBCO (10 nm) via preformed NCs nanocomposite films (red triangle) compared with spontaneously segregated YBCO nanocomposite films (black sphere).[39]

Since $BaHfO_3$ seems to be more effective in nanocomposites, we decided to study the dependency of the nanostructure and therefore the superconducting properties with the NCs sizes. The $BaHfO_3$ NCs diameter that was used for this studied was 5 nm, and the YBCO nanocomposite was prepared using 20 mol% of NCs concentration. The STEM image presented in Figure 5.18A-B shows a uniform distribution of the NCs in the YBCO matrix, similar as in the case of 10 nm $BaHfO_3$. Also, an increment up to almost 15 nm is detected for some NCs, meanwhile other NCs remains unchanged.

Figure 5.18C-D analyses the evolution of J_c with magnetic field at 5 and 77 K. At both temperatures it is appreciable that the nanocomposite with $BaHfO_3$ NCs at 5 nm show an overall J_c enhancement, with a smoother decay at higher magnetic fields than the nanocomposite with $BaHfO_3$ NCs of at 10 nm. Therefore showing a higher J_c values at those NCs with smaller size.

2D XRD analysis and the correspond integrated spectrum is presented in (Figure 5.19). The (110) $BaHfO_3$ peak is clearly observed in the XRD spectrum confirming the presence of the $BaHfO_3$ NCs. Furthermore, a high epitaxy of YBCO layer is confirmed, demonstrating that the presence of $BaHfO_3$ NCs does not degrade the correct texture of YBCO.

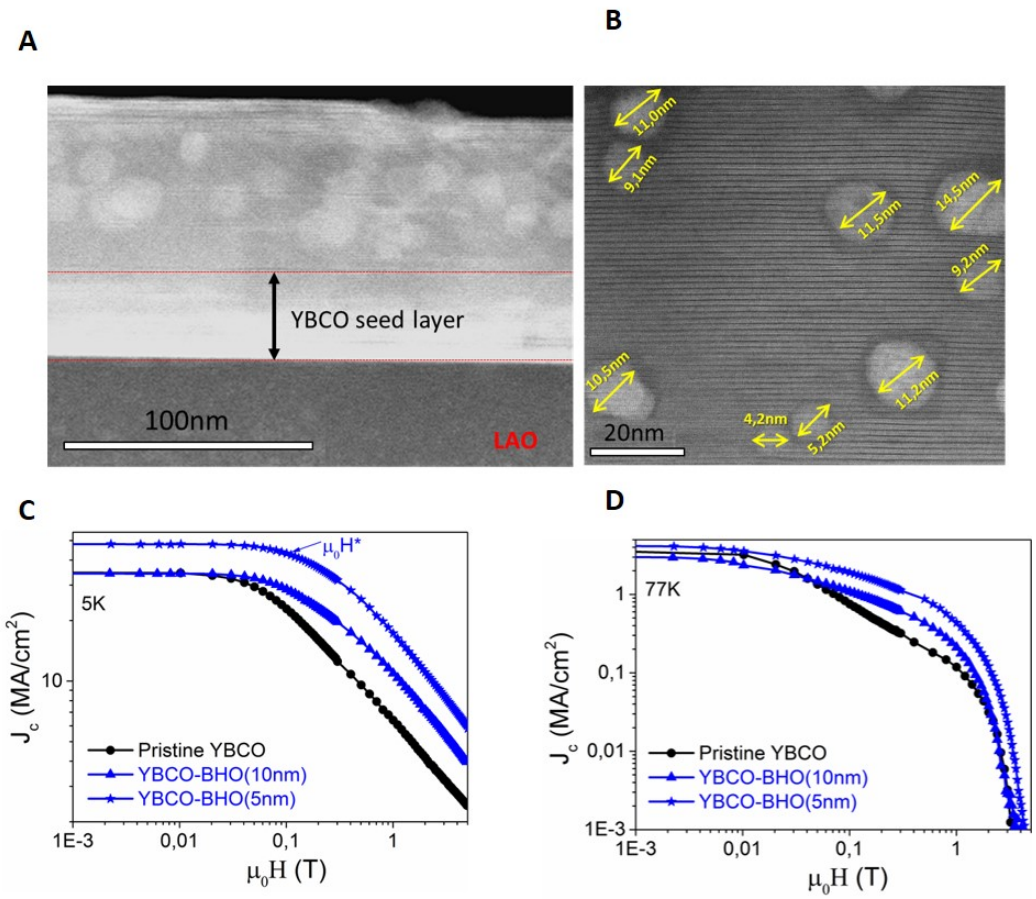

Figure 5.18. (A) STEM image of 20 mol% $BaHfO_3$-YBCO at 5 nm. (B) HRSTEM image of of 20 mol% $BaHfO_3$-YBCO at 5 nm. Critical current density versus magnetic field comparing $BaHfO_3$ (BHO) at 10 and 5 nm with 20 mol%, (C) at 5 K and (D) at 77 K.

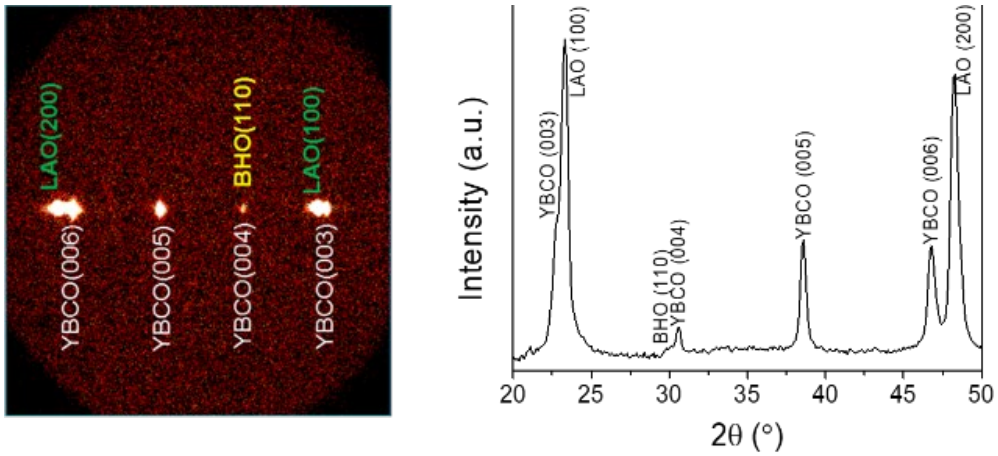

Figure 5.19. 2D-XRD pattern of $BaHfO_3$ (20 %mol at 5 nm)/TFA-YBCO, showing the main peak of $BaHfO_3$ NCs, thus the present of NCs on the nanocomposites.

Using the CTA growth process, we have been able to achieve high performances YBCO nanocomposites. We have compared the spontaneous

segregation methodology with our preformed NCs methodology, and we demonstrated that the preformed NCs have a more satisfying behaviour in YBCO nanocomposites. What we have notice is a slight increment in the NC sizes during growth process, evet thought this increment does not seem to affect the superconducting properties of the YBCO nanocomposites

5.3.1.3 Growth process via flash heating

In the last section we have seen that even though the performances of the YBCO nanocomposites were excellent we still do not have a complete control over the increment in size of the NCs during growth. In order to achieve a tight control over the NCs sizes we have implemented an alternative growth process called flash heating (FH). This process consists in very high heating rates (1200°C/min) up to the growth temperature. We hope that these high heating rate could prevent the growth of NCs size. To study the effect of FH process on the YBCO nanocomposites

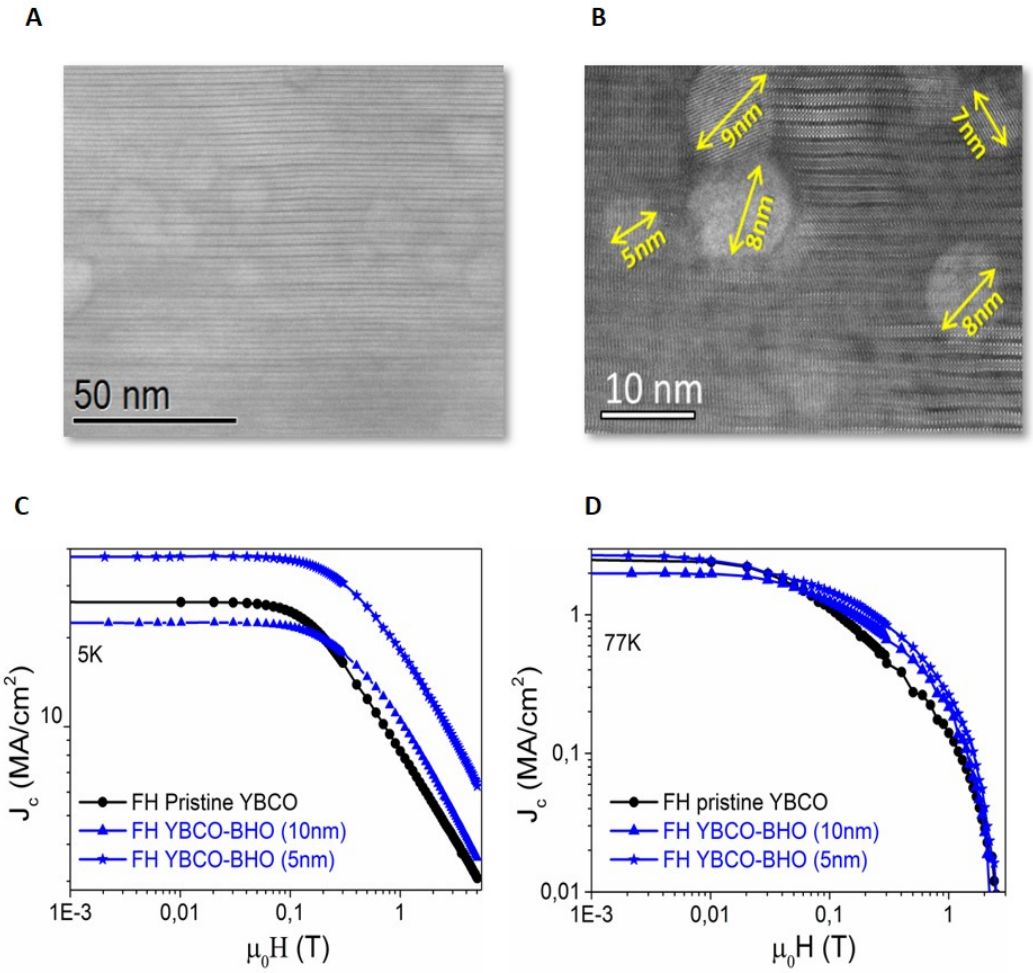

Figure 5.20 (A) STEM image of 20 mol% $BaHfO_3$ (5 nm) by applying FH growth ramp and (B) the respectability high resolution image of the $BaHfO_3$ on YBCO matrix. (C) and (D) critical current density versus magnetic field comparing $BaHfO_3$ (BHO) at 10 and 5 nm with 20 mol%, at 5 and 77 K respectively.

we have chosen 20 mol% $BaHfO_3$+YBCO with an average size of $BaHfO_3$ NCs of 5 nm. After the growth process, Figure 5.20A shows homogeneous distribution and randomly orientated NCs into the matrix. Even though we can still observe a growth in the NCs size we can see an improvement with respect to CTA growth process. In FH growth process the NCs diameter can increase up to 9 nm compared to almost 15 nm as in the case of CTA. This suggest a more controlled coarsening effect.

Figure 5.20C-D present a $J_c(H)$ dependency by comparing YBCO pristine, YBCO nanocomposites with $BaHfO_3$ of at 10 and 5 nm, in both cases with a concentration of 20 mol% measured at 5 and 77 K. As it is observed, the nanocomposite samples show a decay of J_c at much higher values of magnetic field than the YBCO pristine sample. As in the case of CTA YBCO nanocomposites we can also observe a better behaviour with magnetic field for the YBCO nanocomposites that have 5 nm NCs.

To better understand the difference between the two processes, a representation of the normalized J_c^{srt} versus a magnetic field was performed. Figure 5.21 compares the results obtained with both processes (CTA and FH) at using different NCs composition ($BaZrO_3$ and $BaHfO_3$) and different NCs size (10 and 5 nm). By comparing $BaZrO_3$ at different sizes 10 and 5 nm, it is observable that at reducing the sizes the J_c improves. Therefore, these results emphasise the fact that the NCs sizes have a direct effect on pinning performance. Besides at comparing smaller NCs (5 nm) from the different NCs ($BaZrO_3$ and $BaHfO_3$) it was achieved

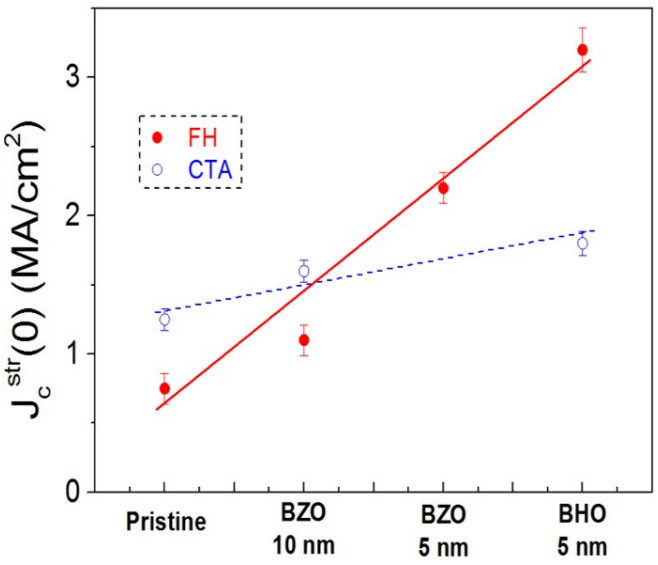

Figure 5.21. Comparation of J_c^{srt} at 0 K between the two main growing process from TFA route, via conventional thermal annealing (CTA) and Flash heating (FH). Measured at 7 T Showing different composition of the NCs: $BaZrO_3$ (BZO) and $BaHfO_3$ (BHO) and different NCs sizes (10 and 5 nm). Besides the pristine values are shown in order to a better comparison.

better superconducting properties in the case of $BaHfO_3$ NCs. We have noticed that the best combination to achieve high performance YBCO nanocomposite is smaller NCs (5 nm) and $BaHfO_3$ NCs via FH growth process. [30]

The performance in field of the nanocomposite are superior to the ones of the pristine layers. We assume that this is due the presence of the NCs. If the NCs are small enough (<6 nm) act as artificial pinning centres,[10,41] meanwhile the large ones are leading to the formation of stalking faults.

5.3.1.4 Multideposition process

The previous studies were performed with thin layers to demonstrate which NCs compositions, size and concentration are the most suitable to enhance the superconductivity properties. The best strategy to control the NCs in the growth process was demonstrated to be the FH growth process. In order to achieve better performances in terms of I_C for the nanocomposite we will have to increase the thickness of the layers. This can be done either by spin coating using multideposition or by inkjet printing from one single deposition. In this section we will discuss the multideposition methodology. The multideposition bring new doubt about the final behaviour of the NCs into matrix due to the increment of the interlayers resulting from the multideposition and pyrolysis processes.

Using the multideposition technique we can increase the thickness of the YBCO nanocomposites from 150 nm (seed layer + NCs/YBCO) to an increment of ~100 nm per NCs/YBCO layer (Figure 5.22A). We can achieve a thickness of 250 nm after growth by the deposition and pyrolysis of one extra layer or 350 nm after growth by the deposition and pyrolysis of 2 extra layers.

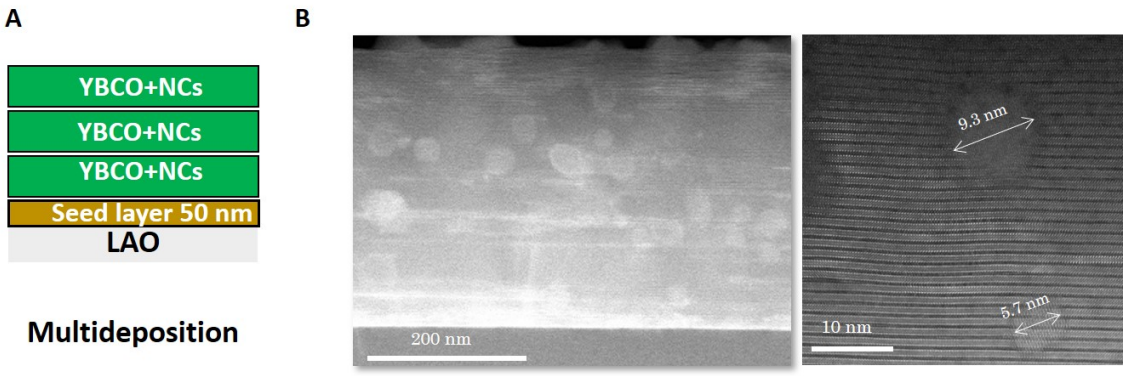

Figure 5.22. (A) Scheme of the multideposition layers onto the LAO substrate, with a seed layer of 50 nm, and a respectively layers of NCs/YBCO of ~ 100 nm each. (B) STEM of low (left) and high (right) resolution image of 350 nm YBCO 20 mol% NCs of $BaHfO_3$ at 5 nm growth process of FH.

To better see the effect on multideposition technique on the NCs distribution we have grown 350 nm thick layers of YBCO nanocomposites using the FH growth process. As we can observe from the STEM images in Figure 5.22B the NCs distribution in the YBCO matrix is not affected neither by the thickness increment or by the apparition of extra interlayers. Moreover, by using the FH growth process the interlayers are barely visible. The NCs are uniformly distributed through the YBCO matrix and the increment in size does not achieve 10 nm. Also, no precipitates or agglomerations are observed.

Table 5.1. μ_0H^* values by varying the thickness on the final layers by using $BaHfO_3$ at 5 nm with a concentration of 20 mol% and the implementation of FH process.

NCs	Thickness (nm)	μ_0H^* (mT)
$BaHfO_3$ (5 nm)	150	195
$BaHfO_3$ (5 nm)	250	216
$BaHfO_3$ (5 nm)	350	270

In table 5.1 we have enlisted the values of μ_0H^* for all the thicknesses studied. The μ_0H^* indicates us the values of the magnetic field at which the critical current density starts to decay. Higher the μ_0H^* value, longer it takes for the J_C to degraded. For a thickness of 350 nm with μ_0H^*= 270 mT we have achieved one of the highest μ_0H^* value obtained in preformed nanocomposites.[6,9]

5.3.2 LF-YBCO nanocomposites

Another way to increase the YBCO nanocomposites properties is to use inkjet printing (IJP). The main advantage of this methodology consists in achieving higher thicknesses layers by a one single deposition.

In order to succeed in growing higher thickness of YBCO the growth conditions had to change. In this case a higher P_{H_2O} was used.[42] Also the precursor YBCO solution had to change in order to adapt the IJP deposition. For this 5 mol% $Ag(CF_3COO)$ and 6 % v/v polymer were added to the YBCO nanocomposite colloidal precursor solution. This modification on the final solution could have a direct effect on the NCs, thus a stabilization test on this new system must be performed. DLS stabilization measurements show a shift of the hydrodynamic radius (Figure 5.23), less that in the case of the standard LF-YBCO precursor solution. The Z-average have also lower values in the IJP LF-YBCO nanocomposite precursor solutions compared to LF-YBCO standard solution (Table 5.2), suggesting a higher stability of NCs in this new media.

Table 5.2. DLS measurements sizes and Z-average to compared between as-synthesised $BaZrO_3$ and the addition of this NCs to LF-YBCO (standard) and LF-YBCO solution to IJP (addition of 5 mol% Ag(TFA), and 6%v/v polymer). All the measurements made after the addition of the $BaZrO_3$ NCs.

Sample	DLS (nm)	Z-average (nm)
$BaZrO_3$ 12%mol	9	38
$BaZrO_3$/LF-YBCO	28	218
$BaZrO_3$/LF-YBZO(IJP)	21	102

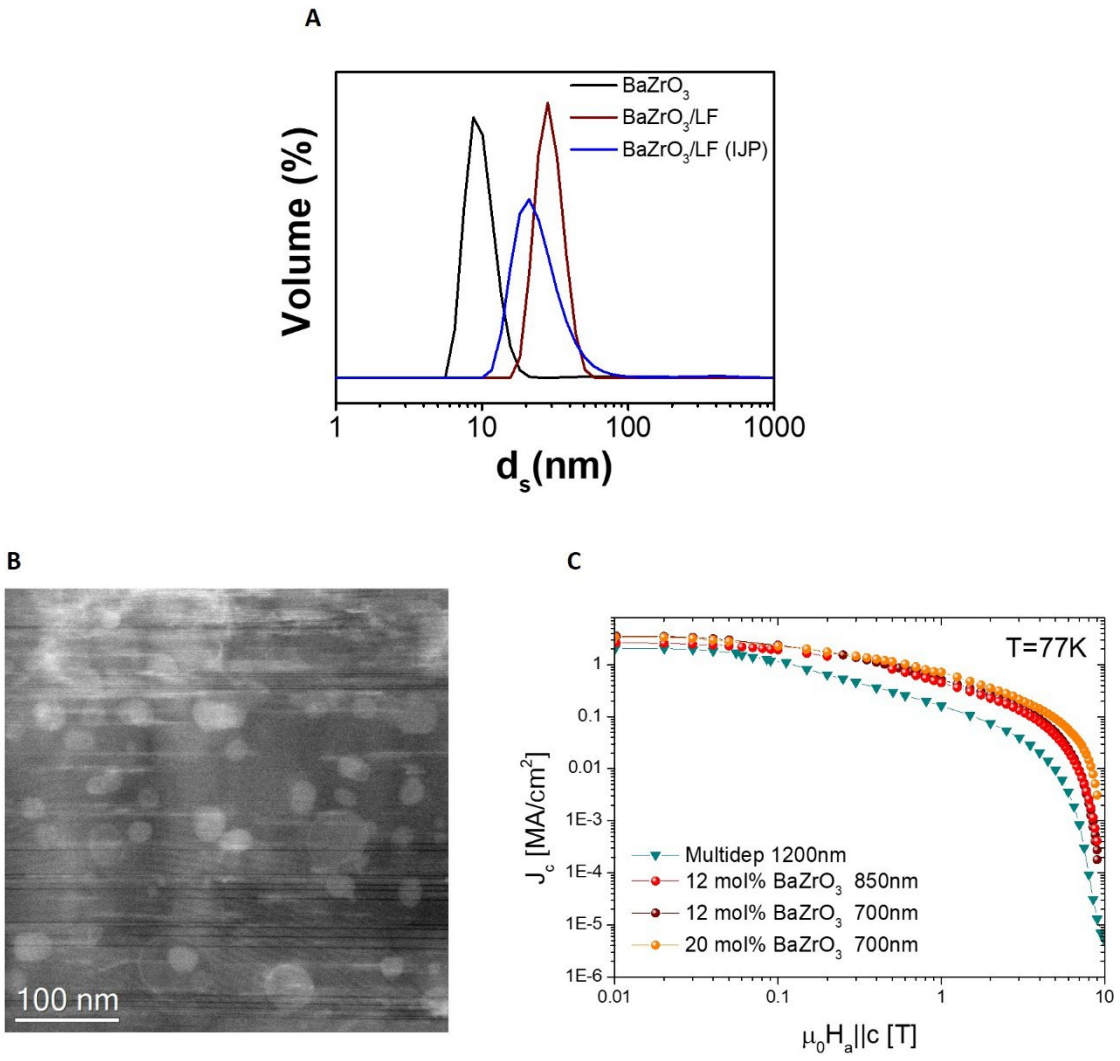

Figure 5.23.(A) stabilization study by DLS of $BaZrO_3$ 12 mol%, $BaZrO_3$/LF-YBCO and $BaZrO_3$/LF-YBCO(IJP) precursors solution. All three measurements done to the final homogeneous colloidal solution after the addition of NCs to the respectively YBCO precursors solution. (B) shows STEM image of a nanocomposite of LF-YBCO with $BaZrO_3$ at 12 mol% deposited by IJP onto LAO substrate with a YBCO seed layer, and a final thickness of 850 nm. (C) magnetic field dependency of critical current density J_c of $BaZrO_3$ at 12 and 20 mol% LF-YBCO nanocomposite. The IJP layers have been compared with a multideposition LF-YBCO thick films with a final thickness of 1200 nm.

The major drawback of the IJP LF-YBCO colloidal precursor solution is the presence of Ag salts. These salts are highly sensitive to light, therefore the IJP LF-YBCO colloidal solution is stable only for a few hours. In consequence, the colloidal solution must be used fresh right after being prepared. In order to achieve the highest performance possible for these thick YBCO-LF nanocomposites a 50 nm YBCO seed layer had to be used.

Figure 5.23B presents a STEM image, where it can be appreciate the $BaZrO_3$ NCs. It is observable that the NCs are randomly oriented and exhibit a uniform distribution through the YBCO matrix. No agglomerations can be observed, but a slight coarsening effect can be detected. The NCs size have incremented, like in the case of thin TFA-YBCO nanocomposite, but without affecting the correct texture of YBCO.

Regarding the superconductive properties, we can see in Figure 5.23C, that the thick YBCO nanocomposites have a better behaviour with the increase of magnetic field than the thick multideposition LF-YBCO pristine layers, which makes them extremely attractive to high magnetic fields applications. It is noticing an increment of J_c by compering layers with the same thickness (700 nm) and increasing the NCs concentration from 12 to 20 mol%. Besides to increase slightly the J_c at comparing the same concentration of NCs with the thickness layer from 700 nm and 850 nm. Consequently, the use of IJP to prepared thick layers suggests, once again, a higher superconducting property as well as good texture films.

5.3.3 FF-YBCO nanocomposite

Up to now the studies made have successfully demonstrated that by using preformed NCs both in TFA and LF-YBCO precursor solutions we are able to achieve high performance YBCO nanocomposites. The next step is to do the same for FF-YBCO precursor solutions. The FF-YBCO nanocomposites have been grown using a novel growth technique called Transient Liquid Assisted Growth (TLAG). This process is quite complex and it is based on the control of a quasi-simultaneous nucleation using a solid liquid reaction[43,44] as is have been described in L.Sole PhD[45] and J.Jareño PhD[46] studies.

Previous works involving TLGA route to grow pristine FF-YBCO layers have shown that controlling the supersaturation of yttrium in the liquid is key to achieve epitaxial films.[45] Parameters such as: heating ramp, growth temperature and P_{O_2}, have been found to have a direct influence on the final texture of the YBCO layers, so a strict control of these are needed. To achieve highly epitaxial FF-YBCO layers using TLAG process two routes have been studied the as-called temperature route

(fast change of temperature at a constant P_{O_2}) and the as-called P_{O_2} route (change from low P_{O_2} to the optimum P_{O_2} at the growth temperature).

In order to study the behaviour of $BaZrO_3$ and $BaHfO_3$ NCs in FF-YBCO nanocomposite we have used the P_{O_2} route. The NCs used to obtain FF-YBCO nanocomposite have 5 nm in diameter both for the case of $BaZrO_3$ and of $BaHfO_3$. Since we have used a 12 mol% of NCs the use of YBCO 50 nm seed layer was mandatory. In Figure 5.24A STEM image of a grown 90 nm thick FF-YBCO nanocomposite is presented.

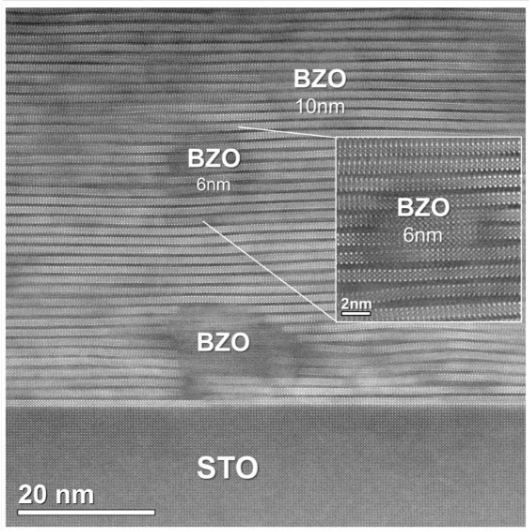

Figure 5.24. HRSTEM image of a homogeneous film with 12 mol% of NCs $BaZrO_3$(BZO) pyrolysed on the top of a seed layer, an amplification of one NCs is remarked and measured.

We can see that the NCs are homogeneously distributed throug the YBCO matrix and the increment in NCs size to 6 – 10 nm shows a low degree of coarsening effect.

In Figure 5.25 we compare the performances of FF-YBCO nanocomposites obtained by TLAG process with a pristine YBCO sample achieved by the same process. Although the J_c value could be optimized to reach the value of the pristine films, it is observed in Figure 5.25 a crossover at both temperatures, above which the nanocomposites have higher values of the $\mu_0 H^*$. This implies a higher J_C performance with magnetic field in the case of nanocomposites

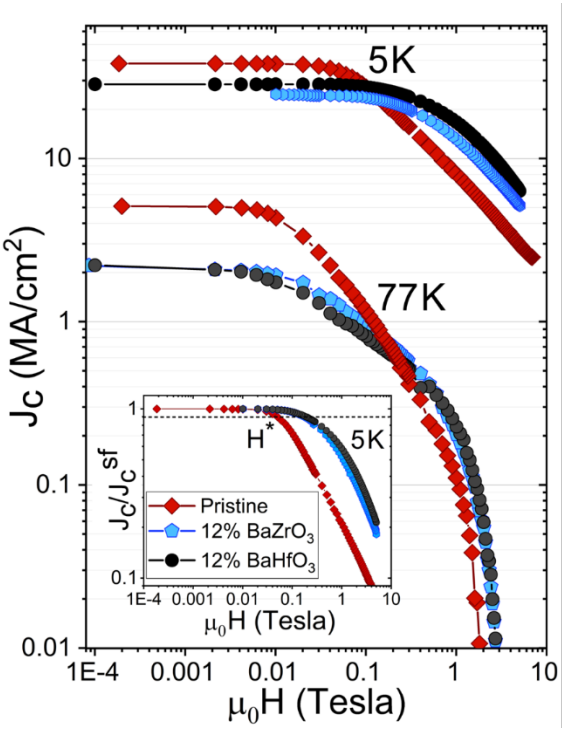

Figure 5.25. Critical current density, Jc, dependence on the magnetic field at 5 K and 77 K for a pristine YBCO film and 12 % molar $BaZrO_3$ and 12 % molar $BaHfO_3$/YBCO-nanocomposites by following the PO2-route. Samples are 90 nm thick.

Therefore, the use of both $BaZrO_3$ and of $BaHfO_3$ NCs to achieve quality TLAG FF-YBCO nanocomposite is quite promising.

5.4 Conclusions

We have demonstrated that using the $BaZrO_3$ and $BaHfO_3$ NCs we are able to obtain high performance YBCO nanocomposites. The use of preformed NCs has proven to be a success in replacing the spontaneous segregated NCs and brings new advantages like better size control and reactivity control.

The stability of $BaZrO_3$ and $BaHfO_3$ NCs has been successfully achieved for all the colloidal YBCO precursor solutions: TFA-YBCO, LF-YBCO and FF-YBCO. This stability was demonstrated for different sizes of NCs as well as different concentrations.

In order to grow the YBCO nanocomposites using $BaZrO_3$ and $BaHfO_3$ NCs two different growth processes were performed. This study has been made in the case of TFA-YBCO nanocomposites and the growth processes used were CTA and FH. It was found that to achieve good quality YBCO nanocomposites at high concentrations of NCs a YBCO pyrolyzed seed layer of 50 nm is required. In terms of composition the $BaHfO_3$ NCs seem to be most promising for the use in YBCO

nanocomposites. The $BaHfO_3$/YBCO nanocomposites exhibit better homogeneity and also reach higher performances that the ones using $BaZrO_3$. NCs In terms of size we have demonstrated that smaller the NCs size, higher the YBCO nanocomposite performance. In terms of the growth process, we have achieved our best results using FH growth process. This is due to better control of NCs size during growth. This conclusion is valid even if we increase the thickness of the YBCO nanocomposite films by multideposition; FH still remains the most adequate growth process to achieve high performance YBCO nanocomposites.

When increasing the thickness of the LF-YBCO nanocomposite using IJP once again we have obtained high performances. We have successfully achieved 850 nm of YBCO nanocomposite from one single deposition. The $BaZrO_3$ NCs, studied in this case has shown high stability in the new YBCO precursor solution. After growth these NCs are uniformly embedded in the YBCO matrix. No agglomerations were detected, even though a slight coarsening effect was noticed.

When we grow TLAG FF-YBCO nanocomposite using preformed NCs we achieve very promising results, despite de complexity of the TLAG process. We have actually shown that in this case the coarsening effect is even lower that in the TFA route, and even though in this case the nucleation and growth of the YBCO is quite different, this does not affect the uniformity in distribution of the NCs through the YBCO matrix.

As a general conclusion we have demonstrated that the use of preformed $BaZrO_3$ and $BaHfO_3$ NCs for YBCO nanocomposites had led to high performance layers that are extremely interesting for high field applications.

5.5 Reference

1 D. Larbalestier, A. Gurevich, D. M. Feldmann and A. Polyanskii, *Nature*, 2001, **414**, 368–377.

2 X. Obradors and T. Puig, *Supercond. Sci. Technol.*, 2014, **27**, 044003.

3 Y. Shiohara, T. Taneda and M. Yoshizumi, *Jpn. J. Appl. Phys.*, 2012, **51**, 010007.

4 S. V. Samoilenkov, O. V. Boytsova, V. A. Amelichev and A. R. Kaul, *Supercond. Sci. Technol.*, 2011, **24**, 055003.

5 A. Llordés, A. Palau, J. Gázquez, et al., *Nat. Mater.*, 2012, **11**, 329–336.

6 P. Cayado, K. De Keukeleere, A. Garzón, et al., *Supercond. Sci. Technol.*, 2015, **28**, 124007.

7 K. Matsumoto and P. Mele, *Supercond. Sci. Technol.*, 2010, **23**, 014001.

8 M. Coll, S. Ye, V. Rouco, et al., *Supercond. Sci. Technol.*, 2013, **26**, 015001.

9 K. De Keukeleere, P. Cayado, A. Meledin, et al., *Adv. Electron. Mater.*, 2016, **2**, 1–9.

10 L. Soler, J. Jareño, J. Banchewski, et al., *Nat. Commun.*, 2020, **11**, 344.

11 H. Rijckaert, G. Pollefeyt, M. Sieger, et al., *Chem. Mater.*, 2017, **29**, 6104–6113.

12 Z. Li, M. Coll, B. Mundet, et al., *Sci. Rep.*, 2019, **9**, 5828.

13 L. A. Dobrzanski and Szindler, *J. Achiev. Mater. Manuf. Eng.*, 2012, **52**, 7–14.

14 J. Chang, *Cailiao Daobao/Materials Reports*, 2019, **33**, 1919–1920.

15 M. Vilardell, X. Granados, S. Ricart, et al., *Thin Solid Films*, 2013, **548**, 489–497.

16 B. Derby, *Annu. Rev. Mater. Res.*, 2010, **40**, 395–414.

17 S. Engel, T. Thersleff, R. Hühne, L. Schultz and B. Holzapfel, *Appl. Phys. Lett.*, 2007, **90**, 2005–2008.

18 J. Gutiérrez, A. Llordés, J. Gázquez, et al., *Nat. Mater.*, 2007, **6**, 367–373.

19 A. Goyal, S. Kang, K. J. Leonard, et al., *Supercond. Sci. Technol.*, 2005, **18**, 1533–1538.

20 A. Gupta, R. Jagannathan, E. I. Cooper, E. A. Giess, J. I. Landman and B. W. Hussey, *Appl. Phys. Lett.*, 1988, **52**, 2077–2079.

21 V. Solovyov, I. K. Dimitrov and Q. Li, *Supercond. Sci. Technol.*, 2012, **26**, 13001.

22 T. Araki and I. Hirabayashi, *Supercond. Sci. Technol.*, 2003, **16**, R71–R94.

23 A. A. Armenio, A. Augieri, L. Ciontea, et al., *Supercond. Sci. Technol.*, 2011, **24**, 115008.

24 X. Palmer, C. Pop, H. Eloussifi, et al., *Supercond. Sci. Technol.*, 2016, **29**, 024002.

25 A. Llordés, K. Zalamova, S. Ricart, et al., *Chem. Mater.*, 2010, **22**, 1686–1694.

26 Y. Chen, C. Wu, G. Zhao and C. You, *Supercond. Sci. Technol.*, 2012, **25**, 62001.

27 G. Shaw, S. B. Blanco Alvarez, J. Brisbois, et al., *Metals (Basel).*, 2019, **9**, 1022.

28 R. W. Schwartz, *Chem. Mater.*, 1997, **9**, 2325–2340.

29 P. Mikheenko, J. S. Abell, A. Sarkar, et al., *J. Phys. Conf. Ser.*, 2010, **234**, 022022.

30 M. Miura, B. Maiorov, M. Sato, et al., *NPG Asia Mater.*, 2017, **9**, e447–e447.

31 D. R. Uhlmann, B. Chalmers and K. A. Jackson, *J. Appl. Phys.*, 1964, **35**, 2986–2993.

32 J. Pötschke and V. Rogge, *J. Cryst. Growth*, 1989, **94**, 726–738.

33 Y. Shiohara and A. Endo, *Mater. Sci. Eng. R Reports*, 1997, **19**, 1–86.

34 A. . Carrillo, T. Puig, J. Plain, J. Figueras and X. Obradors, *Phys. C Supercond.*, 2000, **336**, 213–226.

35 E. Bartolomé, P. Cayado, E. Solano, et al., *Adv. Electron. Mater.*, 2017, **3**, 1700037.

36 X. Obradors, T. Puig, S. Ricart, et al., *Supercond. Sci. Technol.*, 2012, **25**, 123001.

37 P. Cayado, *Multifunctional nanostructured superconductors by chemical routes: towards high current conductors. Phd thesis, Universitat Autònoma de Barcelona,* 2016.

38 X. Obradors, T. Puig, A. Pomar, et al., *Supercond. Sci. Technol.*, 2006, **19**, S13--S26.

39 Ziliang Li, *Growth and Characterization of Nanocomposite YBa2Cu3O7-x - BaMO3 (M= Zr, Hf) thin films from colloidal solutions. PhD thesis, Universitat Autonoma de Barcelona*, 2018.

40 O. Casta o, A. Cavallaro, A. Palau, et al., *Supercond. Sci. Technol.*, 2003, **16**, 45–53.

41 X. Obradors, T. Puig, Z. Li, et al., *Supercond. Sci. Technol.*, 2018, **31**, 044001.

42 C. Pop, B. Villarejo, F. Pino, et al., *Supercond. Sci. Technol.*, 2018, **32**, 15004.

43 C. Klemenz and H. J. Scheel, *J. Cryst. Growth*, 1999, **200**, 435–440.

44 C. Krauns, M. Sumida, M. Tagami, Y. Yamada and Y. Shiohara, *Zeitschrift für Phys. B Condens. Matter*, 1994, **96**, 207–212.

45 L. Soler, *Liquid-assisted ultrafast growth of superconducting films derived from chemical solutions. PhD thesis, Universitat Autonoma de Barcelona*, 2019.

46 J. Jareño, *Growth of YBCO nanocomposite films through TLAG. PhD thesis, Universitat Autonoma de Barcelona*, 2020.

6

General conclusions and perspectives

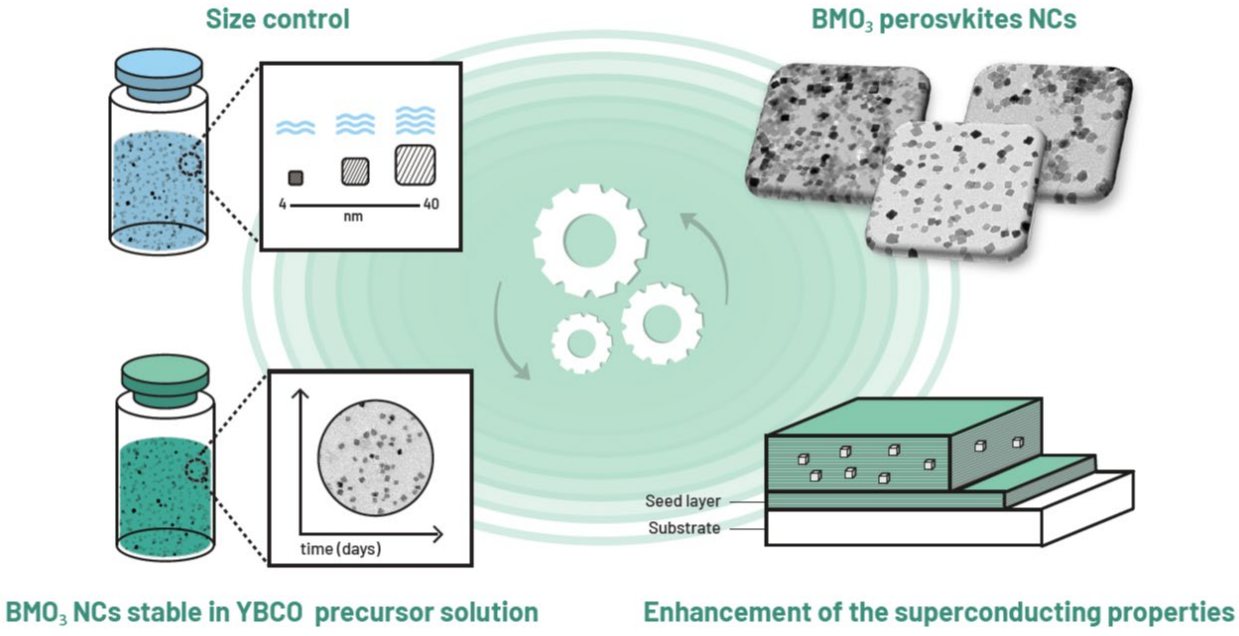

6.1. General conclusions

In this Thesis we report the insight of the BMO_3 NCs perovskites synthesis and we explore in detail the synthetic parameters aiming to provide a better understanding of the system. Overall, the studies performed during this thesis are a clear example of achievements obtained thanks to integrating as-synthesised NCs and their applications.

Here we summarized the most relevant aspects as an overview of the main conclusions of the entire work presented.

In this thesis, we have successfully synthesised $BaZrO_3$ NCs using a hybrid methodology which combines sol-gel reactions and a solvothermal route. In contrast with conventional solvothermal routes the dual-method we propose is faster and requires lower temperature. The NCs obtained have proven to be stable in alcohol media for at least 6 months with little requirements for proper storage. They remain monodisperse, exhibit a high crystallinity and show no tendency of agglomeration even after all this time stored.

A complete study of the parameters involved in the synthesis of these NCs has been performed, finding an optimal reaction temperature (180ºC) and duration (1 hour). The size of the NCs does not change with increasing temperature or the reaction time. Two factors are critical to control the size of the nanoparticles: water content in the sol-gel process and the polyol used as stabilizer. In this way, modifying the hydrolytic step (amount of water added), allowed us to obtain a wide range of sizes of the NCs (from 4 to 40 nm).

The compatibility of our sol-gel reaction with microwave activation has been also studied. The results highlight a significant reduction of reaction time from 1 hour in solvothermal route to 5 minutes using microwave activation. Of note, NCs obtained with traditional solvothermal route or microwave route described in this Thesis present similar characteristics.

We extended the hybrid methodology to the synthesis of other perovskites NCs from the same BMO_3 family by changing the tetravalent and the divalent cations. Changing the tetravalent cations with Ti^{4+} and Hf^{4+} atoms leads to a purely cubic-phase NCs ($BaTiO_3$ and $BaHfO_3$ NCs). A study over the synthetic parameters from $BaMO_3$ (M= Ti^{4+}, Zr^{4+} and Hf^{4+}) established a high similarity between $BaZrO_3$ and $BaHfO_3$ NCs sharing same process parameters (*i.e.,* reaction time, temperature reaction). Moreover, both follows the same mechanism for tailoring the NCs sizes by controlling the hydrolytic step.

In the case of $BaTiO_3$ NCs we have found that the process parameter are quite different compared to the other two cases ($BaZrO_3$ and $BaHfO_3$). First of all, $BaTiO_3$ NCs needs lower reaction temperatures (100 ^oC) in order to be fully formed. Also, the NCs sizes in this case is not dependent on the hydrolytic step, but on the amount of the metal precursors.

The exchanges of the B-sites, using Sr^{2+} instead of Ba^{2+} into BMO_3 (M= Ti^{4+}, Zr^{4+} and Hf^{4+}) NCs has led to a distortion in the perovskite crystalline structure. We have been able to successfully synthesis $SrTiO_3$ NCs that presents an ideal cubic structure. In the case $SrZrO_3$ and $SrHfO_3$ NCs the tolerance factor is 0.95 indicating that the final structure is distorted, shifting from the ideal cubic structure. Therefore, we realized that the hybrid methodology seems to show higher efficiency for those BMO_3 perovskites NC which follow an ideal cubic structure.

One of the applications of these BMO_3 NCs is their use as a secondary phase in High Temperature superconductor ceramic nanocomposites (YBCO). We have successfully implemented our $BaZrO_3$ and $BaHfO_3$ NCs in this application. These NCs have been found to be stable and compatible giving homogenous colloidal solution with all the types of the YBCO precursor solutions (TFA, LF and FF). We consider relevant to mention that the use of the preformed non-reactive perovskites-type NCs in superconductor nanocomposites has never been successfully achieved previous to this work.

Thick (~800 nm) and thin (~150 nm) YBCO nanocomposite layers have been successfully grown via chemical solution deposition. The nanocrystals remains stable and homogenously distributed within the YBCO matrix during the overall thermal process (both pyrolysis and growth). These layers exhibit enhanced performances compared to the pristine YBCO layers. This confirms the suitability of these NCs as artificial pinning centres. The proposed NCs do not show any pushing effect and do not react with the YBCO matrix. The only deviation observed is a slight increment in the size of these NCs after the layer's growth. This increase of the NCs size during the growth of the YBCO can be explained by migration of Y^{3+} in the perovskite structure BMO_3 of the NCs. A solution to this issue was found by doping BMO_3 NCs with Y^{3+}. We have successfully performed doping of $BaZrO_3$ NCs up to 10% of Y^{3+}. Size control of these NCs is still under study.

6.2. Future work

Even though this thesis has finished our investigation path has not. Still certain issues remain unsolved and should be addressed as future work.

The hybrid methodology that we present in this thesis can be further applied to a large range of other cations. For instance, could we use Pb^{2+} as a divalent cation? Could another tetravalent cation be used? Is this methodology only applicable to binary oxide NCs perovskites or could it be applicable to ternary oxide NCs perovskites too? All these questions could be a starting point to establish our methodology as a general pathway to synthesise several other NCs perovskites.

As expected in these complex nanoscales systems, there are still several parameters to control and to understand. Our next steps will provide better understanding of the NCs surface chemistry. A better control of these NCs surface could lead to better control of their stability a new range of solvents, thus opening a new horizon for further applications.

More efforts should be invested obtaining fully tetragonal $BaTiO_3$ NCs. The tetragonal phase generates excellent ferroelectric properties which could lead to interesting application such as ceramics capacitors, multiferroics and energy conversion.

Regarding the nanocomposite application the effect of Y^{3+} doped $BaZrO_3$ still needs to be addressed. We have to confirm whether 10 % Y^{3+} is the saturating level of doping or there is still room to achieve better control of final NCs sizes after the growth process. Besides, following up in the superconducting applications there is still plenty of new possibilities just applying these two NCs ($BaZrO_3$ and $BaHfO_3$). For instance, using new superconductors precursors solution in order to enhance the current density.

Scientific output

Conference contributions

- SolGel 2019, Saint Petersburg, Russian Federation. Poster presentation: "Tunable-sized perovskite BaMO3 (M= Ti, Zr and Hf) nanoparticles stable on YBa2Cu3O7 superconducting nanocomposites" **Natalia Chamorro**, Teresa Puig, Xavier Obradors, Ramón Yáñez, Susagna Ricart.3rd Scientific

- SolGel 2017, Liege (Belgium). Poster presentation. "Synthesis of ABO_3 perosvkites type nanoparticles" **Natalia Chamorro,** Josep Ros, Susagna Ricart and Ramón Yáñez.

- 7th International Colloids Conference Sitges (Spain) (2017). Poster presentation: "Colloidal solutions of nanoparticles for nanocomposite growth of functional oxides" **Natalia Chamorro,** Ziliang Li, Mariona Coll, Bernat Mundet, Jaume Gazquez, Teresa Puig, Xavier Obradors, Josep Ros, Susagna Ricart and Ramón Yáñez.

- NANOSELECT annual meeting, Sant Feliu de Guíxols (Spain) (2016). Poster presentation: "Synthesis of ABO3 perovskite type nanoparticles by polyol methodology" **Natalia Chamorro**, Susagna Ricart, Josep Ros and Ramón Yañez

- NANOSELECT annual meeting, Sant Feliu de Guíxols (Spain) (2017). Poster presentation: "Colloidal solution of nanoparticlesf for nanocomposite growth of

- functional oxides" **Natalia Chamorro**, Susagna Ricart, Josep Ros and Ramón Yañez

- AMAES Summer School, Cologne, Germany (2016). Poster presentation. "Synthesis of ABO3 provskite type NPs and its application in the ceramics nanocomposite functional film formation" **Natalia Chamorro,** Teresa Puig, Xavier Obradors, Susagna ricart, Ramón Yáñez and Josep Ros.

Publication in international journals

- **Chamorro, N.;** Martínez-Esaín, J.; Puig, T.; Obradors, X.; Ros, J.; Yáñez, R.; Ricart, S. Hybrid Approach to Obtain High-Quality BaMO 3 Perovskite Nanocrystals. *RSC Adv.* **2020**, *10* (48), 28872–28878. DOI: 10.1039/D0RA03861J

- Soler, L.; Jareño, J.; Banchewski, J.; Rasi, S.; **Chamorro, N.;** Guzman, R.; Yáñez, R.; Mocuta, C.; Ricart, S.; Farjas, J.; et al. Ultrafast Transient Liquid Assisted Growth of High Current Density Superconducting Films. *Nat. Commun.* **2020**, *11* (1), 344. DOI: 10.1038/s41467-019-13791-

- Li, Z.; Coll, M.; Mundet, B.; **Chamorro, N.;** Vallès, F.; Palau, A.; Gazquez, J.; Ricart, S.; Puig, T.; Obradors, X. Control of Nanostructure and Pinning Properties in Solution Deposited YBa 2 Cu 3 O 7–x Nanocomposites with Preformed Perovskite Nanoparticles. *Sci. Rep.* **2019**, *9* (1), 1–14. DOI: 10.1038/s41598-019-42291-

- Obradors, X.; Puig, T.; Li, Z.; Pop, C.; Mundet, B.; **Chamorro, N.;** Vallés, F.; Coll, M.; Ricart, S.; Vallejo, B.; et al. Epitaxial YBa 2 Cu 3 O 7– x Nanocomposite Films and Coated Conductors from Ba M O 3 (M = Zr, Hf) Colloidal Solutions. *Supercond. Sci. Technol.* **2018**, *31* (4), 044001. DOI: 10.1088/1361-6668/aaaad7